Thermography in semitransparent media based on mid-infrared thermotransmittance

Coline Bourges

université de BORDEAUX

THÈSE PRÉSENTÉE

POUR OBTENIR LE GRADE DE

DOCTEURE DE L'UNIVERSITÉ DE BORDEAUX

École Doctorale Sciences Physiques et de l'Ingénieur

Spécialité : Mécanique

Par **Coline BOURGES**

Thermographie dans des milieux semi-transparents à l'infrarouge par thermotransmittance

Thermography in semitransparent media based on mid-infrared thermotransmittance

---

Sous la direction de : **Stefan DILHAIRE**
Co-direction : **Christophe PRADERE**, Encadrement : **Stéphane CHEVALIER**

Soutenue le 12 septembre 2023

Membres du jury :

Mme. Agnès DELMAS	Maître de conférences HDR, INSA Lyon	**Rapporteure**
M. Jean-Laurent GARDAREIN	Professeur, Polytech Marseille	**Rapporteur**
M. Franck ENGUEHARD	Professeur, Université Poitiers	**Président**
M. Josep ALTET	Associate Professor, UPC Barcelone	**Examinateur**
M. Bruno QUESSON	Directeur de recherche, CNRS Bordeaux	**Examinateur**
M. Stéphane CHEVALIER	Maître de conférences, ENSAM Bordeaux	**Examinateur**
M. Christophe PRADERE	Directeur de Recherche, Epsyl	**Co-directeur**
M. Stefan DILHAIRE	Professeur, Université Bordeaux	**Directeur**
M. Jérémie MAIRE	Chargé de Recherche, CNRS Bordeaux	**Invité**

Remerciements

Au cours de ces trois années de thèse riches, tant sur le plan scientifique que personnel, j'ai eu la chance d'être soutenue par des personnes admirables qui m'ont aidée à me dépasser pour aller au bout de cette très belle aventure.

Je tiens tout d'abord à remercier mes deux rapporteurs de thèse, Agnès Delmas et Jean-Laurent Gardarein, qui ont chaleureusement accepté d'évaluer mes travaux, ainsi que pour les échanges très enrichissants lors de la soutenance. Un grand merci également à Franck Enguehard d'avoir présidé le jury, ainsi qu'à Josep Altet et Bruno Quesson d'avoir examiné ces travaux. A tous, j'ai apprécié vos remarques très enrichissantes lors de la soutenance.

Je souhaite également remercier mes encadrants de thèse auprès de qui j'ai grandi et appris durant ces trois années. Jérémie, nous avons fait ensemble nos premiers pas à l'I2M, et ça a été un plaisir de travailler avec toi. Stéphane, merci d'avoir gardé ta bonne humeur, même dans les moments difficiles, pour ton aide et tes conseils très précieux, et surtout merci de m'avoir fait confiance. Christophe, merci pour toutes ces discussions très enrichissantes, bien que non linéaires comme tu me l'as souvent mentionné, et surtout merci d'avoir été à l'écoute lorsque j'en ai eu besoin. Enfin Stefan, un très grand merci d'avoir rejoint cette aventure. En plus de nos échanges scientifiques où j'ai beaucoup appris, tu m'as permis de prendre confiance en moi. Je garderai très précieusement tous tes conseils.

Merci ensuite à tous les chercheurs de l'équipe pour leurs conseils au cours de ces trois années : Jean-Christophe Batsale, Jean-Luc Battaglia, Andrzej Kusiak, Emmanuelle Abisset-Chavanne, Fouzia Achchaq, Marie-Marthe Groz et Alain Sommier. Alain, merci pour ta bonne humeur, mais également pour tes conseils et ton aide très précieuse en instrumentation. Enfin Marie-Marthe, j'espère que nous aurons l'occasion de refaire des sorties musicales ensemble !

A toute la bande de la salle de manip, merci d'avoir égayé ces trois années. De belles rencontres, des sorties bienvenues mais aussi beaucoup d'entraide. Merci donc à Thomas et Hamza pour votre aide lorsque je suis arrivée au laboratoire, Marine, Kevin et Clément pour les nombreux fous rires, Théo pour ta bonne humeur communicative. Caroline, Zineb et Malo, vous avez été de supers colocataires de bureau, et enfin, merci à Hugo, Odelin, Alejandro, Célia et Florian !

Je tiens à remercier ma famille qui m'a toujours encouragée à faire ce que j'aimais. A mes parents pour avoir été à mes côtés et m'avoir soutenue jusqu'au bout, à mes frères pour leur bonne humeur inébranlable et leur soutien. Merci également à Catherine et Bruno pour tous vos encouragements.

Enfin, Théo merci de m'avoir soutenue dans les plus belles réussites comme dans les moments difficiles. Merci pour ta patience, tes encouragements et ton soutien quotidien. Merci de me suivre dans la suite de ces belles aventures. Merci.

Résumé

Ces travaux de thèse s'inscrivent dans le cadre du développement de méthodes de caractérisation non destructive multi-physique de nouveaux matériaux ou de systèmes énergétiques, et en particulier de la caractérisation de transferts de chaleur volumiques dans des milieux semi-transparents. En effet, le cas des milieux semi-transparents à l'infrarouge est actuellement peu abordé dans la littérature en raison de la difficulté à analyser le signal infrarouge émis par ces objets. Néanmoins, la propriété de semi-transparence permet de "voir à travers" le matériau et rendrait possible la mesure directe de sources volumiques en combinant la thermographie infrarouge à un dispositif d'imagerie tomographique. Ainsi, l'objectif de ces travaux de thèse est de développer et de valider une méthode de mesure quantitative de tomographie thermique pour caractériser des milieux semi-transparents. La méthode choisie est basée sur la dépendance en température des propriétés optiques des matériaux, et plus particulièrement les variations de leur transmittance en fonction de la température. Ce phénomène est appelé thermotransmittance : l'échantillon est éclairé par une source infrarouge, et les variations mesurées du signal transmis par l'échantillon sont directement proportionnelles à ses variations de température. Ainsi, connaissant le coefficient de proportionnalité entre ces deux grandeurs, le coefficient de thermotransmittance, il est possible d'obtenir des champs de température dans un milieu semi-transparent à partir des mesures du signal transmis. Finalement, la mesure de thermotransmittance combinée à un dispositif tomographique doit permettre de reconstruire des champs volumiques de température dans des milieux semi-transparents.

Le principal verrou scientifique identifié pour l'implémentation de cette méthode est le très faible niveau de signal de thermotransmittance mesuré en comparaison du bruit de mesure et du rayonnement infrarouge émis par l'objet et son environnement. Dans un premier temps, les travaux se sont donc focalisés sur le développement d'une méthode de détection du signal de thermotransmittance avec la mise en place d'un dispositif expérimental robuste aux bruits de mesure. Pour atteindre cet objectif un premier banc expérimental composé d'instruments sensibles mais mono-points (mono-détecteur, détection synchrone) a été développé. A priori, deux mesures à des températures différentes sont suffisantes pour mesurer un signal de thermotransmittance. Néanmoins, pour améliorer le rapport-signal à bruit, le choix a été de travailler avec une température de l'échantillon modulée, nécessitant une démodulation du signal mesuré par le détecteur infrarouge. La méthode est d'abord testée sur une lame de silicium d'épaisseur 250μm et de diamètre 50mm, dont les propriétés optiques sont constantes sur le spectre étudié. De plus ce matériau est un bon conducteur thermique ce qui permet de travailler à une température constante dans tout l'échantillon dans les conditions expérimentales choisie (fréquence d'excitation thermique de 10 mHz, variations de température de $\pm 10°C$). Un modèle thermique a été développé pour vérifier cette hypothèse de travail. Ainsi, ce premier banc expérimental 1D testé avec une lame de silicium a permis de valider la mesure d'un signal de thermotransmittance et d'extraire le coefficient de thermotransmittance de l'échantillon. Les résultats ont été comparés à la littérature à l'aide d'un modèle thermo-optique.

Après avoir validé la méthodologie avec des mesures mono-point, le travail s'est porté sur

l'adaptation du banc expérimental pour obtenir des cartographies 2D du champ de thermotransmittance d'un échantillon. Le détecteur mono-point a donc été remplacé par une caméra infrarouge, ce qui a nécessité de modifier tout le post-traitement des données expérimentales, y compris la méthode de démodulation du signal de thermotransmittance. De plus, afin d'imager des champs de température non-homogènes, l'échantillon de silicium a été substitué par une lame de verre Borofloat, d'épaisseur 500μm et de diamètre 50 mm, qui est plus isolant thermiquement. Néanmoins, dans cette étude, la température reste constante dans l'épaisseur de l'échantillon. Les propriétés optiques de ce matériau ont également l'avantage de ne pas être constantes dans la gamme spectrale étudiée, ce qui en fait un candidat intéressant pour analyser la dépendance spectrale du coefficient de thermotransmittance. L'étude de la lame de Borofloat a permis de mesurer ses propriétés thermiques (diffusivité et conductivité) ainsi que son coefficient de thermotransmittance. Le dispositif expérimental permet de détecter des variations de température de $0.5°C$ dans le Borofloat. De plus, comme le coefficient de thermotransmittance mesuré est dépendant de la longueur d'onde d'illumination, la question sur l'origine de ce signal s'est posée. Afin de mieux en comprendre la source, un modèle thermo-optique basé sur la théorie de Drude-Lorentz a été développé. Dans le cas du Borofloat, les variations du signal de thermotransmittance en fonction de la longueur d'onde viennent des variations de l'absorbance du matériau. Cela signifie que le signal provient du volume de l'échantillon, ce qui en fait un bon candidat pour développer le tomographe thermique.

La suite des travaux porte donc naturellement sur l'implémentation du tomographe thermique. La première étape consiste à générer un champ de température volumique non-homogène dans l'échantillon. Le choix a été de réduire la taille du dispositif de chauffage et la zone de mesure. Ainsi, de fines résistances métalliques en or alimentées par un courant modulé ont été déposées à la surface du nouvel échantillon (lame de verre d'épaisseur 2mm) pour le chauffer par effet Joule. De plus, la caméra infrarouge équipée d'un objectif de microscope permet d'atteindre une résolution spatiale de $15\mu m$/pixel. Dans cette nouvelle configuration, la température n'est plus constante dans l'épaisseur de la lame. Par conséquent, un nouveau modèle thermique a été développé pour décrire les transferts thermiques. De plus, la mesure de thermotransmittance à micro-échelle est combinée à une mesure 3ω qui permet de mesurer en parallèle les variations de température de la résistance métallique, afin d'avoir une sonde de température locale pour calibrer le coefficient de thermotransmittance de l'échantillon. Finalement, après calibration, la mesure de thermotransmittance donne la température moyenne dans l'épaisseur de l'échantillon.

Enfin, la dernière partie de ces travaux de thèse se concentre sur la reconstruction du champ de température volumique à partir des mesures 2D à l'échelle microscopique. Plusieurs dispositifs sont possibles pour réaliser une tomographie, le principe de base étant de mesurer le signal 2D transmis par l'échantillon pour plusieurs positions de ce dernier, et de reconstruire l'information volumique à partir des différentes mesures. En raison de la géométrie de l'échantillon étudié qui a un grand rapport d'aspect, la méthode retenue est la laminographie. Dans cette configuration, l'échantillon est incliné par rapport à l'axe optique puis tourne sur lui-même à l'aide d'un moteur de rotation. Une mesure du signal transmis est réalisée pour chaque angle de rotation. Associé à un algorithme spécifique de reconstruction 3D, le jeu de

données permet d'obtenir le champ volumique de l'objet étudié. Afin de valider dans un premier temps l'algorithme de reconstruction 3D, de premières reconstructions ont été réalisées sur des objets numériques. L'analyse des résultats obtenus a montré des artefacts dans la reconstruction ce qui nécessitera pour la suite des travaux d'améliorer l'algorithme de reconstruction. Néanmoins, malgré ces artefacts, nous avons montré que nous reconstruisons bien la forme de l'objet numérique 3D. L'étape suivante a donc été de réaliser de premières mesures, en laissant pour l'instant la thermique de côté, sur des échantillons tests parfaitement calibrés à l'échelle micrométrique. Cette étude préliminaire a permis de valider le dispositif expérimental et de déterminer la résolution de la reconstruction selon les trois directions (x, y, z). Finalement, en combinant la mesure de thermotransmittance au banc de laminographie, nous avons obtenu une première reconstruction de champ de thermotransmittance volumique dans une lame de verre, permettant notamment de localiser les points chauds.

Contents

List of Acronyms

1D, 2D, 3D	One, Two, Three Dimensions
BRDF	Bidirectional Reflectance Distribution Function
CL	Computed Laminography
CT	Computed Tomography
DAQ	Data AcQuisition system
DC component	Mean amplitude of a signal
DL	Digital Level
FBP	Filtered Back-Projection
FFT	Fast Fourier Transform
FT	Fourier Transform
FTIR	Fourier Transform InfraRed (spectroscopy or spectrometer)
InSb	Indium antimonide
IR	Infrared
IRT	InfraRed Thermography
LIA	Lock-In Amplifier
MRI	Magnetic Resonance Imaging
NIR	Near InfraRed
NUC	Non-Uniformity Correction
OCT	Optical Coherence Tomography
PID	Proportional Integral Derivative
PSD	Power Spectral Density
PSF	Point Spread Function
RMS	Root Mean Square
ROI	Region Of Interest
SNR	Signal-to-Noise Ratio
TCR	Temperature Coefficient of Resistance
TTC	ThermoTransmittance Coefficient
TTL	Transistor-Transistor Logic
USAF	United States Air Force

Nomenclature

Greek alphabet

Γ (Γ_0)	Transmittance (at ambient temperature)	-
$\Delta\Gamma$	Transmittance variation	-
ΔT	Temperature variation	K or °C
Δ_{res}	Residuals	DL
Φ_0	Incident IR flux	W/m^2
Φ_Γ, Φ_R	Transmitted and Reflected fluxes	W/m^2
Φ_{tot}	Total flux	W/m^2
α	Attenuation coefficient	m^{-1}
α_γ	Temperature coefficient of damping rate	K^{-1}
α_{ω_0}	Temperature coefficient of resonant angular frequency	K^{-1}
α_{ω_p}	Temperature coefficient of plasma pulsation	K^{-1}
α_n	Eigenvalue	m^{-1}
β	Temperature Coefficient of Resistance	K^{-1}
γ	Damping rate	s^{-1}
δ	Dirac Distribution	-
ε_∞	Dielectric constant	-
$\tilde{\varepsilon}_r$, ε'_r, ε''_r	Complex relative permittivity, real and imaginary parts	-
$\varepsilon_{\text{residuals}}$	Residuals	V or DL
ϑ	Azimuth coordinate	rad
κ	Thermotransmittance coefficient	K^{-1}
κ_R	Thermoreflectance coefficient	K^{-1}
κ_α	Thermo-absorbance coefficient	K^{-1}
λ	Wavelength	m
λ_0	Resonant wavelength	m
ξ	Laminographic angle	rad
ρ	Mass density	kg/m^3
ρ_{md}, ρ_{pix}	Proportionality factors	-
σ_x	Standard deviation of x	*x unit*
τ_c	Time constant	s
τ_{cam}	Camera time step	s
ϕ	Phase	rad
φ	Flux	W/m^2
ψ	Rotation angle	rad
ω	Angular frequency	rad/s
1ω, 2ω, 3ω	Angular frequencies of the 3ω method	rad/s

ω_0	Resonant angular frequency	rad/s
ω_c	LIA cutoff angular frequency	rad/s
ω_T	Thermal angular frequency	rad/s

Latin alphabet

A	Absorbance	-
Bi	Biot number	-
$\mathcal{C}$	Contrast	-
E	Parasitic signals	W/m^2 or DL
H	Loss factor	m^{-2}
$\mathcal{H}$	Transfer function	-
I, I_0	Current	A
$\mathcal{I}_0$	Modified Bessel function of first kind	-
$\mathcal{J}$	Cost function	
$\mathcal{K}_0$	Modified Bessel function of second kind	-
L_o	Optical path (laminography)	m
L_x	Distance along the x-axis	m
L_z	Thickness	m
$\mathcal{M}$	Matrix	*depending on the context*
$\mathcal{P}$	2D Projection	*depending on the context*
R_Ω ($R_{\Omega,0}$)	Resistance (at ambient temperature)	Ω
R (R_0)	Reflectance (at ambient temperature)	-
$S_x[y]$	Sensitivity of x to the parameter y	*x unit*
T	Temperature	K or °C
T_0	Ambient temperature	K or °C
T_{CAM}	Camera temperature	K or °C
$U_{\mathrm{LIA}}^{\mathrm{LP}}$	LIA output signal	V
U_S	Signal measured by the mono-detector	V
U_R	Reference signal	V
U_{pix}	Signal measured by one pixel	DL
a	Thermal diffusivity	W/m^2
c_p	Specific heat capacity	$J/m^2/K$
f	Frequency	Hz
f_c	Chopper frequency	Hz
f_I	Current frequency	Hz
f_T	Thermal frequency	Hz
h	Convection coefficient	$W/m^2/K$
i	Imaginary unit	-
k	Thermal conductivity	W/m/K

$\tilde{n}$, n', n''	Complex refractive index, real and imaginary parts	-
r	Radial distance	m
r_0	Radius	m
t	Time	s
t_{int}	Integration time	s
(u, v)	Coordinates of measured projections	-
x	Pixel/voxel coordinate (columns)	-
y	Pixel/voxel coordinate (lines)	-
z	Voxel coordinate (depth)	-

Physical constant

c	Speed of light	3×10^8 m/s

Chapter 1

Introduction

Contents

1.1 General context

I conducted my thesis work at the I2M laboratory within the ICT team (*Imagerie et Caractérisation Thermique*). The main activity is the non-destructive quantitative thermal characterization of multi-scale systems and materials, such as multi-layers or microfluidic cells. The methods used by the research team combine infrared thermography and inverse methods to characterize heat and mass transfer, or the chemical composition of systems. However, regarding complex systems with sophisticated geometries or inhomogeneous media with volumetric temperature gradients, we need a priori knowledge to be able to use inverse methods (thermal properties, structure of the material...). Therefore, the need for multi-physical tomography measurements is growing, and specially at the micrometric scale to address the study of miniaturized energy systems.

Two options are available to conduct 3D characterization of heat transfer in a sample. If the material is opaque, one can perform a temperature surface measurement and use inverse methods to reconstruct the volume. This is efficient for media whose structure and thermal properties are known: inversion is possible although limited by measurement noise. This method is already performed by the team. On the other hand, if the sample is semitransparent, one can perform direct 3D measurements which allows to address more complex geometries without prior knowledge of the system. This technique enables the determination of the thermal properties of complex systems using a single tomography and a suitable model.

In the thermal community, this approach on semitransparent media is not yet well matured. Therefore, this thesis work aims to propose an experimental setup and associated post-processing methods for direct measurement of the 3D temperature field of a semitransparent system. We focus on contactless techniques not to damage the sample which is now a prerequisite for many industrial applications, and not to disturb the heat transfer under study.

As a result, the first step is to identify a contactless method suitable for measuring volumetric temperature fields in semitransparent media.

In addition, this thesis includes microscale measurements to characterize micro-systems in future work, for instance monitoring heat transfer in microfluidic cells, already studied in the laboratory. Measurement timescales are of the order of a few seconds/minutes, but we have taken care to choose a method that can operate at faster rates if required.

1.2 Contactless temperature sensing

First, we present existing contactless 2D temperature techniques to identify a candidate for tomography measurements. This section reviews contactless temperature sensing in opaque and semitransparent materials, and particularly in the mid-infrared range although some techniques can be used in other spectral ranges. We highlight the pros and cons of the different methods, and explain why we have chosen to explore thermotransmittance.

Opaque materials

Most contactless temperature sensing methods are developed for opaque materials in the mid-infrared or visible range. Although we do not study these media in this work, the techniques presented are interesting as they can be adapted for use with semitransparent materials. This section introduces the principle of infrared thermography and thermoreflectance. Both techniques allow imaging measurements, using either an infrared camera as a detector, or a scanning device.

Infrared thermography (IRT)

A popular method is the infrared thermography, which is based on the detection of the emission of a material depending on its temperature according to the Planck law [1]. These radiations, also called proper emission in this study, are weighted by the sample emissivity, $\varepsilon_m \in [0-1]$, which depends on the wavelength, temperature, or surface roughness, among others [2].

Two techniques are used in IRT: active and passive methods [3]. Passive thermography enables to observe the IR radiations from an object without interacting with it [4], for instance to detect heat leakages, or control electrical installations. Active thermography [5] consists in heating the sample to highlight cracks [6], or to measure its thermal properties such as thermal diffusivity [7, 8], emissivity [9], or determine thermal resistances between several layers [10]. Multiple techniques are used to heat the sample: flash excitation [11], flying-spot [12], pulsed or modulated excitation [13] such as lock-in thermography [14]. This last technique is more robust to measurement noise, and we use this methodology in our work. In addition, IRT measurements cover a wide range of spatial and temporal scales, from kilosecond measurements of building heat leakage [4] to nanosecond thermal characterization of nanometric multi-layers

[15].

Furthermore, IRT allows temperature measurement by converting the signal measured by the IR detector into Kelvin [16, 17]. This operation requires a calibration procedure using a blackbody to have the correspondence between the measured signal and the temperature of the blackbody [18, 19]. In addition, the material to be characterized must have a known emissivity or must be coated with a paint whose emissivity is close to 1 (i.e. black body configuration). This last option has two main disadvantages: it damages the material and the paint can interfere with measurement, particularly with micro devices. The calibration is only valid at a fixed distance from the sample [20], and the same experimental conditions used for calibration must be maintained (optics, solid angle, ambient temperature), which is very restrictive. As a consequence, this method is perfectly adapted for opaque materials with emissivity close to 1, but more restrictive for highly reflective or semitransparent media which require surface coating or an additional calibration [21]. In the next section, we will discuss extending IRT to semitransparent media. The following method is well suited to highly reflective media in the IR or visible range.

Thermoreflectance

To deal with highly reflective and opaque materials, such as metals or samples with metal transducer at their surface, an appropriate technique is thermoreflectance [22]. Since the optical properties of materials vary with temperature [23], the reflectance at the surface of the material is a function of temperature. When the sample is illuminated with a monochromatic incident flux Φ_0, the reflected flux $\Phi_0 R(T)$ varies with temperature, through the reflectance coefficient $R(T)$. At first order, the relative variations of R are proportional to the temperature variations ΔT: $\Delta R/R = \kappa_R \Delta T$. The proportionality factor, κ_R (K^{-1}), is the thermoreflectance coefficient which depends among others on the illumination wavelength, the material, or the roughness [24].

This technique is widely used to characterize the thermal conductivity and interfaces of thin multi-layer materials at the nanometric scale [25, 26]. Here is a non-exhaustive lists of techniques based on thermoreflectance showing the importance of this method: time-domain thermoreflectance [27, 28], frequency-domain thermoreflectance [29, 30], or CCD-based thermoreflectance [31, 32] (see the review [33] for pros and cons of each methods and their applications). In addition, thermoreflectance can be used to measure the temperature of the materials, by first calibrating the thermoreflectance coefficient [34, 35].

The great advantage of thermoreflectance is the spatial (nanometer) and temporal ($<$ picosecond) resolution that can be achieved, enables characterizing nanometric materials and phonon and electron behavior with temperature for instance. However, the thermoreflectance coefficient is weak, $\kappa_R \in [10^{-5} - 10^{-3}]$ K^{-1}, which means that to detect small temperature variations $\Delta T < 1$ K, it is essential to improve the signal-to-noise ratio (SNR) and work with highly sensitive detectors. Most of the time the illumination source is a laser, and the heat excitation of the sample is modulated or repetitively pulsed to improve the SNR.

Finally, thermotransmittance is suitable for reflective material, but is significantly less sensitive to absorbent media: the thermal signal must comes from interfaces of the sample and not from its volume to be measured. Nevertheless, a similar technique, but sensitive to volume absorption, would be perfectly suited to our problem. We discuss this technique, namely thermotransmittance, in the next section.

To conclude, IRT and thermoreflectance enable contactless thermal properties and temperature measurements in opaque and reflective media, each addressing different materials and applications. The next section describes similar methods, based on same phenomena, adapted to semitransparent media.

Semitransparent materials

In this thesis work, the semitransparent materials under study are non-scattering at their surface as their roughness is much lower than the illumination wavelength $\lambda \in [2-6]$ µm, and the reflectance at their surface is considered specular. All our samples are double-side polished to remain in this working hypothesis. In addition, we use homogeneous materials, whose scattering in the volume is negligible compared to the absorbance. We develop the experiment mainly using a double-side polished glass wafer. In addition, these materials can reflect or absorb a part of the incident light, as shown in Figure 1.1.

We now present some contactless methods to measure temperature of semitransparent materials, without coating them. First, we introduce the IRT applied to semitransparent media. Second, we discuss Raman thermometry and, third, we detail the principle of thermotransmittance, which is similar to thermoreflectance.

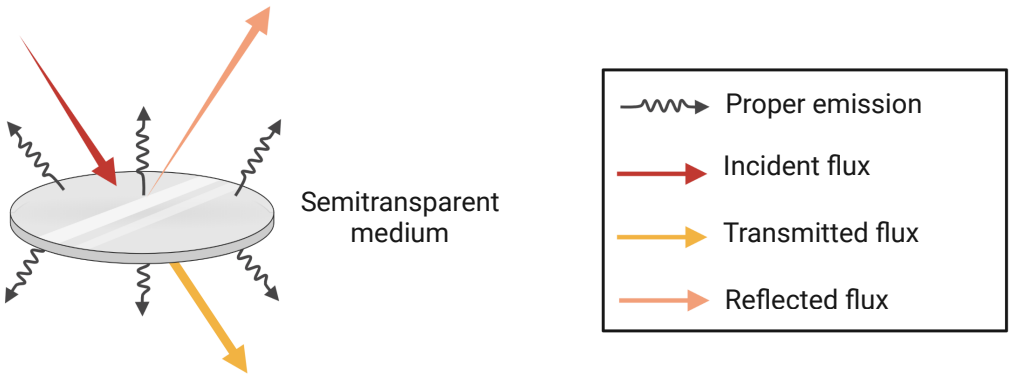

Figure 1.1 – IR radiations interactions with a semitransparent medium.

IRT applied to semitransparent materials

Measuring temperature in semitransparent media using IRT is much more challenging than in opaque one. The proper emission comes from the two material surfaces, but also from its

volume. The emissivity is no longer defined for these materials: one uses the apparent emissivity [36] or emittance [37]. In addition, it is essential to consider the radiations from the environment, which are reflected, absorbed, and transmitted through the material [38].

Because of these challenges, IRT in semitransparent media is not yet widely used, although several groups are interested in it and develop specific calibration processes. For instance, some works measured the emittance, such as [39, 38, 40, 41], but the definition may vary from one study to another, and not always take into account the direction of radiations. Other works focused on thermal properties measurements of these materials, such as the thermal diffusivity [42]. In this thesis work, we propose an alternative method that does not require the knowledge of the emittance of the medium and allows to discriminate the signal of interest from the radiation coming from the environment.

Raman thermometry

It is also interesting mentioning Raman spectroscopy [43, 44] for a more exhaustive overview of contactless temperature measurements in semitransparent media. This method consists in illuminating the sample, generally in the visible spectrum, and measuring the scattered light. Due to the Raman phenomenon, a part of the scattered light has a different energy from the incident light. After analyzing this signal [45], we obtain a spectrum with peaks corresponding to the vibrations of molecules within the material.

Raman spectroscopy is a widely used technique to analyze the molecular composition, bonding, and crystallographic structures of materials [46, 47]. The position and width of Raman peaks vary with temperature [48], which had convey to the development of Raman thermometry [49, 50, 51, 52, 53]. In addition, confocal Raman can be used to measure 3D composition of materials [54]. As a consequence, Raman thermometry should be a good candidate for measuring temperature fields in semitransparent media by combining both confocal and thermometry techniques.

However, the Raman signal is weak since the phenomenon affects about 1 photon over 1 million [33]. Thus, measuring the Raman signal requires a laser, filters to eliminate unwanted photons, a sensitive detector, and a long acquisition period. Furthermore, detecting the thermal dependency of the peaks requires even more signal, making measurement very challenging or impracticable for weak or no Raman active materials, such as metals or amorphous materials [33, 55]. Since we do not have a Raman instrument at our disposal, and it is not guaranteed that we will be able to measure the Raman thermal signature of our samples, we have not chosen this method to develop our 3D thermograph.

Thermotransmittance

Finally, we introduce the thermotransmittance phenomenon, which is similar to thermoreflectance. Since it is possible to measure the thermal dependence of the light reflection using thermoreflectance, it is also possible to detect the temperature dependence of the transmitted

light in non-opaque materials [56]. This technique is called thermotransmittance. The thermotransmittance signal is directly proportional to the temperature variations of the sample, as explained in section 1.3. As a consequence, to measure temperature using thermotransmittance, we need the proportionality factor: the thermotransmittance coefficient κ (K^{-1}). Unfortunately, there is no database on the coefficient κ. Nevertheless, we can calculate κ with the thermal dependency of the refractive index of materials, $\tilde{n}$, characterizing the ability of a medium to interact with light (see section 1.3 and appendix B). This property is often measured but mostly in the visible or NIR range [57].

Preliminary studies reported promising results in calibrating the thermotransmittance coefficient for various materials across different spectral ranges, including mid-infrared [58] and terahertz [59]. Additionally, works demonstrated the temperature dependency of absorbance in water-ethanol mixtures within the near-infrared spectrum [60, 61]. As the thermotransmittance signal is affected by both absorbance and reflectance variations (see section 1.3), it has potential applications for diverse semitransparent media, providing either a measurement of thermoreflectance, thermo-absorbance, or a combination of both. Finally, these studies showed that the thermal dependency of absorbance/transmittance varies with the illumination wavelength. As a result, it should be possible to differentiate several components of a semitransparent media depending on their thermotransmittance coefficient behavior as a function of the wavelength, provided the initial spectrum of each component is known.

However, similarly to thermoreflectance, the thermotransmittance coefficient in the mid-IR is usually weak, about 10^{-4} K^{-1}. Therefore, it is essential to heat the sample sufficiently and use sensitive detectors (in the work [58] $\Delta T = 120$ K and detector with a dynamic range of 2^{16}). In addition, to our knowledge, there are no studies that differentiate the contribution of the absorbance and reflectance in the thermotransmittance signal. This information is important because the absorbance provides information of temperature within the volume of the material, whereas reflectance gives information about the temperature of the interfaces of the sample. To develop a 3D thermograph, measurements must be sensitive to the temperature within the volume through absorbance changes with temperature. Consequently, we must carefully select a suitable sample.

Conclusion about contactless temperature sensing

We have presented a brief overview of some commonly used contactless methods for measuring temperature fields in materials. The Raman thermometry is a specific method which addresses Raman-active materials. With the equipment at our disposal, it was not feasible to develop a 3D imaging Raman thermometry setup.

Regarding infrared thermography, the method is much more mature on opaque or black-painted media in the group. Nevertheless, it may be adapted to semitransparent media even though it requires measuring the sample emittance and calibrating the signal recorded by the camera. Emittance measurement is challenging and difficult to define when addressing semitransparent multilayers. Therefore, we have selected a method that enables us to control the

source and trajectory of the measured signal, namely thermotransmittance.

Finally, the thermotransmittance phenomenon is an excellent candidate to perform 3D measurements of semitransparent materials, provided the sample under study absorbs a part of the incident light. Nevertheless, due to the weak thermotransmittance coefficient of materials, we have developed strategies to improve the SNR of the measurements. The following section develops the thermotransmittance principle to understand the different challenges associated with the technique.

1.3 Thermotransmittance working principle and modeling

This section describes the working principle of thermotransmittance. First, the transmitted signal through a non-scattering media is detailed. Second, we introduce the thermal dependence of this signal and present the working hypotheses used in the different parts of this manuscript.

Transmittance of a semitransparent material

When a monochromatic incident flux Φ_0 illuminates a semitransparent material, a part of the flux is reflected at the material surface, and a part is transmitted through the sample [62] depending on the reflectance coefficient R_0, as illustrated in Figure 1.2. As it passes through the medium, the flux is attenuated by the attenuation coefficient α_0 (m^{-1}) within the thickness L_z (m) of the material. At ambient temperature, the transmitted flux is written $\Phi_\Gamma = \Phi_0\Gamma_0$, with Γ_0 the transmittance of the material which is expressed in the following equation.

$$\Gamma_0 = [1 - R_0]^2 e^{-\int_0^{L_z} \alpha_0(z)dz} \tag{1.1}$$

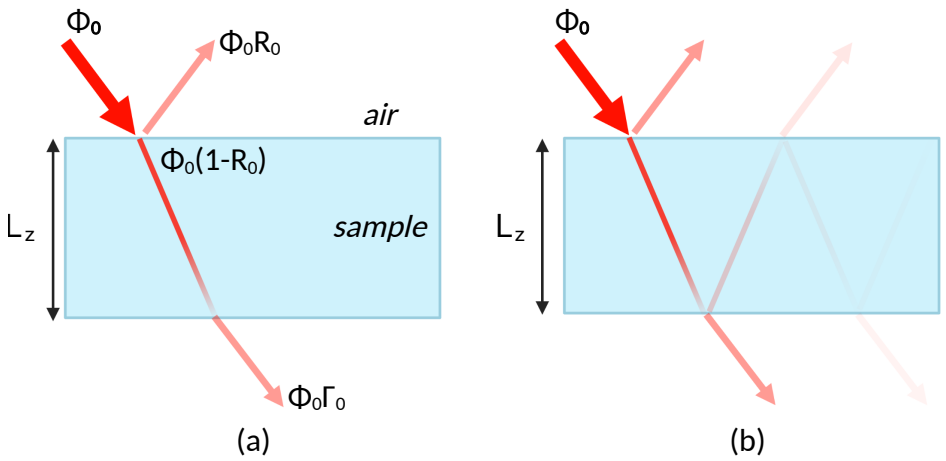

FIGURE 1.2 – (a) Illustration of a light beam path in a semitransparent medium. (b) Illustration of multiple reflections within the sample.

In addition, multiple reflections occur in the medium as a part of the flux is reflected on the second surface, as illustrated in Figure 1.2 (b). The total transmittance is the sum of the components of multiple reflections, and is expressed in equation 1.2.

$$\Gamma_{\text{tot}} = [1 - R_0]^2 e^{-\int_0^{L_z} \alpha(z)dz} \sum_{n=1}^{\infty} R_0^{2(n-1)} e^{-2(n-1)\int_0^{L_z} \alpha(z)dz} \tag{1.2}$$

In practice, the first component is much more significant than the others. Here, for simplicity, we introduce the principle by considering only equation 1.1 and ignoring the multiple reflections. In calculating the optical properties later in this thesis, the multiple reflections have been accounted for.

Expression of the thermotransmittance

Since the optical properties of a material vary with temperature [63, 64, 65, 66], we express the equation 1.1 as a function of temperature in the general case, where both surfaces of the sample are not necessarily at the same temperature.

$$\Gamma(T) = \underbrace{[1 - R(T_1)]}_{\text{Surface 1}} \underbrace{[1 - R(T_2)]}_{\text{Surface 2}} \underbrace{e^{-\int_0^{L_z} \alpha(z,T_z)dz}}_{\text{Volume}} \tag{1.3}$$

The thermal dependency of transmittance comes from both the reflectance and the attenuation coefficient. At the first order, their temperature variations are expressed in the equations 1.4 and 1.5, with $\Delta T = T - T_0$ the temperature variation, κ_R the thermoreflectance coefficient (K^{-1}), and κ_α the thermo-absorbance coefficient (K^{-1}).

$$R(T) = R_0[1 + \kappa_R \Delta T] \tag{1.4}$$
$$\alpha(T) = \alpha_0[1 + \kappa_\alpha \Delta T] \tag{1.5}$$

By injecting 1.4 and 1.5 in the expression 1.3 and linearizing the exponential term, the thermotransmittance relation at first order is given in the following expression (see Appendix A for details).

$$\frac{\Delta\Gamma(T)}{\Gamma_0} \approx \underbrace{-\frac{R_0\kappa_R}{1 - R_0}[\Delta T_1 + \Delta T_2]}_{\text{reflectance}} \underbrace{- \alpha_0\kappa_\alpha \int_0^{L_z} \Delta T(z)dz}_{\text{absorbance}} \tag{1.6}$$

As a result, the reflectance part gives information about the temperature variations at the surfaces of the sample, whereas the absorbance provides information on the temperature gradient through the thickness. In the following, we distinguish two cases of applications:

- In the first part of the manuscript, we consider a uniform temperature along the material thickness ($\Delta T_1 = \Delta T_2 = \langle \Delta T \rangle_z = \Delta T$). The thermotransmittance has a simple expression:

$$\frac{\Delta\Gamma(T)}{\Gamma_0} = \kappa\Delta T \tag{1.7}$$

κ is the thermotransmittance coefficient (K^{-1}) which contains both absorbance and reflectance thermal dependencies.

- In the second part, we focus on measuring 3D temperature field in the material. For that, we select a material whose absorbance is primarily responsible for thermal dependency, and neglect the impact of reflectance. In that case, the thermotransmittance expression is expressed as:

$$\frac{\Delta\Gamma(T)}{\Gamma_0} = \kappa\frac{1}{L_z}\int_0^{L_z}\Delta T(z)dz \tag{1.8}$$

Note that the equation is weighted by the thickness of the material to get a thermotransmittance coefficient in K^{-1} and be consistent with the first case (eq. 1.7).

In addition, the optical properties of materials depend on the wavelength λ of the incident light. As a consequence, the thermotransmittance coefficient $\kappa(\lambda)$ is also a function of the wavelength, and it is more interesting to perform measurements at some wavelengths [61] than others to maximize the signal. However, few works studied how temperature affects the optical properties of semitransparent media, particularly in the mid-infrared spectrum. Most of the time, researchers focused on metals [67, 68, 69] and/or worked on the visible spectral range [70, 71].

Due to the lack of literature, we have developed a model to forecast the thermotransmittance coefficient based on the wavelength, and distinguish between the contributions of reflectance and absorbance in order to select a material for 3D measurements. To perform such a study, we have used the Drude-Lorentz model [72, 73, 74] which describes the response of a material to an incident electromagnetic wave, through the *relative permittivity* $\tilde{\varepsilon}_r(\lambda, T)$ [75, 76]. This property is then linked to the attenuation coefficient and reflectance of the material [62]. All these expressions are detailed in the Appendix B.

1.4 Objectives of the thesis work

As a reminder, the final objective of this thesis work is to measure 3D heat transfer in microscale semitransparent materials. We have identified that thermotransmittance is an excellent candidate for conducting such measurements. In order to reach our objective, we address the following challenges:

→ Development and validation of the thermotransmittance imaging technique, since this measurement was not available in the laboratory at the beginning of the thesis. The main challenge is to detect the signal since the thermotransmittance coefficient is weak, about 10^{-4} K^{-1} depending on materials and illumination wavelengths.

→ Calibration of the thermotransmittance coefficient to convert the measured signal into temperature, which requires the knowledge of the sample temperature using heat transfer model, measurement, or a combination of both.

→ Selection of an appropriate sample to develop the 3D thermotransmittance experimental setup. As mentioned in the previous section, the signal of interest must come from the volume of the sample through its absorbance.

→ Development and validation of a tomographic experimental setup at the micrometric scale, and integration of thermotransmittance measurement in the tomograph.

To develop the 3D thermograph, the work was gradually extended from 1D measurements on macroscopic sample to 3D measurements on microscopic sample. This manuscript is divided into two parts, each with two chapters. The main objective of the **Part 1** is to develop and validate the imaging thermotransmittance experimental setup with macroscopic simple media whose temperature is constant along their thickness (eq. 1.7).

- In chapter 2 we use high sensitive but single-point instruments to improve the signal-to-noise ratio and ensure measurement of a thermotransmittance signal. Additionally, we develop a heat transfer model to determine optimal measurement conditions. In this section, we choose a straightforward sample with non-dispersive optical properties within the studied spectrum.

- In chapter 3 we upgrade the setup from single-point to imaging. Furthermore, we change the sample to a more sophisticated one whose thermo-optical properties vary with the wavelength which allows us to study the origin of the thermotransmittance signal. To better understand the thermal dependency of the optical properties and determine if the sample suits tomographic development, we implement the Drude-Lorentz model.

Part 2 focuses on the implementation of the microscale tomographic setup.

- Chapter 4 presents the microscopic sample designed for tomography development, with a non uniform temperature along its thickness. We upgrade the setup described in Chapter 3 to perform microscopic thermotransmittance measurement. Then, we measure the 2D thermotransmittance field of the microscopic sample as an average of the temperature within its thickness.

- In chapter 5 we discuss the options for tomographic measurements and explain why we choose laminography. The laminography experimental setup is presented, as well as the tomographic reconstruction algorithm. Finally, we comment the first measurements of 3D thermotransmittance at the micro-scale.

Part I

Development of the modulated thermotransmittance measurement

Chapter 2

Single-point thermotransmittance methodology

Contents

2.1 Introduction

This part describes the experimental setup developed to measure the thermotransmittance signal of semitransparent materials. We study two cases that enable us to validate and improve the method in order to progress towards 3D temperature field measurement.

- First, we start with silicon, an optically non-dispersive material in the mid-infrared spectrum. Its thermo-optical properties remain constant in the spectral range under study. We used highly sensitive but single-point instruments, which enable us to validate the measurement method without being limited by the SNR.
- In a second step described in chapter 3, we upgrade the setup from a single-point to a 2D measurement, using an infrared camera as a detector. In addition, we switch to a more sophisticated sample whose thermo-optical properties vary with wavelength.

In all our operating conditions, the temperature is constant along the thickness of the sample to avoid us to deal with the in-depth temperature profile. The corresponding thermotransmittance expression is given in equation 2.1, with $\Delta T = T - T_0$ (K) the temperature

variation, and Γ the transmittance of the sample. In the second part of the manuscript, we extend the measurements to 3D temperature field reconstruction.

$$\frac{\Gamma(T) - \Gamma(T_0)}{\Gamma_0} = \kappa \Delta T \tag{2.1}$$

As mentioned in the introduction, only a limited amount of literature is available on the thermotransmittance coefficient κ and on the thermal dependency of the optical properties of materials in the mid-infrared range. In terms of optical properties, most of the time there is no information on absorbance, and databases are often derived from modeling. As a consequence, we cannot calculate κ from the optical properties in the studied spectrum. To measure the temperature using thermotransmittance, we first calibrate the thermotransmittance coefficient. This process requires measuring the thermotransmittance signal, $\Delta\Gamma/\Gamma_0$, and knowing the corresponding temperature variation ΔT. In this thesis work, we combine measurements and modeling to estimate ΔT.

To obtain the thermotransmittance signal, we need to measure the transmittance $\Gamma(T)$ of the sample at different temperatures. Several options are possible:

- A priori, two measurements are enough to obtain κ, for instance at T_1 and T_2 [58]. However, this method is not efficient: due to the low thermotransmittance signal, the measurement is strongly affected by the measurement noise. In addition, the signal detected by the devices is likely to drift during the time needed to reach the second temperature setpoint. As a consequence, it is much easier to measure the drift of the devices than the thermotransmittance signal if the heating is low and/or the dynamic range of the detector is limited. After several unsuccessful attempts, I do not recommend this method.

- Another option is measuring the transmitted IR signal in the transient regime. Again, this type of measurement is sensitive to the measurement noise but more robust against instrument drifts. However, it is challenging to ensure that the temperature is homogeneous in the thickness of the material. This method can be interesting for a heat-conducting material but is not adapted to insulators. I did not retain this option either.

- A third approach is modulating the sample temperature at a low enough frequency f_T to limit the thermal gradient in its thickness. The temperature of the sample, $T(t)$, is given in the equation 2.2. As a result, the sample transmittance is also modulated at the thermal frequency f_T (see equation 2.3).

$$T(t) = T_0 + \Delta T \cos(2\pi f_T t) \tag{2.2}$$
$$\Gamma(t) = \Gamma_0[1 + \kappa \Delta T \cos(2\pi f_T t)] \tag{2.3}$$

  By demodulating $\Gamma(t)$, we get the DC component Γ_0 and the f_T component $\Gamma_0 \kappa \Delta T$ from which the thermotransmittance coefficient κ can be extracted, knowing the temperature

variation ΔT. The great advantage of the modulation/demodulation method is that it filters out measurement noise and parasitic radiations. This is the reason why I chose it.

The chapter describes the experimental setup for measuring the thermotransmittance signal applied on a thin silicon wafer. We provide details on the heating system and the acquisition chain. To discriminate between the thermotransmittance and the sample proper emission signals, we modulate the IR source in addition to the temperature. We detail the double-demodulation method to extract the term $\Delta\Gamma/\Gamma_0$, and the model required to determine the sample temperature variation ΔT. Finally, we present the calibration of the thermotransmittance coefficient, κ, knowing $\Delta\Gamma/\Gamma_0$ and ΔT, and compare the results to the literature using optical modeling.

2.2 Modulated single-point thermotransmittance experimental setup

This section presents the method to measure the thermotransmittance signal applied to a wafer of silicon. The following elements are needed:

1. A monitored heating system to modulate the temperature of the sample.
2. An infrared source combined with a detector to measure the thermotransmittance signal.
3. A hardware device or post-processing algorithm to demodulate the measured thermotransmitted signal.

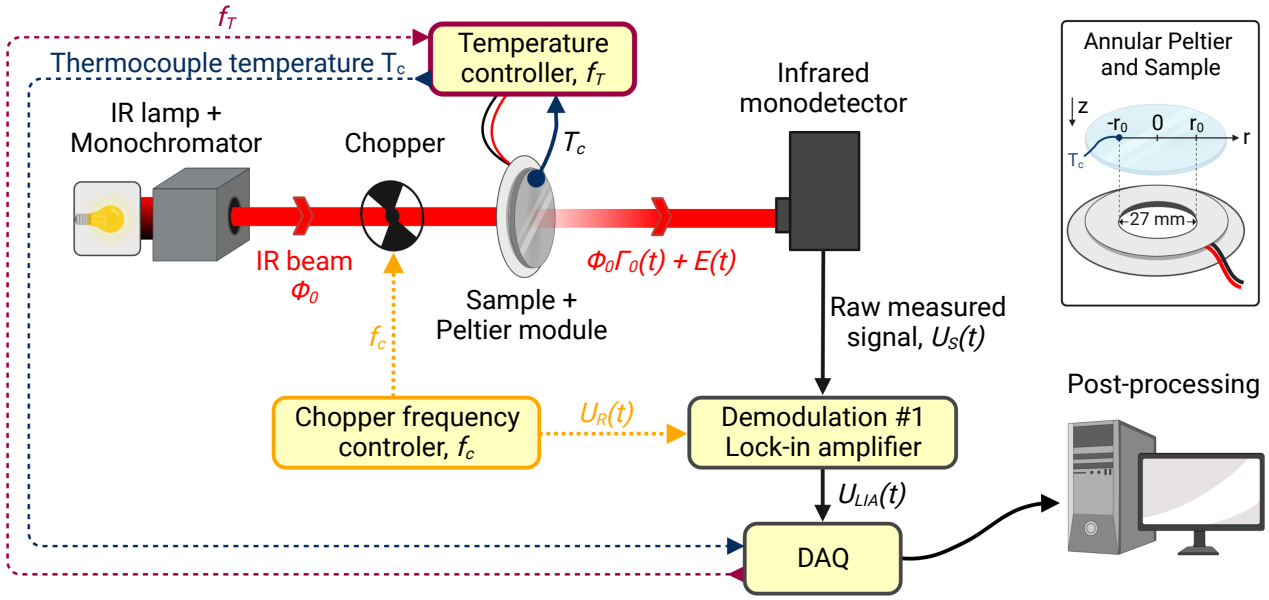

FIGURE 2.1 – Illustration of the experimental setup for single-point thermotransmittance measurements. The insert shows the Peltier module and its dimensions.

Heating the sample

To study the induced variation of its transmittance, the sample is first heated by an ring-shaped Peltier module. The geometry of the Peltier module is essential to let the light pass through the sample. The temperature is modulated around T_0, at the thermal frequency f_T (see equation 2.2). Due to the limitation of the Peltier module, we cannot exceed an excitation frequency of a few tens of mHz to get a temperature rise of several degrees. Typically, the temperature variation, $\Delta T(r_0)$, is set at 10°C, and $T_0 = 30$°C. A homemade LabView PID controller combined with a thermocouple integrated into the Peltier module guarantees temperature monitoring as illustrated in Figure 2.2. However, this technique does not provide a stable reference signal of the modulation frequency f_T, which has an impact on the choice of the demodulation method as detailed in section 2.3.

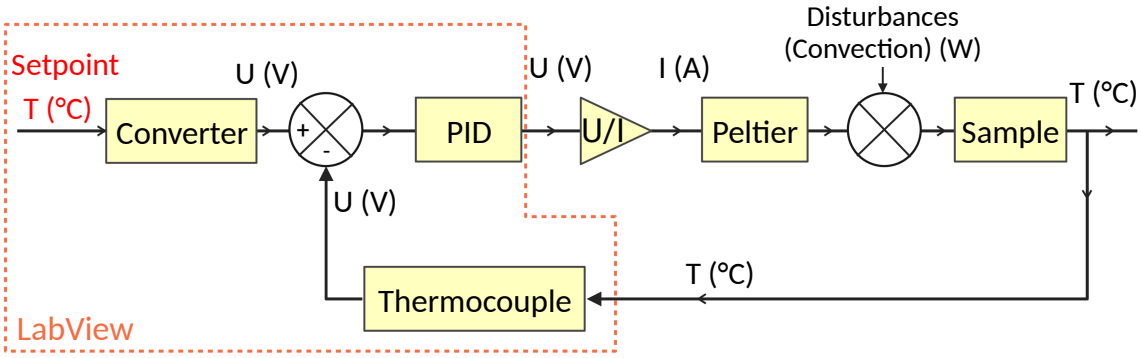

FIGURE 2.2 – Diagram of the temperature regulation, using a homemade LabView program.

Infrared source and detector

The sample is illuminated by an infrared flux Φ_0 coming from a stabilized black-body source (IR-Si217, $T_{\text{source}} = 1385$°C), as illustrated in Figure 2.1. We can select the illumination wavelength thanks to a monochromator with a motorized diffraction gratings (Bentham Instruments, TMc300).

Then, the infrared flux transmitted through the sample, $\Phi_0\Gamma(t) = \Phi_0\Gamma_0[1+\kappa\Delta T\cos(2\pi f_T t)]$, is recorded by using a Indium Antimonide (InSb) mono-detector (Teledyne Judson Technologies, J10D). Its spectral range is $\lambda \in [1-5.5]$ μm with optimum performances between 3.5 μm and 5 μm (see figure 2.3), and the size of its active pixel is 0.1 mm (diagonal). The device converts the total incident infrared flux, Φ_{tot} (W/m^2), into an electrical signal, $U_S(t)$ (V). These signals are proportional: $U_S(t) = \rho_{\text{md}}\Phi_{\text{tot}}(t)$. The proportionality factor ρ_{md} depends among other things on the integration time and the spectral sensitivity of the detector.

However, the detector does not only collect the transmitted flux of interest $\Phi_0\Gamma(t)$, but also the proper emission of the sample, and the parasitic radiations from the environment (see figure 2.4). In addition, the detector has an intrinsic noise, $\varepsilon_{\text{det}}(t)$, composed of dark shot noise, or readout noise among others. To simplify notation, all the unwanted signals are grouped under

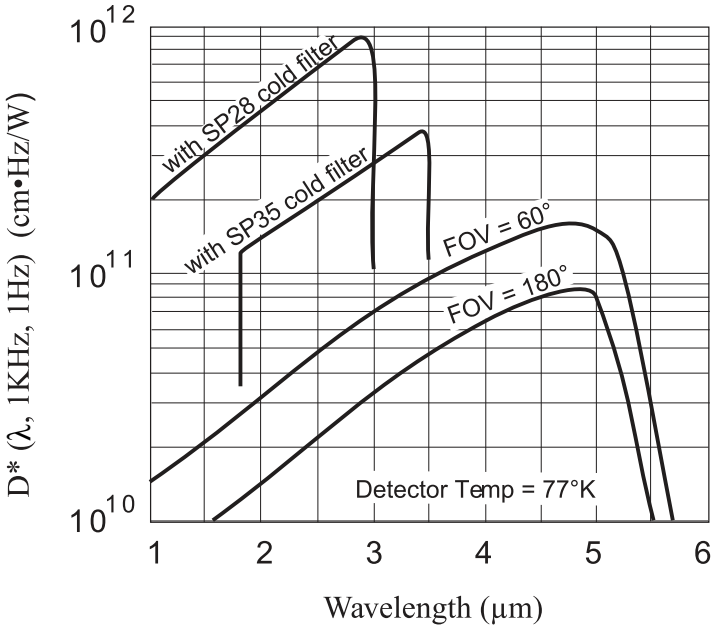

FIGURE 2.3 – Mono-detector sensitivity (Teledyne Judson Technologies, J10D, datasheet).

the term $E(t)$. Let us detail the expression of $U_S(t)$ when the temperature of the sample is modulated at the frequency f_T.

$$U_S(t) = \rho_{\text{md}}\Phi_{\text{tot}}(t) \tag{2.4}$$
$$U_S(t) = \rho_{\text{md}}[\Phi_0\Gamma(t) + E(t)] \tag{2.5}$$
$$U_S(t) = \rho_{\text{md}}[\Phi_0\Gamma_0(1 + \kappa\Delta T\cos(2\pi f_T t)) + E(T,t)] \tag{2.6}$$

Since both the transmitted signal and proper emission vary with temperature (see Equation 2.6), demodulating U_S at this stage does not allow us to discriminate these signals. Since we cannot influence the proper emission, a solution consists in modulating the IR source with a mechanical chopper at the frequency f_c. When the chopper cuts the IR source, we only measure parasitic signals ($\mathcal{C}(t) = 0$), and when the light beam passes through the sample we measure both transmitted IR beam and parasitic radiations ($\mathcal{C}(t) = 1$), as illustrated in Figure 2.4. We only consider the first harmonic of the chopper function $\mathcal{C}(t)$ thanks to the lock-in amplifier detection at the fundamental frequency used in this study. In this configuration, the measured signal $U_S(t)$ is decomposed as follows:

$$U_S(t) = \underbrace{\rho_{\text{md}}\Phi_0\Gamma_0[\cos(2\pi f_c t) + \frac{1}{2}\kappa\Delta T\cos(2\pi(f_c \pm f_T)t)]}_{\text{signal of interest}} + \underbrace{\rho_{\text{md}}E(T,t)}_{\text{parasitic signal}} \tag{2.7}$$

The signal $U_S(t)$ must be demodulated once at $f_c \pm f_T$, or twice at both frequencies f_c and f_T, to extract the term of interest $\kappa\Delta T$.

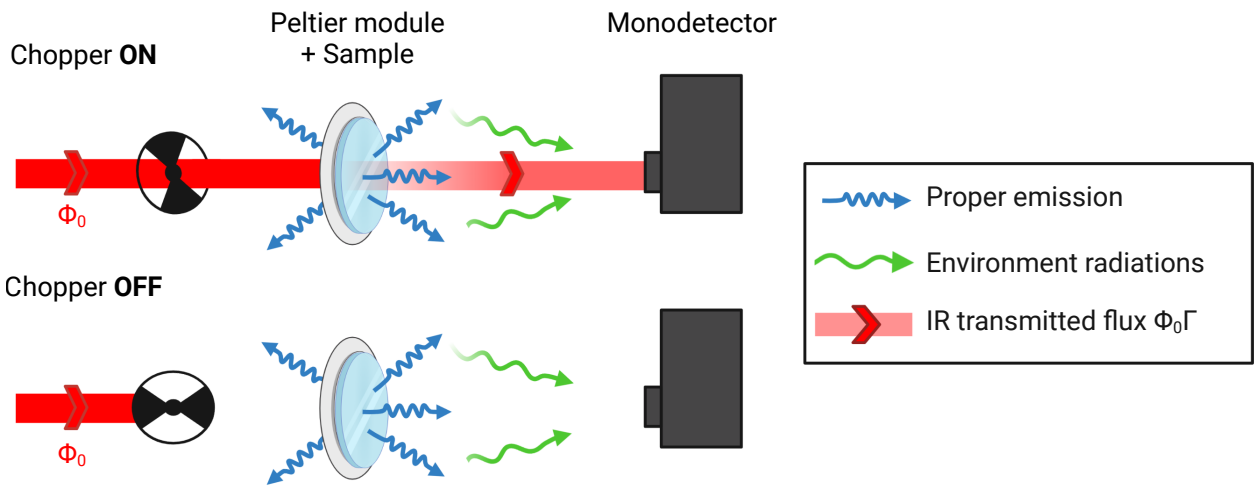

FIGURE 2.4 – Illustration of the signals recorded by the detector depending on the chopper position.

Demodulating the thermotransmittance signal

There are several ways to demodulate the thermotransmittance signal. The following section presents all the details about the double demodulation method. Let us mention here that we use a hardware lock-in amplifier (Stanford research systems, SR830 DSP) to demodulate with respect to f_c, and a post-processed Fast-Fourier Transform (FFT) algorithm to demodulate with respect to f_T.

2.3 Double-demodulation of the thermotransmittance signal

This section discusses the double-demodulation of the signal measured by the detector, $U_S(t)$, to extract the thermotransmittance term of interest $\kappa\Delta T$. To demodulate the signal, we have several options at our disposal:

- A hardware **lock-in amplifier** (LIA) [77] allows us to remove parasitic signals such as proper emission and IR radiations from the environment. However, this device needs a reference signal at the same frequency and phase as the modulated signal, which is not always possible depending on the experimental setup. For example, we do not have such a reference signal at the frequencies f_T and thus $f_c \pm f_T$, due to our temperature monitoring performed by LabView, shown in Figure 2.2 .
- Decomposing the signal into frequencies using a **Fast Fourier Transform** (FFT) algorithm in post-processing [78]. This method requires recording several periods of modulation to be efficient, particularly by working with noisy signals.
- If we cannot record multiple periods, we can use the **four-image algorithm** to demodulate the signal [79, 80]. This algorithm extracts both the amplitude and phase of a signal

using four equidistant points within a single period. We implement this technique in the next chapter to post-process the signal recorded by the IR camera (see section 3.3.2).

Regarding this study, we focus on the signal amplitude. First, we use a hardware lock-in amplifier (LIA) at f_c to filter out the parasitic signals including the sample proper emission. Since we do not have reference signal at frequency f_T, we cannot use a second LIA to demodulate with respect to f_T. Thus, the output signal of the LIA, $U_{\text{LIA}}^{\text{LP}}(t)$ is decomposed into frequencies with a Fast Fourier Transform algorithm. By measuring the DC component of the frequency spectrum and the one at $f = f_T$ we extract the term $\kappa\Delta T$.

2.3.1 IR source demodulation: hardware lock-in amplifier (LIA)

The principle of a lock-in amplifier is based on two main steps, the mixing and filtering, that we detail hereafter.

Mixing operation

First, the measured signal $U_S(t)$ is mixed with a reference signal, $U_R(t)$, which has the same frequency f_c and phase as the chopper modulation. The reference signal $U_R(t)$ is the TTL (Transistor-Transistor logic) signal coming from the chopper controller. As mentioned in the introduction, to simplify the expressions, we only consider the first harmonic of the chopper function:

$$U_R(t) \propto \cos(2\pi f_c t) \tag{2.8}$$

The simplified mixing operation between the signals $U_S(t)$ and $U_R(t)$ is the following:

$$\begin{aligned} U_{\text{LIA}}(t) &= U_S(t) \times U_R(t) \\ &= \overbrace{\boxed{\rho_{\text{md}}\frac{\Phi_0\Gamma_0}{2}}}^{\text{DC component}} + \overbrace{\boxed{\rho_{\text{md}}\frac{\Phi_0\Gamma_0}{2}\kappa\Delta T\cos(2\pi f_T t)}}^{\text{Thermotransmittance signal}} + \rho_{\text{md}}\frac{\Phi_0\Gamma_0}{2}\cos(4\pi f_c t) \\ &\quad + \rho_{\text{md}}\frac{\Phi_0\Gamma_0}{4}\kappa\Delta T\cos(2\pi(2f_c \pm f_T)t) + \rho_{\text{md}}E(T,t)\cos(2\pi f_c t) \end{aligned} \tag{2.9}$$

The mixing operation reveals components at different frequencies: f_T, f_c, $2f_c$, $2f_c \pm f_T$, and a DC part (see Figure 2.5 (b)). The thermotransmittance signal of interest is at the frequency f_T as highlighted in red in Equation 2.9: $\rho_{\text{md}}\frac{\Phi_0\Gamma_0}{2}\kappa\Delta T$. The DC part, in blue, helps to extract $\rho_{\text{md}}\frac{\Phi_0\Gamma_0}{2}$, so it is in our interest to keep this component. All the components at frequencies higher than f_T are then filtered out.

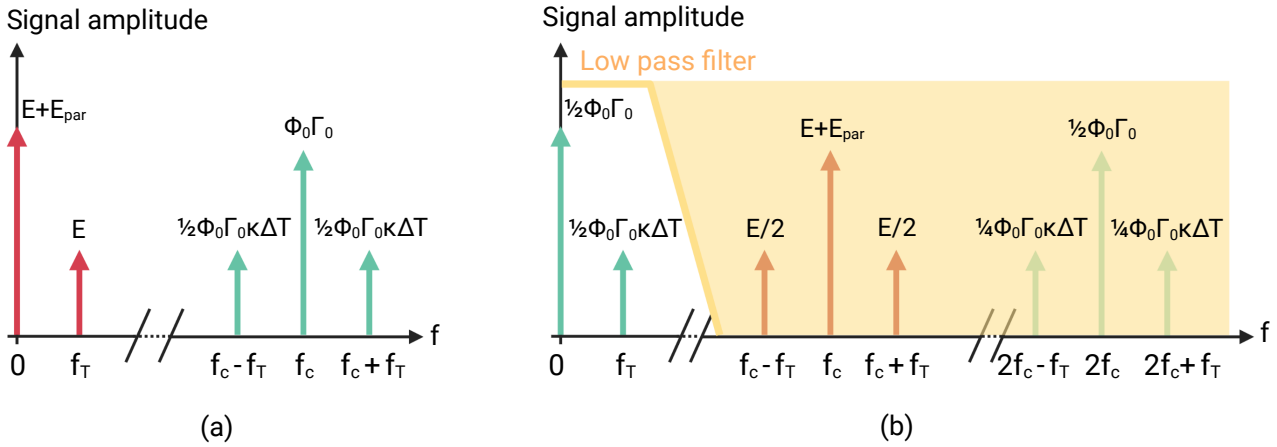

FIGURE 2.5 – (a) Frequency decomposition of the raw signal $U_S(t)$. (b) Frequency components after the mixing operation. The action of the low-pass filter is illustrated in orange.

Low-pass filtering

A low-pass filter is then applied to the mixed signal, $U_{\mathrm{LIA}}(t)$. Equation 2.10 gives the transfer function $\mathcal{H}(\omega)$ of a n-order low-pass filter. The cutoff frequency is proportional to the inverse of the time constant τ_c: $f_c = \tau_c^{-1}$. Before starting the measurements, it is necessary to determine the order n and the time constant τ_c of the filter to eliminate the frequencies containing parasitic signals without attenuating too much the one at the frequency f_T.

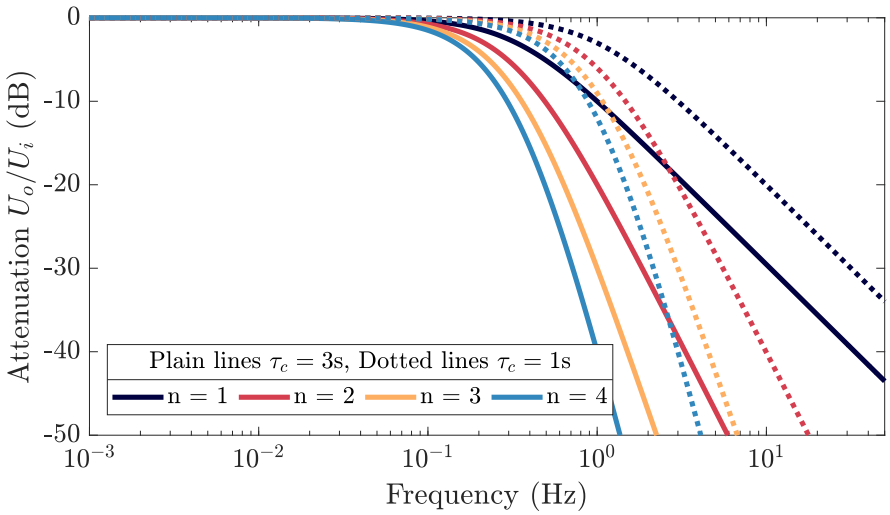

FIGURE 2.6 – Filter response as a function of frequency, for $\tau_c = 3$s (plain lines) and $\tau_c = 1$s (dotted lines), and for several orders n.

Transfer function of a n-order low-pass filter [77]:

$$\mathcal{H}(\omega) = \left(\frac{\omega_c}{\omega_c + i\omega}\right)^n = \left(\frac{1}{1 + i\omega\tau_c}\right)^n \tag{2.10}$$

According to Figure 2.5 and equation 2.9, we want the filter to cut the components at frequencies higher than f_T without attenuating the one at f_T. The orders of magnitude of the studied frequencies are $f_T \approx 10$ mHz and $f_c \approx 20$ Hz. Figure 2.6 plots the attenuation of the output signal after filtering with several filter orders. The attenuation of the signal at 20 Hz is around 26 dB with the 1-order filter with $\tau_c = 1s$, and 35 dB with $\tau_c = 3s$. In comparison, the 2-order filter gives respectively 52 dB and 71 dB. Consequently, the first-order filter is not well-adapted to our measurements since it is not selective enough. In addition, its slope does not cut the parasitic noise frequencies enough, we therefore discard it. As expected, the higher the time constant, the more selective the filter. Increasing the time constant should be an interesting approach to reduce the noise components at low frequencies. Nevertheless, we have to be sure that we will not attenuate the signal at the frequency f_T. Whatever the chosen time constant (τ_c equals 1s or 3s), all the filters shown in Figure 2.6 attenuate the signal at $f = 10$ mHz by less than 0.02 dB, which is acceptable by comparison to the attenuation at 20 Hz.

To validate the theoretical filters behavior, we check if the LIA response fits with analytical transfer function. We measure the system step response depending on the order of the low-pass filter with $\tau_c = 3$s. The input signal is generated by a waveform generator (Agilent 33220A) at the frequency $f = 20$ Hz to be consistent with the experimental conditions. We record the input signal and the step response of the LIA with a National Instruments card 9201. The card acquisition frequency is 50 Hz, that is why the input signal presented in Figure 2.7 (a) is under-sampled. Nevertheless, the lock-in amplifier is not affected by this issue. Figure 2.7 (b) shows the different step responses of the LIA depending on the low-pass filter order. We compare the measurements to the theoretical behavior expressed by the filter transfer function $\mathcal{H}(\omega)$ and observe that our system response agrees with the theoretical model.

The remainder of the filtering operation, $U_{\text{LIA}}^{\text{LP}}(t)$, is the sum of the DC component, the one at f_T, and a residual $\varepsilon_{\text{residuals}}(t)$ which depends on the chosen filter.

$$U_{\text{LIA}}^{\text{LP}}(t) = \underbrace{\rho_{\text{md}} \frac{\Phi_0 \Gamma_0}{2}}_{DC\, f=0} + \underbrace{\rho_{\text{md}} \frac{\Phi_0 \Gamma_0}{2} \kappa \Delta T}_{f=f_T} \cos(2\pi f_T t) + \underbrace{\varepsilon_{\text{residuals}}(t)}_{f>f_T} \tag{2.11}$$

2.3.2 Thermal demodulation: Fast Fourier Transform (FFT)

Regarding equation 2.11, the last operation consists in demodulating $U_{\text{LIA}}^{\text{LP}}(t)$ at the thermal frequency f_T. Let $\tilde{U}_{\text{LIA}}(f = f_T)$ be the frequency component at f_T, and $\tilde{U}_{\text{LIA}}(f = 0)$ the DC component. To get the term $\kappa\Delta T$, $\tilde{U}_{\text{LIA}}(f = f_T)$ is divided by $\tilde{U}_{\text{LIA}}(f = 0)$ as shown in equation 2.14. All the proportionality factors have no influence on the thermotransmittance measurement since only relative variations are involved.

For this second demodulation to discriminate the DC component from the f_T component, we implement a Fast Fourier Transform algorithm since we do not have a reference signal at f_T to use a second LIA. This operation is performed in post-processing with Matlab but could also be implemented in LabView as a real time operation. However, since this is a preliminary study whose post-processing is not reused in the following, I have decided not to spend more

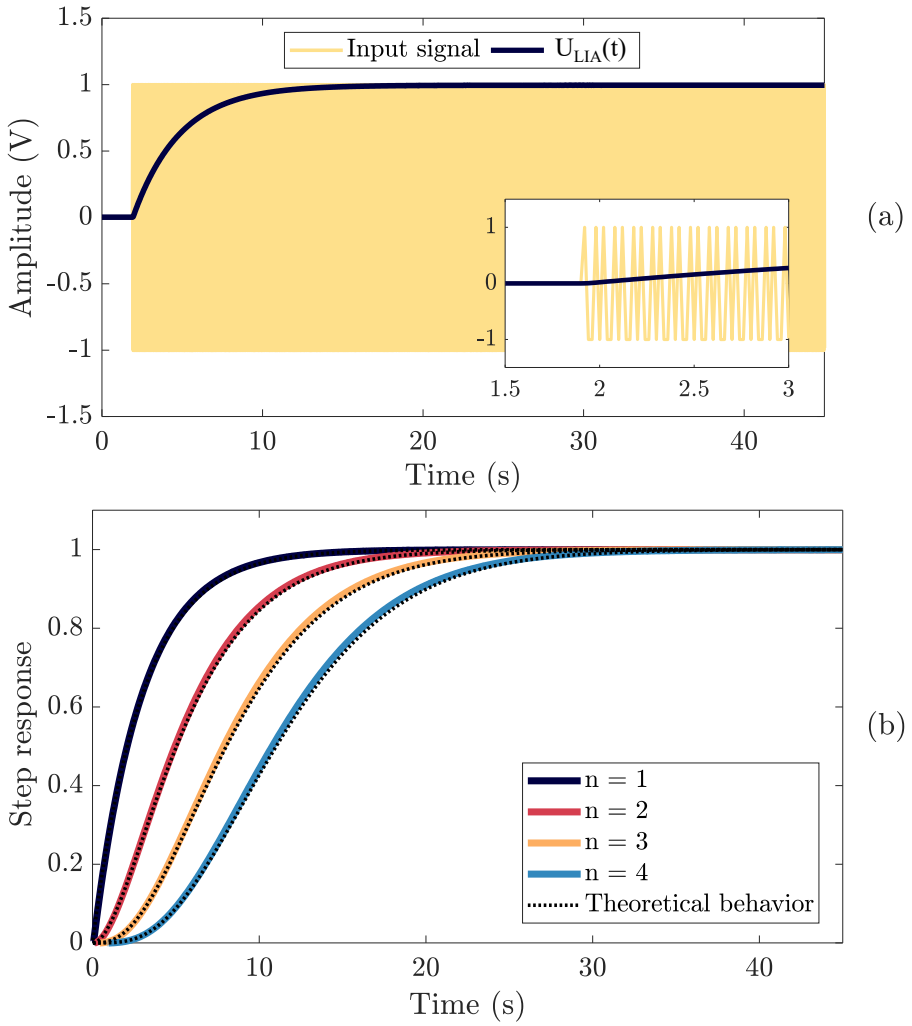

FIGURE 2.7 – (a) Step response of the LIA (black curve) for a 1-order low-pass filter with $\tau_c = 3$s. The frequency of the input signal (yellow) is $f = 20$ Hz. The insert is a zoom at the beginning of the acquisition. (b) Measured step response of the lock-in amplifier depending on the selected filter, and comparison with the theoretical behavior (dotted lines). The time constant is set at 3s

time on it.

$$\tilde{U}_{\mathrm{LIA}}(f = f_T) = \rho_{\mathrm{md}} \frac{\Phi_0 \Gamma_0}{2} \kappa \Delta T \tag{2.12}$$

$$\tilde{U}_{\mathrm{LIA}}(f = 0) = \rho_{\mathrm{md}} \frac{\Phi_0 \Gamma_0}{2} \tag{2.13}$$

$$\frac{\tilde{U}_{\mathrm{LIA}}(f = f_T)}{\tilde{U}_{\mathrm{LIA}}(f = 0)} = \kappa \Delta T \tag{2.14}$$

At the end of the double-demodulation process, we extract the term $\kappa \Delta T$ (see equation 2.14). To calibrate the thermotransmittance coefficient, the last step is to determine the temperature variation of the sample, ΔT, by combining modeling and measurements. The next section presents the modeling of heat transfer in the silicon wafer.

2.4 Heat transfer modeling of a thin wafer in cylindrical coordinates

This section studies the heat transfer in a thin silicon wafer heated at its edges by a ring-shaped Peltier module. We calculate the temperature variation ΔT in the sample, and determine the operating modulation frequency f_T.

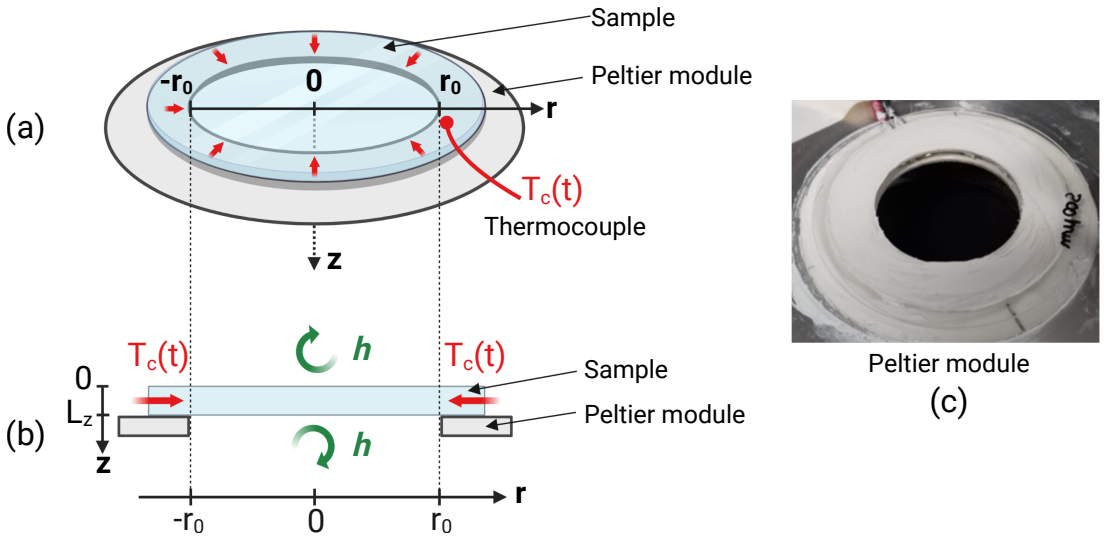

FIGURE 2.8 – Illustration of the heat transfer problem. (a) 3D view of the Peltier module and the sample heated to a modulated temperature $T_c(t)$. (b) Cross-sectional view with boundary conditions. (c) Image of the Peltier module.

2.4.1 Solving the heat transfer equation

The shape of the heating system is important to let the incident flux Φ_0 passing through the sample. The sample and the Peltier module are positioned vertically, as shown in the illustration of the experimental setup 2.1. Figure 2.8 illustrates the geometry of the problem with the boundary conditions. Let's consider a sample of radius r_0 (m) and thickness L_z (m), of thermal diffusivity a (m^2/s) and thermal conductivity k (W/m/K). Due to the geometry of the wafer and the heating system, we use the cylindrical coordinate system (r, ϑ, z). As the sample is homogeneously heated at its edges, we do not consider the azimuth coordinate ϑ: the temperature does not depend on the angle ϑ. The final coordinate system is (r, z).

Boundary conditions

The temperature is set to the modulated temperature $T(t) = T_0 + \Delta T \cos(\omega_T t)$ at the edges of the sample ($r = r_0$ and $r = -r_0$), with T_0 the ambient temperature and $\omega_T = 2\pi f_T$ the angular frequency (rad/s). For symmetry reasons, at the position $r = 0$, the radial flux is assumed to be equal to zero. We impose convection losses at the surfaces $z = 0$ and $z = L_z$, with h being the convection coefficient (W/m^2/K). The system of equations [2.15 to 2.20] expresses the heat transfer problem in cylindrical coordinates with boundary conditions over time t.

$$
\begin{cases}
\dfrac{\partial^2 T(r,z,t)}{\partial r^2} + \dfrac{1}{r}\dfrac{\partial T(r,z,t)}{\partial r} + \dfrac{\partial^2 T(r,z,t)}{\partial z^2} = \dfrac{1}{a}\dfrac{\partial T(r,z,t)}{\partial t} & (2.15)\\
-k \left.\dfrac{\partial T(r,z,t)}{\partial z}\right|_{z=0} = -h(T(r,z=0,t) - T_0) & (2.16)\\
-k \left.\dfrac{\partial T(r,z,t)}{\partial z}\right|_{z=L_z} = h(T(r,z=L_z,t) - T_0) & (2.17)\\
\left.\dfrac{\partial T(r,z,t)}{\partial r}\right|_{r=0} = 0 & (2.18)\\
T(r=r_0,z,t) = T_0 + \Delta T(r_0)\cos(\omega_T t) & (2.19)\\
T(r,z,t=0) = T_0 & (2.20)
\end{cases}
$$

Linearization of convective losses

The silicon thermal conductivity is about $k \approx 130$ W/m/K [81], and the convection coefficient is approximately $h \approx 10$ W/m^2/K for the vertical configuration [82] used in the experimental setup. This leads to a Biot number $B_i \approx 2.10^{-5} \ll 1$, which means that the temperature is homogeneous in the sample thickness. As a result, the partial derivative with respect to z can be linearized, as expressed in equation 2.21. We substitute this result in the previous system of equations.

$$\frac{\partial^2 T(r,z,t)}{\partial z^2} \approx \frac{\frac{\partial T(r,z,t)}{\partial z}\Big|_{z=L_z} - \frac{\partial T(r,z,t)}{\partial z}\Big|_{z=0}}{L_z} \approx -\frac{2h}{kL_z}(T(r,z=L_z,t)-T_0) \tag{2.21}$$

Temperature decomposition as periodic function

To solve the system, the temperature is decomposed into a constant and a term depending on the angular frequency ω_T:

$$\underline{T}(r,t) = T_0 + \Delta\underline{T}(r,\omega_T)e^{i\omega_T t} \tag{2.22}$$

With $\Delta\underline{T}(r,\omega_T)$ the complex temperature amplitude at the frequency f_T. After substituting the partial derivative with respect to z and the expression of $\underline{T}(r,t)$, the previous system of equations [2.15 to 2.20] becomes:

$$\begin{cases} \dfrac{d^2\Delta\underline{T}(r,\omega_T)}{dr^2} + \dfrac{1}{r}\dfrac{d\Delta\underline{T}(r,\omega_T)}{dr} - \dfrac{2h}{kL_z}\Delta\underline{T}(r,\omega_T) = \dfrac{i\omega_T}{a}\Delta\underline{T}(r,\omega_T) & (2.23) \\ \dfrac{d\Delta\underline{T}(r,\omega_T)}{dr}\Big|_{r=0} = 0 & (2.24) \\ |\Delta\underline{T}(r=r_0,\omega_T)| = \Delta T(r_0) & (2.25) \end{cases}$$

Solution of the system

The solution of the system is given in equation 2.26 [83], with $H = 2h/kL_z$ the loss factor (m^{-2}), $\mathcal{I}_0$ and $\mathcal{K}_0$ the modified Bessel functions of first and second kind.

$$\Delta\underline{T}(r,\omega_T) = A\mathcal{I}_0\left(r\sqrt{H+i\frac{\omega_T}{a}}\right) + B\mathcal{K}_0\left(r\sqrt{H+i\frac{\omega_T}{a}}\right) \tag{2.26}$$

A and B are determined with the boundary conditions:

- When the distance r tends towards zero, the function $\mathcal{K}_0(r)$ tends towards ∞. Since the temperature variation cannot diverge at the center $r=0$, B must be equal to zero.
- At the edge $r=r_0$, the boundary condition gives: $A = \Delta T(r_0)/\mathcal{I}_0\left(r_0\sqrt{H+i\frac{\omega_T}{a}}\right)$.

Finally, the complex temperature field as a function of the position r and the frequency f_T is expressed in equation 2.27. In this chapter, we use only the amplitude $|\Delta\underline{T}(r,\omega_T)|$ of the temperature variation field.

$$\Delta\underline{T}(r,\omega_T) = \Delta T(r_0)\frac{\mathcal{I}_0\left(r\sqrt{H+i\frac{\omega_T}{a}}\right)}{\mathcal{I}_0\left(r_0\sqrt{H+i\frac{\omega_T}{a}}\right)} \tag{2.27}$$

2.4.2 Application to the silicon wafer

Table 2.1 lists the properties of the studied silicon wafer (Siegert Wafer). First, we would like to determine if the temperature module $|\Delta\underline{T}(r, \omega_T)|$ is uniform along the distance r to simplify the experimental measurements. The evolution of the normalized temperature module at the center $r = 0$, $|\Delta\underline{T}(0, \omega_T)|/\Delta T(r_0)$, as a function of the frequency f_T is given in Figure 2.9. The module is approximately constant up to 50 mHz. Thus, at frequencies lower than 50 mHz, the temperature gradient along the distance r is negligible and depends on the convective losses. We fix the frequency at 10 mHz and study the impact of a change in the thermal properties on the temperature gradient.

Parameters	Values
Thickness, L_z	250 μm
Radius, r_0	13.5 mm *
Thermal conductivity, k	130 W/m/K [81]
Thermal diffusivity, a	80.10^{-6} m^2/s [81]
Convection coefficient, h	10 W/m^2/K
Thermal frequency, f_T	10 mHz
Temperature variation at the edges $\Delta T(r_0)$	10 °C

TABLE 2.1 – Parameters used in the heat transfer modeling. * *The diameter of the wafer is 50.8 mm. However, the inner diameter of the ring-shaped Peltier module being 27 mm, the useful radius is 13.5 mm.*

First, the figure 2.10 shows the temperature module as a function of the distance r for two convection coefficients h. In the worst case, $h = 10$ W/m^2/W [82], the temperature variation is about 3% at $r = 0$ compared to the edge, corresponding to an absolute temperature variation of less than 0.3°C. Then, the Figure 2.11 shows that the temperature variation $|\Delta\underline{T}(r)|$ is slightly impacted by a change in the estimation of the thermal properties of the silicon at the chosen frequency $f_T = 10$ mHz. Consequently, in the worst case with $h = 10$ W/m^2/K and $k = 120$ W/m/K, the temperature variation can be considered constant at the surface of the whole sample: $|\Delta\underline{T}(r)| = \Delta T(r_0)$. We now have all the information to measure the thermotransmittance coefficient κ.

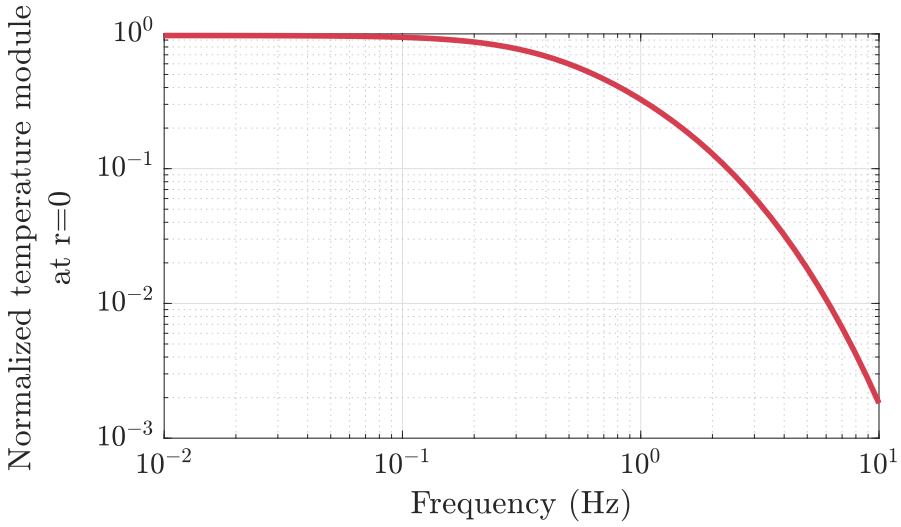

FIGURE 2.9 – Normalized temperature module $|\Delta\underline{T}(0)|/\Delta T(r_0)$ at the center depending on the frequency f_T. The convection coefficient is $h = 10$ W/m^2/K.

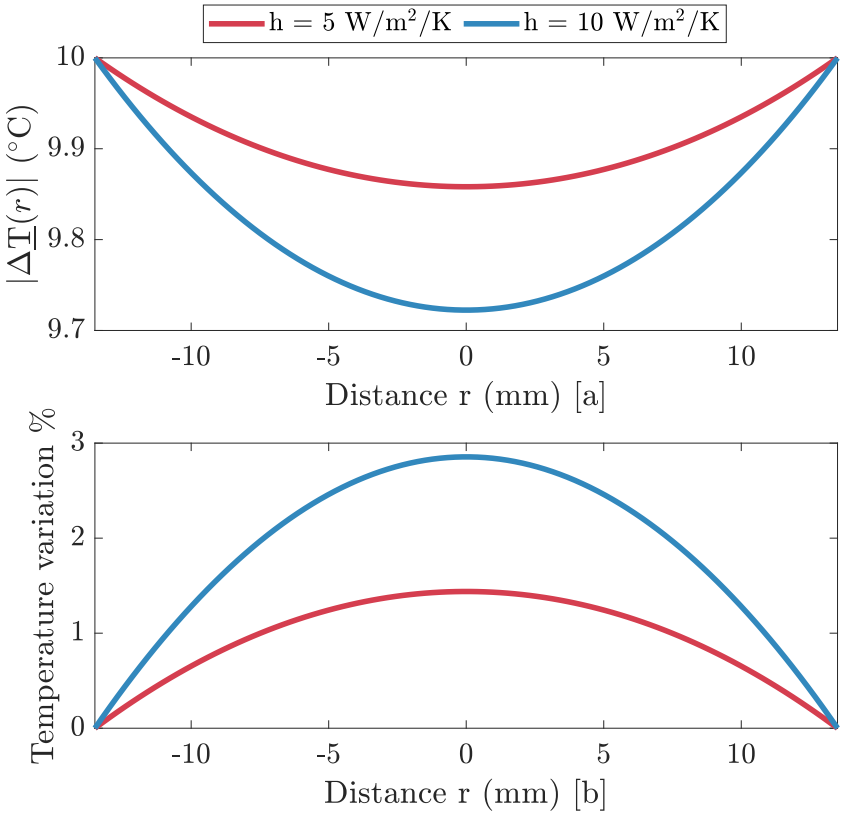

FIGURE 2.10 – (a) Amplitude $|\Delta\underline{T}(r, \omega_T)|$ depending on the distance r (mm). (b) Temperature variation in the sample compared to $\Delta T(r_0)$. The frequency is $f_T = 10$ mHz.

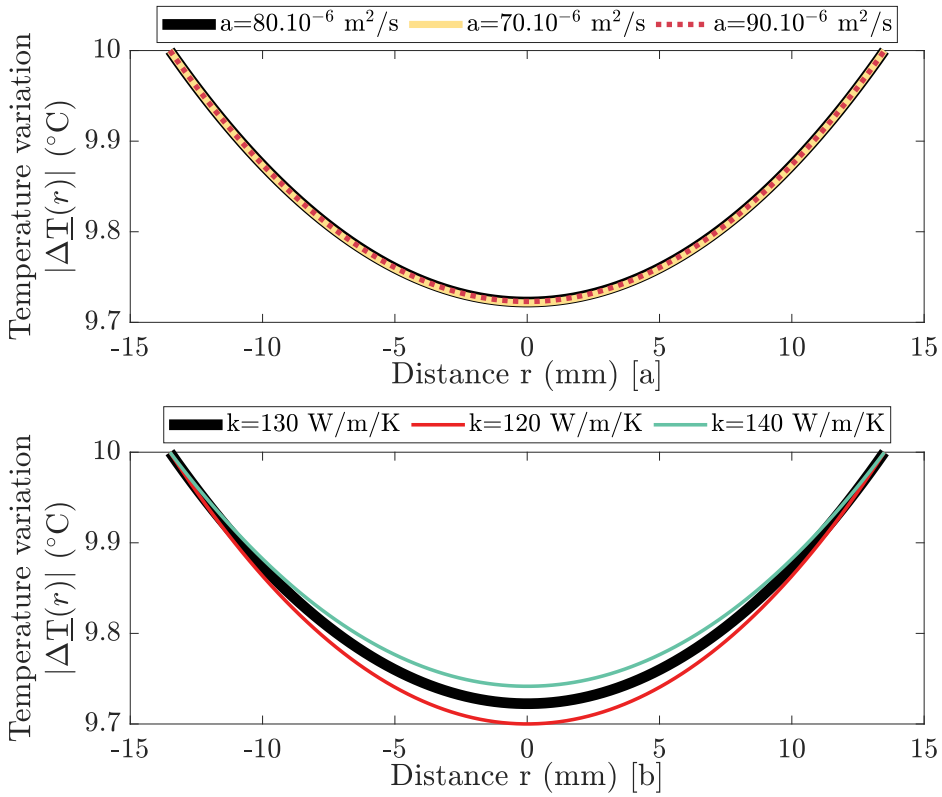

FIGURE 2.11 – Amplitude $|\Delta\underline{T}(r, \omega_t)|$ depending on the distance r (mm) (a) varying the thermal diffusivity with fixed thermal conductivity $k = 130$ W/m/K, and (b) varying the thermal conductivity with fixed thermal diffusivity $a = 80.10^{-6}$ m^2/s. The black line corresponds to the set of data used in the model. The frequency is $f_T = 10$ mHz and the convection coefficient is $h = 10$ W/m^2/K.

2.5 Thermotransmittance measurement of the silicon wafer

In the previous sections, we have learned how to measure the thermotransmittance signal and extract the term $\kappa\Delta T$ using a double demodulation. Then, the model has demonstrated that when we operate at a thermal frequency $f_T = 10$ mHz, the sample temperature is homogeneous at its surface and matched the Peltier setpoint temperature. Consequently, the ratio between the measured $\kappa\Delta T$ and the Peltier setpoint temperature, ΔT, results in the thermotransmittance coefficient of the sample.

Transmittance of the silicon wafer

The studied wafer of silicon is polished on both sides to ensure good transparency and avoid surface scattering. The sample is semitransparent to the mid-infrared as shown in Figure 2.12, and its spectrum is constant in the spectral range $\lambda \in [2.5 - 6]$ μm: $\Gamma = 0.53 \pm 0.02$, meaning its refractive index is also constant and that absorption does not play any role ($\tilde{n}(\lambda) = n'$, see Appendix B). Thus, we assume that the thermotransmittance coefficient of the silicon is constant over the studied spectral range.

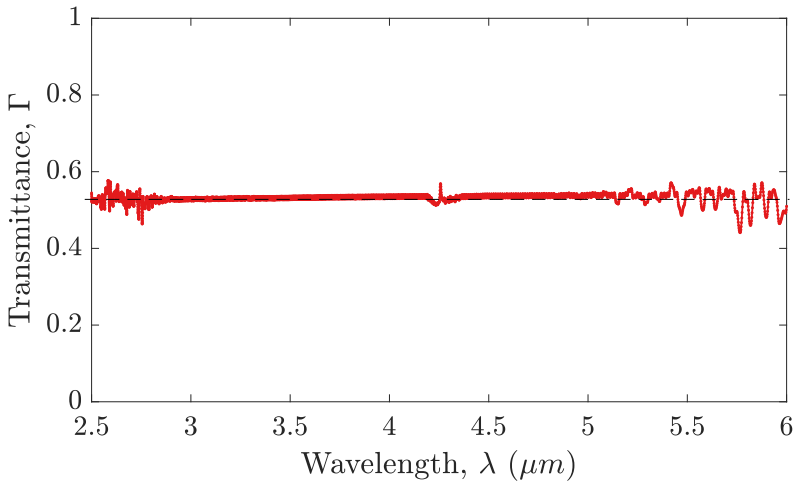

FIGURE 2.12 – Transmittance of the silicon wafer in the spectral range $\lambda \in [2.5 - 6]\,\mu m$, measured with a commercial FTIR (Fourier Transform Infrared spectrometer) [84]. The noise observed above 5.5 μm is due to a measurement artifact.

Experimental conditions

The results presented in this section are measured under the following experimental conditions:

- **Illumination wavelength** - Since the transmittance spectrum of the silicon is constant, any wavelength within the detector sensitivity range can be selected (see Figure 2.3). We set the illumination wavelength at $\lambda = 4$ μm.
- **LIA settings** - According to the LIA study in section 2.3.1, we choose a selective filter ($n = 4$ and $\tau_c = 3$s) to remove as much noise as possible. The experiment have showed us that with a less selective filter, we have much more difficulty measuring the thermotransmittance signal. According to Figure 2.6, the amplitude of the f_T - component is attenuated by 0.015 dB; this attenuation must be compensated afterwards.
- **Chopper configuration** - Theoretically, the higher the chopper frequency, the easier to discriminate the parasitic signals from the thermotransmittance. However, higher chopper frequencies in our initial configuration - with the chopper inside the source housing - may lead to additional noise from the ventilation induced by the chopper on the source. The maximum chopper frequency before deregulating the source with forced convection is 30 Hz. A second option is placing the chopper at the exit of the monochromator, as illustrated in Figure 2.1. The source is no more affected by forced convection, but the chopper can perturb the measurement with its motor heating or a less efficient occlusion of the beam. We compare the results for different chopper frequencies, 22 Hz and 167 Hz, and positions, inside or outside the source housing.

LIA output signal

Figure 2.13 presents the LIA output signal, $U_{\mathrm{LIA}}^{\mathrm{LP}}(t)$, as a function of the temperature $T(t)$ (a) over time. The graph (b) shows the quantization limit of the signal, which is an issue for properly calculating its Fourier transform. To solve that, the signal is amplified using the LIA ($\times 100$), and the resulting signal is shown in the graph (c). The DC component is the average of the signal plotted in graph (b), and the f_T component is extracted from graph (c) after FFT calculation and correction of the expand factor $\times 100$.

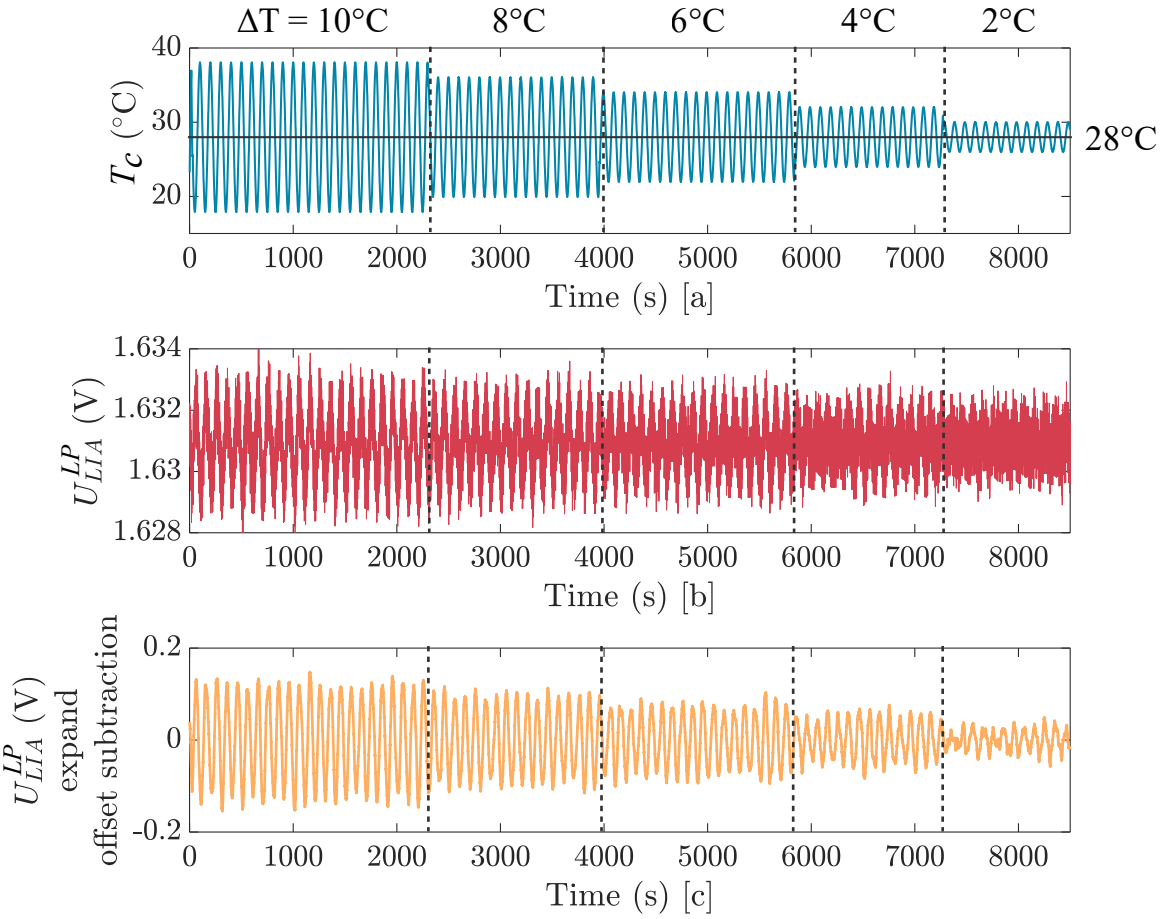

FIGURE 2.13 – [a] Temperature measured by the thermocouple. [b] Output signal of the LIA, $U_{\mathrm{LIA}}^{\mathrm{LP}}(t)$. [c] Output signal of the LIA after DC subtraction and expand $\times 100$, showing that the signal is well resolved.

Fast Fourier Transform

The signal presented in Figure 2.13 is cut into five parts corresponding to the different temperature variations ΔT. For each part, we calculate the Fourier transform of $U_{\mathrm{LIA}}^{\mathrm{LP}}(t)$ after signal expand. Figure 2.14 shows the corresponding Fourier transforms of the signal for different temperature variations $\Delta T \in [2, 4, 6, 8, 10]$ °C. The amplitude $\tilde{U}_{\mathrm{LIA}}(f_T)$ must be corrected from the LIA low-pass filter attenuation, and the expand coefficient. The expression 2.14 gives

the term $\kappa\Delta T$. Finally, plotting $\tilde{U}_{\mathrm{LIA}}(f = f_T)/\tilde{U}_{\mathrm{LIA}}(f = 0)$ as a function of ΔT provides a linear regression whose slope is the thermotransmittance coefficient, κ.

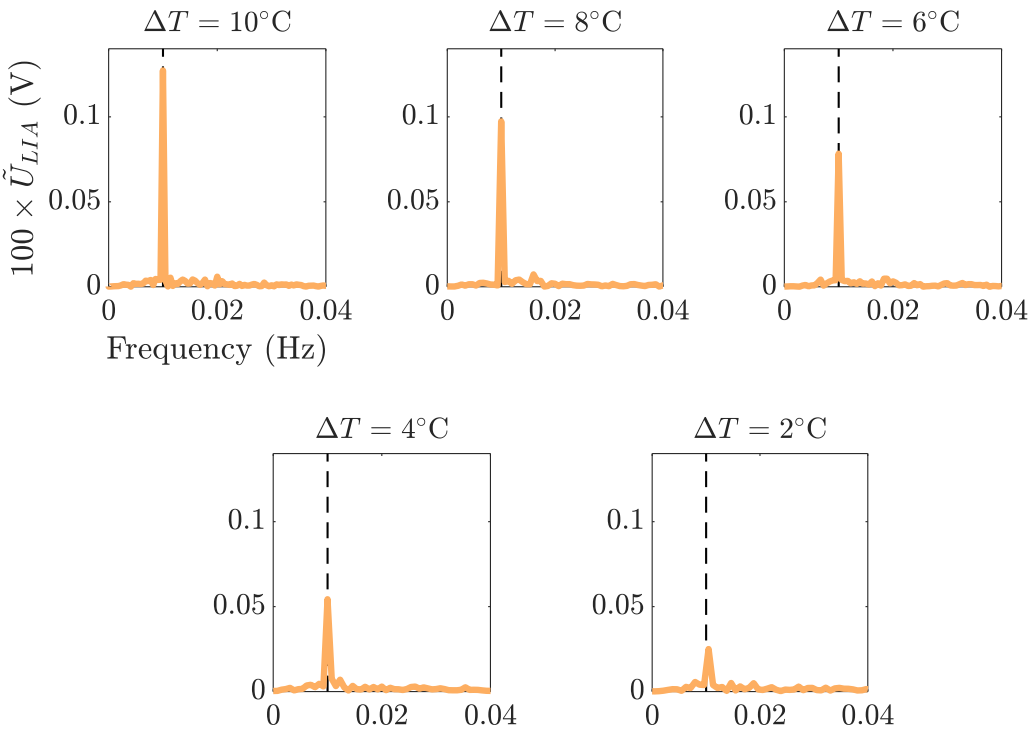

FIGURE 2.14 – Fourier transform of the signal $100 \times U^{\mathrm{LP}}_{\mathrm{LIA}}(t)$ for several temperature variations ΔT. The frequency resolution is $df \in [0.5 - 0.8]$ mHz, depending on the number of periods of $U^{\mathrm{LP}}_{\mathrm{LIA}}(t)$. The dotted line shows the frequency $f_T = 10$ mHz, where we measure $\tilde{U}_{\mathrm{LIA}}(f = f_T)$.

Thermotransmittance coefficient measurement

The measurements are carried out with different experimental conditions. Table 2.2 lists the setup configurations and the corresponding thermotransmittance coefficient, with an uncertainty on the linear regression. Figure 2.15 plots the linear regressions corresponding to each data set. The comparison of the data sets demonstrates that the chopper position or frequency do not significantly influence the measurement of the thermotransmittance coefficient. A further study with a significant number of measurements should be performed to investigate properly the chopper setting influence. Due to the duration of the experiment and that it is only a preliminary feasibility study, I chose not to perform such an analysis.

Finally, the silicon thermotransmittance coefficient at $\lambda = 4$ μm, and for a thickness of 250 μm, is $\kappa_{4\mu m} = -(8.6 \pm 0.6) \times 10^{-5}$ K^{-1}. So far, we have not mentioned the sign of the thermotransmittance coefficient. To determine it, we must compare the phase of temperature variation ΔT and the thermotransmittance signal $U^{\mathrm{LP}}_{\mathrm{LIA}}$, with Figure 2.13 for instance. Here, the negative sign comes from the phase opposition between the temperature and the thermotransmitted signal: the higher the temperature, the more opaque the sample.

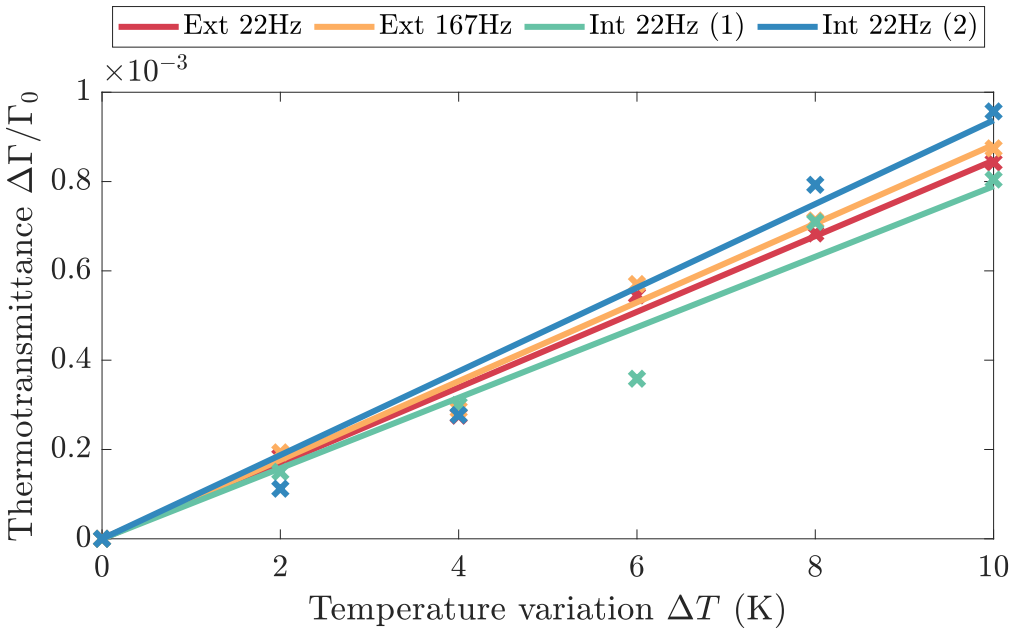

FIGURE 2.15 – Linear regression of thermotransmittance signal as a function of the temperature variation ΔT, for several experimental configurations. The slope gives the thermotransmittance coefficient.

Data-set (figure 2.15)	Chopper position Int. or Ext.	Chopper frequency f_c (Hz)	Thermotransmittance coefficient κ (K^{-1}) for $L_z = 250$ μm
Yellow	External	167	$-(8.8 \pm 0.3) \times 10^{-5}$
Red	External	22	$-(8.5 \pm 0.2) \times 10^{-5}$
Green	Internal	22	$-(7.9 \pm 0.4) \times 10^{-5}$
Blue	Internal	22	$-(9.4 \pm 0.5) \times 10^{-5}$

TABLE 2.2 – Configuration of each data set and associated calculated thermotransmittance coefficient (see Figure 2.15).

2.6 Optical modeling - Comparison with the literature

As mentioned in the introduction, the thermal dependency of the optical properties can be modeled using the Drude-Lorentz model (see Chapter 1 and Appendix B). Regarding the silicon under study, its transmittance spectrum is constant in the mid-infrared. Thus, the relative permittivity is assumed to be constant, $\tilde{\varepsilon_r}(\omega) \approx \varepsilon_\infty$, since there is no absorbance peak.

To determine if the results obtained are consistent, we compare them to the literature. However, very little information exists about the thermotransmittance measurement in the mid-infrared spectral range. To the best of our knowledge, only information about the thermal dependency of the real part of the refractive index $n'(T)$ is available [85]. In addition, the imaginary part of the refractive index, n'', which is responsible for absorbance, is negligible: $n'' < 10^{-6}$ [86, 87, 88, 89]. Consequently, we neglect the absorbance of the sample, and assume

that the thermotransmittance is only due to the variation of the reflectance at both surfaces of the sample, as illustrated in Figure 1.2. In this configuration, measuring thermotransmittance is equivalent to measuring thermoreflectance.

To compare the results of H.H. Li [85] to our measurements, we estimate a thermotransmittance signal from the variations of the refractive index. The estimated transmittance depending on the temperature is expressed in equation 2.28 (see Figure 1.2).

$$\Gamma(T) = [1 - R_1(T)] \times [1 - R_2(T)] = [1 - R(T)]^2 = \left(1 - \left(\frac{n'(T) - 1}{n'(T) + 1}\right)^2\right)^2 \tag{2.28}$$

Then, we calculate an equivalent thermotransmittance coefficient from the previous equation, $\frac{\Gamma(T)-\Gamma(T_0)}{\Gamma(T_0)}$, T_0 is arbitrarily fixed at the first measured value. Then, the ratio is plotted as a function of ΔT. We obtain the figure 2.16 (b). The slope of the linear regressions gives the estimated κ from the publication [85]. Table 2.3 summarizes the thermotransmittance coefficients at different wavelengths.

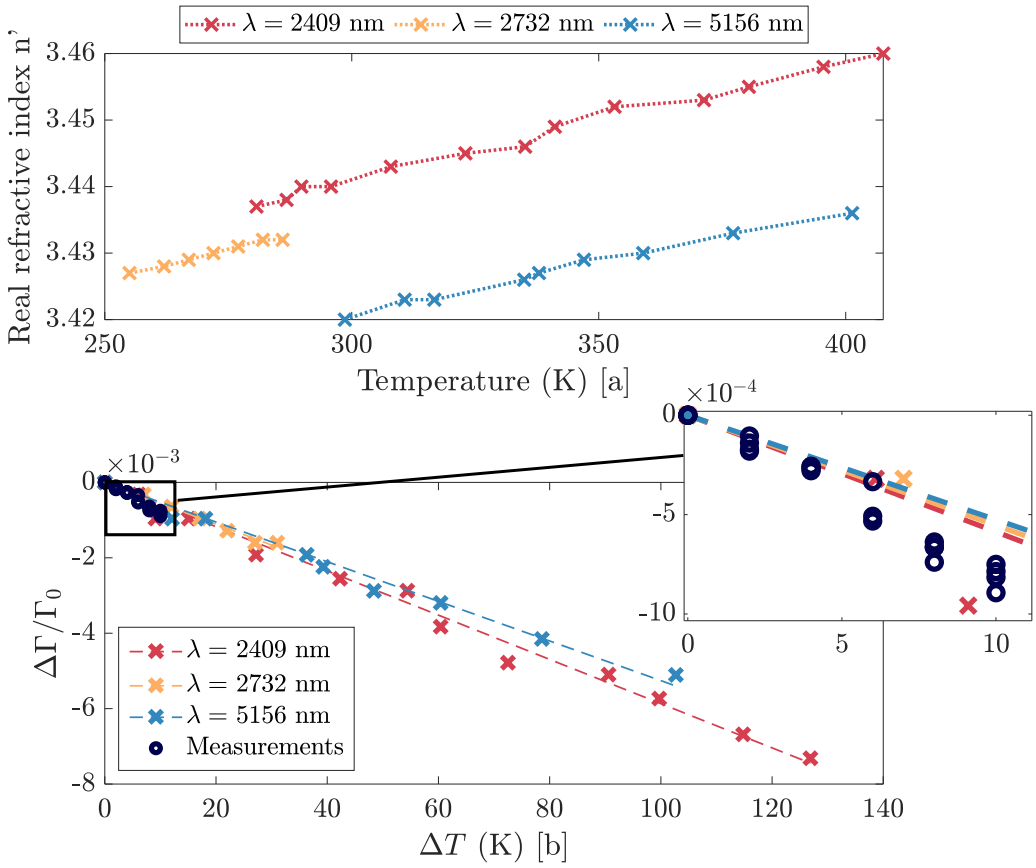

FIGURE 2.16 – [a] Real part of the Silicon refractive index depending on temperature, measured by H.H Li [85]. [b] Estimated thermotransmittance depending on temperature from the thermal dependency of the refractive index, for several wavelengths. The insert shows our measurements for $\Delta T \in [0 - 10]$°C and $\lambda = 4$ μm.

Wavelength, λ (nm)	Thermotransmittance coefficient, κ (K^{-1})
2409	-5.9×10^{-5}
2732	-5.6×10^{-5}
5156	-5.3×10^{-5}

Table 2.3 – Estimated thermotransmittance coefficient from H.H. Li publication [85].

The thermotransmittance coefficient calculated from the literature is of the same order of magnitude as the one obtained from our measurements; we also retrieve the negative sign. The difference may come from the thermotransmittance calculation from the refractive index, or the difference of the studied silicon (doping, roughness ...). In addition, these results show that the thermotransmittance of the silicon is approximately constant for $\lambda \in [2000 - 5000]$ nm, which was expected as the transmittance is constant in this range.

2.7 Conclusion

This preliminary study shows that it is possible to measure a thermotransmittance signal with the double-modulation method. Using a lock-in amplifier coupled with a digital Fourier transform, the demodulation process allows us discriminating the signal of interest from all the parasitic radiations.

We assumed in section 2.6 that the thermotransmittance signal of the silicon is primarily from its interfaces (reflectance) and not sensitive to temperature in the volume (absorbance). As a result, the thermotransmittance coefficient of the silicon should be independent from its thickness. In addition, as expected, the measured thermotransmittance coefficient is weak: for a temperature variation of $\Delta T = 1°C$, the variation of the silicon transmittance is less than 0.01%. Thus, a highly sensitive detector is required to measure slight temperature variations, $\Delta T < 1°C$. In the current setup, we have seen that the measurement at $\Delta T = 2°C$ is already at the limit of the detection threshold. It would be interesting to repeat these measurements with other materials to determine which are suitable for thermotransmittance, based on their respective κ.

In the next chapter, we conduct 2D thermotransmittance measurements to obtain the temperature field of the sample. For that, we replace the mono-detector by an IR camera and use a more optically sophisticated material to develop spectral measurements and modeling.

Chapter 3

Thermotransmittance imaging

Contents

3.1 Introduction

In the previous chapter, we used sensitive instruments such as the LIA and mono-detector to measure the thermotransmittance signal of a silicon wafer. This allowed us to validate the method with 1D measurements. The next objective is to upgrade the experimental setup to measure a 2D temperature field. We have two options for this: using a scanning device coupled with the mono-detector and the IR source, or replacing the mono-detector with an infrared camera. A scanning method is unsuitable here because we operate in modulated mode over long periods of several tens of seconds. As a consequence, for the following, we replace the mono-detector with an infrared camera containing more than 3×10^5 pixels.

However, this detector involves collecting a significant amount of data, usually exceeding 1 Gigabyte per measurements. Contrary to the previous study, we record a maximum of two

thermal modulation periods, which has an impact on the demodulation process. First, we cannot use the hardware LIA due to the output format of the camera, which is a 2D array. In addition, since we record only one or two thermal modulation periods, the Fast-Fourier transform is no longer adapted, specially for extracting low-frequency signals.

An efficient way of demodulating the IR images with a small number of periods combines two steps. First, the parasitic signals (proper emission and radiations from the environment) are removed using the two-image subtraction [90], described in section 3.3.1. Second, the thermotransmittance signal is demodulated with respect to the thermal frequency f_T, using the four-image algorithm [79], detailed in section 3.3.2.

This chapter presents the upgrade of the experimental setup to perform 2D thermal transmittance measurements, as it involves more than just using an IR camera. In addition, we change the silicon wafer with a thin Borofloat glass sample for two reasons:

- Since the new sample is a thin thermal insulator compared to the silicon, we observe a significant temperature gradient at its surface, which is of interest in thermotransmittance imaging.
- In addition, the optical properties of the Borofloat vary with wavelength within the mid-infrared range. This allows us to analyze the spectral dependency of the thermotransmittance coefficient and develop the optical modeling.

The thermotransmittance expression used in this chapter is the following, taking into account spectral dependency and assuming the temperature is still constant in the sample thickness.

$$\overbrace{\boxed{\frac{\Delta\Gamma(x,y,\lambda)}{\Gamma_0(x,y,\lambda)}}}^{Measurement} = \kappa(\lambda)\overbrace{\boxed{\Delta T(x,y)}}^{Modeling} \tag{3.1}$$

As in the previous chapter, we do not have information about the spectral thermotransmittance coefficient of the Borofloat. We must calibrate it, combining the measurement of the thermotransmittance signal and the knowledge of the corresponding temperature variation. Contrary to silicon, Borofloat is a heat insulator, which means that a slight discrepancy in the thermal properties estimation significantly impacts the temperature field (see section 3.4). As a result, we must measure its thermal properties to properly calculate the temperature variation field $\Delta T(x, y)$.

In this chapter, we discuss the experimental methodology to extract the thermal properties of Borofloat combining the measurement of the thermotransmittance signal and the heat transfer model. Then, we present the spectral calibration of the thermotransmittance coefficient, using measurement of $\Delta\Gamma/\Gamma_0$ and the calculation of the temperature variation ΔT. Finally, the Drude-Lorentz model is developed to analyze the Borofloat thermo-optical behavior based on the wavelength.

3.2 Modulated thermotransmittance imaging experimental setup

Figure 3.1 illustrates the experimental setup for modulated thermotransmittance imaging. We identify the same elements as in the previous study: the IR source combined with the monochromator, the mechanical chopper for modulating the source, the annular Peltier module for heating the sample, and an infrared camera as detector. In addition, as we want to image the temperature field of the entire sample, a beam expander composed of two parabolic mirrors adjusts the size of the incident infrared beam to the sample dimensions. The double-demodulation is post-processed, the corresponding operations are detailed in section 3.3.

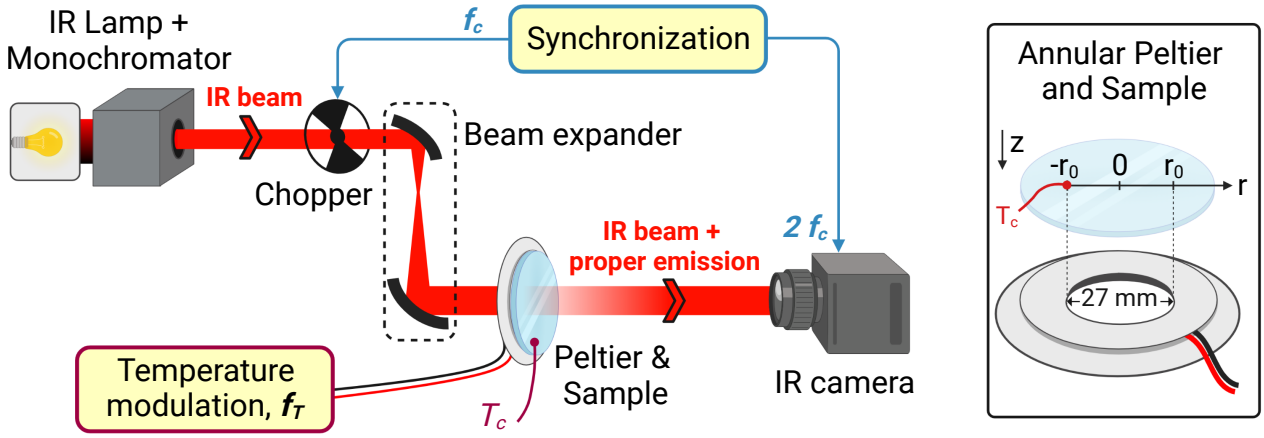

FIGURE 3.1 – Experimental setup for modulated thermotransmittance imaging measurement. The insert illustrates the Peltier module with its dimensions.

Heating of the sample

As in the previous chapter 2, the sample is heated using a ring-shaped Peltier module. The temperature at the edges of the wafer is modulated at $T(t) = T_0 + \Delta T \cos(2\pi f_T t)$, with $T_0 = 30°\text{C}$ and $\Delta T = 10°\text{C}$. We choose the modulation frequency f_T in the section 3.4 studying heat transfer in the Borofloat wafer.

Infrared camera properties

We use an infrared camera as detector (FLIR SC7000). The camera has an Indium-antimonide sensor composed of 512 x 640 pixels with a pitch of 15 μm. The focal length of the objective is 50 mm, and the spatial resolution of the images recorded by the camera is 107 μm/pixel measured on a calibrated USAF target [91]. In addition, the camera spectral sensitivity range is $\lambda \in [2.5 - 5.5]\ \mu m$. Figure 3.2 plots the normalized spectral sensitivity of the acquisition system, which includes the spectral responses of the camera, the lens objective, the air absorption, and the IR lamp emission. We are not able to differentiate the different contributions with the available equipment. However, the absorption peak at $\lambda = 4300$ nm is

the signature of the CO_2 in the air [92]. Therefore, it is in our interest to work around $\lambda = 4000$ nm or $\lambda = 4500$ nm if the sample transmittance allows it.

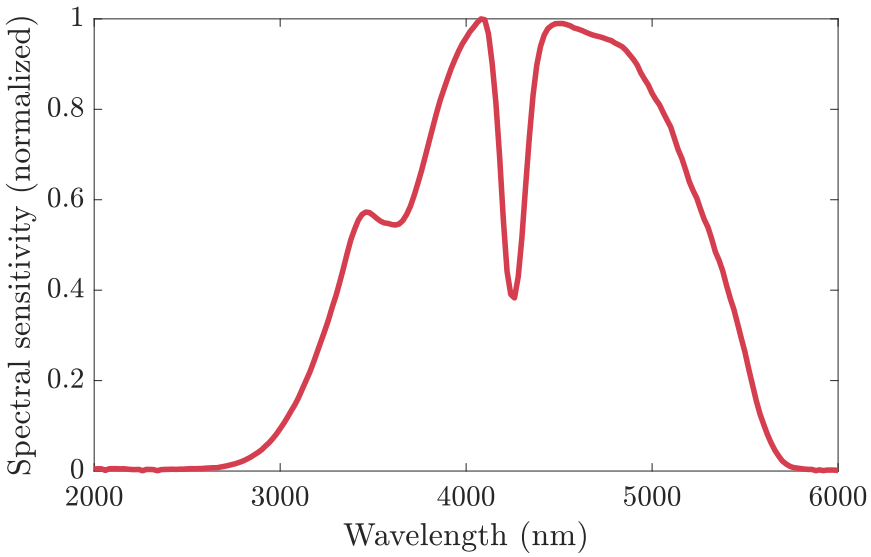

FIGURE 3.2 – Spectral sensitivity of the acquisition chain, measured by scanning the illumination wavelength with the monochromator. The peak around $\lambda = 4300$ nm corresponds to the CO_2 absorption.

The signal measured by each pixel, $U_{\text{pix}}(t)$, is directly proportional to the total flux $\Phi_{\text{tot}}(t)$ it receives. Depending on the received flux, each pixel generates an electrical signal: $U_{\text{pix}} = \rho_{\text{pix}}\Phi_{\text{tot}}$, with ρ_{pix} a proportionality factor specific to each pixel since they are all slightly different (size, black noise, offset, ...). To compensate for these differences, we perform a non-uniformity correction (NUC) before starting the measurements [93]. The method consists in taking several images of a black body covering the entire field of view of the camera. After calculating the temporal and spatial average of the signal, a correction coefficient is applied to each pixel. This operation is performed by the software of the camera (Altair).

In addition, the IR camera converts the voltage signal of each pixel in digital levels (DL). Since the camera has a dynamic range of 14 bits, the pixel value is in the range [0 ; 2^{14}-1] DL. If the incident flux is too intense, the pixel is saturated, and its value is theoretically 16 383 DL. However, the upper limit of the camera operating range is 14 000 DL. Beyond that, the incident flux and pixel value are no longer proportional, and the signal should be saturated. In addition, below 2 000 DL, the camera does not operate optimally either. Therefore, always be sure to work in the [2 000 - 14 000] DL range.

Finally, a Stirling cools the camera to a temperature of $T_{\text{CAM}} \approx 79$ K. As long as the camera is not properly cooled, the recorded signal is not stable enough. We propose to determine this drift by placing an ambient black body at 30 cm in front of the camera and regularly recording the measured signal. Figure 3.3 shows the drift of the measured signal over time. The sensor

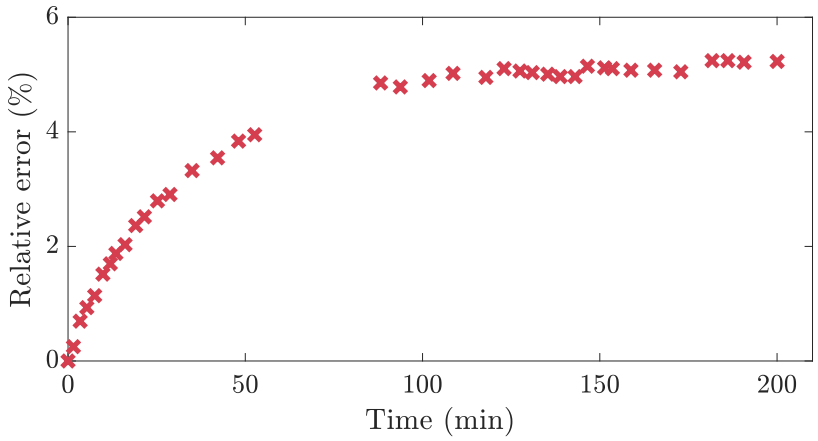

FIGURE 3.3 – Drift of the signal recorded by the camera over time, measured on a ROI of 50x50 pixels.

is only stable after two hours of operation: the measured signal at $t = 200$ min varies by more than 5% compared to the beginning of the measurement. That shows the importance of letting the camera cool down for at least two hours before making the measurements. Working with modulated signals reduces the impact of the camera drift on the results.

Mechanical chopper settings

In this setup, the camera is synchronized with the mechanical chopper to record one frame when the chopper cuts the IR beam, and another when the light passes through the sample [90]. The only requirement for the chopper frequency f_c is $f_c \gg f_T$ to properly remove the proper emission of the sample. We choose $f_c = 22$ Hz to let the chopper in the source housing, and the camera acquisition frame rate is $f_{\text{cam}} = 44$ Hz. The output signal of each pixel of the camera is given in the equation 3.2: the IR transmitted signal is only measured every other frame, at the frequency f_c. $\mathcal{C}(t)$ is the chopper rectangular wave function equals to 1 when the IR beam passes through the sample, and 0 when it is cut. The next section presents the double-demodulation method, applied on the images recorded by the camera.

$$U_{\text{pix}}(t) = \rho_{\text{pix}} \left[\Phi_0 \Gamma_0 (1 + \kappa \Delta T \cos(2\pi f_T t)) \mathcal{C}(t) + E(T, t)\right] \tag{3.2}$$

$$\begin{cases} \mathcal{C}(t) = 0, \text{ when the chopper cuts the IR beam} \\ \mathcal{C}(t) = 1, \text{ when the IR beam passes through the sample} \end{cases} \tag{3.3}$$

3.3 Double-demodulation method applied on images

As mentioned in the introduction, the camera output signal does not allow us to use a hardware lock-in amplifier to demodulate at the frequency f_c. Instead, we use the two-image method, subtracting the proper emission thanks to the synchronization of the camera with the chopper. In addition, since we record a maximum of two modulation periods, we cannot perform an efficient FFT to extract the signal at low frequencies. Thus, we detail the four-image method which is well-suited to retrieve the amplitude and phase of a signal with few periods.

The presented methods allow us to demodulate simultaneously the signal recorded by all the pixels of the camera. We do not work in real time but post process the films recorded during the experiment.

3.3.1 Proper emission subtraction: the two-image method

As mentioned in the description of the experimental setup, the camera is synchronized with the mechanical chopper to discriminate the transmitted flux $\Phi_0\Gamma(t)$ from the parasitic signal $E(t)$. The camera successively records one frame when the chopper lets the light passing through the sample (U_{on}) and another when it cuts the light beam (U_{off}). The frequency of the camera is $f_{\text{cam}} = 2f_c$ with f_c the chopper frequency, we introduce $\tau_{\text{cam}} = 1/f_{\text{cam}}$ (s). The difference between two consecutive frames results in equation 3.4.

$$U_{\text{on}}(t) - U_{\text{off}}(t + \tau_{\text{cam}}) = \rho_{\text{pix}}\Phi_0\Gamma_0[1 + \kappa\Delta T\cos(2\pi f_T t)] + \Delta_{\text{res}} \tag{3.4}$$

The term Δ_{res} is the residuals of the parasitic radiations and noise measurement after the subtraction: $\Delta_{\text{res}} = E(t) - E(t + \tau_{\text{cam}})$. These residuals are negligible compared to the thermotransmittance signal, providing some conditions:

- The proper emission must be constant between two consecutive frames, otherwise the residual Δ_{res} varies with temperature, and the demodulation is not correctly performed. This is why the chopper frequency, f_c, is set much higher than the thermal frequency, f_T. The first experimental measurement is to check if the proper emission is correctly removed with the chosen frequencies (f_T, f_c) (see section 3.5.1).

- The second point concerns the chopper position. If the chopper is outside the source housing, there is a risk of adding radiations coming from the chopper, E_{chop}, at the subtraction stage. The advantage of having it inside the source housing is that the monochromator filters out most of its radiation. As mentioned in the previous chapter, this configuration imposes $f_c < 30$ Hz.

Figure 3.4 shows the two-image method on two consecutive frames recorded by the IR camera, when the IR flux passes through the sample (a) and when it is cut by the chopper (b). The subtraction of the two images results in frame (c). As mentioned in section 3.2, the camera has a limited dynamic range of 14 bits. Since all the parasitic radiations are added to the useful IR transmitted flux, the remaining signal after two-image subtraction may be weak.

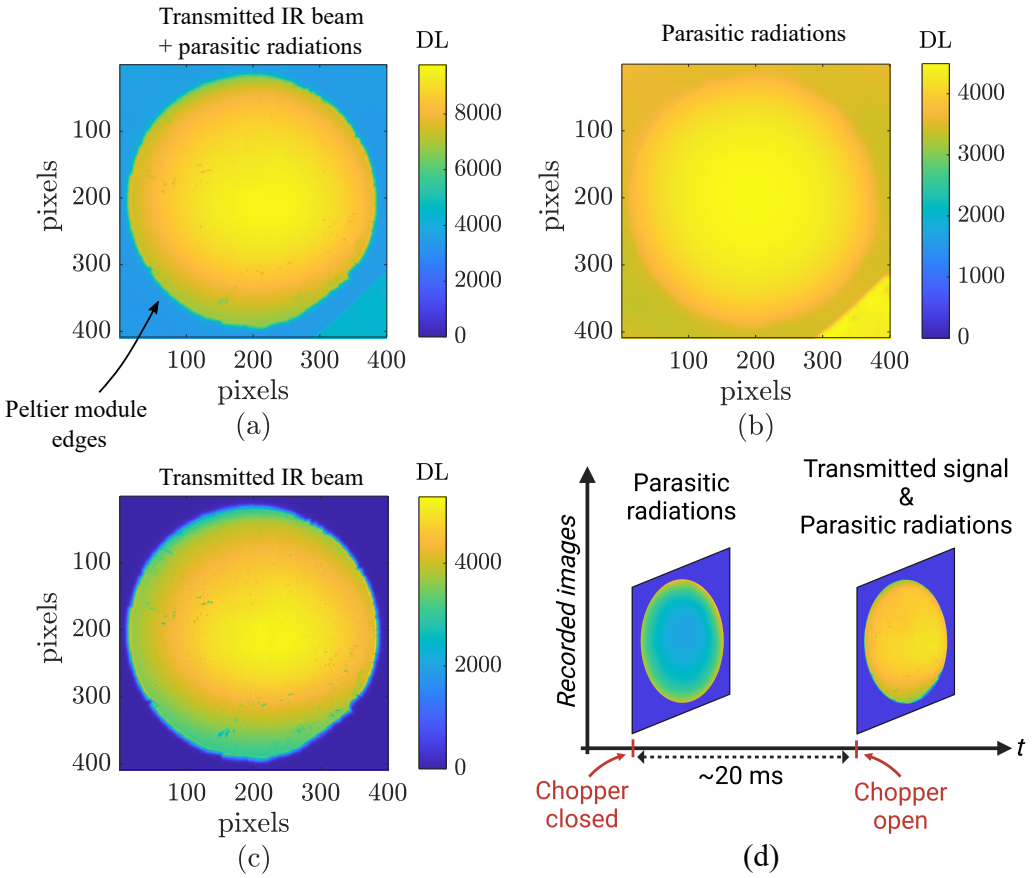

FIGURE 3.4 – Images of (a) IR transmitted beam with proper emission, $U_{\text{on}}(t)$, (b) proper emission and parasitic radiations, $U_{\text{off}}(t+\tau_{\text{cam}})$, and (c) IR beam after proper emission subtraction, $U_{\text{on}}(t) - U_{\text{off}}(t+\tau_{\text{cam}})$. (d) Illustration of the two-image process.

So, we understand the interest of maximizing the IR flux compared to the unwanted radiations. Several strategies are possible:

- As we cannot influence the proper emission of the sample, we must operate on the IR incident beam. One possibility is to concentrate its power. The higher the intensity of the transmitted beam, the more we can decrease the integration time of the camera and, thus, the component of the proper emission.

- The wavelength of the IR beam is chosen where the measured IR transmitted beam is maximal. This wavelength depends on the camera sensitivity and the transmittance of the sample.

- We can use an IR bandpass filter between the sample and the camera. That eliminates the components of the proper emission outside the filter. The filter must be adapted to the wavelength of the IR beam.

Using a filter generates parasitic reflections, attenuates the transmitted IR beam, and must be changed according to the wavelength. As a consequence, we focus on the first two points

for the following. Finally, after the two-image subtraction, we get the signal $U_{\text{pix,IR}}(t)$ at the chopper frequency f_c.

$$U_{\text{pix,IR}}(t) = \rho_{\text{pix}}\Phi_0\Gamma_0[1 + \kappa\Delta T\cos(2\pi f_T t)] + \Delta_{\text{res}} \tag{3.5}$$

3.3.2 Thermotransmittance demodulation: the four-image method

After subtracting the proper emission, the next step is demodulating the remaining signal of each pixel, $U_{\text{pix,IR}}(t)$, with respect to the temperature variation frequency. Instead of using a FFT as in chapter 2, we use the four-image algorithm [79, 80] which retrieves the amplitude and phase of a modulated signal. It requires only four temporally equidistant measurements in the modulation period $\tau = 1/f_T$ to implement the method: $t_n = n\tau/4 + t_0$ with $n \in [1, 2, 3, 4]$. In the case of the measured signal $U_{\text{pix,IR}}(t)$ without residual noise, $\Delta_{\text{res}} = 0$, we get the equations 3.6 and 3.7, with ΔT the amplitude of temperature variation. The process is illustrated in the figure 3.5.

$$\rho_{\text{pix}}\Phi_0\Gamma_0\kappa\Delta T = \frac{1}{2}\sqrt{[U_{\text{pix,IR}}(t_1) - U_{\text{pix,IR}}(t_3)]^2 + [U_{\text{pix,IR}}(t_2) - U_{\text{pix,IR}}(t_4)]^2} \tag{3.6}$$

$$\phi_{\text{pix}} = \tan^{-1}\left(\frac{U_{\text{pix,IR}}(t_4) - U_{\text{pix,IR}}(t_2)}{U_{\text{pix,IR}}(t_1) - U_{\text{pix,IR}}(t_3)}\right) + \phi_0 \tag{3.7}$$

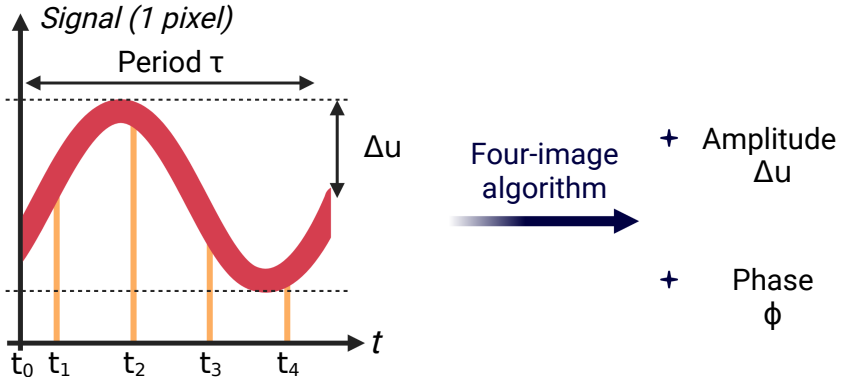

FIGURE 3.5 – Illustration of the four-image algorithm.

Theoretically, only four points are necessary to extract $\kappa\Delta T$, but experimentally the residuals Δ_{res} skew the results (see figure 3.6 (b)). To quantify the impact of residuals on the measured phase and amplitude, we first generate a modulated digital signal, $u(t) = 1 + \Delta u\cos(2\pi f t)$, with $f = 10$ mHz and $\Delta u = 1 \times 10^{-3}$, plotted in figure 3.6 (a). Second, a white noise is added to u(t): $u_{\text{noise}}(t) = u(t) + \varepsilon(t)$, (see Figure 3.6 (b)). Third, the amplitude Δu is calculated using the equation 3.6 for both signals.

We use a random set of four, but equidistant, points. We repeat the operation 5 000 times to obtain a statistical batch. The results are regrouped in Table 3.1: several measurements are required to recover the amplitude of the noisy signal with a weak standard error. Therefore,

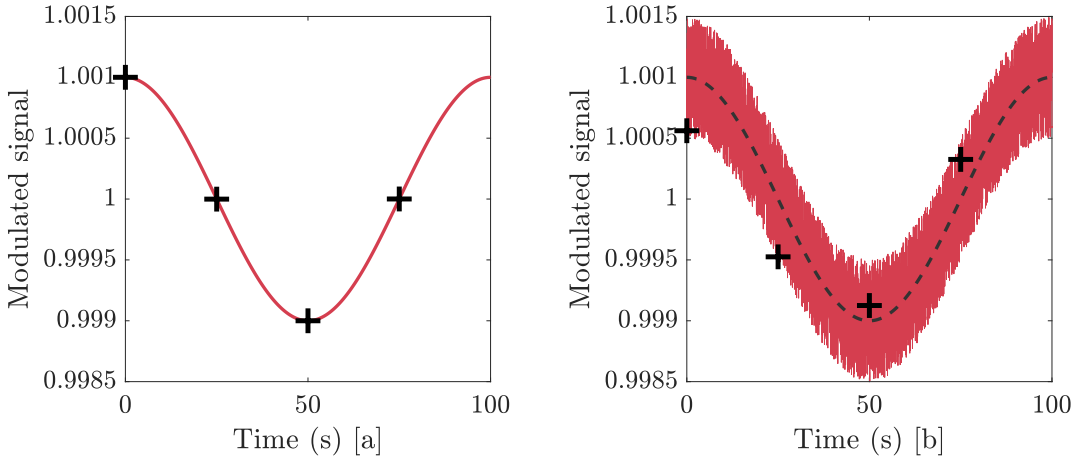

FIGURE 3.6 – (a) Signal $u(t) = 1 + \Delta u \cos(2\pi f t)$ with $f = 10$ mHz and $\Delta u = 1 \times 10^{-3}$. (b) Noisy signal $u_{\text{noise}}(t) = u(t) + \varepsilon(t)$, with $\varepsilon(t) \in [-0.5\Delta u \quad 0.5\Delta u]$. The black crosses represent a set of four points.

the strategy is to repeat the calculation on several sets of points. To do this, we implement a **four-image rolling algorithm**. We start with the first point of the period, identify the other three based on the period duration, and calculate the amplitude and phase. Then we take the second point of the period and repeat the process. We reiterate for all the points; hence the term *rolling*. Figure 3.7 (a) shows the noisy modulated signal $u_{\text{noise}}(t)$ over two periods. Let's detail the obtained amplitude and phase using the rolling four-image algorithm.

Amplitude Table 3.1 lists the amplitude and the corresponding standard error as a function of the number of iterations N of the rolling algorithm. As expected, the noise decreases by $\sqrt{N}$. Figure 3.7 (b) gives the compilation of all the measurements: the average over all the iterations allows to retrieve the amplitude: $\Delta u = 1.10^{-3} \pm \sigma$, with $\sigma = 2.10^{-6}$ for 5000 iterations. Same behavior is observed regarding the phase. We understand the advantage of measuring on a large number of iterations to improve the SNR.

Number of measurements	Amplitude $\Delta u(t)$	Standard error σ
1	1.10×10^{-3}	1.4×10^{-4}
10	0.95×10^{-3}	4.4×10^{-5}
100	1.00×10^{-3}	1.4×10^{-5}
500	1.00×10^{-3}	6.3×10^{-6}
5000	1.00×10^{-3}	2.0×10^{-6}

TABLE 3.1 – Amplitude and standard error of the noisy signal $u_{\text{noise}}(t)$ as a function of the number of measurements using the rolling four-image algorithm. Noise decreases by $\sqrt{N}$, with N the number of iterations.

Phase Figure 3.7 (c) shows a phase shift caused by the first point temporal displacement, Δt, during the iterations of the rolling algorithm. As a consequence, we measure a rolling phase, ϕ_{roll}, which depends on the phase shift between two consecutive points as expressed in Equation 3.8. We extract ϕ_{pix} by subtracting ϕ_{shift} from ϕ_{roll}, as shown in Figure 3.7 (d). Finally, the average over N iterations gives the signal phase with a weak standard error.

$$\phi_{\text{roll}} = \phi_{\text{pix}} + \underbrace{2\pi N f \Delta t}_{\phi_{\text{shift}}} \tag{3.8}$$

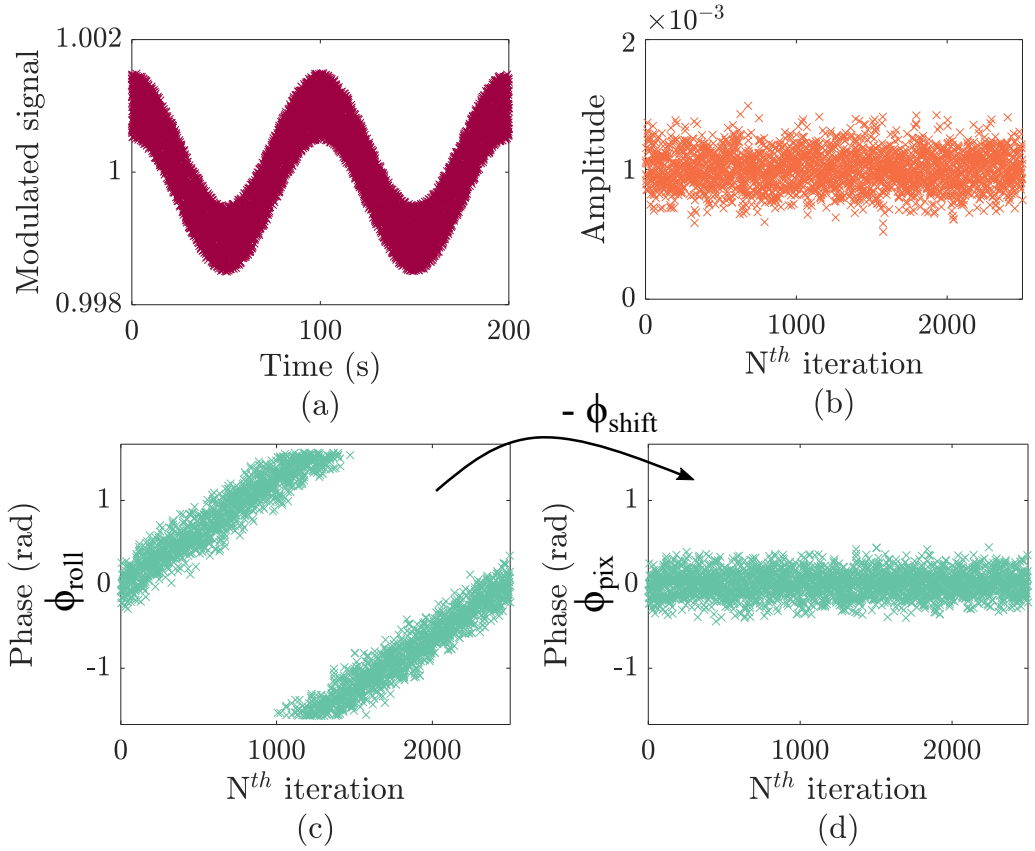

FIGURE 3.7 – (a) Modulated noisy signal, $u_{\text{noise}}(t)$, at $f = 10$ mHz. For each iteration of the rolling four-image algorithm, we get the amplitude (b) and the phase ϕ_{roll} (c) from which we extract the phase ϕ_{pix} (d).

Conclusion about the demodulation process

At the end of the demodulation process, we get the phase and amplitude of the transmitted IR beam, $\rho_{\text{pix}}\Phi_0\Gamma_0\kappa\Delta T$, for each pixel. In addition, the DC term $\rho_{\text{pix}}\Phi_0\Gamma_0$ is the average signal over the period. The absolute phase ϕ_{pix} of a single pixel is not of interest, but the spatial phase shift between the different pixels of the image can be linked to the thermal properties of the material as it is shown in next section.

Finally, the ratio between the component f_T and the DC one is proportional to the temperature variation, as expressed in the following equation.

$$\frac{\overbrace{\rho_{\text{pix}}\Phi_0\Gamma_0\kappa\Delta T}^{f_T \text{ component}}}{\underbrace{\rho_{\text{pix}}\Phi_0\Gamma_0}_{\text{DC component}}} = \kappa \overset{\text{Modeling}}{\boxed{\Delta T}} \tag{3.9}$$

The next step is modeling the temperature variation, ΔT, to calibrate the thermotransmittance coefficient κ.

3.4 Heat transfer modeling applied to the Borofloat wafer

This section models the heat transfer in a thin Borofloat wafer heated at its edges by the ring-shaped Peltier module under the same conditions as the study described in section 2.4. We calculate the sample temperature variation ΔT, evaluate the impact of inaccurately estimating its thermal properties, and determine the operating modulation frequency f_T.

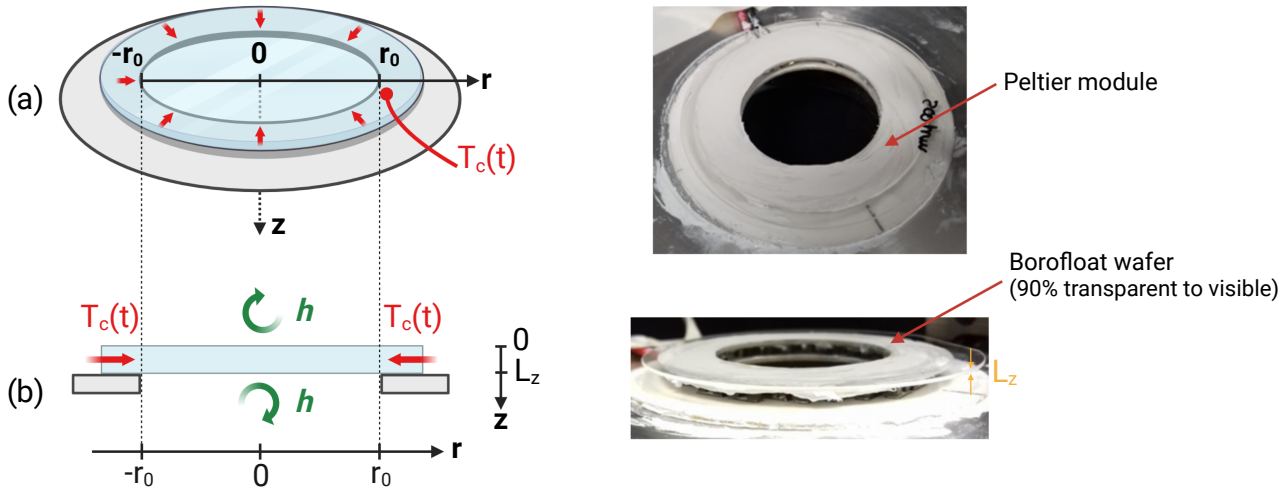

FIGURE 3.8 – Reminder of the Peltier module geometry, with heat transfer boundary conditions and corresponding images.

We perform a first modeling using the average values for the thermal properties of glass extracted from the literature [94], to anticipate the temperature rise in the material and determine the modulation frequency f_T. Table 3.2 provides the values used for the numerical implementation of the heat transfer model in the Borofloat wafer. In the second step, we measure the thermal properties to accurately calculate the temperature variation in the sample and determine the thermotransmittance coefficient.

The Biot number of the Borofloat wafer is: $B_i = hL_z/k \approx 5 \times 10^{-3} \ll 1$. Thus, the temperature along the thickness is considered homogeneous and we can use the heat transfer model developed for the Silicon wafer (see section 2.4). As a reminder, the complex temperature

Parameters	Values
Thickness, L_z	500 μm
Radius, r_0	13.5 mm *
Thermal conductivity, k	1 W/m/K [94]
Thermal diffusivity, a	7×10^{-7} m^2/s [94]
Convection coefficient, h	10 W/m^2/K
Thermal frequency, f_T	5 mHz and 10 mHz
Temperature variation at the edges, $\Delta T(r_0)$	10 °C

TABLE 3.2 – Parameters used for the heat transfer model (Borofloat 33). ** The diameter of the wafer is 50.8 mm. However the inner diameter of the ring-shaped Peltier module being 27 mm, the useful radius r_0 is 13.5 mm.*

variation field at the frequency f_T, $\Delta\underline{T}(r, \omega_T)$, is expressed in Equation 2.27, with $H = 2h/kL_z$ and $\Delta T(r_0)$ the temperature variation at the edge of the sample.

Choice of the thermal frequency f_T

Figure 3.9 shows the temperature module ratio $|\Delta\underline{T}(r = 0, f_T)|/|\Delta\underline{T}(r_0, f_T)|$ at the center of the wafer as a function of the thermal frequency. At very low frequencies $f_T < 10^{-3}$ Hz, the ratio is ≈ 0.26 and only depends on the convective losses. In the frequency range $f_T \in [1 - 10]$ mHz, the ratio varies from 0.26 to 0.14. The smaller the ratio, the greater the temperature gradient. Regarding the choice of the experimental thermal frequency, we do not exceed 10 mHz: beyond, the temperature variations at the center should be too weak to be measured with the current setup (see section 3.5.4).

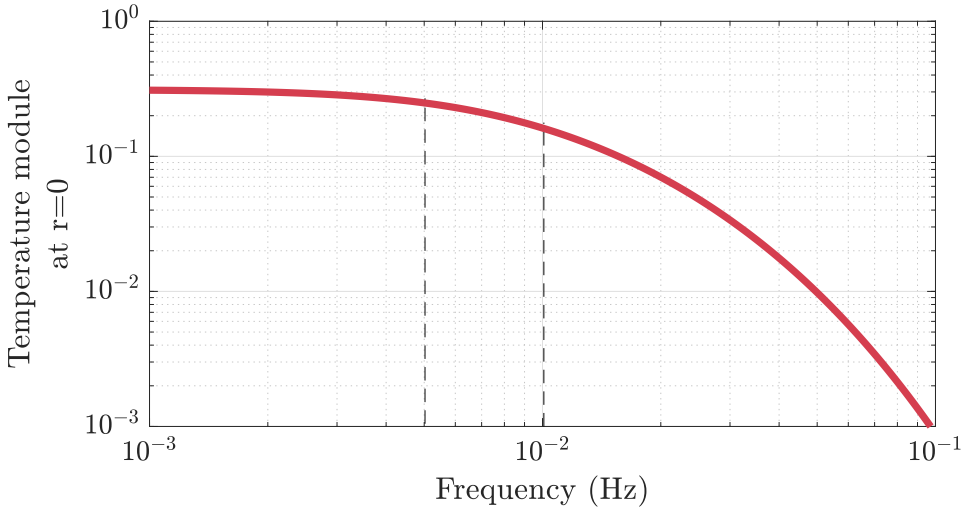

FIGURE 3.9 – Temperature module ratio, $|\Delta\underline{T}(r = 0, f_T)|/\Delta T(r_0)$, at the center of the wafer, depending on the thermal frequency f_T. The dotted lines shows the studied frequencies, 5 mHz and 10 mHz.

In addition, Figure 3.10 shows the temperature amplitude (a) and phase (b) profiles across the Borofloat wafer surface. Two thermal frequencies are tested: $f_T = 5$ mHz and $f_T = 10$ mHz. At the center, $r = 0$ mm, the modules are $|\Delta\underline{T}(r = 0, f_T = 5 \text{ mHz})| = 2.1°C$, and $|\Delta\underline{T}(r = 0, f_T = 10 \text{ mHz})| = 1.5°C$. For the following, we work at a frequency of 5 mHz. Due to the detection threshold and the uncertainty on the thermal properties estimation, it is not certain that we will detect a variation smaller than 1.5°C at $r = 0$ (see section 3.5.4). Figure 3.10 shows theoretical amplitude (c) and phase (d) maps of the temperature variation at the surface of the Borofloat wafer at the frequency $f_T = 5$ mHz to help us visualizing the expected measurements.

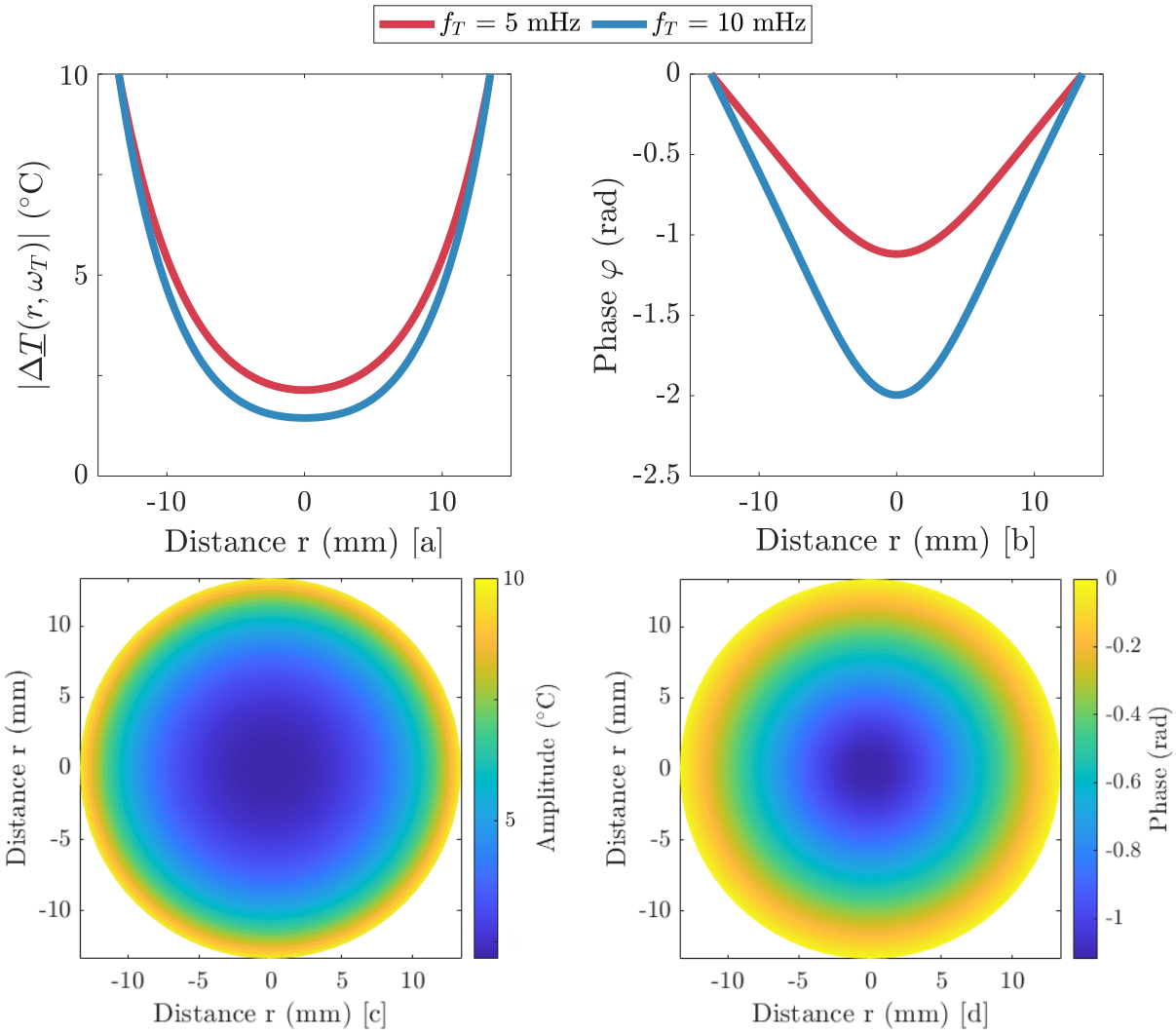

FIGURE 3.10 – Profiles of (a) amplitude $|\Delta\underline{T}(r, \omega_T)|$, and (b) phase $\phi(r, \omega_T)$ of the temperature variation through the Borofloat wafer. Theoretical maps of amplitude (c) and phase (d) at the frequency $f_T = 5$ mHz.

Sensitivity of the amplitude and phase of $\Delta\underline{\mathrm{T}}(r)$ to the thermal properties

Figure 3.11 shows that the temperature variation $|\Delta\underline{\mathrm{T}}(r)|$ is significantly impacted by a change in the estimation of the thermal properties. For instance, at $r = 0$, $|\Delta\underline{\mathrm{T}}(r = 0)|$ varies between 1.6°C and 2.3°C for respectively $a = 4\times10^{-7}$ m^2/s and $a = 10\times10^{-7}$ m^2/s, with $k = 1$ W/m/K. Regarding the thermal conductivity, for $k \in [0.5 - 1.5]$ W/m/K with $a = 7 \times 10^{-7}$ m^2/s, the temperature is in the range $|\Delta\underline{\mathrm{T}}(r = 0)| \in [0.8 - 2.9]$°C. In the same way, the convection coefficient h also has an impact on $\Delta\underline{\mathrm{T}}(r)$. Hence, it is necessary to measure these properties to determine precisely the temperature variation $\Delta\underline{\mathrm{T}}(r)$ at the sample surface. To do so, we have three unknowns to determine: a, k, and h. However, rather than finding all three simultaneously, we can determine a and $H = 2h/kL_z$, which is sufficient for our calculations. Equations 3.10 and 3.11 enable us to derive k and h from a and H, supposing known the mass density ρ and the specific heat capacity c_p of the material.

$$k = a\rho c_p \tag{3.10}$$

$$h = \frac{HkL_z}{2} \tag{3.11}$$

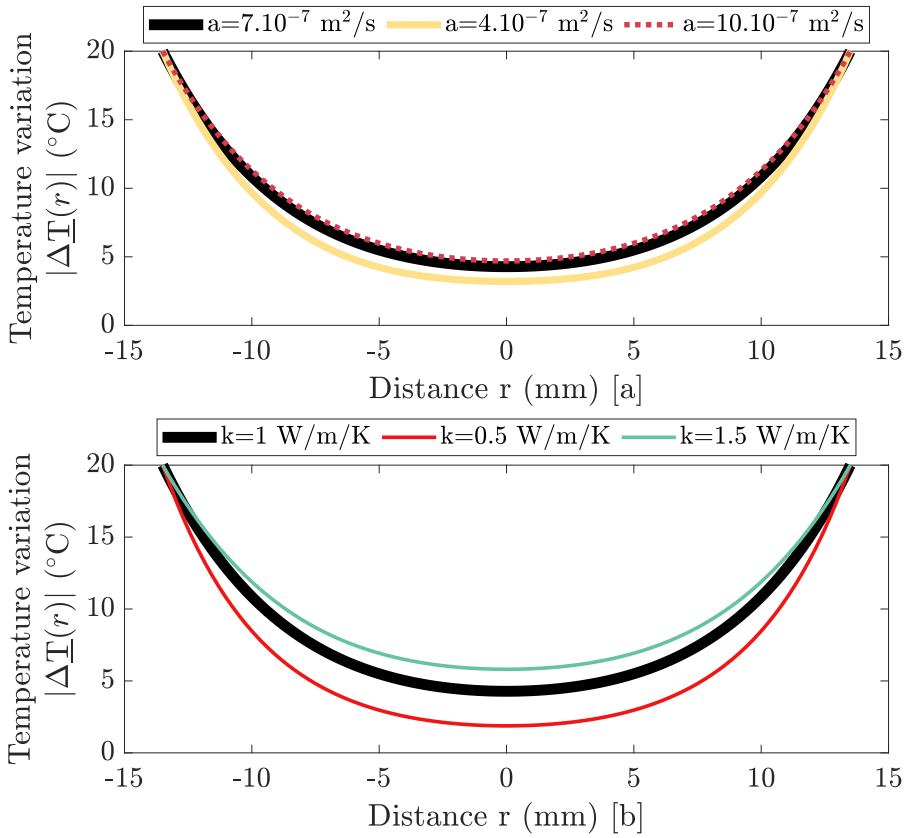

FIGURE 3.11 – Amplitude $|\Delta\underline{\mathrm{T}}(r, \omega_t)|$ as a function of the distance r (mm) (a) varying the thermal diffusivity with fixed thermal conductivity $k = 1$ W/m/K, and (b) varying the thermal conductivity with fixed thermal diffusivity $a = 7.10^{-7}$ m^2/s. The frequency is $f_T = 5$ mHz and the convection coefficient is $h = 10$ W/m^2/K. The black lines correspond to the set of data used in the model.

Fortunately, the 2D measurements combined with the model allow us to extract the thermal properties of the sample. We perform a sensitivity study of the temperature field to the thermal properties to determine which of the amplitude or the phase enable us to identify these parameters. Equations 3.12 and 3.13 give the expressions of the amplitude and phase sensitivities with respect to a and H. The study is conducted for a thermal frequency of 5 mHz, and each parameter varies by 10% of its value: $a = (7.0 \pm 0.7) \times 10^{-7}$ and $H = (4 \pm 0.4) \times 10^{4}$ m^{-2}.

$$S_{|\Delta T|}[a](r) = a\frac{\partial|\underline{\Delta T}(r,a,H)|}{\partial a} \qquad S_{|\Delta T|}[H](r) = H\frac{\partial|\underline{\Delta T}(r,a,H)|}{\partial H} \tag{3.12}$$

$$S_{\phi}[a](r) = a\frac{\partial\phi(r,a,H)}{\partial a} \qquad S_{\phi}[H](r) = H\frac{\partial\phi(r,a,H)}{\partial H} \tag{3.13}$$

Figures 3.12 (a) and (b) show the sensitivities to each parameter, as a function of the distance r. The phase is more sensitive to the thermal diffusivity than to the convective losses, and the amplitude has the opposite behavior. In addition, a and H are not correlated at the center of the sample in the range $r \in [-7.5 \quad 7.5]$ mm, which allows reliable identification of these two parameters.

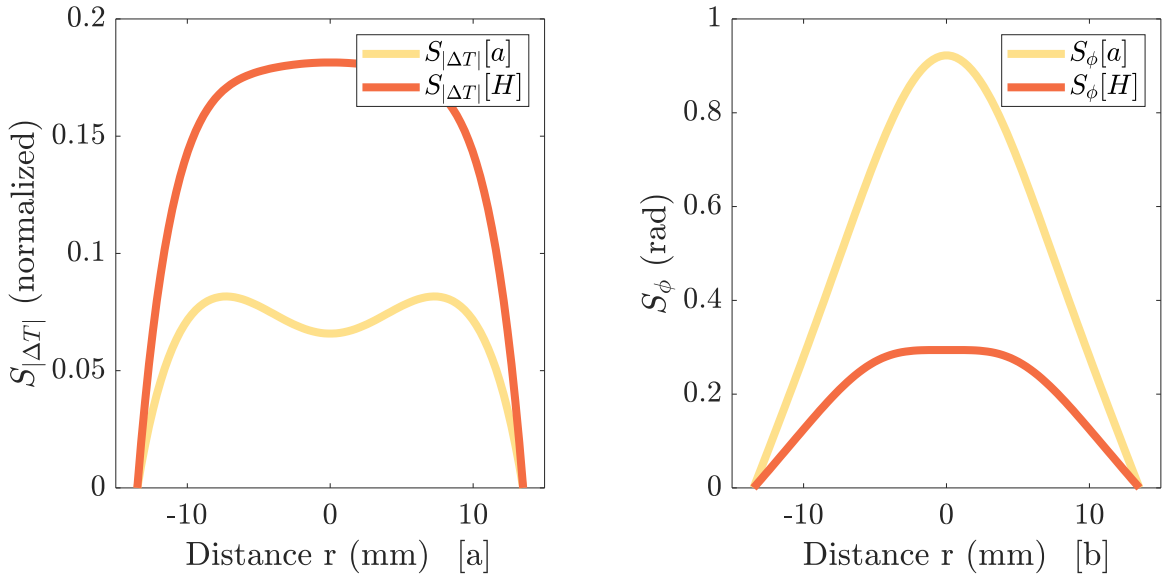

FIGURE 3.12 – Temperature variations amplitude (a) and phase (b) sensitivity to the thermal diffusivity a and the loss factor H.

3.5 Thermotransmittance measurement of the Borofloat

In sections 3.2 and 3.3 we have demonstrated the method for measuring the thermotransmittance signal and extracting its amplitude and phase at the thermal frequency f_T through double-demodulation. Then, in section 3.4, we have determined the operating frequency f_T, and confirmed the importance of precise measurement of thermal properties to calculate the temperature variation ΔT.

This section describes the measurement of the thermotransmittance coefficient for several illumination wavelengths λ. To achieve this result, the following steps must be executed. First, we ensure that the residuals Δ_{res} of the two-image subtraction do not vary with temperature. Then, we identify the thermal diffusivity, a, and the loss factor, H, of the Borofloat wafer, using the amplitude and phase of the thermotransmittance signal. Finally, we calculate the temperature variation in the sample and extract the thermotransmittance coefficient using the relation 3.9.

3.5.1 Checking the efficiency of parasitic radiations subtraction

We have mentioned in section 3.3.1 that we must check that the residuals of the parasitic signal after the two-image subtraction, Δ_{res}, are not temperature dependent. This could happen if the chopper frequency f_c is not high enough compared to f_T to ensure that the sample proper emission is constant between two consecutive frames.

To perform this check, we still modulate the temperature at the frequency f_T and record frames at the frequency $2f_c$, but the IR beam remains cut off. We then apply the double-demodulation method described in section 3.3. If the proper emission is constant between two successive images, we should obtain an amplitude of zero. Nevertheless, we observe a non-zero amplitude, which must be of the same order of magnitude than the measurement noise. Therefore, we conduct another measurement without thermal excitation to determine this noise ($\Delta T = 0$).

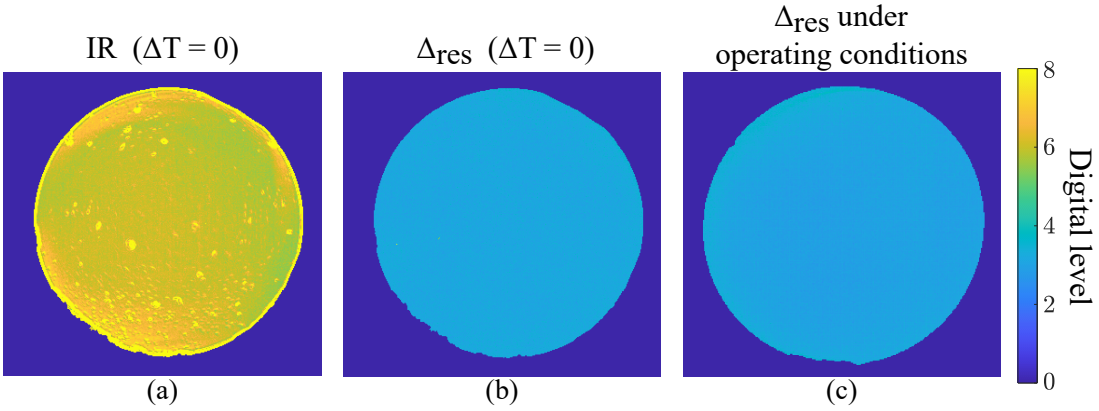

FIGURE 3.13 – Noise measurement of the IR transmitted flux (a) and proper emission residuals Δ_{res} without heating the sample ($\Delta T = 0$), and (c) Δ_{res} by heating the sample at frequency $f_T = 5$ mHz with $\Delta T(r_0) = 10°\text{C}$. The chopper frequency is $f_c = 20$ Hz.

Figure 3.13 shows the noise measurement of the IR transmitted flux (a) and residuals Δ_{res} (b) without heating the sample, and the residuals Δ_{res} in our experimental conditions at frequency $f_T = 5$ mHz and $\Delta T(r_0) = 10°\text{C}$ (c). As a result, the residuals with and without temperature excitation are identical (≈ 3 DL), and they are smaller than the measurement noise of the transmitted flux (≈ 6 DL) mainly caused by the source fluctuations. In conclusion, the proper emission variation between two successive frames is negligible at working frequencies ($f_T = 5$ mHz and $f_c = 20$ Hz).

3.5.2 Measurement of thermal properties of the Borofloat

We have confirmed that the proper emission is correctly removed using the two-image subtraction at the working frequencies f_T and f_c. Now, we use the four-image algorithm to extract the phase and amplitude of the thermotransmittance signal. The first operation is to determine the thermal properties of the material by minimizing the difference between the model and the measurements.

Measurement of the thermotransmittance amplitude

First, the four-image demodulation retrieves the amplitude for each pixel, $\Delta U_{\text{pix,IR}}$ (see equation 3.14). To obtain the thermotransmittance expression we divide the amplitude by the average signal over time, $\bar{U}_{\text{pix,IR}}$, as shown in equation 3.16.

$$\Delta U_{\text{pix,IR}} = \rho_{\text{pix}} \Phi_0 \Gamma_0 \kappa \Delta T \tag{3.14}$$

$$\bar{U}_{\text{pix,IR}} = \rho_{\text{pix}} \Phi_0 f_T \int_0^{1/f_T} \Gamma(t)\, \mathrm{d}t = \rho_{\text{pix}} \Phi_0 \Gamma_0 \tag{3.15}$$

$$\frac{\Delta U_{\text{pix,IR}}}{\bar{U}_{\text{pix,IR}}} = \kappa \Delta T \tag{3.16}$$

Figure 3.14 (a) plots the IR transmitted signal of two pixels over time, $\frac{\Delta\Gamma(t)}{\Gamma_0}$: one at the edge of the sample (150,30) and one at the center (150,150). We observe that the signal is modulated at f_T for the both pixels with a significant measurement noise of $\varepsilon_{\text{pix}} \approx 2.5 \times 10^{-3}$. With the rolling four-image algorithm, we extract the amplitude of the recorded signal for all the pixels. Figure 3.14 (b) gives the results for the pixels (150,30) and (150,150): their mean value is respectively $\Delta\Gamma/\Gamma_0(150{,}30) = 5.0 \times 10^{-3}$ and $\Delta\Gamma/\Gamma_0(150{,}150) = 1.6 \times 10^{-3}$ with a standard error of 1.5×10^{-5}.

Finally, Figure 3.15 (a) shows the mean thermotransmittance amplitude for each pixel. The corresponding standard error is presented in figure 3.15 (b). Most of pixels have a standard error about 1.5×10^{-5}, with some spots corresponding to scratches on the sample surface. Moreover, the standard error is higher at the edges of the sample than in the center. We assume that it is due to the vibrations caused by the camera Stirling cooler which amplifies the artifacts at the edges where the temperature gradient is more intense. In addition, discerning the limit between the wafer and the Peltier module is challenging, and the vibrations cause this boundary to shift between successive frames.

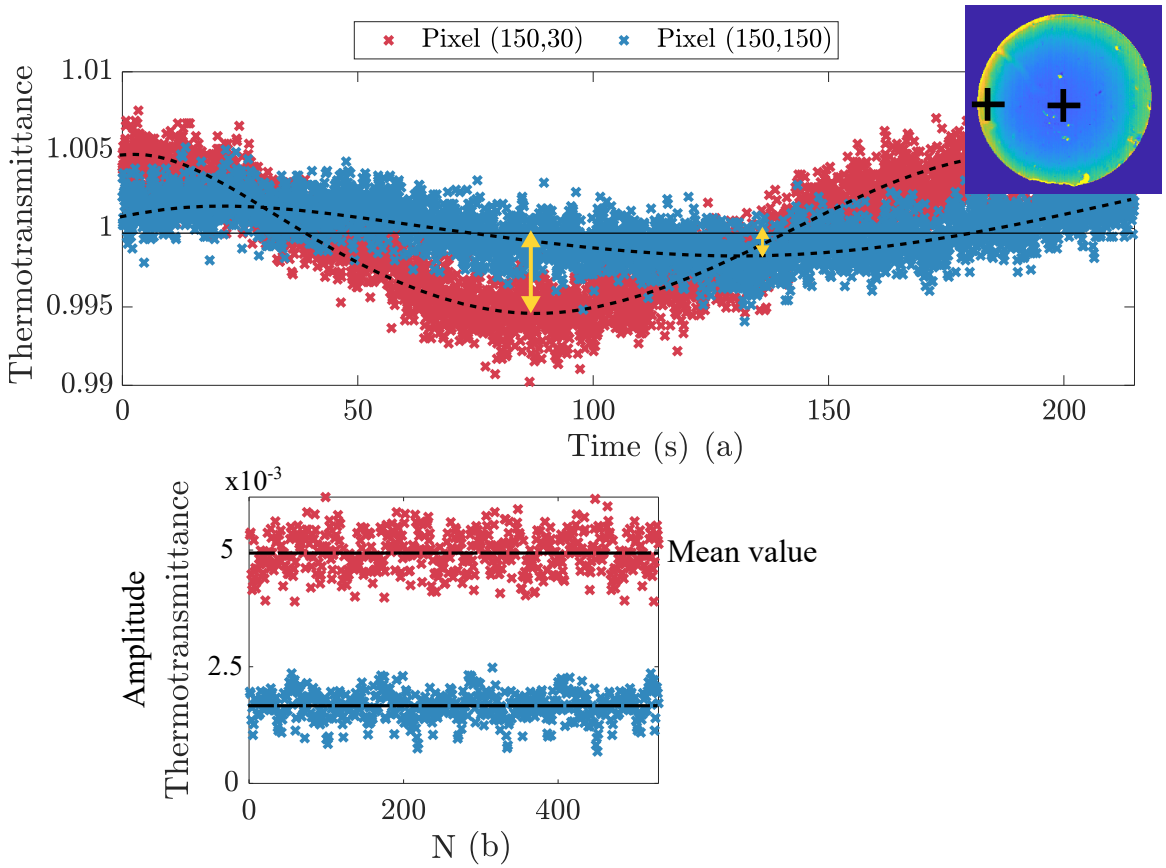

FIGURE 3.14 – (a) Thermotransmittance signal over time, $\Delta\Gamma/\Gamma_0(t)$. (b) Amplitude measured with the rolling 4-image algorithm for pixel (150,30) and pixel (150,150) for several iterations. The final amplitude is the mean of all these values.

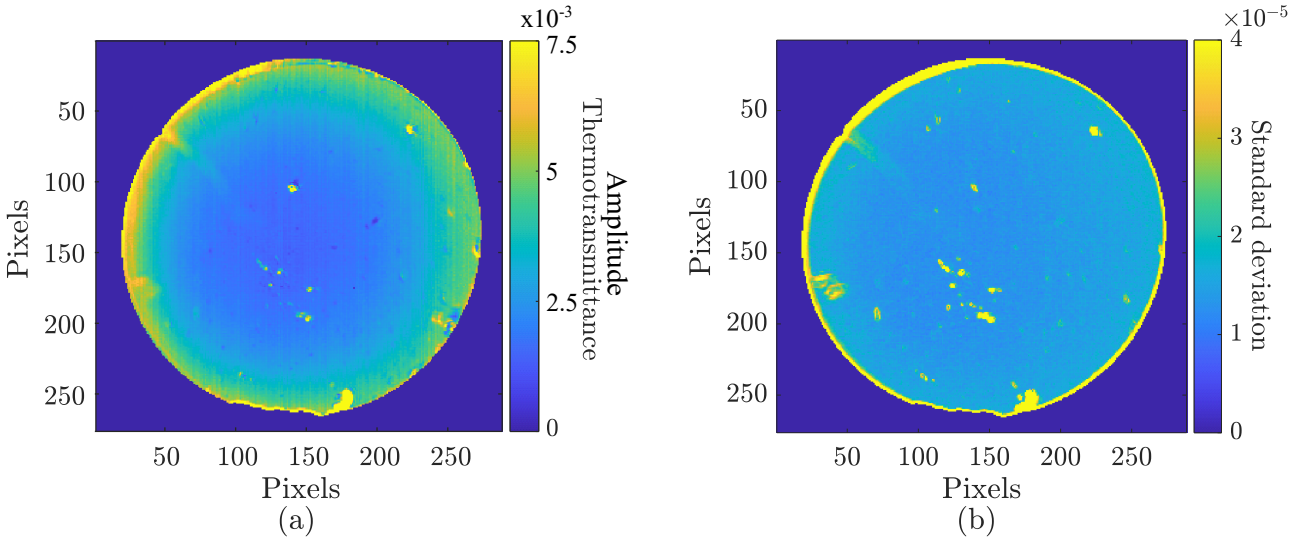

FIGURE 3.15 – (a) Map of the thermotransmittance amplitude for each pixel, and corresponding standard error calculated with all the values measured with the rolling four-image algorithm (b).

Measurement of the thermotransmittance phase

Second is the measurement of the thermotransmittance phase, calculated with the rolling four-image algorithm for N iterations (see equation 3.8). Figure 3.16 (a) shows the mean phase map calculated from all the values extracted with the rolling four-image algorithm. Graph (c) plots the phase of the pixels (150,30) and (150,150) for each iteration. The standard error of the phase is presented in figure 3.16: the error varies between 0.001 and 0.01 rad as a function of the distance r. Unlike the amplitude, the error is higher at the center of the wafer if we exclude the few pixels at the border of the Peltier module and the scratches on the surface.

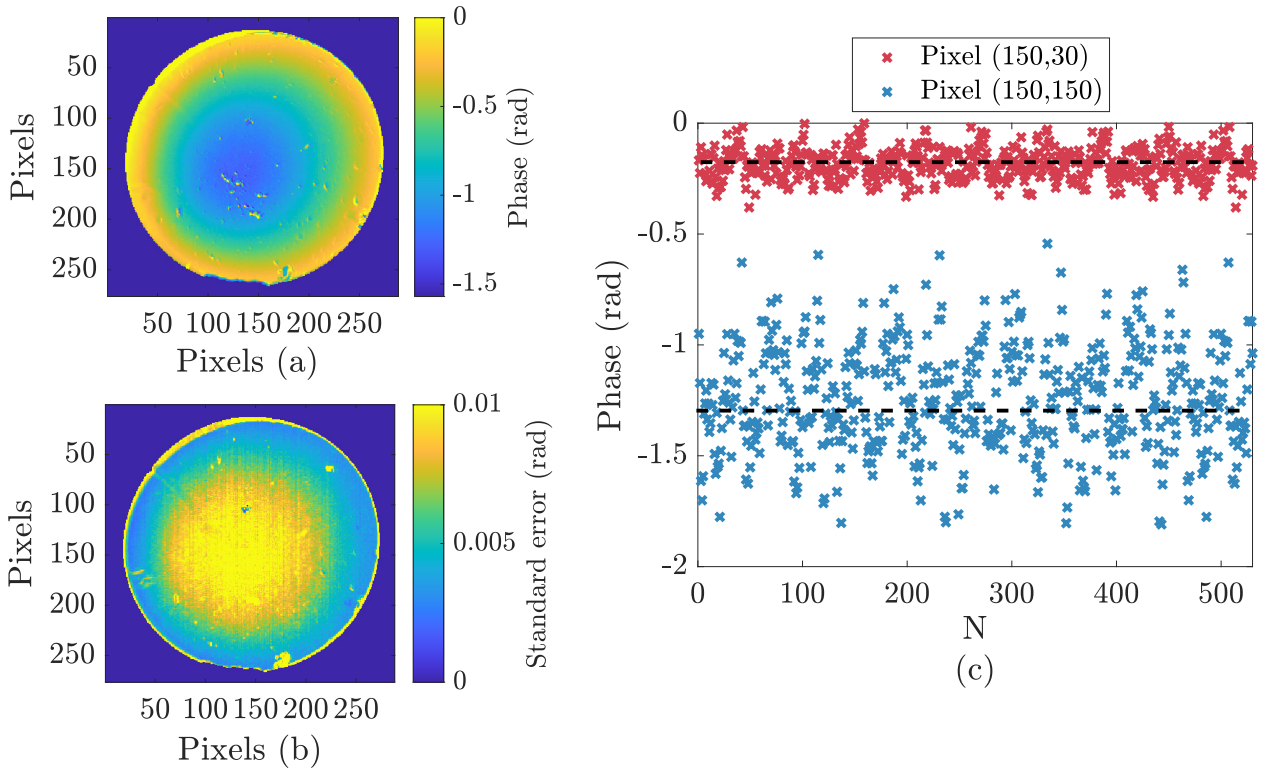

FIGURE 3.16 – (a) Phase of the thermotransmittance for each pixel, and corresponding standard error (b). (c) Phase for two pixels (150,30) and (150,150) for several iterations of the rolling four-image algorithm. We observe that the standard error is higher at the center of the wafer.

Minimization algorithm to determine the thermal properties

Third, using the phase and amplitude maps of the thermotransmittance signal, we can determine the thermal properties of the Borofloat [95]. For that, we compare the measurements to the heat transfer model described in section 3.4. The minimization algorithm is detailed below:

1. Each pixel with coordinates (n_x, n_y) has a corresponding distance r from the center of the wafer (n_{x_0}, n_{y_0}), determined by the spatial resolution of 107 μm/pixel.

$$r_{(x,y)} = \sqrt{[(n_x - n_{x_0}) \times 107\mu m/pix]^2 + [(n_y - n_{y_0}) \times 107\mu m/pix]^2} \tag{3.17}$$

2. The amplitude and phase maps are reshaped into vectors and sorted by the radial distance r.

3. To remove the thermotransmittance coefficient from the equation, the amplitude is normalized. This can be done by choosing any position, but typically we use the amplitude at $r = 0$.

$$\frac{\Delta\Gamma(r)}{\Gamma_0} \times \frac{\Gamma_0}{\Delta\Gamma(0)} = \frac{|\Delta\underline{T}(r, \omega_T)|}{|\Delta\underline{T}(0, \omega_T)|} \tag{3.18}$$

4. To ensure that $\phi(r_0) = 0$, we subtract the term ϕ_0 from the measurements.

5. The cost function, $\mathcal{J}$, calculates the difference between the model and the measurements for both the amplitude and phase at the same time.

$$\mathcal{J}(a, H) = \left\| \frac{\Delta\Gamma(r, \omega_T)/\Gamma_0}{\Delta\Gamma(0, \omega_T)/\Gamma_0} - \frac{|\Delta\underline{T}(r, \omega_T, a, H)|}{|\Delta\underline{T}(0, \omega_T, a, H)|} \right\|^2 + \|\phi_{\text{measured}}(r, \omega_T) - \phi_{\text{model}}(r, \omega_T, a, H)\|^2 \tag{3.19}$$

6. To find (a, H) by minimizing the value of $\mathcal{J}$, we use a simplex derivative-free algorithm [96] (*fminsearch* function, Matlab [97]). The simplex algorithm varies the values of a and H until a local minimum of the cost function $\mathcal{J}$ is obtained. At the end of the process, we get the optimal values of a and H .

   Note that there are various types of minimization algorithms that are commonly used in thermal applications, such as Bayesian methods [98, 99, 10], gradient descent [100], ... In this thesis, we focus on developing the thermotransmittance measurement and not on improving the minimization algorithm, which is a topic of its own. However, it would be worthwhile to explore this topic further in the future.

Measurement of the thermal properties

The amplitude (a) and phase (b) of the thermotransmittance signal as a function of the radial distance r to the center of the wafer are presented in figure 3.17. There are 52 623 points in each graph, and the red lines represent the model that uses the estimated values of a and H. Some outliers are present in the center and on the edges, which are caused by scratches on the sample surface and the rough edge of the Peltier module. However, these outliers do not significantly affect the estimation of thermal properties due to the large number of data points collected.

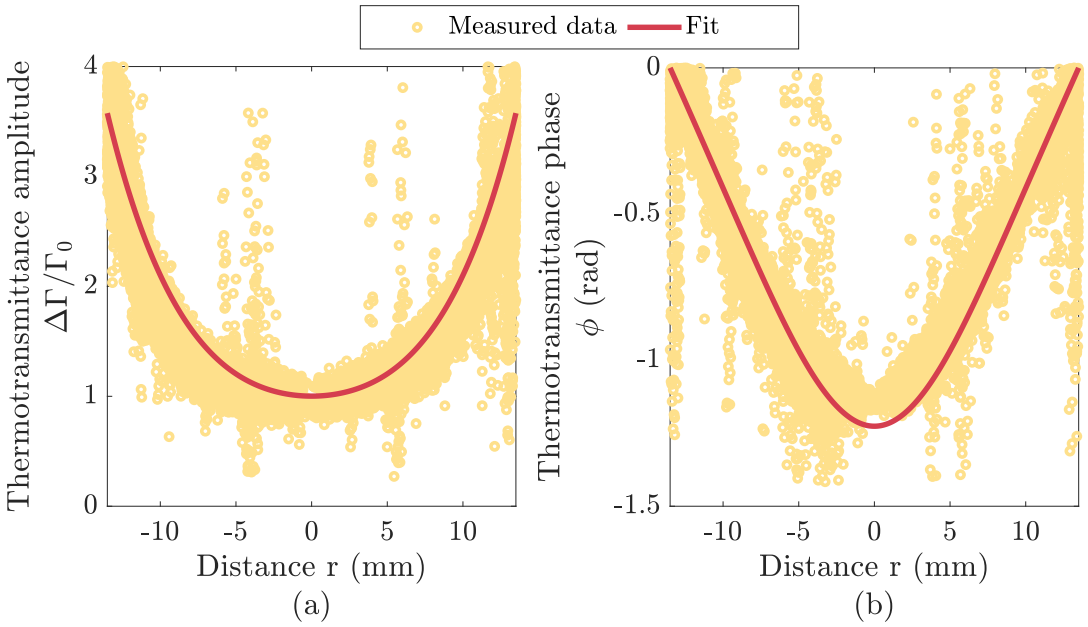

FIGURE 3.17 – (a) Amplitude normalized at $r = 0$ and (b) phase, as a function of the distance to the center r. Yellow circles: measurements at $\lambda = 3300$ nm and $f_T = 5$ mHz. Red lines: heat transfer model.

Table 3.3 lists the thermal properties obtained with several measurements with different illumination wavelengths. Each study includes five measurements. At the end, the thermal diffusivity is $a = (8.2 \pm 0.7) \times 10^{-7}$ m^2/s, the loss factor is $H = (2.86 \pm 0.41) \times 10^4$ m^{-2}. The uncertainties are calculated using all measurements presented Table 3.3.

By using the mass density, $\rho = 2200$ kg/m^3, and specific heat capacity, $c_p = 800$ J/m^2/K, provided by the Borofloat data-sheet [101], it is possible to estimate the thermal conductivity and convection coefficient with the equations 3.10 and 3.11. The thermal conductivity is $k = (1.4 \pm 0.2)$ W/m/K and the convection coefficient is $h = (10 \pm 2)$ W/m^2/K, which is consistent with the literature for a glass material [102] in a vertical position [82].

Wavelength, λ (nm)	Thermal diffusivity, a (m^2/s)	Loss factor, H (m^{-2})
3100	$(9.7 \pm 2.5) \times 10^{-7}$	$(3.10 \pm 0.50) \times 10^4$
3300	$(7.4 \pm 0.6) \times 10^{-7}$	$(2.90 \pm 0.48) \times 10^4$
3400	$(8.1 \pm 0.6) \times 10^{-7}$	$(2.98 \pm 0.64) \times 10^4$
3800	$(8.4 \pm 0.7) \times 10^{-7}$	$(3.23 \pm 0.12) \times 10^4$
4000	$(8.7 \pm 0.8) \times 10^{-7}$	$(3.19 \pm 0.33) \times 10^4$
4200	$(8.3 \pm 1.2) \times 10^{-7}$	$(2.40 \pm 0.65) \times 10^4$
4400	$(7.9 \pm 0.9) \times 10^{-7}$	$(2.80 \pm 0.50) \times 10^4$
4600	$(8.7 \pm 0.3) \times 10^{-7}$	$(2.54 \pm 0.10) \times 10^4$
Average	$(8.2 \pm 0.7) \times 10^{-7}$	$(2.86 \pm 0.41) \times 10^4$

TABLE 3.3 – Measured thermal properties of the Borofloat wafer, for several illumination wavelengths.

3.5.3 Thermotransmittance coefficient κ as a function of the wavelength λ

With the knowledge of the thermal properties of the sample a and H, we calculate the temperature variation $|\Delta\underline{T}(r)|$ in the sample using the equation 2.27. We first present the transmittance spectrum of the Borofloat to determine the studied wavelengths, and show the measured thermotransmittance coefficients.

Transmittance of the Borofloat wafer

Figure 3.18 shows the Borofloat transmittance in the mid-infrared spectral range measured with a commercial FTIR [84], and the monochromator setup by scanning the illumination wavelength. Both methods give similar results, but the monochromator setup is not adapted for $\lambda < 2600$ nm due to the camera sensitivity (see figure 3.2). In addition, considering the large bandwidth of the IR beam coming out of the monochromator, transmittance peaks are slightly smoothed with this setup, contrary to one acquired with the FTIR. Finally, the measurements are compared to the supplier data-sheet for a sample with a thickness of 700 μm (no data available for $L_z = 500$ μm). The shapes are similar, and the thickness difference explains most likely why the supplier data is lower than the measured one. According to the transmittance spectrum, we should be able to measure the thermotransmittance of the Borofloat from $\lambda = 2700$ nm to $\lambda = 4600$ nm. In practice, due to the camera sensitivity, we can only measure a thermotransmitted signal from $\lambda = 3100$ nm.

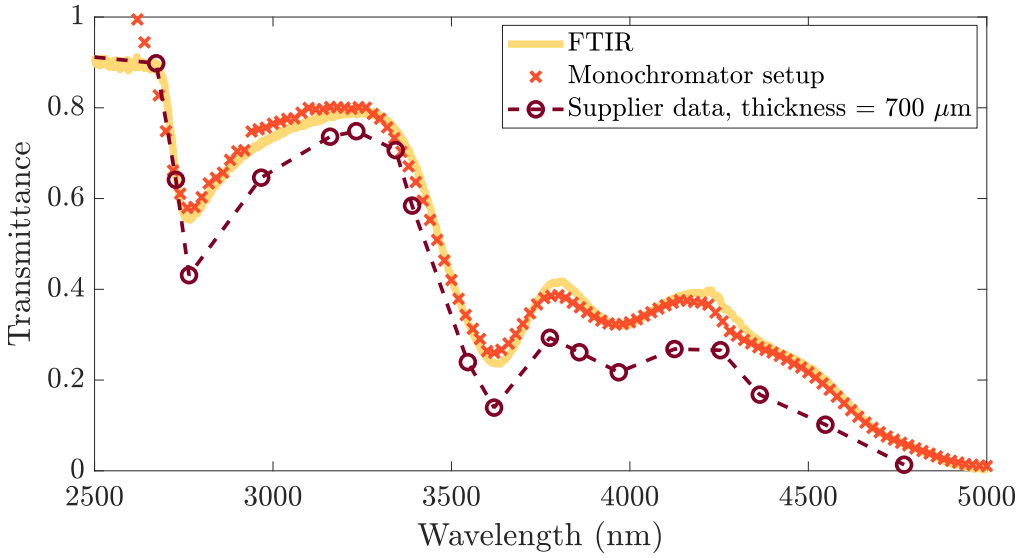

FIGURE 3.18 – Borofloat transmittance in the mid-infrared spectral range measured using our monochromator and a commercial FTIR.

Thermotransmittance coefficient of the Borofloat, as a function of the wavelength

Figure 3.19 shows the measured amplitude of the thermotransmittance signal $\Delta\Gamma/\Gamma_0$ depending on the temperature variation $|\Delta\underline{T}(r)|$, at $\lambda = 3300$ nm. The slope of the linear regression corresponds to the thermotransmittance coefficient κ.

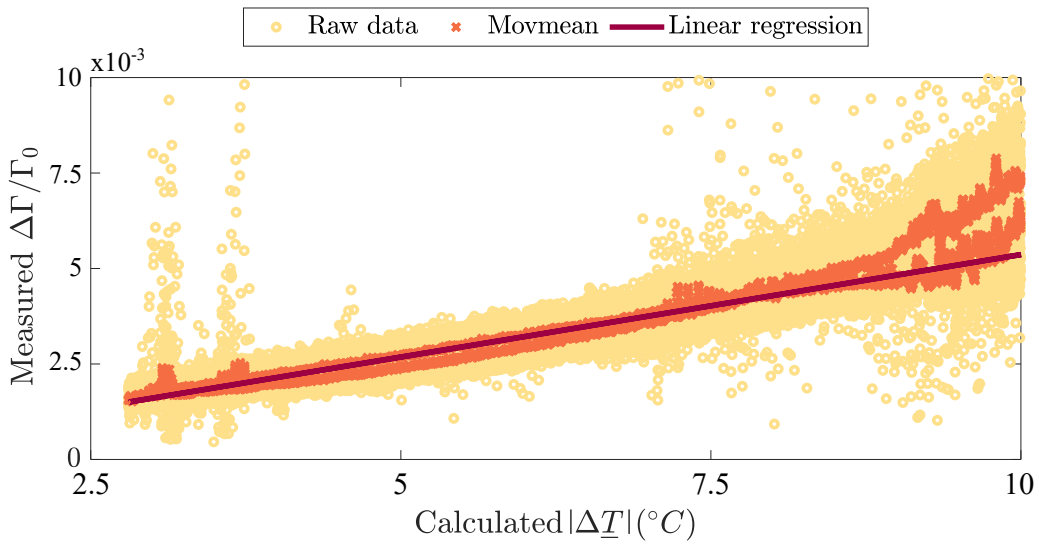

FIGURE 3.19 – Thermotransmittance amplitude versus temperature variation amplitude $|\Delta\underline{T}|$. Yellow circles: 52 623 measurements. Orange crosses: 50-point moving average. Red line: linear regression; its slope gives the thermotransmittance coefficient.

We observe some measurements issues at the edges, corresponding to temperatures variations between 9.5°C and 10°C. Several hypotheses can explain this phenomenon:

- An error in the position of the sample center (n_{x_0}, n_{y_0}) has a great impact on the edges where the temperature gradient is highest.
- As mentioned previously, camera vibrations further affect data at the edges of the sample.
- Stray reflections may also occur at the internal edges of the Peltier module (see image 3.8).

The thermotransmittance coefficient values measured for several illumination wavelengths are listed in Table 3.4 and plotted in Figure 3.20 (b). For the Borofloat wafer under study, the higher the wavelength, the greater the thermotransmittance coefficient in absolute value. However, the measured signal may not necessarily be higher at longer wavelengths due to the sensitivity of the acquisition system. Figure (c) represents the absolute variations for a temperature rise of $\Delta T = 1$ K (red crosses) weighted by the acquisition chain sensitivity (blue crosses). The best illumination wavelengths to measure the Borofloat thermotransmittance are $\lambda = 4000$ nm and 4400 nm.

When we calculate the thermotransmittance amplitude, we loose the information about the sign of the thermotransmittance coefficient. By comparing the phase of the proper emission and the thermotransmittance, we notice that the two signals are in phase opposition. This indicates that the thermotransmittance coefficient is negative for the Borofloat wafer at the studied wavelengths.

Wavelength, λ (nm)	Thermotransmittance coefficient, κ (K^{-1})
3100	$-(5.8 \pm 0.3) \times 10^{-4}$
3300	$-(5.2 \pm 0.2) \times 10^{-4}$
3400	$-(4.7 \pm 0.2) \times 10^{-4}$
3500	$-(4.7 \pm 0.2) \times 10^{-4}$
3600	$-(4.9 \pm 0.3) \times 10^{-4}$
3700	$-(9.0 \pm 0.3) \times 10^{-4}$
3800	$-(8.7 \pm 0.2) \times 10^{-4}$
4000	$-(9.7 \pm 0.3) \times 10^{-4}$
4200	$-(12 \pm 0.3) \times 10^{-4}$
4400	$-(13 \pm 0.3) \times 10^{-4}$
4600	$-(15 \pm 0.3) \times 10^{-4}$

TABLE 3.4 – Mid-IR spectral thermotransmittance coefficient of the Borofloat wafer.

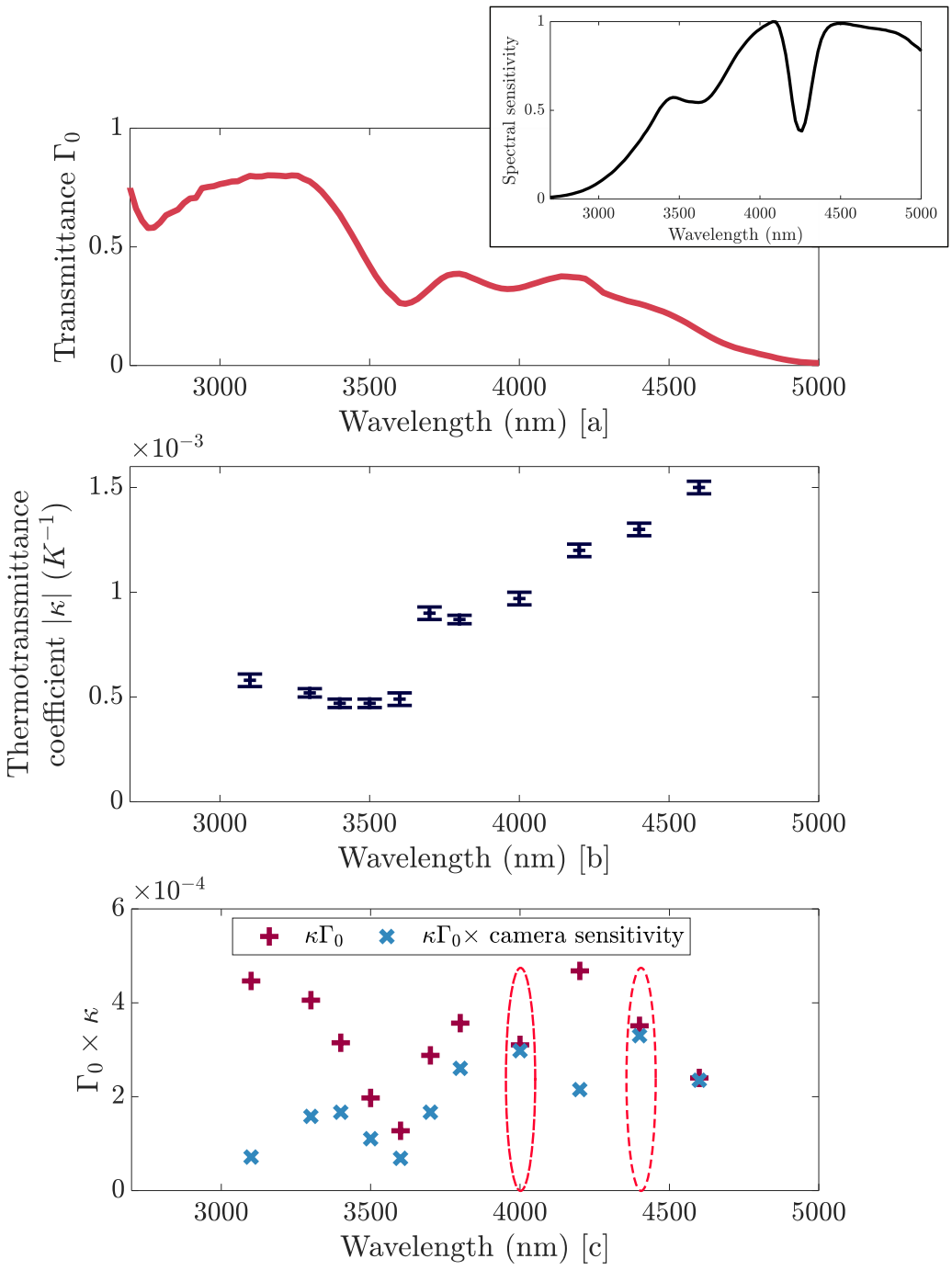

FIGURE 3.20 – [a] Reminder of transmittance spectrum Γ_0, and spectral sensitivity of the acquisition chain in the insert. [b] Spectral thermotransmittance coefficient $|\kappa(\lambda)|$ (absolute value). [c] Absolute variations $\Delta\Gamma$ for a temperature rise of $\Delta T = 1$ K (red crosses). Blue crosses correspond to signal weighted by the sensitivity of the acquisition chain (see insert in (a)). The dotted red boxes show the best wavelengths to measure thermotransmittance of the Borofloat with the current setup.

3.5.4 Temperature map and minimum temperature detected

By using the thermotransmittance coefficient, we can measure the temperature fields on the surface of the Borofloat material. The obtained temperature map is presented in figure 3.21, where we notice some vertical bands caused by the sensor, known as fixed-pattern noise [103]. Moreover, the thermotransmittance signal is sensitive to scratches and dust on the surface of the sample, as the light path on these areas is unpredictable.

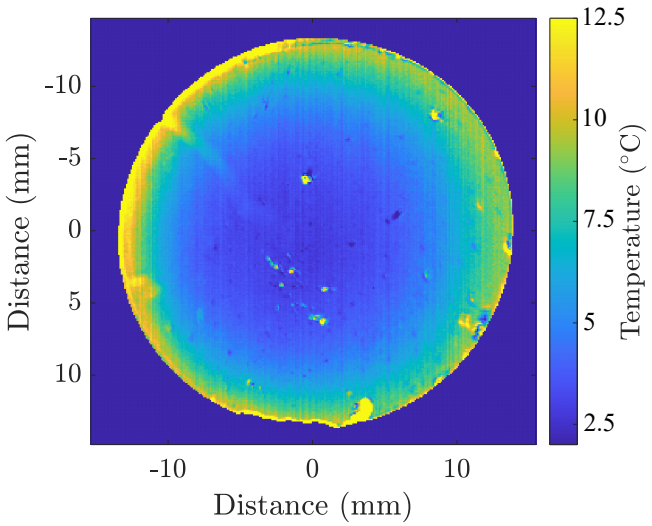

FIGURE 3.21 – Measured temperature field, at the frequency $f_T = 5$ mHz.

Finally, we characterize the temperature detection threshold of the current setup. For that, the transmitted IR beam is recorded over time without heating the sample as presented in Figure 3.13. Due to the noise measurement presented in section 3.5.1, we obtain a detection threshold which is: $\sigma_{\Delta\Gamma/\Gamma_0,\text{thresh}} = 0.6 \times 10^{-3}$. Then, this value is converted into an equivalent temperature with the thermotransmittance coefficient. Table 3.5 lists the minimum temperature detected as a function of the illumination wavelength. By comparing these values and the corresponding thermotransmittance coefficient in Figure 3.20 (b), the higher the wavelength and κ, the better the temperature detection.

Wavelength, λ (nm)	3100	3300	3400	3800	4000	4200	4400	4600
Temperature threshold, ΔT_{thresh} (°C)	1.0	1.1	1.3	0.7	0.7	0.5	0.5	0.4

TABLE 3.5 – Minimum temperature detected as a function of the illumination wavelength.

3.6 Optical modeling: Drude-Lorentz model for a dielectric material

Figure 3.20 shows that the thermotransmittance measurement is more sensitive at specific wavelengths than others. This phenomenon is a result of the Borofloat optical properties dispersion depending on the wavelength, contrary to the silicon wafer studied in section 2.6.

In this section, we would like to answer the following questions: Can we predict the most sensitive wavelengths to optimize the thermotransmittance measurement? Can we differentiate between the effects of the thermal dependencies of absorbance and reflectance? Therefore, we explore how the optical properties of the Borofloat are affected by changes in temperature. To proceed, the first step is modeling the Borofloat transmittance and reflectance spectra at the ambient temperature. Then, we add the thermal dependency in the equations.

3.6.1 Optical properties modeling

The first step is to retrieve the transmittance Γ_0 and reflectance R_0 of the Borofloat at ambient temperature, using the expression of the relative permittivity $\tilde{\varepsilon_r}(\omega)$ as a sum of oscillators according to the Drude Lorentz theory, as detailed in Appendix B and equation 3.20. We must determine the dielectric constant ε_∞, the number N of oscillators and the corresponding resonant pulsations ω_0, plasma pulsations ω_p, and damping rates γ. The variables we can determine through experiments are the number of oscillators and their associated resonant frequency. The remaining parameters are estimated by minimizing the difference between the model and the measured spectra of R_0 and Γ_0.

$$\tilde{\varepsilon_r}(\omega) = \varepsilon_\infty + \sum_n^N \frac{\omega_{p,n}^2}{\omega_{0,n}^2 - \omega^2 + i\omega\gamma_n} \tag{3.20}$$

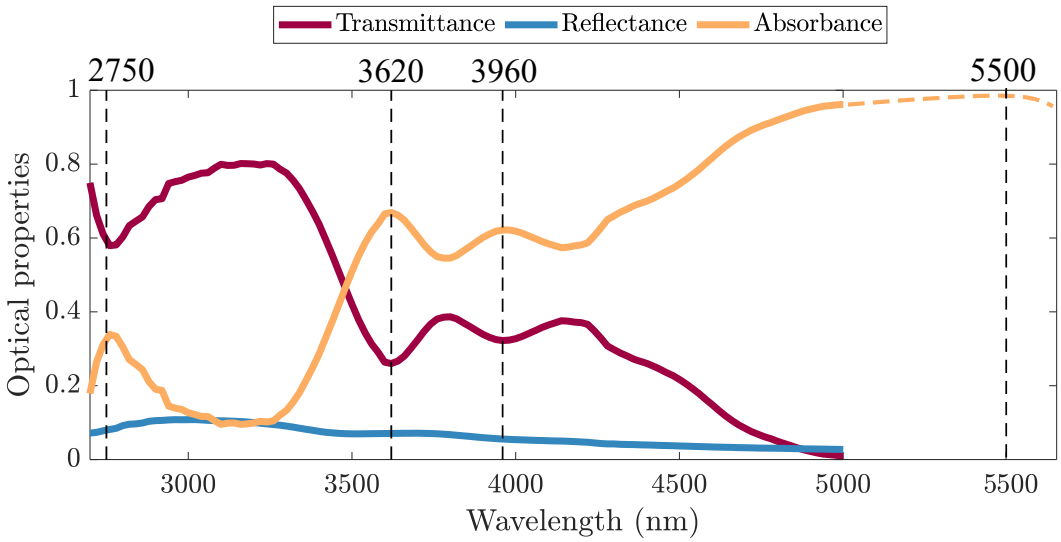

FIGURE 3.22 – Measured reflectance, transmittance and absorbance of the Borofloat wafer. Resonant wavelengths, λ_0, are identified with black dotted lines.

Estimation of the unknown ω_0, ω_p, γ and ε_∞

The optical properties of the Borofloat wafer as a function of the wavelength are plotted in figure 3.22. The reflectance and transmittance are measured with the scanning monochromator setup, and the absorbance is calculated using the equation 3.21. The reflectance remains relatively constant across the studied spectral range, contrary to the absorbance. Therefore, we assume that the spectral dependency of κ comes from the absorbance of the Borofloat, unlike the silicon. This assumption is validated in the following section.

The dotted lines in the figure indicate the position of the resonant wavelengths, λ_0, which are determined based on the absorbance peaks. Table 3.6 lists these wavelengths and their associated resonant angular frequencies, $\omega_0 = 2\pi c/\lambda_0$, with c the speed of light. The first three resonant wavelengths are easily identifiable, while the last one is arbitrarily chosen beyond 5000 nm where the transmittance becomes negligible. Without this resonance, the transmission spectrum would increase at high wavelengths instead of decreasing, due to the dielectric constant ε_∞. We choose $\lambda_0 = 5500$ nm, neither too close nor too far from the transmission threshold, which is difficult to estimate accurately. We can also add a resonance at 4300 nm, but we ignore it because it is much less significant than the others.

$$R(\lambda, T_0) + \Gamma(\lambda, T_0) + A(\lambda, T_0) = 1 \tag{3.21}$$

Resonant wavelength, λ_0 (nm)	2750	3620	3960	5500
Resonant frequency, ω_0 (rad/s)	6.85×10^{14}	5.20×10^{14}	4.76×10^{14}	3.43×10^{14}

TABLE 3.6 – Resonant wavelengths, λ_0, and associated angular frequencies ω_0 (see figure 3.22).

The next step is to estimate the unknown couples $(\omega_p, \gamma)_n$ and the dielectric constant ε_∞, which corresponds to a total of nine variables. By minimizing the value of the cost function given in equation 3.22, we obtain the unknown plasma pulsation and damping rate for each resonant frequency, listed in table 3.7. Furthermore, the estimated dielectric constant is $\varepsilon_\infty = 2.6 \pm 0.3$, and its corresponding real refractive index is $n_\infty = \sqrt{\varepsilon_\infty} = 1.6$. This value is similar to the mean refractive index of glass in the mid-infrared range (SiO2 [104, 105]), indicating that our estimation is consistent with the literature.

$$\begin{aligned}\mathcal{J}(\omega_{p,n}, \gamma_n, \varepsilon_\infty) = &\left\|\Gamma_{0,\text{mes}}(\lambda) - \Gamma_{0,\text{mod}}(\lambda, \omega_{p,n}, \gamma_n, \varepsilon_\infty)\right\|^2 + \\ &\left\|R_{0,\text{mes}}(\lambda) - R_{0,\text{mod}}(\lambda, \omega_{p,n}, \gamma_n, \varepsilon_\infty)\right\|^2\end{aligned} \tag{3.22}$$

Resonant frequency, λ_0 (nm)	Plasma pulsation ω_p (rad/s)	Damping rate γ (s^{-1})
2750	$3.1 \pm 0.3 \times 10^{12}$	$3.3 \pm 0.8 \times 10^{13}$
3620	$4.8 \pm 0.2 \times 10^{12}$	$2.5 \pm 0.3 \times 10^{13}$
3960	$4.2 \pm 0.5 \times 10^{12}$	$3.8 \pm 0.8 \times 10^{13}$
5500	$1.4 \pm 0.4 \times 10^{13}$	$1.2 \pm 0.6 \times 10^{12}$

TABLE 3.7 – Estimated plasma pulsation and damping rate for each resonant wavelength. Uncertainties are calculated with the a posteriori Jacobian matrix.

Comparison between the model and the measurements

Figure 3.23 (a) compares the model to the measurements for the transmittance and reflectance spectra of the Borofloat. Figure (b) gives the corresponding absolute errors. The model describes the data correctly, although a discrepancy is observed around the peak at $\lambda = 3300$ nm. This shows that other type of contributions should be added to the model such as the effect of free electrons [106]. It can also come from the influence of the visible and the NIR spectra, which are not considered in this study. In addition, we observe a gap between the model and measurements at 4300 nm, due to the resonant frequency we have not considered. Nevertheless, the absolute error is below 0.05, which is acceptable.

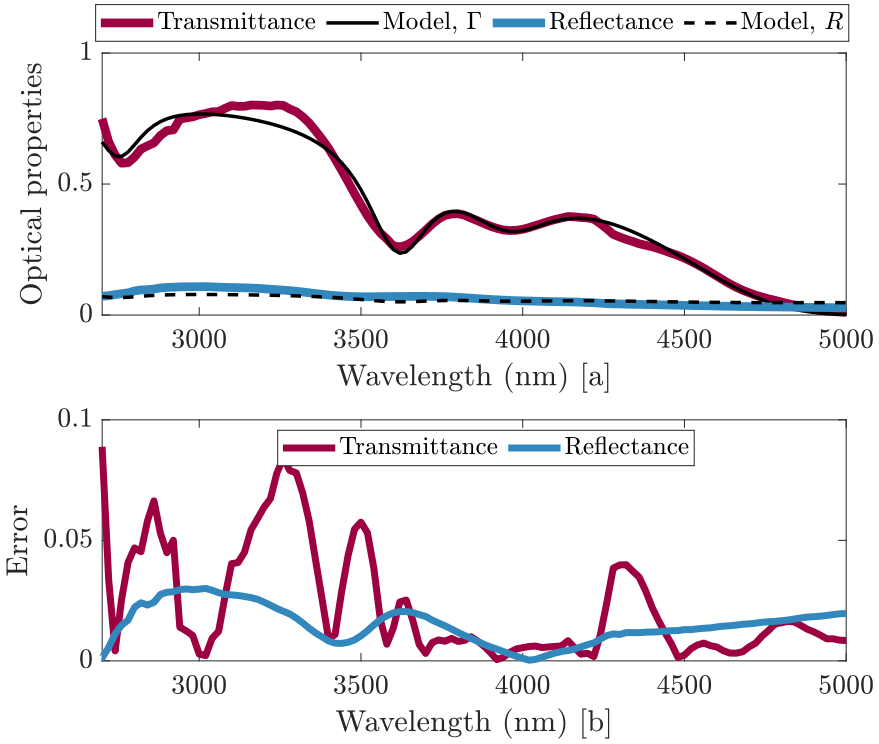

FIGURE 3.23 – [a] Transmittance and reflectance measurements and associated models (black lines). [b] Absolute errors between the model and the measurements.

Effect of each variable on the transmittance spectrum

To evaluate the effect of each variable on the transmittance spectrum, panel 3.24 shows the transmittance sensitivity to each of them, calculated with the equation 3.23, with $x = [\varepsilon_\infty, \omega_{p,n}, \omega_{0,n}, \text{or } \gamma_n]$. Each figure from [c] to [f] corresponds to a triplet $(\lambda_0, \omega_p, \gamma)$. To better illustrate the impact of uncertainty on the measured position of λ_0, the study is performed for $\lambda_0 \pm 5\%$. We observe that the measurement error of this parameter shifts the transmittance spectrum. Regarding the parameters ω_p and γ, they are strongly correlated regardless of the triplet being studied: we cannot estimate the *true* value of these parameters individually. Nevertheless, each triplet mainly influences the transmittance spectrum around its resonant wavelength and is uncorrelated with the others. Consequently, the resulting triplet is meaningful even if the individual parameter values are not. In addition, the dielectric constant ε_∞ [b] affects the entire spectrum but is locally less dominant than the plasma pulsation or the damping rate.

$$S_\Gamma[x](\lambda) = \frac{\Gamma(\lambda, x) - \Gamma(\lambda, x + dx)}{dx} x \tag{3.23}$$

Effect of each resonance on the transmittance spectrum

To better understand how the resonances impact the transmittance spectrum, we examine the effect of triplets $(\lambda_0, \omega_p, \gamma)_n$ individually. The transmittance corresponding to each triplet is calculated using the equation 3.24, and the resulting transmittance spectra are plotted in Figure 3.25. As shown with the sensitivity study, each resonance, except the one at $\lambda_0 = 5500$ nm, has a local impact: the absorption bandwidth depends on the damping rate and the peak strength is related to the plasma pulsation. The resonance at $\lambda_0 = 5500$ nm affects the general aspect of the spectrum, which is a continuous decrease. Without this component, the transmittance would increase to 0.9 at wavelengths higher than 4500 nm due to the dielectric constant ε_∞.

$$\tilde{\varepsilon_{r,n}}(\omega) = \varepsilon_\infty + \frac{\omega_{p,n}^2}{\omega_{0,n}^2 - \omega^2 + j\omega\gamma_n} \tag{3.24}$$

Effect of the thickness on the transmittance spectrum

Finally, we change the sample thickness in the model, still using the parameters at ambient temperature listed in Table 3.2. We compare the results with the supplier data-sheet as shown in Figure 3.26. We notice that the discrepancy around $\lambda = 3300$ nm increases with the thickness. However, for wavelengths greater than 3500 nm, the model accurately describes the data, which is encouraging for the relevance of the model.

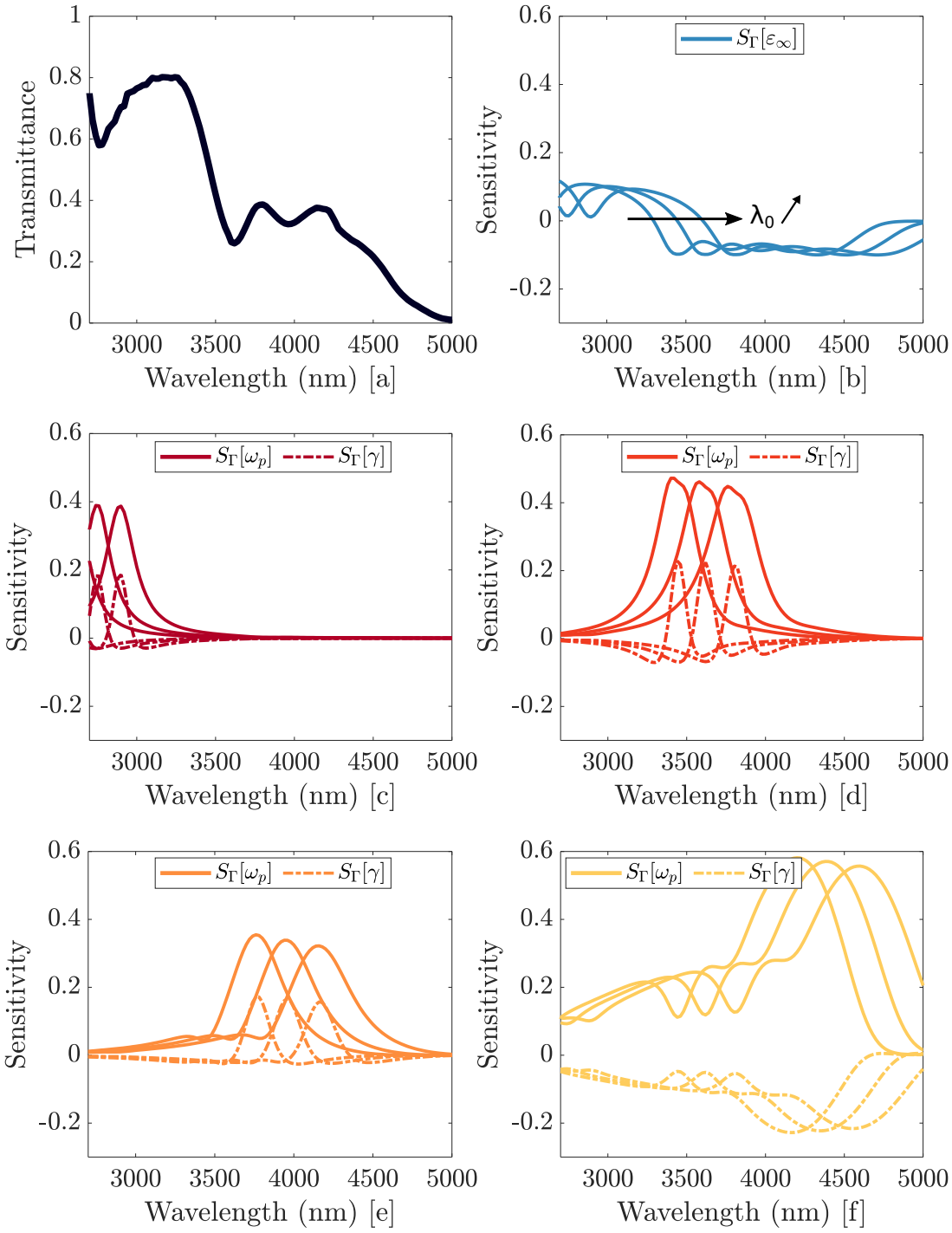

FIGURE 3.24 – [a] Reminder of the Borofloat spectral transmittance. [b] Transmittance sensitivity to ε_∞, for a variation of λ_0 of $\pm 5\%$. [c to f] Transmittance sensitivity to ω_p (plain lines) and γ (dotted lines) with a variation of 10%, at each resonant wavelength. [c] $\lambda_0 = 2750$ nm $\pm 5\%$, [d] $\lambda_0 = 3620$ nm $\pm 5\%$, [e] $\lambda_0 = 3960$ nm $\pm 5\%$, and [f] $\lambda_0 = 5500$ nm $\pm 5\%$.

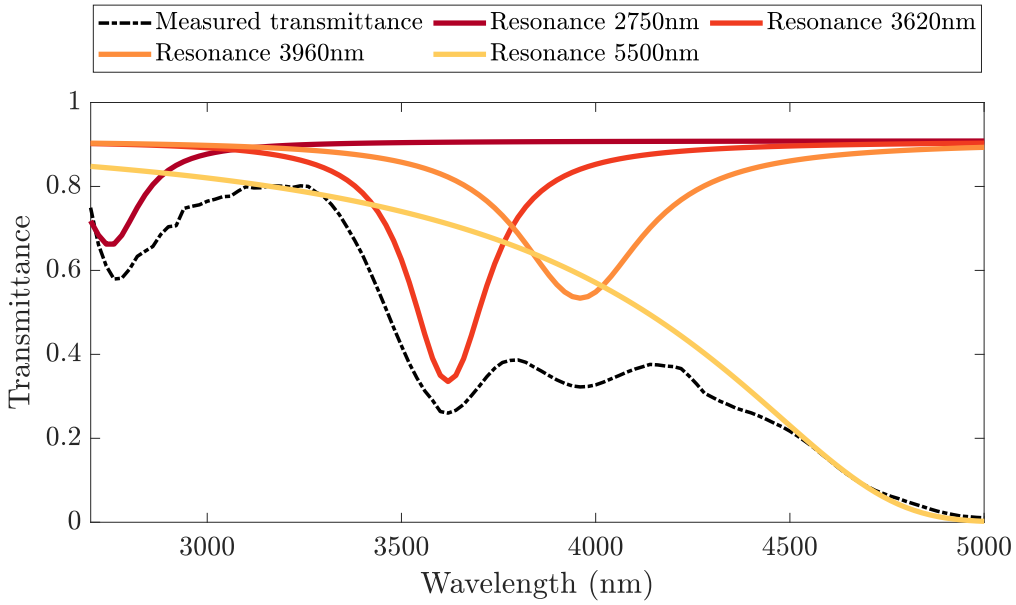

FIGURE 3.25 – Contribution of each triplet $(\lambda_0, \omega_p, \gamma)$ on the transmittance spectrum.

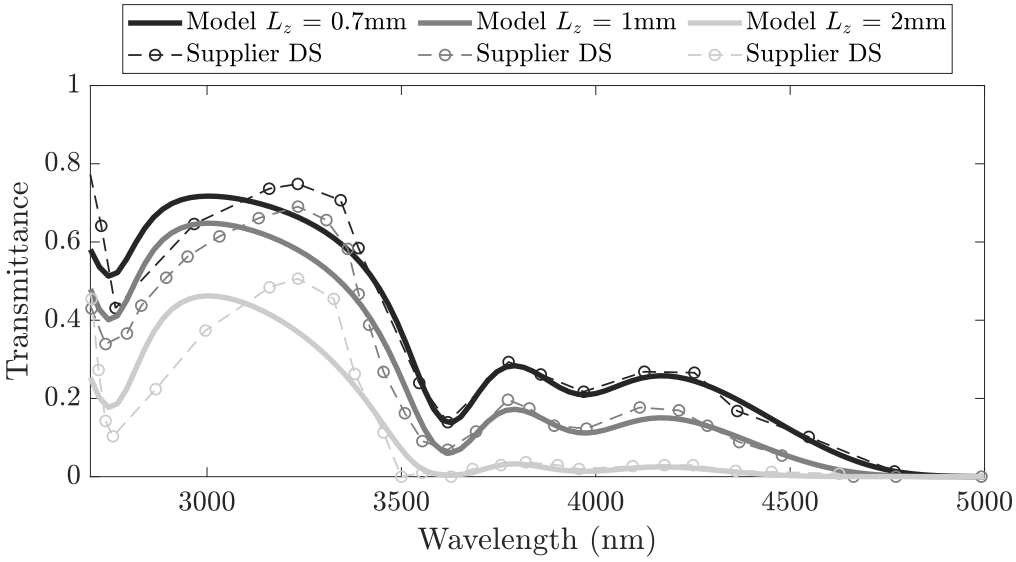

FIGURE 3.26 – Comparison between the model and the supplier data-sheet for different thicknesses of the Borofloat wafer.

3.6.2 Thermal dependency of the optical properties

Knowing the coefficients at the ambient temperature, we investigate how they are affected by changes in temperature. As a reminder, the resonant angular frequency, $\omega_0(T)$, plasma pulsation $\omega_p(T)$ and damping rate $\gamma(T)$ are temperature-dependent (see Appendix B). We assume that these variables are first-order function of temperature, with $\Delta T = T - T_0$, and the temperature coefficients α_{ω_0}, α_{ω_p}, and α_γ (K^{-1}).

$$\omega_0(T) = \omega_0(T_0) \times (1 + \alpha_{\omega_0}\Delta T) \tag{3.25}$$
$$\omega_p(T) = \omega_p(T_0) \times (1 + \alpha_{\omega_p}\Delta T) \tag{3.26}$$
$$\gamma(T) = \gamma(T_0) \times (1 + \alpha_\gamma \Delta T) \tag{3.27}$$

We start by identifying each set of values $(\alpha_{\omega_0}, \alpha_{\omega_p}, \alpha_\gamma)_n$ by minimizing the difference between the measured thermotransmittance coefficient and the model. We use the simplex algorithm, which has been used in previous studies [97]. The cost function is expressed by equation 3.28.

$$\mathcal{J}(\alpha_{\omega_0}, \alpha_{\omega_p}, \alpha_\gamma) = \left\| \kappa_{\text{measured}}(\lambda) - \frac{\Gamma(\omega_0, \omega_p, \gamma, T_0, \lambda) - \Gamma(\omega_0, \omega_p, \gamma, \alpha_{\omega_0}, \alpha_{\omega_p}, \alpha_\gamma, T, \lambda)}{\Gamma(\omega_0, \omega_p, \gamma, T_0, \lambda) \times (T - T_0)} \right\|^2 \tag{3.28}$$

Resonant wavelength λ_0 (nm)	Coefficient α_{ω_0} (K^{-1})	Coefficient α_{ω_p} (K^{-1})	Coefficient α_γ (K^{-1})
2750	-4.5×10^{-5}	2.5×10^{-2}	2.8×10^{-2}
3620	-7.6×10^{-6}	2.0×10^{-5}	-5.5×10^{-5}
3960	-1.1×10^{-5}	5.6×10^{-4}	-8.5×10^{-4}
5500	-1.2×10^{-4}	4.7×10^{-4}	-9.1×10^{-4}

TABLE 3.8 – Temperature coefficients estimated at each resonant wavelength.

The results are listed in Table 3.8, however, it is important to note that the coefficients obtained are highly dependent on the previously estimated values of $(\omega_0, \omega_p, \gamma)_n$. As a consequence, the estimated values do not make sense on their own, a sensitivity study is more meaningful (see equation 3.29 with $x = [\alpha_{\omega_p}, \alpha_{\omega_0}, \text{or } \alpha_\gamma]$). By comparing the sensitivities presented in Figures 3.27 [b] to [e], it appears that the most significant contribution comes from the triplet $(\alpha_{\omega_0}, \alpha_{\omega_p}, \alpha_\gamma)$ at $\lambda_0 = 5500$ nm. The resonances at $\lambda_0 = 3620$ nm and $\lambda_0 = 3960$ have a slight effect on the thermotransmittance coefficient spectrum around the corresponding λ_0, and no effect on its general shape. The triplet at $\lambda_0 = 2750$ nm only affects the thermotransmittance coefficient at the beginning of the measured spectrum.

$$S_\kappa[x](\lambda) = \frac{\kappa(\lambda, x) - \kappa(\lambda, x + dx)}{dx} x \tag{3.29}$$

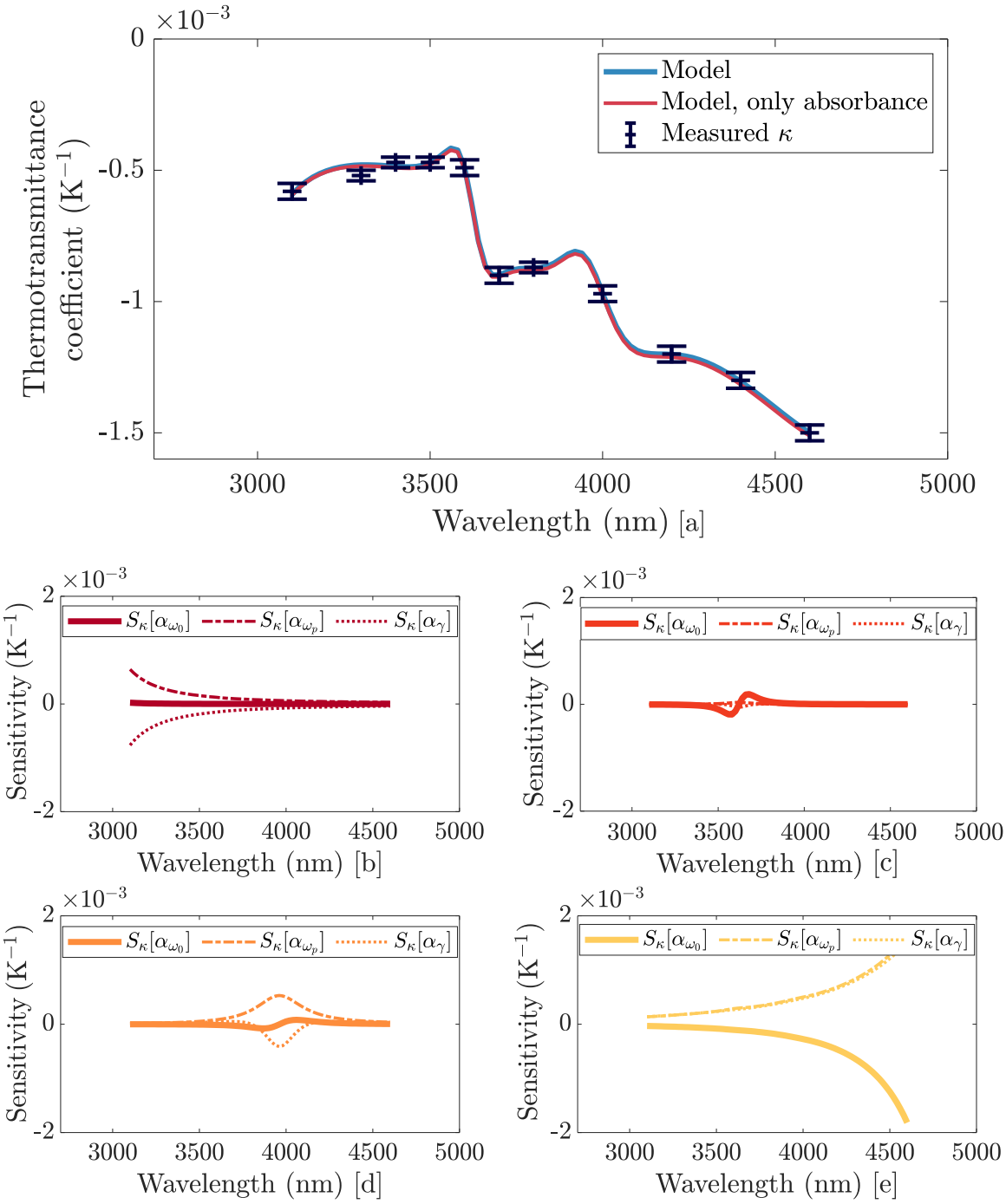

FIGURE 3.27 – [a] Comparison between the measured thermotransmittance coefficient κ and the model. [b to e] Sensitivity of κ to the thermal coefficients $(\alpha_{\omega_0}, \alpha_{\omega_p}, \gamma)$ at each resonant frequency: [b] $\lambda_0 = 2750$ nm, [c] $\lambda_0 = 3620$ nm, [d] $\lambda_0 = 3960$ nm, and [e] $\lambda_0 = 5500$ nm.

Comparing Figures 3.22 and 3.27 (a), the higher the absorbance, the higher the thermotransmittance coefficient. According to the optical model and measurements, using an illumination wavelength that matches the material absorbance peak is ideal, as long as sufficient light passes through the sample.

Finally, the thermotransmittance coefficient is calculated using the regular expression of the transmittance $\Gamma(\lambda, T)$ (see equation 1.3), and by neglecting the reflectance thermal dependency, as shown in Figure 3.27. It is interesting to note that the thermotransmittance of Borofloat is primarily due to its absorbance. As a consequence, the measurement varies based on the thickness of the material, which affects the value of κ, contrary to the silicon (see section 2.6). This regard, the Borofloat is a good candidate to develop the 3D thermotransmittance measurement.

3.7 Conclusion and perspectives

In this chapter, we have demonstrated that using modulated thermotransmittance is an efficient method for measuring thermal properties and imaging temperature fields in semitransparent materials. We have measured the thermal diffusivity and loss factor (from which we have extracted thermal conductivity) of Borofloat with 10% uncertainty. In addition, the setup can detect temperature variations from 0.5°C. To enhance the setup performances, various approaches need to be investigated:

- To improve the SNR, we need to enhance the illuminated flux which is currently about 1 W/m^2 on the sample. In addition, reducing the sample size to concentrate the available flux is also a good strategy, specially if we have only this source at our disposal. Along with a more powerful source, we should use a detector with a higher dynamic range and sensitivity.
- In addition, we should optimize the minimization algorithm described in section 3.5.2 to measure the thermal properties. A Bayesian approach could be explored in future works to facilitate the consideration of uncertainties in the measurement and model, including uncertainties on the center position and edges of the Peltier module.
- Another limitation of the current setup is the low thermal excitation frequency needed to heat the sample sufficiently. To address this, we downsize both sample and heating system in the next part.
- Due to time constraints, we did not study the proper emission of the sample. However, since its signal is much stronger than that of thermotransmittance, combining both signals to improve the SNR and extract other material properties, such as its emittance, should be interesting.

In addition, we have shown that the material sensitivity to the thermotransmittance phenomenon varies with wavelength of illumination. By using the Drude-Lorentz model, we have a better understanding of how the material optical properties are affected by temperature.

Specifically, the thermotransmittance of the Borofloat mainly comes from its absorbance, unlike the silicon (see section 2.6). Nevertheless, we were able to measure a thermotransmittance signal for both cases. This method must be used to expand the database on optical properties dependency in the mid-IR range of various materials. This would enable us to study semi-transparent multi-layers by differentiating the materials properties by spectral analysis, using the variation of the thermotransmittance coefficient κ depending on the wavelength.

Finally, the Borofloat, or SiO2-based materials, are excellent candidate to evaluate 3D thermotransmittance measurements since the thermotransmittance signal comes from the volume of the sample through absorbance. Such a measurement is not relevant with silicon since the signal comes from its interfaces, due to reflectance. In the following part, we implement the experimental setup to measure 3D temperature fields in semitransparent materials whose thermotransmittance comes from their absorbance.

Part II

Towards microscopic and tomographic thermotransmittance measurement

Chapter 4

Microscopic thermotransmittance imaging

Contents

4.1 Introduction

In the first part of this manuscript, we have designed and validated the thermotransmittance imaging experimental setup. In this part, we develop the tools needed to conduct microscale tomographic thermotransmittance measurements. To proceed, we require the following:

- First, the studied material and heating device are downsized to increase the thermal frequency f_T and observe a temperature gradient along the thickness of the material. Therefore, we adapt the experimental setup and thermal model to perform microscopic thermotransmittance imaging.

- The second step is to develop a tomographic technique suited to the sample being studied, which is discussed in Chapter 5.

This chapter focuses on the development of a microscopic thermotransmittance imaging setup. We have found that Borofloat or SiO2-based media are ideal for conducting tomographic thermotransmittance measurements, as previously studied in section 3.6. We have selected a SiO2 wafer with thin gold metal resistors deposited on its surface, as shown in Figure 4.1. The resistors are supplied with current to heat the SiO2 material using the Joule effect.

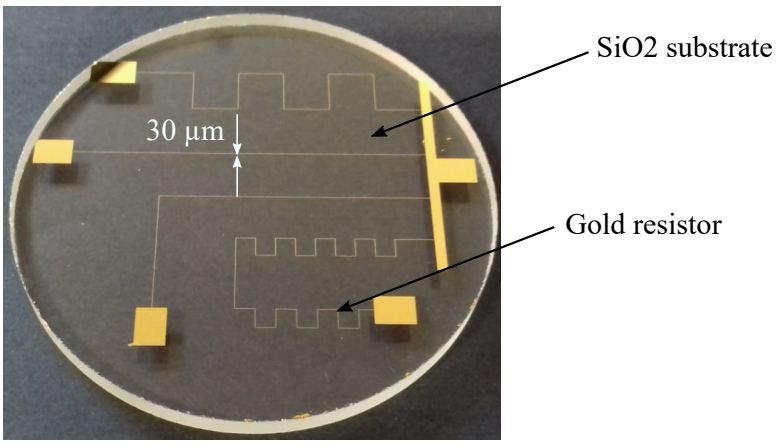

FIGURE 4.1 – Picture of a SiO2 sample with gold resistors at its surface.

In this configuration, we observe a temperature gradient along the thickness of the material. In addition, using SiO2, we assume the sample interfaces do not play a role in the thermotransmittance signal (see sections 1.3 and 3.6). Therefore, the thermotransmittance expression is given in Equation 4.1 (see section 1.3), and the measured signal is proportional to the average temperature along the sample thickness $\langle \Delta T \rangle_z$.

$$\overbrace{\boxed{\frac{\Delta\Gamma(x,y)}{\Gamma_0(x,y)}}}^{\text{Measurement}} = \kappa \overbrace{\boxed{\langle \Delta T(x,y) \rangle_z}}^{\text{Model \& measurement}} \tag{4.1}$$

As in chapter 3, we measure the thermotransmittance signal and model the temperature variations to calibrate the thermotransmittance coefficient. However, unlike the previous study, the temperature is not uniform along the thickness of the material necessitating the development of a new heat transfer model.

This chapter is organized as follows. First, we develop the new heat transfer model corresponding to the geometry of our sample. We require two parameters to fully calculate $\langle \Delta T(x,y) \rangle_z$: the thermal diffusivity and a local temperature probe to predict the temperature field. We obtain a temperature reference using the 3ω method applied to the gold resistors which is both a heater and a temperature probe. Following this, we introduce the microscopic thermotransmittance imaging setup to measure the phase and amplitude of thermotransmittance. Then, we extract the thermal diffusivity using the thermotransmittance phase, and finally, present the calibration of the thermotransmittance coefficient using the amplitude.

4.2 Heat transfer 2D model in the SiO2 medium near the gold resistor

Figure 4.2 (a) illustrates the system coordinates centered on the gold resistor, which has a width of 30 μm. To solve the heat transfer problem, we assume that the temperature field is symmetrical on both sides of the resistor and focus on one side, between $x = 0$ and $x = L_x$. The studied area is located far from the terminals of the resistor, so we assume that the temperature field is constant along the y-axis. Therefore, the problem is modeled in a 2D geometry with coordinates (x, z), as shown in Figure 4.2 (b).

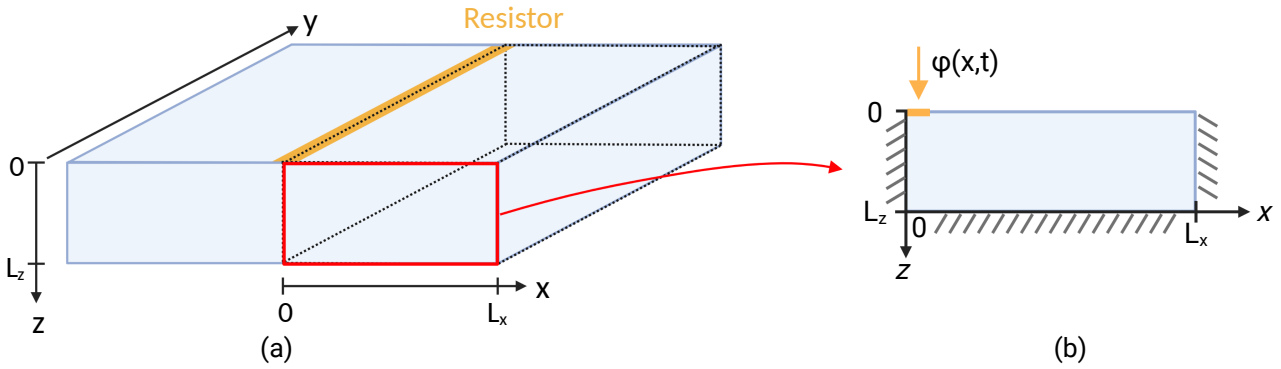

FIGURE 4.2 – (a) Illustration of the 3D geometry centered on the gold resistor, and the 2D geometry used in the model (b).

Hypotheses and boundary conditions

To solve the 2D heat transfer model along the distance x and the thickness z of the sample, we use the following hypotheses:

- In anticipation of the resolution, the system cannot be considered semi-infinite along the z-axis because the heat reaches the edge at the studied frequencies. In addition, we neglect the heat convective losses, the reader can refer to the Appendix C for the justification of this assumption. As a result, the system is adiabatic at the depths $z = 0$ and $z = L_z$.
- The system is also considered adiabatic at the position $x = L_x$, far from the gold resistor.
- The flux delivered by the gold resistor at $(x = 0, z = 0)$ is modulated at the frequency f_T and is expressed as: $\varphi(x,t) = \varphi_0 \delta(x) \cos(\omega_T t)$, with δ a Dirac distribution.

Solving the heat transfer equation

The heat transfer equation in coordinates (x, z) and the associated boundary conditions are detailed in the following system.

$$\begin{cases} \dfrac{\partial^2 T(x,z,t)}{\partial x^2} + \dfrac{\partial^2 T(x,z,t)}{\partial z^2} = \dfrac{1}{a}\dfrac{\partial T(x,z,t)}{\partial t} & (4.2) \\ -k \left.\dfrac{\partial T(x,z,t)}{\partial z}\right|_{z=0} = \varphi(x,t) & (4.3) \\ \left.\dfrac{\partial T(x,z,t)}{\partial z}\right|_{z=L_z} = 0 & (4.4) \\ \left.\dfrac{\partial T(x,z,t)}{\partial x}\right|_{x=0} = 0 & (4.5) \\ \left.\dfrac{\partial T(x,z,t)}{\partial x}\right|_{x=L_x} = 0 & (4.6) \\ T(x,z,t=0) = T_{\text{amb}} & (4.7) \end{cases}$$

To solve the system, the first step consists in decomposing the temperature into a constant and a term depending on the angular frequency, $\omega_T = 2\pi f_T$.

$$\underline{\mathrm{T}}(x,z,t) = T_0(x,z,t) + \Delta\underline{\mathrm{T}}(x,z,\omega_T)e^{i\omega_T t} \tag{4.8}$$

At the angular frequency ω_T, the previous system of equations becomes:

$$\begin{cases} \dfrac{\partial^2 \Delta\underline{\mathrm{T}}(x,z,\omega_T)}{\partial x^2} + \dfrac{\partial^2 \Delta\underline{\mathrm{T}}(x,z,\omega_T)}{\partial z^2} = \dfrac{i\omega_T}{a}\Delta\underline{\mathrm{T}}(x,z,\omega_T) & (4.9) \\ -k \left.\dfrac{\partial \Delta\underline{\mathrm{T}}(x,z,\omega_T)}{\partial z}\right|_{z=0} = \varphi_0\delta(x) & (4.10) \\ \left.\dfrac{\partial \Delta\underline{\mathrm{T}}(x,z,\omega_T)}{\partial z}\right|_{z=L_z} = 0 & (4.11) \\ \left.\dfrac{\partial \Delta\underline{\mathrm{T}}(x,z,\omega_T)}{\partial x}\right|_{x=0} = 0 & (4.12) \\ \left.\dfrac{\partial \Delta\underline{\mathrm{T}}(x,z,\omega_T)}{\partial x}\right|_{x=L_x} = 0 & (4.13) \end{cases}$$

The second step is to use a cosine integral transform on the spatial component x for both the temperature variation and the incoming flux as shown in eqs. 4.14 and 4.15. The eigenvalues α_n are: $\alpha_n = n\pi/L_x$, with $n = 0, 1, ...$ [107].

$$\Delta\widetilde{\underline{\mathrm{T}}}(\alpha_n, z, \omega_T) = \int_0^{L_x} \Delta\underline{\mathrm{T}}(x,z,\omega_T)\cos(\alpha_n x)\,\mathrm{d}x \tag{4.14}$$

$$\tilde{\varphi}(\alpha_n, \omega_T) = \varphi_0 \int_0^{L_x} \delta(x)\cos(\alpha_n x)\,\mathrm{d}x \tag{4.15}$$

The system [from Eqs 4.9 - 4.13] becomes:

$$\begin{cases} \dfrac{d^2\Delta\underline{\widetilde{\mathrm{T}}}(\alpha_n,z,\omega_T)}{dz^2} - Q^2\Delta\underline{\widetilde{\mathrm{T}}}(\alpha_n,z,\omega_T) = 0 & (4.16) \\ -k\left.\dfrac{d\Delta\underline{\widetilde{\mathrm{T}}}(\alpha_n,z,\omega_T)}{dz}\right|_{z=0} = \tilde{\varphi}(\alpha_n,\omega_T) & (4.17) \\ \left.\dfrac{d\Delta\underline{\widetilde{\mathrm{T}}}(\alpha_n,z,\omega_T)}{dz}\right|_{z=L_z} = 0 & (4.18) \end{cases}$$

The solution of the system [from 4.16 to 4.18] is expressed in equation 4.19, with $Q^2 = \alpha_n^2 + \frac{i\omega_T}{a}$.

$$\Delta\underline{\widetilde{\mathrm{T}}}(\alpha_n,z,\omega_T) = Ae^{Qz} + Be^{-Qz} \tag{4.19}$$

The boundary conditions are used to calculate the constants A and B: the resolution gives the expressions 4.20 for A, and 4.21 for B.

$$A = \frac{-\tilde{\varphi}(\alpha_n,\omega_T)}{kQ}\frac{1}{1-e^{2QL_z}} \tag{4.20}$$

$$B = Ae^{2QL_z} \tag{4.21}$$

Finally, the inverse cosine transform gives the 2D temperature variation, $\Delta\underline{\mathrm{T}}(x,z,\omega_T)$, at the frequency f_T.

$$\Delta\underline{\mathrm{T}}(x,z,\omega_T) = \frac{1}{L_x}\Delta\underline{\widetilde{\mathrm{T}}}(\alpha_0,z,\omega_T) + \frac{2}{L_x}\sum_{n=1}^{N}\Delta\underline{\widetilde{\mathrm{T}}}(\alpha_n,z,\omega_T)\cos(\alpha_n x) \tag{4.22}$$

Integral along the z-axis

In this study, the amplitude of the thermotransmittance signal is proportional to the average temperature along the thickness of the material (see Eq. 4.1). Therefore, we calculate the expression of $\langle\Delta\underline{\mathrm{T}}(x,\omega_T)\rangle_z$, using the linearity of the integral transforms:

$$\begin{aligned} \left\langle\Delta\underline{\widetilde{\mathrm{T}}}(\alpha_n,\omega_T)\right\rangle_z &= \frac{1}{L_z}\int_0^{L_z}\Delta\underline{\widetilde{\mathrm{T}}}(\alpha_n,z,\omega_T)\,\mathrm{d}z \\ &= \frac{A}{L_z}\int_0^{L_z}(e^{Qz} + e^{2QL_z}e^{-Qz})\,\mathrm{d}z \\ &= \frac{A}{L_z}\left[\frac{1}{Q}(e^{QL_z}-1) + \frac{e^{2QL_z}}{-Q}(e^{-QL_z}-1)\right] \\ &= \frac{\tilde{\varphi}(\alpha_n,\omega_T)}{kQ^2L_z} \end{aligned} \tag{4.23}$$

Finally, the integral along the z axis in spatial cosine-space has a simple form (4.23). The last step is to apply an inverse cosine integral transform to get the integral depending on x at the angular frequency ω_T.

$$\langle \Delta \underline{\mathrm{T}}(x, \omega_T) \rangle_z = \frac{1}{L_x} \frac{\tilde{\varphi}(\alpha_0, \omega_T)}{kQ_0^2 L_z} + \frac{2}{L_x} \sum_{n=1}^{N} \frac{\tilde{\varphi}(\alpha_n, \omega_T)}{kQ^2 L_z} \cos(\alpha_n x) \tag{4.24}$$

Numerical implementation

The flux $\varphi(t)$ coming from the Joule effect is delivered by the resistor at the position $(x = 0, z = 0)$. As we consider only one side of the sample, the equivalent resistor width is 15 μm, therefore, we choose a mesh of 15 μm for numerical application. Regarding the sample size along the x-axis, we set arbitrarily $L_x = 20$ mm, which corresponds approximately to the distance between the resistor and the edge of the SiO2 wafer. The parameters used for the following numerical application are listed in Table 4.1.

Parameters	Values
Meshing	15 µm
Number of eigenvalues α_n	1300
Distance, L_x	20 mm
Thickness, L_z	2 mm
Thermal diffusivity, a	2×10^{-7} m^2/s
Thermal conductivity, k	1 W/m/K

TABLE 4.1 – Parameters used for numerical implementation of heat transfer model [83].

Figure 4.3 plots the normalized temperature field at several depths as a function of the distance x (a), and at several positions x as a function of z (b) at $f_T = 40$ mHz. The second figure shows that the temperature field is uniform in the thickness for x higher than 1.5 mm. Near the gold resistor, for example at $x = 0$ and $z = 0.5$ mm, the module drops to less than 20% of its initial value. Since we measure the average along the thickness of the temperature field, we do not expect to detect the signal beyond 1 mm from the edge of the gold resistor.

Finally, Figure 4.4 shows the normalized temperature module at $x = 1$ mm depending on the thermal frequency f_T. In the studied frequency range, $f_T \in [10 - 100]$ mHz, the module varies from 0.67 to 0.28, which is quite significant. Unlike the previous study, reducing the system allows us to work at a frequency almost ten times higher than 5 mHz. The best compromise we have found between signal and acquisition speed is $f_T = 40$ mHz.

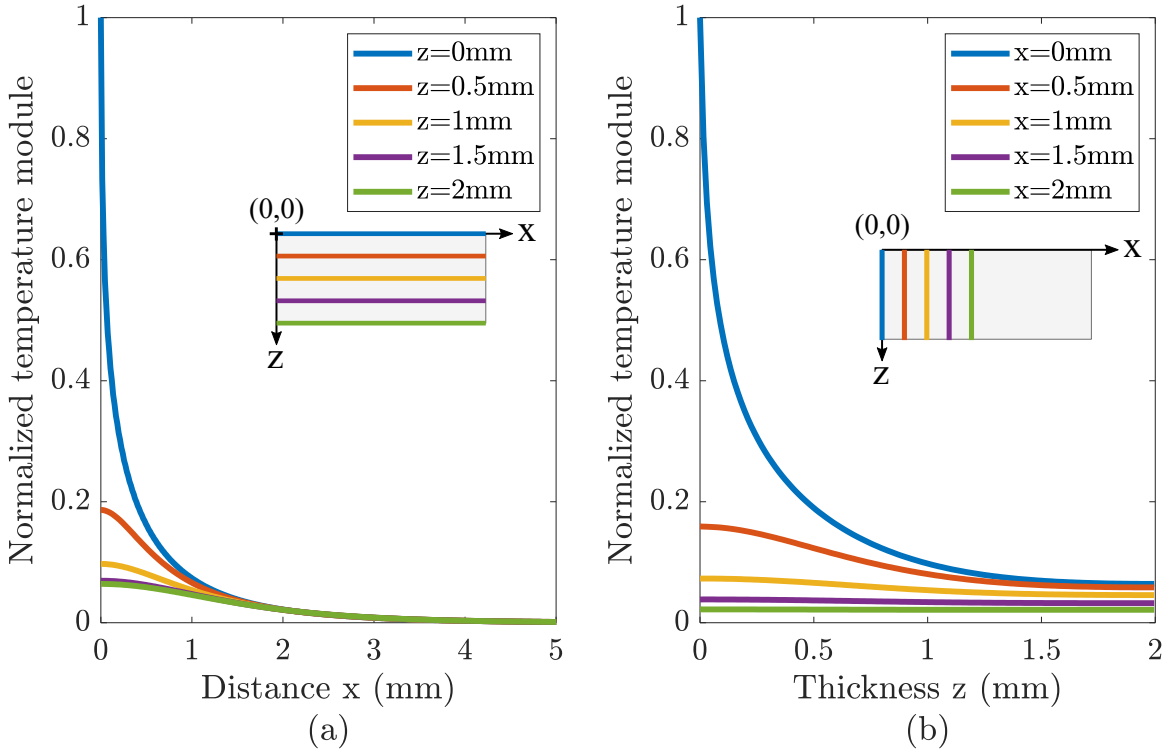

FIGURE 4.3 – Module of the temperature field $|\Delta\underline{T}(x,z,\omega_T)|/|\Delta\underline{T}(x=0,z=0,\omega_T)|$ (a) for several depths depending on the distance x, (b) for different positions x through the thickness, for $f_T = 40$ mHz.

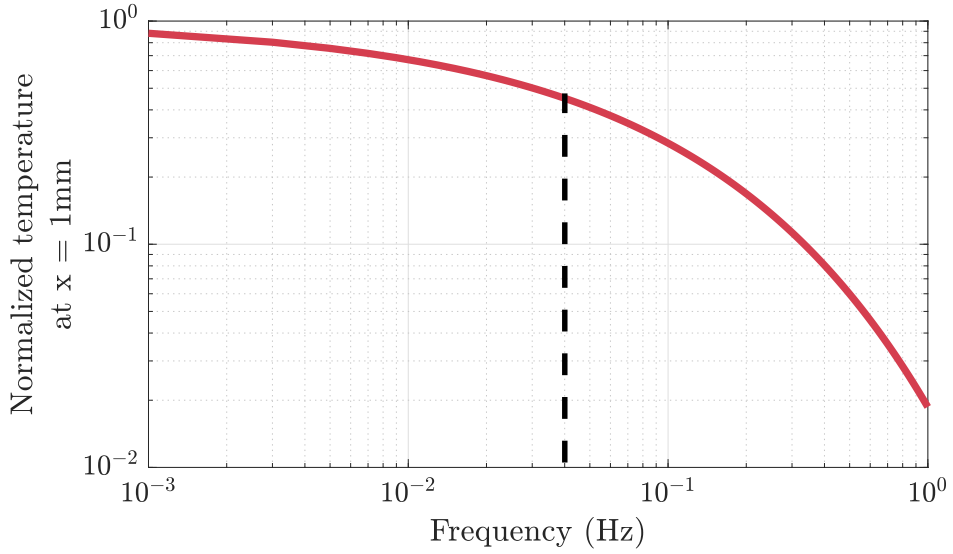

FIGURE 4.4 – Module $|\langle\Delta\underline{T}(x=1\text{mm},\omega_T)\rangle_z / \langle\Delta\underline{T}(x=0,\omega_T)\rangle_z|$, as a function of the modulation frequency f_T. The dotted line shows the working frequency $f_T = 40$ mHz.

Conclusion about the 2D model

In this section, we have developed the 2D heat transfer model to calculate the average temperature along the sample thickness. Calibrating the thermotransmittance coefficient requires the knowledge of $\langle \Delta \underline{T}(x, \omega_T) \rangle_z$ in the material, which can be obtained by using a local temperature probe and knowing the thermal properties of the material. The measurements of these properties are described in the next sections.

4.3 Temperature variation of the resistor using 3ω technique

This section describes the method to use the resistor as a local temperature probe with the 3ω technique. The temperature variation of the resistor corresponds to the amplitude $|\Delta \underline{T}(x = 0, z = 0)|$ in our model (see Figure 4.2). First, the 3ω method principle is detailed, followed by the calibration of the temperature coefficient of resistance (TCR) required to convert 3ω signal into temperature. Then, we validate the 3ω measurement on our setup and finally determine the temperature variation of the resistor during the experiment.

4.3.1 3ω method principle

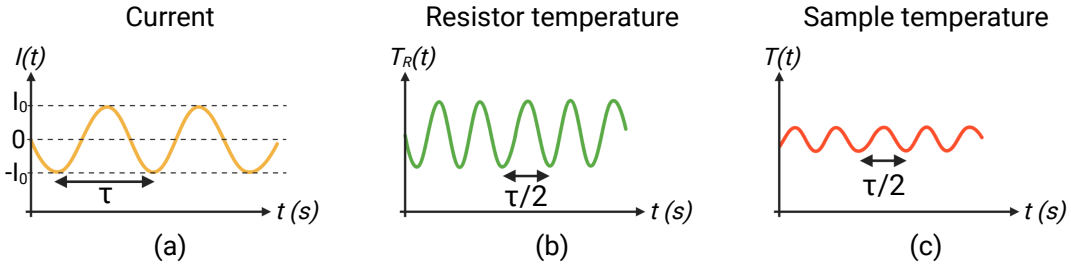

FIGURE 4.5 – Illustration of the different signals of the 3ω method. (a) Current delivered to the resistor (ω). (b) Temperature of the resistor (2ω). (c) Temperature of a sample point (2ω).

The 3ω method was generalized by Cahill [108] in 1990 to measure the thermal conductivity of materials. A thin metallic resistor is deposited on the surface of the sample being studied. When an electric current passes through the resistor, the Joule effect causes the metal to heat up, and this heat propagates in the sample below. A power supply delivers a sinusoidal current $I(t)$ to the resistor with an amplitude I_0 and a period $\tau = 1/f_I = 2\pi/\omega$ (see figure 4.5 (a)).

$$I(t) = I_0 \cos(\omega t) \tag{4.25}$$

The power dissipated by Joule effect is: $P(t) = R_\Omega(t) I(t)^2$, with R_Ω the electrical resistance of the resistor which varies with temperature. Equation 4.26 expresses R_Ω as a function of the temperature variation ΔT_R, and the temperature coefficient of resistance specific to the resistor,

usually $\beta = 3 \times 10^{-3}$ K^{-1} for gold. $R_{\Omega,0}$ is the electrical resistance at the ambient temperature T_0.

$$R_\Omega(T) = R_{\Omega,0} \times (1 + \beta \Delta T_R) \tag{4.26}$$

Assuming that $\beta \Delta T_R$ is small compared to 1, the power dissipated by Joule effect is:

$$P(t) \approx \frac{1}{2} R_{\Omega,0} I_0^2 (1 + \cos(2\omega t)) \tag{4.27}$$

The temperature variation is proportional to the dissipated power $\Delta T_R(t) \propto P(t)$. So, according to the equation 4.27, it can be decomposed into a DC component, ΔT_{DC}, and 2ω component, $|\Delta \underline{\text{T}}(x = 0, z = 0)|$ (see figure 4.5 (b)).

$$\Delta T_R(t) = \Delta T_{\text{DC}} + |\Delta \underline{\text{T}}(x = 0, z = 0)| \cos(2\omega t) \tag{4.28}$$

Combining equations 4.26 and 4.28, the resistance is expressed as follows:

$$R_\Omega(t) = R_{\Omega,0} \left(1 + \beta \Delta T_{\text{DC}} + \beta |\Delta \underline{\text{T}}(x = 0, z = 0)| \cos(2\omega t)\right) \tag{4.29}$$

Finally, the voltage $U(t)$ measured at the resistor terminals is given in equation 4.30. The signal is composed of two terms. The first one, at the angular frequency ω, is a function of ΔT_{DC} and $|\Delta \underline{\text{T}}(x = 0, z = 0)|$: it does not allow us to discriminate between the two components. The second one, at the angular frequency 3ω, only depends on $|\Delta \underline{\text{T}}(x = 0, z = 0)|$. Thus, it enables the estimation of the temperature variation $|\Delta \underline{\text{T}}(x = 0, z = 0)|$. The measurement of the voltage amplitude $U_{3\omega}$, therefore, gives the temperature variation of the resistor, $|\Delta \underline{\text{T}}(x = 0, z = 0)|$, provided that the coefficient β has been measured beforehand (see equation 4.31).

$$\begin{aligned} U(t) =& I_0 R_{\Omega,0} \left[(1 + \beta \Delta T_{\text{DC}}) + \frac{1}{2}\beta |\Delta \underline{\text{T}}(x = 0, z = 0)|\right] \cos(\omega t) \\ &+ \underbrace{I_0 R_{\Omega,0} \frac{1}{2} \beta |\Delta \underline{\text{T}}(x = 0, z = 0)| \cos(3\omega t)}_{\text{Component } 3\omega} \end{aligned} \tag{4.30}$$

Thus, measuring the 3ω component of the voltage at the resistor terminals enables us to extract the temperature $|\Delta \underline{\text{T}}(x = 0, z = 0)|$ with the equation 4.31.

$$|\Delta \underline{\text{T}}(x = 0, z = 0)| = \frac{2 U_{3\omega}}{R_{\Omega,0} I_0 \beta} \tag{4.31}$$

4.3.2 Calibration of the temperature coefficient of resistance, β

To convert the measured voltage $U_{3\omega}$ into temperature variation, we must calibrate the TCR, β, of the resistor. For that, the sample is placed in a heating chamber whose maximum temperature is set at 45°C to avoid damaging the sample. The resistance and the oven temperature are measured over time with a step of 2 s. Figure 4.6 shows the evolution of the resistance of the resistor named R_{n2} as a function of the temperature T (see figure 4.9 to get the geometry

of the studied resistor). The result of the linear regression is given in equation 4.32. The resistance is expressed as a function of β and the temperature variation ΔT (equation 4.33).

$$R_\Omega(T) = 195.2 + 0.584T \tag{4.32}$$

$$R_\Omega(T) = R_{\Omega,0} \times (1 + \beta \Delta T) \tag{4.33}$$

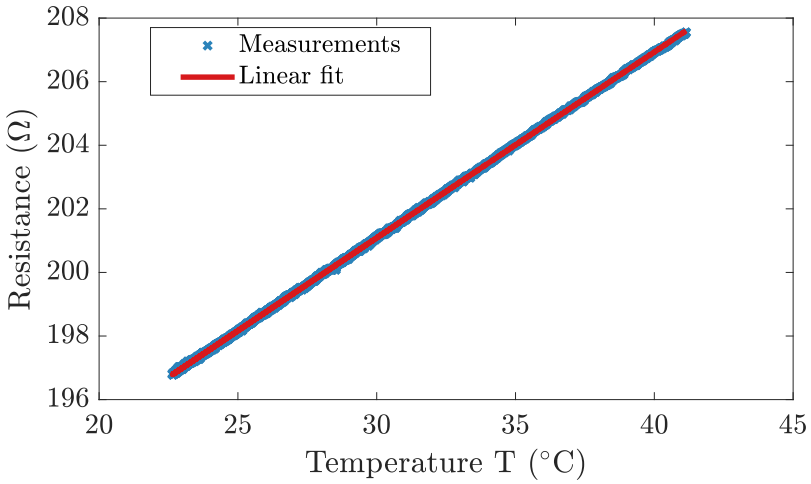

FIGURE 4.6 – Resistance of the deposit R_{n2} depending on its temperature.

Finally, we measure $\beta = 3.0 \times 10^{-3}$ K^{-1}, with an accuracy of 10^{-6} K^{-1}, that is consistent with the literature [109].

Several resistors were deposited on the sample surface. We only measure the TCR of the resistor named R_{n2} (see Appendix D). As they were manufactured at the same time, in the same environmental conditions, we assume their TCR equal.

4.3.3 Experimental validation of the 3ω measurement

Before starting the 3ω measurements, we must check if our experimental setup detects the $U_{3\omega}$ signal. According to equation 4.31 and knowing that $|\Delta\underline{T}(x = 0, z = 0)| \propto P_{2\omega}$, we get the proportionality relation $U_{3\omega} \propto I_0^3$. As a consequence, to check if the experimental setup is efficient in measuring the 3ω signal, we record the voltage at the resistor terminal over time $U_{\mathrm{V,mes}}(t)$, for various current I_0. Then, we apply a Fourier transform to this signal and extract the 3ω component, $U_{3\omega}$. We plot $\log(U_{3\omega})$ as a function of $\log(I_0)$ and should get a slope equal to 3 if the measurement works well.

The result is presented in Figure 4.7: we measure a slope of 3.2 ± 0.5, which is in good agreement with the theory. To conclude, the experimental setup is well-suited to detect the 3ω signal and measure the temperature variation of the resistor.

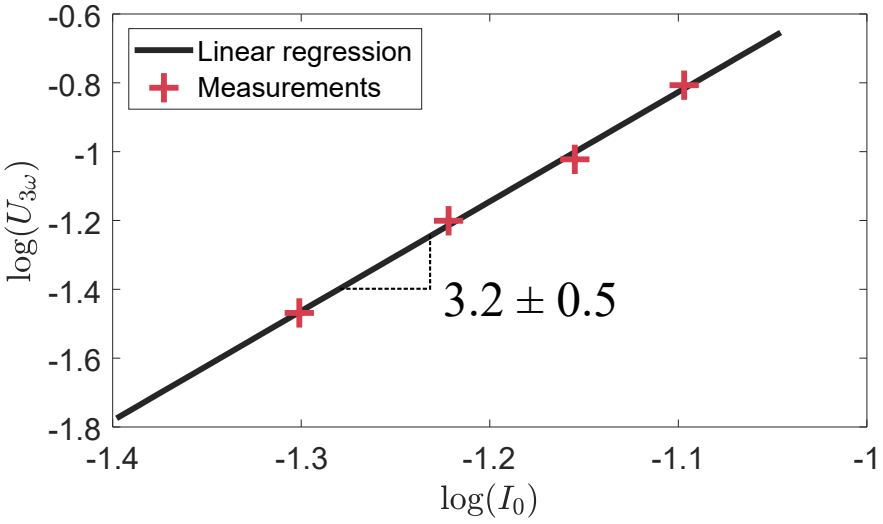

FIGURE 4.7 – Experimental validation of the 3ω measurement. The slope of the linear regression is 3.2 ± 0.5, which is consistent with the relation $U_{3\omega} \propto I_0^3$.

4.3.4 Measurement of the temperature variation of the resistor

Finally, we measure the temperature variation of the resistor during the experiment. The measurement is repeated twice with identical experimental conditions (#1 and #2). For example, Figure 4.8 presents the measurement #2 at the frequency $f_I = 20$ mHz. In addition, we perform another experiment with $f_I = 40$ mHz (#3). After applying a Fast-Fourier Transform on the voltage measured at the resistor terminals, we get its amplitude at the frequencies 1ω and 3ω as we can see in Figure 4.8 (b) and (c). The measurements performed on the three data-sets are presented in Table 4.2

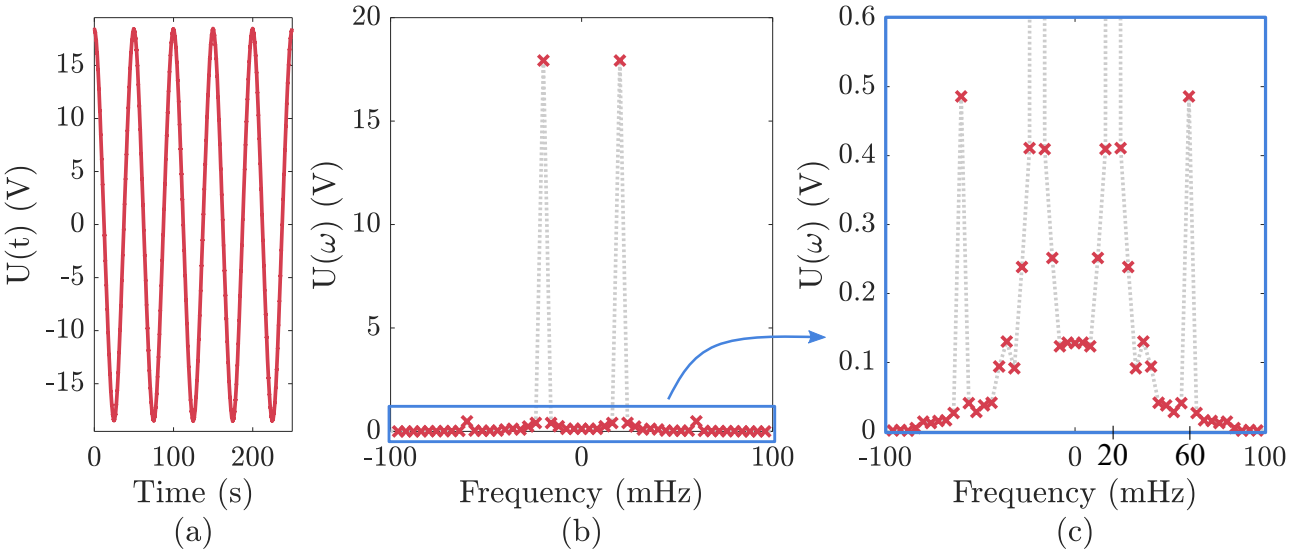

FIGURE 4.8 – (a) Measurement of the voltage at the resistor terminals over time, with the current at frequency 20 mHz. (b) FFT of $U(t)$. (c) Focus on the 3ω frequency.

Properties	Measurement #1	Measurement #2	Measurement #3
Current frequency	20 mHz	20 mHz (see Fig.4.8)	40 mHz
Amplitude ω	$U_{1\omega} = 17.93$ V	$U_{1\omega} = 17.92$ V	$U_{1\omega} = 17.71$ V
Amplitude 3ω	$U_{3\omega} = 0.486$ V	$U_{3\omega} = 0.485$ V	$U_{3\omega} = 0.438$ V
Estimated temperature	$\Delta T = 21.3 \pm 0.3$ °C	$\Delta T = 21.3 \pm 0.3$ °C	$\Delta T = 19.2 \pm 0.2$ °C

TABLE 4.2 – Measurement of the voltage amplitude and temperature $|\Delta\underline{T}(x = 0, z = 0)|$ of the resistor for different data sets.

The temperature variation of the resistor is calculated thanks to the equation 4.31. Its uncertainty $\sigma_{\Delta T}$ is expressed by the equation 4.34, with $\sigma_{U_{3\omega}} = 1$ mV, $\sigma_{R_{\Omega,0}} = 2\ \Omega$, $\sigma_\beta = 10^{-6}$ K^{-1}, and $\sigma_{I_0} = 0.1$ mA. The main source of uncertainty is the measurement of resistance at ambient temperature, $R_{\Omega,0}$.

$$\sigma_{\Delta T}^2 = \left(\frac{\partial \Delta T}{\partial U_{3\omega}}\right)^2 \sigma_{U_{3\omega}}^2 + \left(\frac{\partial \Delta T}{\partial R_{\Omega,0}}\right)^2 \sigma_{R_{\Omega,0}}^2 + \left(\frac{\partial \Delta T}{\partial \beta}\right)^2 \sigma_\beta^2 + \left(\frac{\partial \Delta T}{\partial I_0}\right)^2 \sigma_{I_0}^2 \tag{4.34}$$

4.4 Microscopic imaging thermotransmittance measurement

Now that we have calibrated our temperature probe, we need to determine the thermal diffusivity to calculate $\langle \Delta\underline{T}(x, \omega_T) \rangle_z$. For that, we use the phase of the thermotransmittance signal. This section introduces the experimental setup to conduct microscopic thermotransmittance measurement, adapted from the setup described in section 3.2. We detail how to extract the thermal diffusivity from the phase and present the measurement of the thermotransmittance coefficient of the SiO2 medium.

4.4.1 Overview of the experimental setup

The experimental setup for the microscopic thermotransmittance measurements is illustrated in Figure 4.9. We use exactly the same modulation/demodulation process as the one described in Chapter 3. Thus, we only focus here on the characteristics of the microscopic configuration.

Camera resolution

First, to enhance the spatial resolution we replace the lens with a microscope objective of magnification ×1 and a working distance of 30 cm. To measure the resolution of the camera, we record a USAF 1951 target [91] with the IR camera, the corresponding image is presented in Figure 4.10. For instance, the bands in the (2,1) pattern in the bottom right corner are 125 μm wide. We count 42 pixels for 5 black and white bands in this group. Hence, the camera resolution is res = 14.9 μm/pixel, which is consistent with using an objective of magnification of ×1 with a sensor pixel pitch of 15 μm. In addition the depth of field of the objective is ±0.5 mm around the focal plane, as determined in Appendix E.

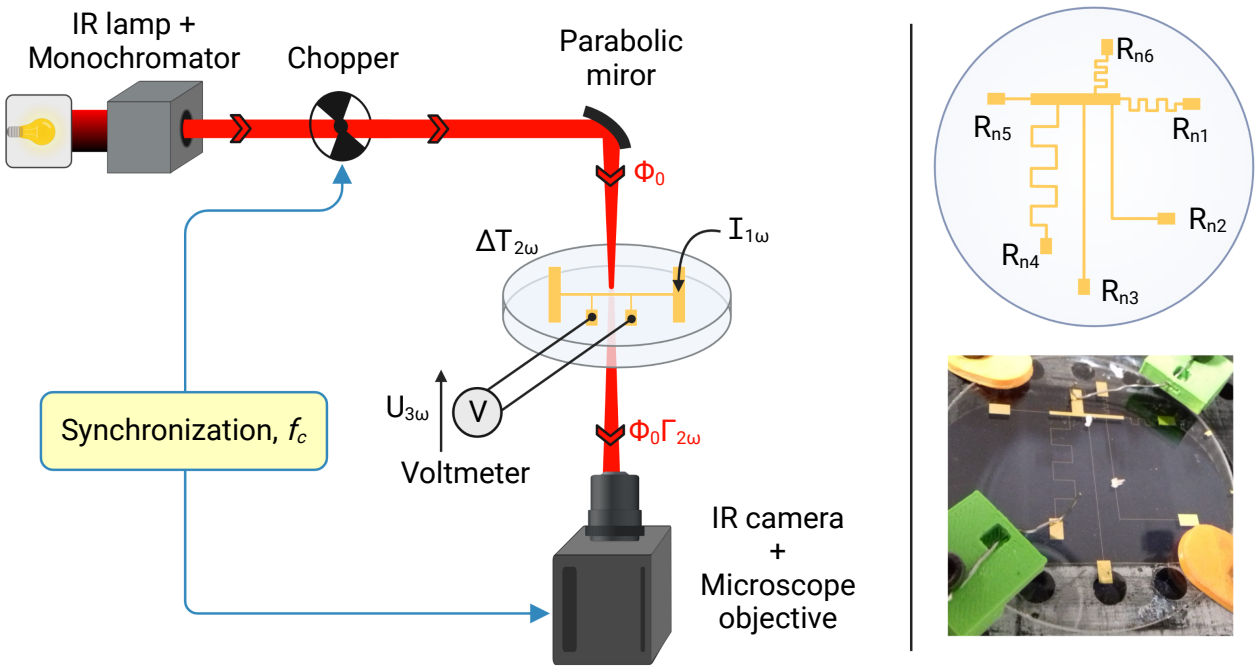

FIGURE 4.9 – Experimental setup for the microscopic thermotransmittance measurement and representation of the sample. For convenience, the resistors are numbered from 1 to 6.

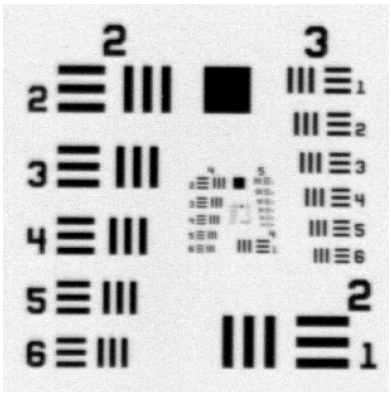

FIGURE 4.10 – USAF target recorded by using the IR camera with the microscope objective.

Description of the sample

As previously mentioned, the sample is a SiO2 glass wafer with a thickness of $L_z = 2$ mm. Several resistors of thickness 300 nm and width 30 μm were deposited on its surface. With such thickness, the metal deposit is entirely reflective in the mid-IR. The dimensions of electrical resistance were chosen to heat the sample sufficiently and to withstand a current of several mA. Table D.1 in Appendix D details each resistor length and resistance.

Configuration of the experiment

In order to heat sufficiently the sample, we choose the resistor R_{n2} which has a high resistance ($R_\Omega = 190\ \Omega$); we observe its straight line far from the bend. We record simultaneously the images taken by the IR camera and the voltage $U(t)$ at the resistor terminals. The latter is measured with a National Instruments card 9201, with a time step $dt = 1$ ms.

The electrical current supplied to the resistor, $I(t) = I_0 \cos(2\pi f_I t)$, is modulated at the frequency $f_I = 20$ mHz with $I_0 = 80$ mA thanks to a Keithley 6221 current source. The frequency of the thermal excitation is $f_T = 40$ mHz. Experience has taught us that the chopper frequency for this configuration must be higher than 30 Hz to remove the proper emission. However, as discussed in 3.3.1, at such frequencies the chopper ventilates the IR source. To prevent this, we use another chopper outside the source housing and set the frequency at $f_c = 91$ Hz.

Resistor number	R_{n2} (see Appendix D)
Resistance	$R_{\Omega,0} = 190 \pm 2\Omega$
Current delivery	$I_0 = 80$ mA at $f_I = 20$ mHz
Camera integration time	$t_{\text{int}} = 250\ \mu m$
Chopper frequency	$f_c = 91$ Hz (Camera 183 Hz), external
Illumination wavelength	$\lambda = 3300$ nm (SiO2 transmission peak) [57]

TABLE 4.3 – Experimental conditions for microscale thermotransmittance imaging

4.4.2 Proper emission subtraction

To extract the amplitude and phase of the thermotransmittance signal we use the same demodulation process as for the macroscopic case (see section 3.3). Consequently, the first operation is to ensure that the proper emission and parasitic radiations are removed, and that the residuals do not vary with temperature. Therefore, we perform a preliminary measurement in the same conditions than the thermotransmittance one, except that the IR source is cut. Each pixel of the camera measures the signal $U_{\text{pix}}(t)$ at a frequency of $f_{\text{cam}} = 2f_c$ (see section 3.5.1). As a reminder, ρ_{pix} is a proportionality factor specific to each pixel (see p.38).

$$U_{\text{pix}}(t) = \rho_{\text{pix}} E(T, t) \tag{4.35}$$

Proper emission signal over time

Figure 4.11 shows the proper emission of the sample over time and graph (b) displays the evolution of the signal recorded by two pixels at different distances from the gold resistor. As expected, the pixel closest to the resistor has the largest amplitude. In addition, we observe a phase shift between the two signals; this behavior depends on the thermal diffusivity. At the center of the image, we can see the gold resistor; we can not deduce much from the signal of the concerned pixels. In the following, we apply a spatial mask to remove this area.

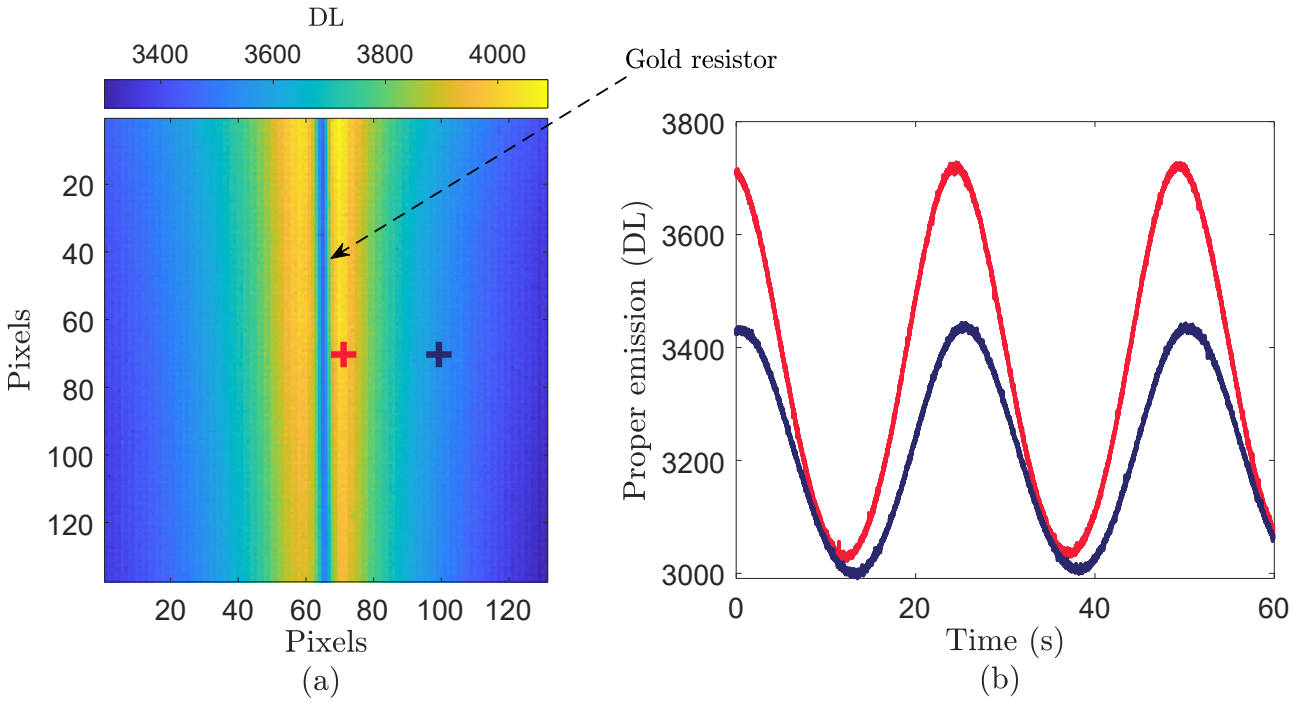

FIGURE 4.11 – (a) Map of the proper emission at $t = 0$ s. (b) Proper emission of the pixels (70,70) and (70,100) as a function of time.

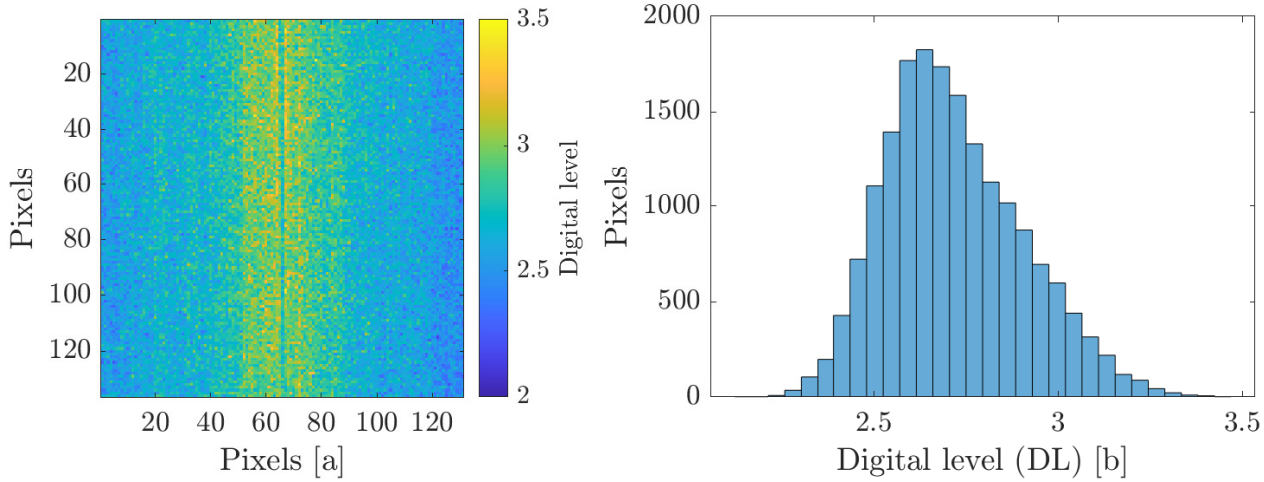

FIGURE 4.12 – (a) Amplitude of the proper emission residuals (DL) when the IR source is off, and corresponding histogram (b).

Proper emission subtraction check

To check the efficiency of the two-image algorithm, we use the method described in the section 3.5.1, which consists in measuring the amplitude of the residuals at f_T and comparing it to the measurement noise. Figure 4.12 (a) displays the amplitude of the residuals, Δ_{res}. The average value of Δ_{res} near the resistor is constant and equals 2.7 ± 0.2 DL. We observe that residuals are higher close to the resistor: the mean value of pixels in columns 50 to 80 is 2.9 ± 0.2 DL which is finally not significant. As a reminder (see section 3.5.1), the measurement noise is about 3 DL, therefore, we can state that the residuals are negligible and are considered as measurement noise.

4.4.3 Measurement of thermal diffusivity of the SiO2 wafer

After verifying we are not measuring the proper emission close to the resistor, the next step is to determine the thermal diffusivity of the sample, in order to calculate $\langle \Delta \underline{T}(x, \omega_T) \rangle_z$ before calibrating the thermotransmittance coefficient.

We assume the material is isotropic: the thermal diffusivity is the same along the x, y and z axes. In addition, the integral is a linear function, therefore, measuring a phase shift along x, z, or using the average along one direction, enables us to extract the thermal diffusivity. As the thermotransmittance signal is proportional to the mean temperature along the thickness of the material, measuring its phase shift along the x-axis enables us to extract the thermal diffusivity of the SiO2 wafer. For that, we use a simple expression of the phase shift depending on the distance x from the resistor, the thermal diffusivity a, and the thermal frequency f_T. Appendix C demonstrates this expression gives same results in the estimation of a than the 2D model averaged along the z axis.

$$\phi(x) = \pm \frac{x}{\sqrt{\frac{a}{\pi f_T}}} \tag{4.36}$$

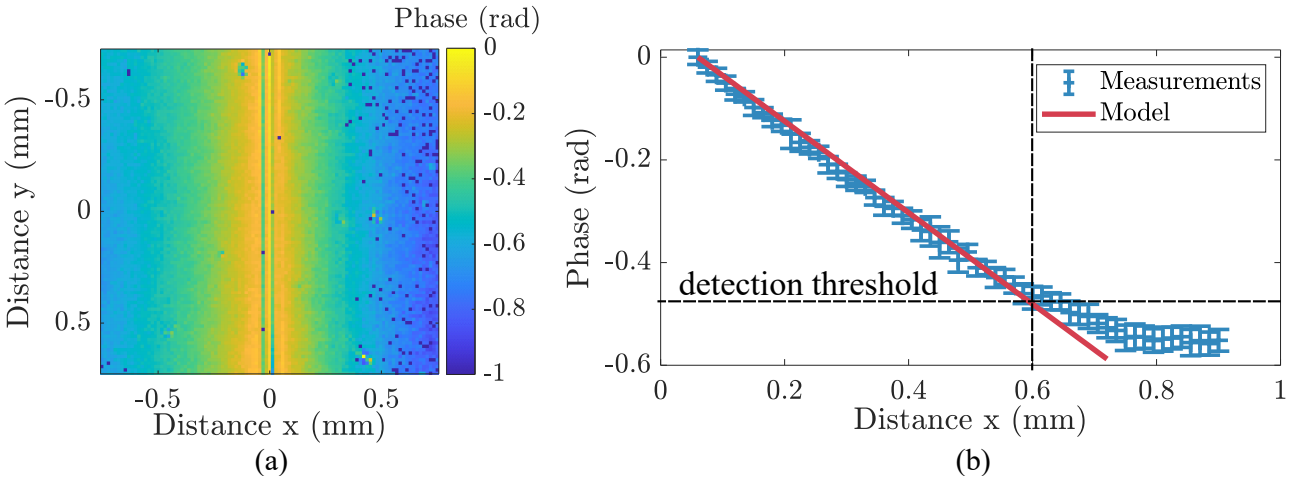

FIGURE 4.13 – (a) Thermotransmittance phase along x and y. (b) Phase (averaged along y to improve the SNR) versus the distance x. The red line corresponds to $\phi = -x/\sqrt{a/\pi f_T}$.

Using this method, the estimated thermal diffusivity is $a = (1.6 \pm 0.4) \times 10^{-7}$ m^2/s. As we can see in the Figure 4.13 (b), the phase reaches an unexpected plateau for x higher than 0.7 mm, which corresponds to the detection threshold for the working frequency. Consequently, we do not use the signal for $x > 0.7$ mm in the post-processing. The uncertainty is calculated using propagation of error, considering $\sigma_\phi = 0.01$ rad, and $\sigma_x = 15$ μm.

4.4.4 Thermotransmittance coefficient of the SiO2 wafer

Now that we have the thermal diffusivity and the temperature $|\Delta\underline{T}(x = 0, z = 0)|$, we are able to calculate the field $|\langle\Delta\underline{T}(x, \omega_T)\rangle_z|$. The final step is to determine the thermotransmittance coefficient of the SiO2 wafer. The idea is to compare the thermotransmittance module with the calculated field $|\langle\Delta\underline{T}(x, \omega_T)\rangle_z|$. The full process to get the thermotransmittance coefficient is described below and illustrated in Figure 4.14.

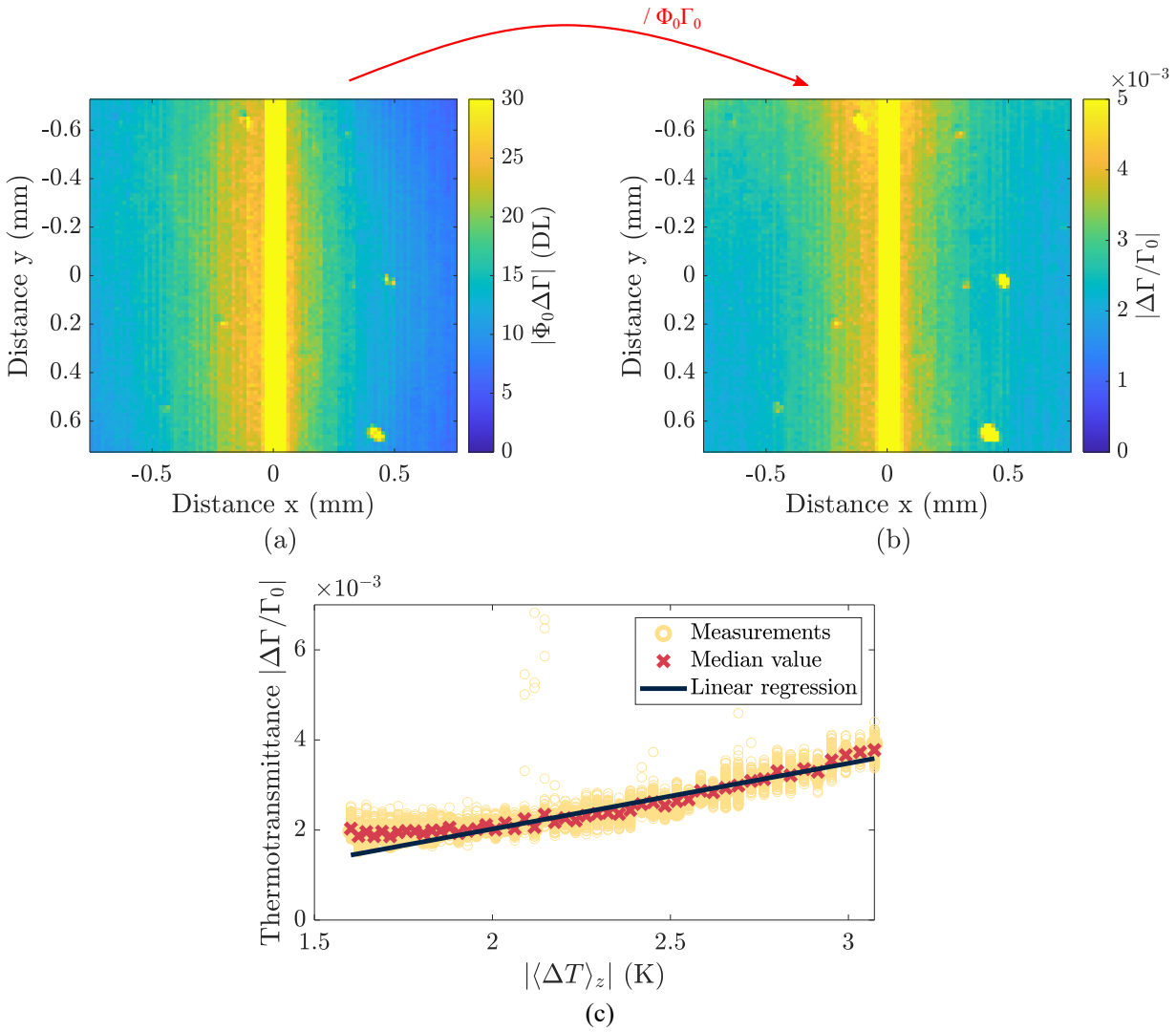

FIGURE 4.14 – Maps of the amplitude of (a) $\Phi_0\Delta\Gamma$ (DL), and (b) $\Delta\Gamma/\Gamma_0$. Thermotransmittance depending on calculated $|\langle\Delta\underline{T}\rangle_z|$. The thermotransmittance coefficient is the slope of the linear regression.

1. We start with the module of the thermotransmittance signal: we assign to each pixel its distance from the resistor. To improve the SNR, we calculate the average value along the y-axis as the temperature is assumed to be constant along this dimension.

2. The 2D model enables to determine $|\langle \Delta\underline{T}(x,\omega_T)\rangle_z|$, using the temperature of the resistor, $|\Delta\underline{T}(x=0,z=0)|$, and the estimated thermal diffusivity of the glass wafer using the equation 4.24.

3. Then, Figure 4.14 shows the thermotransmittance amplitude as a function of the calculated temperature $|\langle \Delta\underline{T}\rangle_z|$. The two variables are aligned with respect to the distance x.

4. According to equation 4.1, the thermotransmittance coefficient is the slope of the linear regression illustrated in figure 4.14: $\kappa = -(1.4 \pm 0.2) \times 10^{-3} K^{-1}$. However, unlike the previous studies, the intercept is not zero but -0.8×10^{-3}.

There are multiple reasons why the non-zero intercept might be present. One explanation could be a bias in the thermotransmittance measurement caused by the sample tilt or parasitic reflections. Moreover, the intercept is greatly affected by the estimation of thermal diffusivity. If we use the lower limit value for thermal diffusivity, which is $a = 1.2 \times 10^{-7}$ m^2/s, the intercept decreases to -0.4×10^{-3}. This small change in thermal diffusivity does not affect the thermotransmittance coefficient.

In addition, the model assumes that all incoming flux is absorbed by the glass. To validate this hypothesis, we compare the temperature calculated from the dissipated Joule power using the 2D model. The dissipated power by Joule effect at ω_T is: $P_J = 0.5 R_0 I_0^2 = 0.6$ W (see equation 4.27). The corresponding flux is $\varphi_0 = P_J/S = 4.5 \times 10^5$ W/m^2, where S is the resistor surface. Using the estimated thermal diffusivity a and the thermal conductivity $k \approx 1.1$ W/m/K [83] of the SiO2, we calculate the temperature variation $|\Delta\underline{T}(x,z,\omega_T)|$ which is presented in Figure 4.15. The temperature at coordinates $(x=0, z=0)$ is 20.9°C, which is similar to the measured temperature of the resistor: 21.3 ± 0.3 °C. Thus, the assumption that the flux mainly goes into glass seems consistent.

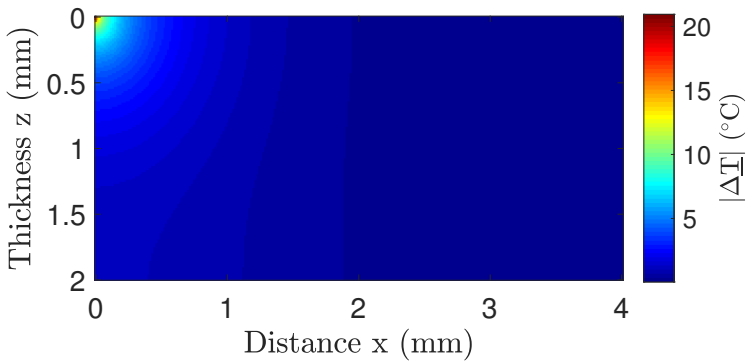

FIGURE 4.15 – Estimated temperature field $|\Delta\underline{T}(x,z,\omega_T)|$ with the flux dissipated by Joule effect.

Finally, according to the general expression presented in the introduction (see Eq. 1.6), if the thermoreflectance coefficient κ_R is not negligible compared to the thermal dependency of the absorbance, a term is added in the thermotransmittance expression. Thermotransmittance measurements of a material with different thicknesses would allow us to discriminate the contributions of interfaces (reflectance) and volume (absorbance) in the thermotransmittance signal.

4.5 Conclusion about microscopic thermotransmittance

The presented study should still be improved to fully understand the thermotransmittance origin in the SiO2. In my opinion, the most important study to conduct is measuring the thermotransmittance signal depending on the thickness of the material. This work will make it possible to fully discriminate the impact of absorbance and reflectance on the thermotransmittance signal. This requires multiple samples of a material in different thicknesses with identical resistors deposited on top, which can be challenging to manufacture.

In addition, it should be interesting to measure the signal at different thermal frequencies. In this work, we were limited by the maximal acquisition time of the camera to ensure a good removal of parasitic radiations, and by the minimal temperature required to heat enough the sample to measure thermotransmittance signal. We had to find the best compromise between signal and acquisition speed.

In this chapter, we have learned how to perform quantitative microscale thermotransmittance imaging by adapting the experimental setup described in Chapter 3 and using a new heat transfer model. Now we are able to measure the average temperature along the thickness of the sample, we would like to discriminate the slices along the z axis. Therefore, the last stage of this thesis work is to combine this measurement with tomography.

Chapter 5

Infrared laminography for 3D thermal field imaging

Contents

5.1 Introduction - Tomography techniques

In this chapter, we develop a tomographic setup to conduct 3D thermotransmittance measurements. Several techniques can be implemented to obtain tomography, such as computed tomography (CT) [110, 111], confocal imaging [112, 113], optical coherence tomography (OCT) [114, 115], or magnetic resonance imaging (MRI) [116, 117]. Due to the time constraints and equipment at our disposal, it was not feasible to develop OCT or confocal microscopy, as these methods are not suitable for conducting 3D thermotransmittance measurements with the current setup (interferometry setup, and strong signal required due to filtering operations).

Therefore, we focus on computed tomography which has already been studied in the team [118].

In computed tomography, the sample under study is illuminated and then rotated until it has completed a 360° rotation. For each angular position, the light transmitted through the sample is measured using a camera: these records are called projections. The theory of 3D tomography reconstruction from the 2D projections of an object was provided by Radon in 1917 [119]. It was not until the 1970's that the method developed significantly in the medical community [120, 121]. Dobbins [122] gave a complete review of the development of computed tomography applied to medicine. In recent years, this 3D imaging technique has been extended to other fields of application, such as archaeology [123], material science [124] or forest research [125], and in different spectral domains such as X-rays [126], visible light [127], or infrared radiations [118, 128, 129].

However, computed tomography is not suited to flat and extended objects [130] such as those studied in this work. In this case, turning the sample through 360° does not allow the object to be reconstructed correctly, as the ratio between its dimensions is too high. A solution consists in using laminography technique [131] as illustrated in Figure 5.1. The principle is based on CT, except that the sample does not rotate in the same way. Several laminography configurations exist, in particular:

- Linear laminography (a): the sample is fixed, the detector and the source translate around it [132].
- Swing laminography (b): the detector and source are fixed, the sample swings around an axis normal to the optical axis without completing a full rotation [133].
- Rotary laminography (c): the sample is tilted along the optical axis from a laminographic angle ξ, while the source and detector are fixed. The sample rotates by 360° in this position [134, 135, 136].

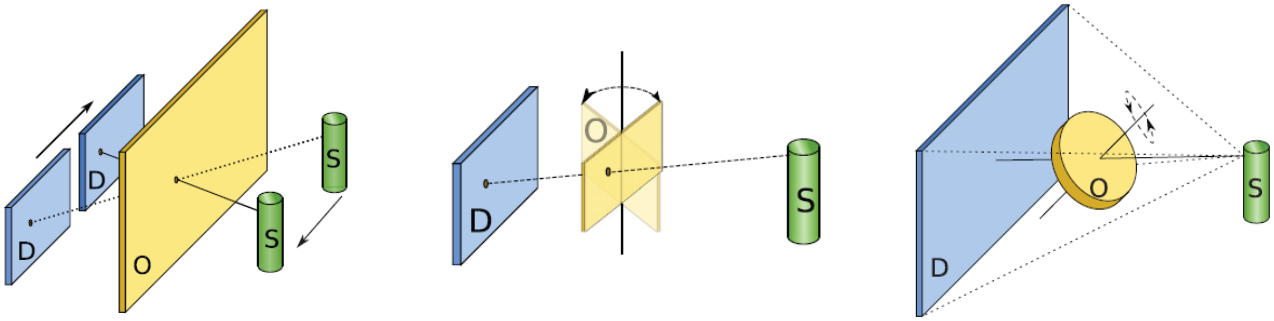

(a) (b) (c)

FIGURE 5.1 – Illustrations of several laminography configurations, extracted from O'Brien laminography review [131]. (a) Linear laminography, (b) Swing laminography, and (c) Rotary laminography. O: object, D: detector, S: source.

For this exploratory work, we have chosen to develop IR rotary laminography to measure 3D thermotransmittance fields. In fact, with our setup, it is much easier to move the sample than the camera and source, and to rotate the sample with a rotary motor than to swing it.

This chapter presents the principle of rotary laminography, applied to a numerical case to determine experimental conditions. Then, the experimental setup to conduct infrared laminography is developed and characterized using calibrated objects such as USAF targets. Finally, we present the first thermotransmittance 3D fields measured on the sample calibrated in the previous chapter 4. This exploratory work aims at setting up tools for 3D thermotransmittance imaging and understanding the various challenges involved in 3D reconstruction of temperature field.

5.2 Rotary laminography principle and reconstruction algorithm

Now that we have chosen rotary laminography, let us examine its principle. First, we describe the algorithm used to recalculate the 3D object from the 2D projections, and then we study a numerical application case to test this algorithm and determine the experimental conditions.

5.2.1 Principle of rotary laminography

Figure 5.2 illustrates the principle of rotary laminography, with the different coordinate systems used in this chapter:

- (x, y, z) is the coordinate system of the 3D object (original and reconstructed),
- (u, v) is the coordinate system of the measured projections in the sensor plane.

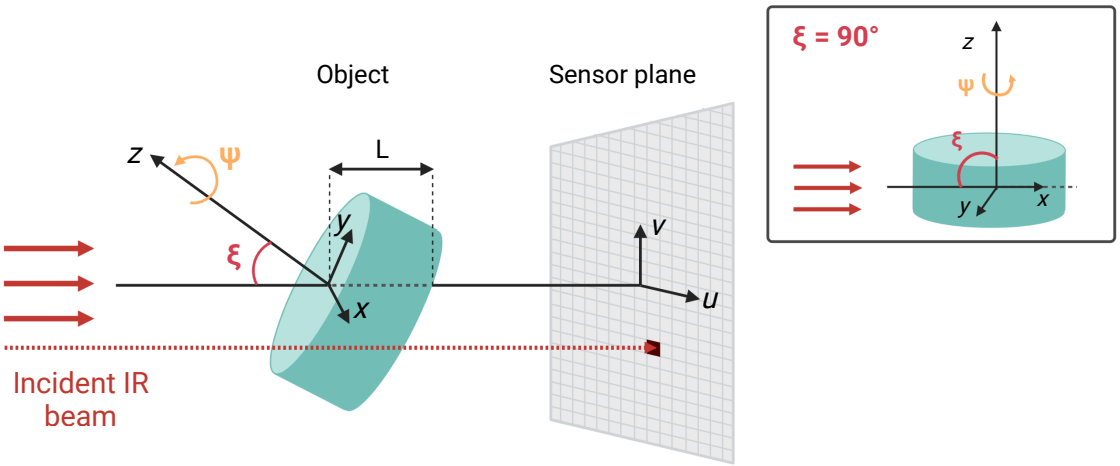

FIGURE 5.2 – Illustration of the rotary laminography and the coordinate systems used in this chapter. The insert illustrates the case $\xi = 90°$ corresponding to the CT configuration.

The sample is illuminated with an IR source aligned with the camera. The sample is tilted by an angle ξ, called laminographic angle, with respect to the optical axis. This angle can be comprised between 0° and 90°, $\xi = 90°$ corresponding to the CT case as illustrated in Figure 5.2. In practice, we set ξ in the range $[20° - 60°]$. Then, the object turns around its z-axis

to complete a 360° rotation with an angular step $\Delta\psi = 2\pi/N$. ψ is the rotation angle, and N the number of recorded projections. Therefore, for a laminography measurement, the angle ψ varies between 0° and 360° by step of $\Delta\psi$. We note ψ_i the rotation angles with $i \in [1-N]$.

Finally, the camera measures the 2D projections $\mathcal{P}_{\xi,\psi_i}$ of the object. Applied to transmittance with a non-reflective material, the projection measured by the camera for a couple (ξ, ψ_i) is:

$$\mathcal{P}_{\xi,\psi_i}(u,v) = \rho_{\text{pix}}\Phi_0\Gamma(t) = \rho_{\text{pix}}\Phi_0 e^{-\int_0^{L_o(\xi,\psi_i)} \alpha(x,y,z)\,\mathrm{d}z} \tag{5.1}$$

The optical path through the tilted sample, $L_o(\xi, \psi_i)$ (m), depends on the angles ξ and ψ_i. It can be decomposed into voxels which are a 3D unit storage equivalent to the 2D pixel. Therefore, the signal recorded by one pixel of the camera comes from a line of voxels, depending on the angles ξ and ψ_i [122]. The reconstruction algorithm consists in back-projecting the signal from a pixel onto the entire corresponding line of voxels. Using several projections $\mathcal{P}_{\xi,\psi_i}$, and an appropriate reconstruction algorithm, we should retrieve the attenuation coefficient α.

Definitions:

- **Back-projection**: Operation consisting in calculating the 3D object using the 2D projections $\mathcal{P}_{\xi,\psi_i}$ by back-projecting the signal from a pixel (u, v) onto the entire corresponding line of voxels.
- **Projection**, $\mathcal{P}_{\xi,\psi_i}(u, v)$: 2D image recorded by the camera of the 3D object tilted by ξ along the optical axis, after a rotation of ψ_i (see equation 5.1).
- **Voxel**: 3D storage unit, equivalent to the 2D pixel. The 3D reconstructed object is composed of several voxels. However, the voxels are not necessarily cubic: their dimensions depend on the number of projections, the spatial resolution of the projections, and the reconstruction algorithm used. Therefore, we experimentally measure the 3D dimensions of a voxel by reconstructing a calibrated object.

5.2.2 Reconstruction algorithm based on back-projection

There are several reconstruction algorithms for laminography in the literature: methods based on back-projection [134, 137], inversion in the Fourier space [138], or iterative methods [139, 140] that should be combined with Bayesian approach [141].

This section describes an algorithm based on Ref. [134] for reconstructing a 3D object from laminographic projections. This method is inspired by the filtered back-projection (FBP) widely used for computed tomography reconstruction [142] based on Radon theory. The different steps of the reconstruction algorithm used in this study ares illustrated in Figure 5.3, and detailed below:

1. The first operation is to determine the center of rotation $(u = 0, v = 0)$ on the projections $\mathcal{P}_{\xi,\psi_i}(u, v)$. Each pixel (u, v) of the projection is then numbered based on its distance from the center.

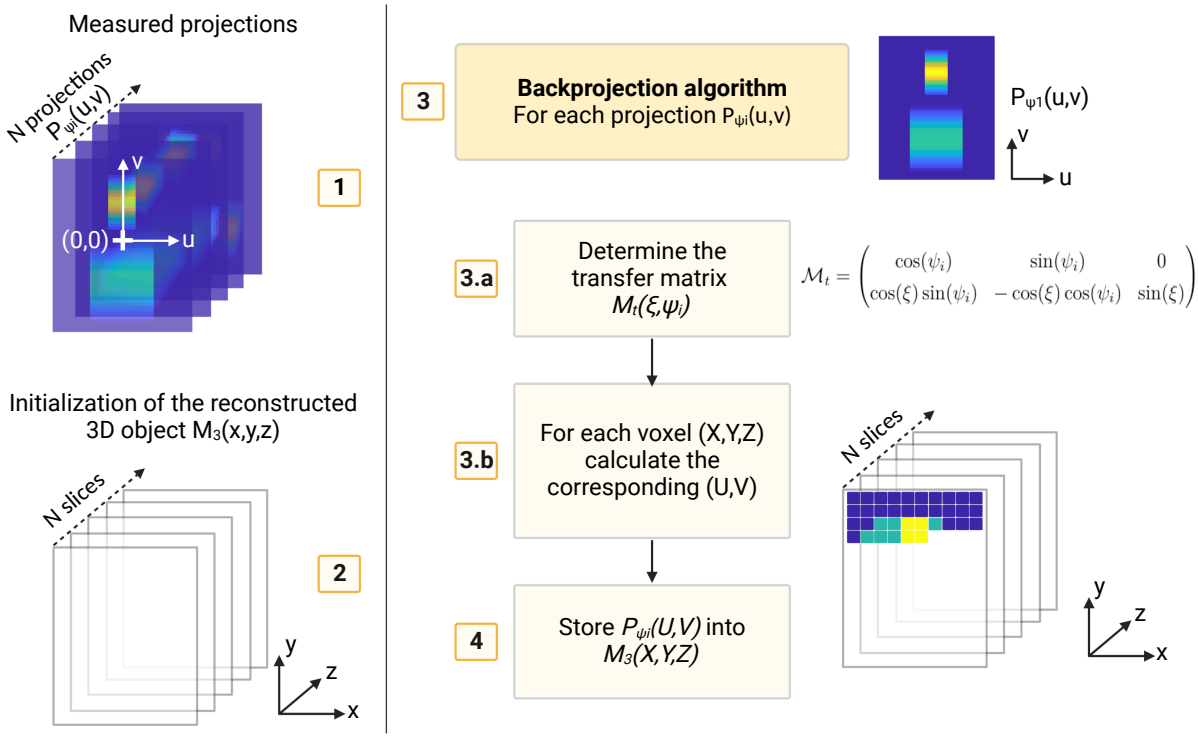

FIGURE 5.3 – Illustration of the laminography reconstruction algorithm.

2. Then, we create an empty 3D matrix, $\mathcal{M}_3(x, y, z)$, to store the reconstructed object. The x and y axes have the same size and are determined by the largest dimension of the projections between the u and v axes. The minimal number of slices along the z-axis, N, is equal to the number of projections [135].

3. For each projection $\mathcal{P}_{\xi,\psi_i}(u, v)$ we apply the back-projection algorithm to fill the matrix $\mathcal{M}_3(x, y, z)$. We proceed as follow:

   (a) We compute the transformation matrix $\mathcal{M}_t(\xi, \psi_i)$ to obtain the correspondence between the voxel (x, y, z) and the pixel (u, v) containing the voxel signal. This matrix depends on the setup geometry, as well as the angles ξ and ψ_i [134, 135, 143].

$$\mathcal{M}_t(\xi, \psi_i) = \begin{pmatrix} \cos(\psi_i) & \sin(\psi_i) & 0 \\ \cos(\xi)\sin(\psi_i) & -\cos(\xi)\cos(\psi_i) & \sin(\xi) \end{pmatrix} \tag{5.2}$$

   (b) For each voxel (x, y, z), we calculate the corresponding pixel (u, v) with the following equation.

$$[u, v] = \mathcal{M}_t(\xi, \psi_i)[x, y, z]^T \tag{5.3}$$

   The calculated values u and v are not necessarily integers: an interpolation algorithm must be used to determine the corresponding pixel, or group of weighted pixels depending on the method. We choose the nearest-neighbor interpolation, to reduce

the computational time compared to linear, cubic, or spline interpolations. Once we obtain the interpolated pixel coordinates (u, v), we check if they fall within the projection range, and if so, we store the corresponding value in the voxel (x, y, z) of the 3D matrix $\mathcal{M}_3$.

4. The process is repeated for each projection. If the voxel (x, y, z) already contains data, the new contribution is added. Finally, $\mathcal{M}_3$ fills up as it goes along, adding new contributions for each projection.

5.2.3 A numerical study of 3D reconstruction from 2D projections

Before conducting infrared laminography measurements, we test the reconstruction algorithm on a numerical case. For that, we generate a basic 3D scene consisting of two spaced bars of different sizes aligned along the z-axis, and calculate the 2D projections depending on the angles (ξ, ψ_i). This configuration is close to the first measurements we will conduct in IR transmission with calibrated objects. Figure 5.4 shows the 3D object and some calculated projections. As expected for such a geometry, the higher the laminographic angle, the more objects separate from each other on the projections.

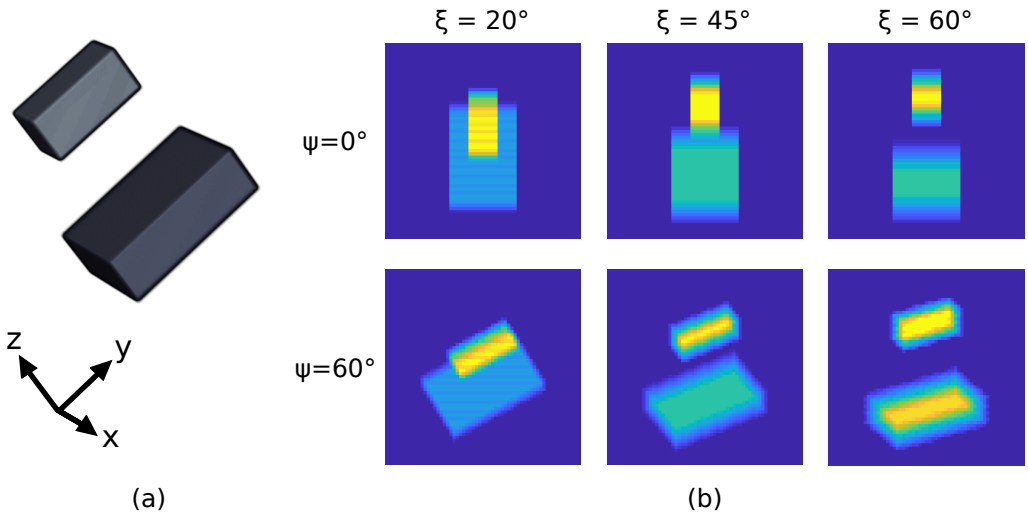

Figure 5.4 – (a) Illustration of the numerical 3D object composed of two bars, and (b) some calculated projections at different angles (ξ, ψ_i).

This study help us to choose a laminographic angle, and determine the number of projections needed to perform a consistent 3D reconstruction. However, the reconstruction algorithm generates artifacts in the 3D object, so we study them to better understand the shape of the reconstructed objects. In the following, the 3D object intensity is normalized as we focus only on the shape and ratio of the different patterns.

Choice of the laminographic angle ξ

In order to select an appropriate tilt angle for the experiment, we examine its effect on the reconstruction of the digital object. The study is performed for three laminographic angles, $\xi = [20; 45; 60]°$, and a rotation step of $\Delta\psi = 2°$, meaning 180 projections.

Slices of the corresponding reconstructed objects are shown in the Figure 5.5 with the theoretical object as a comparison. The higher the laminographic angle, the more easily the bars can be distinguished as it is plotted in the graph (a). With a laminographic angle $\xi = 20°$, the bars are not even identifiable. For $\xi = 45°$, the bars are visible but there is unwanted signal in between due to cross-shaped artifacts which are studied separately later. For the following we do not work with angles lower than 30°, although the choice of the angle depends on the spacing between the different patterns of the 3D object. The closer they are to each other, the larger the angle have to be to differentiate them.

In addition, we observe that the ratio between the intensity of the reconstructed bars depends on the laminographic angle. Regarding this numerical study, the theoretical ratio is 0.5, while reconstruction gives 0.54 for $\xi = 45°$, and 0.71 for $\xi = 60°$. As a consequence, $\xi = 60°$ gives better results for differentiating bars, while $\xi = 45°$ better preserves the ratio between elements. As a consequence, we need to find a compromise between preserving shape and intensity ration, depending on the geometry of the object, or conduct measurements with several laminographic angles.

Published works [135, 138] proposed some laminographic filters to correct the intensity of the reconstructed object and artifacts. We have not addressed this challenge yet, but future works must determine an adapted filter depending on the measurement conditions, the reconstruction algorithm, and the shape of the 3D field under study.

Choice of the rotation step, $\Delta\psi$

The second factor to consider is the number of projections required for a sharp reconstruction, denoted as N. As a reminder, the rotation angle step is $\Delta\psi = 360°/N$. Figures 5.6 and 5.7 show the reconstructed object for two different laminographic angles, $\xi = 45°$ and $\xi = 60°$, with varying numbers of projections in the ZY, ZX, and XY planes. By examining these graphs, we can make the following assertions:

- The reconstruction with a single projection (see figure 5.6 column 1), consists in back-projecting a measured pixel (u, v) on all the voxels along the corresponding light path. This is insufficient for reconstructing the shape of the 3D object.
- Using two projections (see column 2), we start to identify the object position in a single plane, here ZY plane due to the selected rotation angles ψ_i, which are spaced π apart.
- Four projections enable to locate the object in the all planes ZX, ZY, and XY. As shown from the XY slice, four projections are sufficient here, since we are studying square

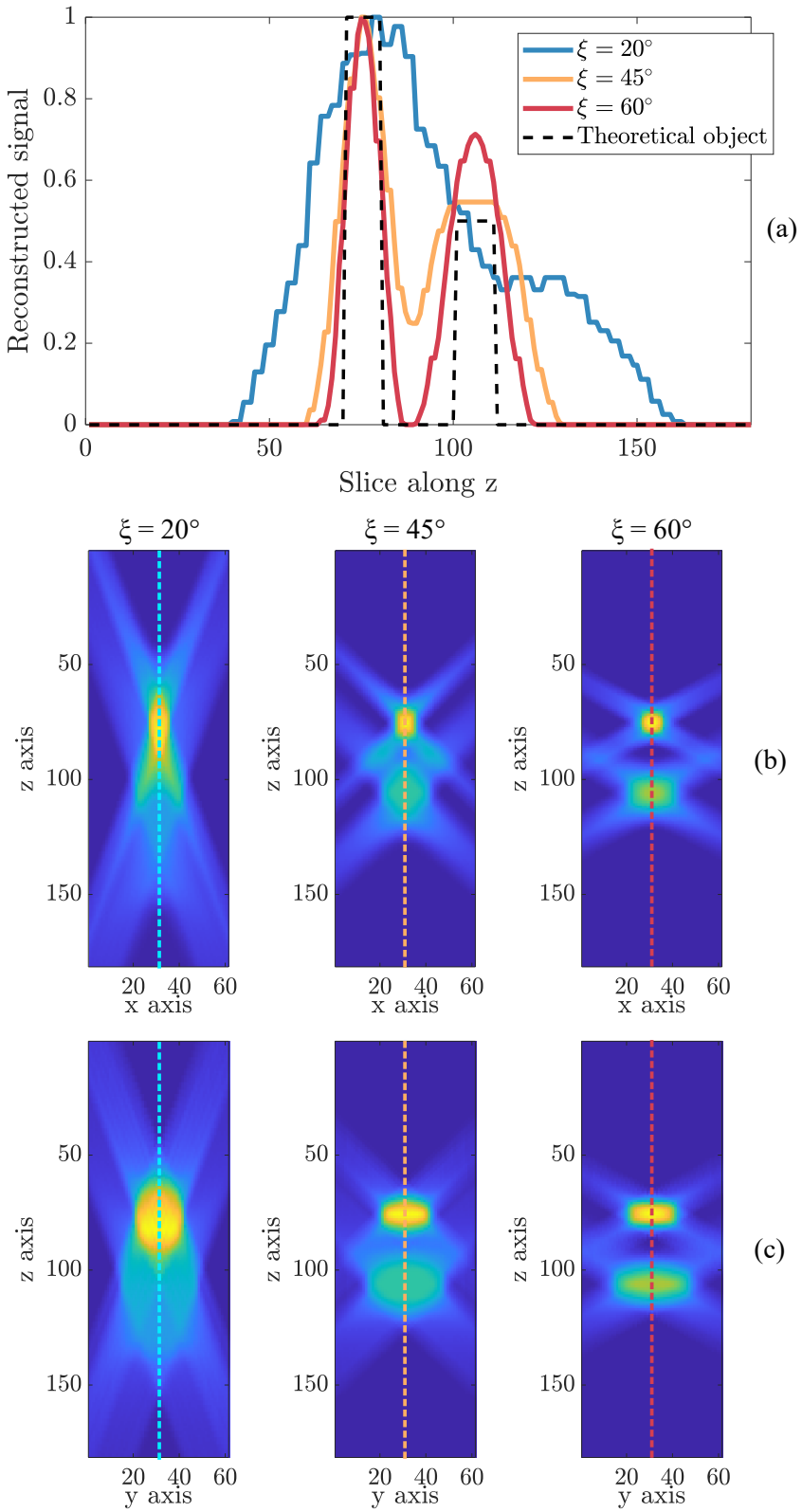

FIGURE 5.5 – (a) Reconstructed signal using different laminographic angles $\xi = [20°; 45°; 60°]$, for the voxels along z at $x = 31$ and $y = 31$. Corresponding ZX (b) and ZY (c) planes.

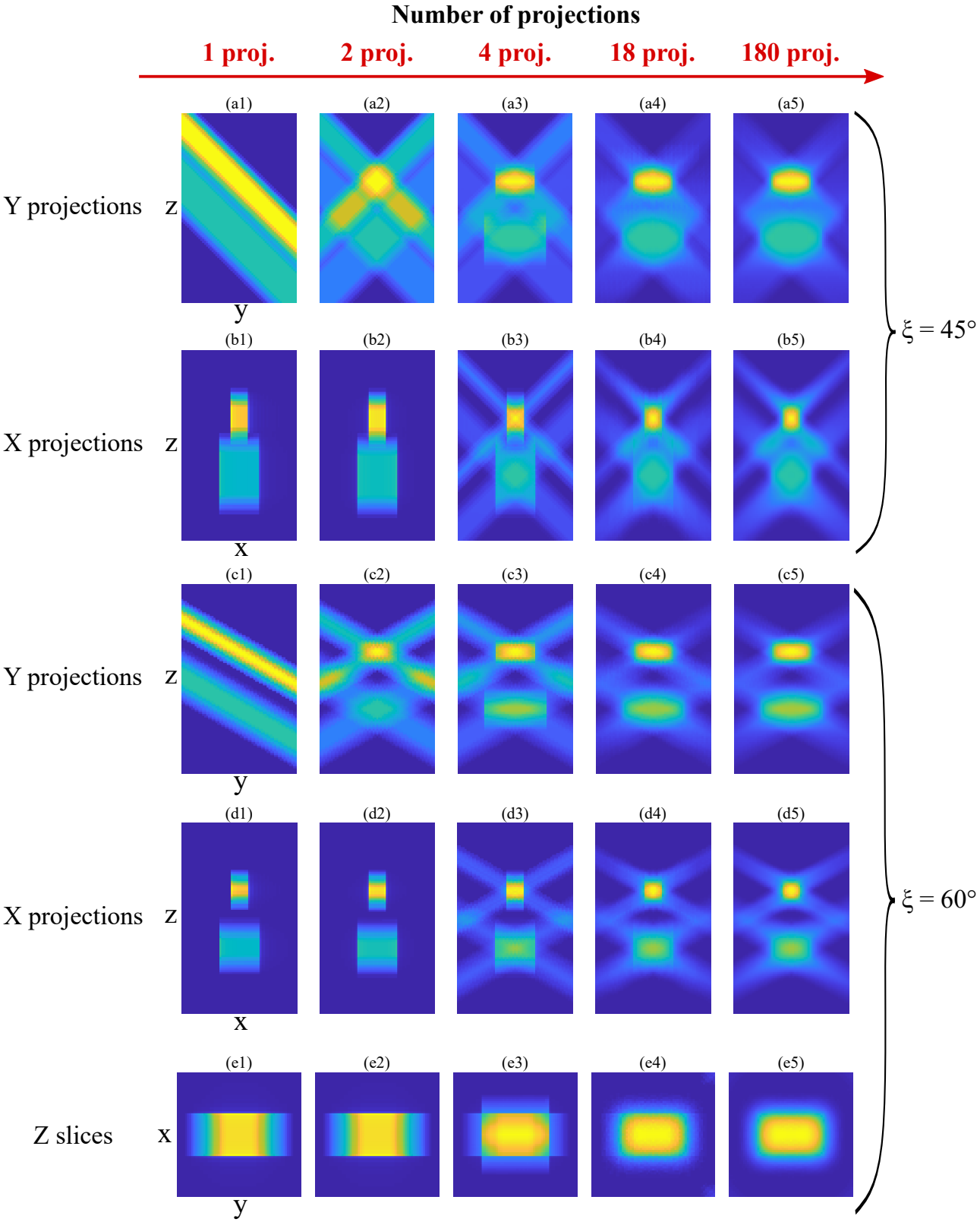

FIGURE 5.6 – Slices of the reconstructed objects for several laminographic angles, ξ, and numbers of projections: (.1) one projection $\psi = 0°$, (.2) two projections $\psi = [0; 180]°$, (.3) $\Delta\psi = 90°$, (.4) $\Delta\psi = 20°$, and (.5) $\Delta\psi = 2°$. Figures (e_i) correspond to the plane XY of the reconstructed object, for z=106.

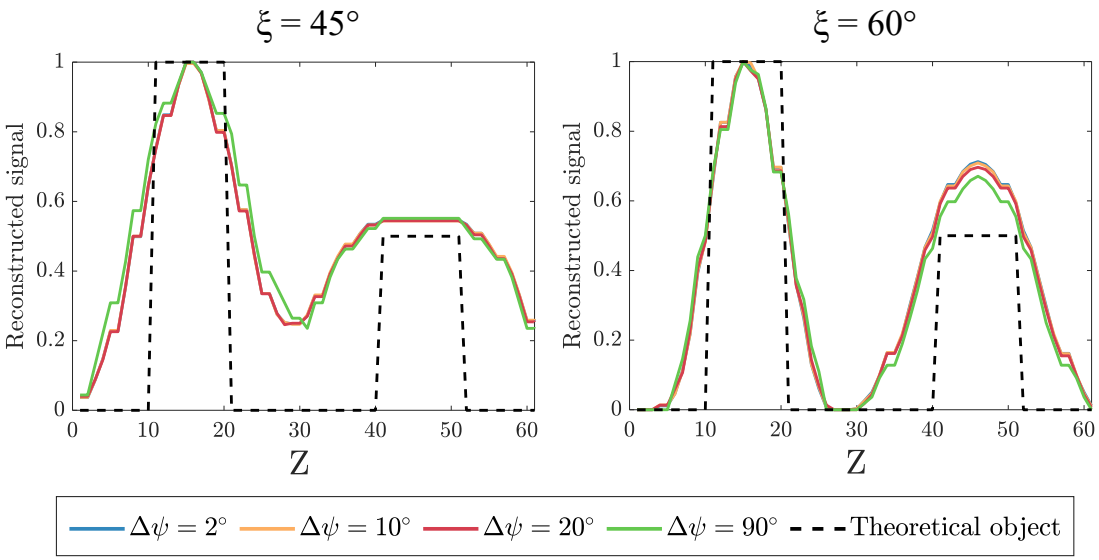

FIGURE 5.7 – Profiles of the reconstructed object depending on the laminographic angle, $\xi = 45°$ (left) and $\xi = 60°$ (right), for different rotation angle step sizes. The graphs (a_i) correspond to $x = 31$ and $y = 31$.

objects. As a result, to estimate the location of a 3D object, a minimum of four projections is required, provided $\Delta\psi = 90°$. However, for more complex geometries, the number of projections must be increased to obtain the shape of objects.

- Figures 5.6 and 5.7 show that the object being studied can be reconstructed with only a few projections, meaning $\Delta\psi = 20°$ seems to be enough.

- As the number of projections increases, the estimation of the edges of the bars becomes more precise. Regarding this numerical case, the number of projections has little impact on the reconstructed signal if we focus on the Z-slice which passes along the middle of the bars (see Figure 5.7). However, cross-artifacts appear in the reconstructed object, regardless of the number of projections. In the next paragraph, we examine this issue more closely.

To conclude, determining the approximate location of 3D objects in each plane requires at least four projections ($\Delta\psi = 90°$). For accurate edges estimation, especially when studying objects with complex shapes, the more projections, the better. In practice, it is important to find a compromise between the time needed to scan several projections, the resulting data storage, and the required reconstruction quality such as image contrast, and edges sharpness.

3D reconstruction artifacts

The last point to discuss is the cross-shaped artifacts resulting from the reconstruction algorithm, as shown in Figures 5.5 and 5.6. To analyze these artifacts, we reconstruct an object composed of a single voxel of coordinates ($x = 0, y = 0, z = 0$). The reconstructed voxel is located at the center of the cross-shaped artifact whose angle depends on the laminographic

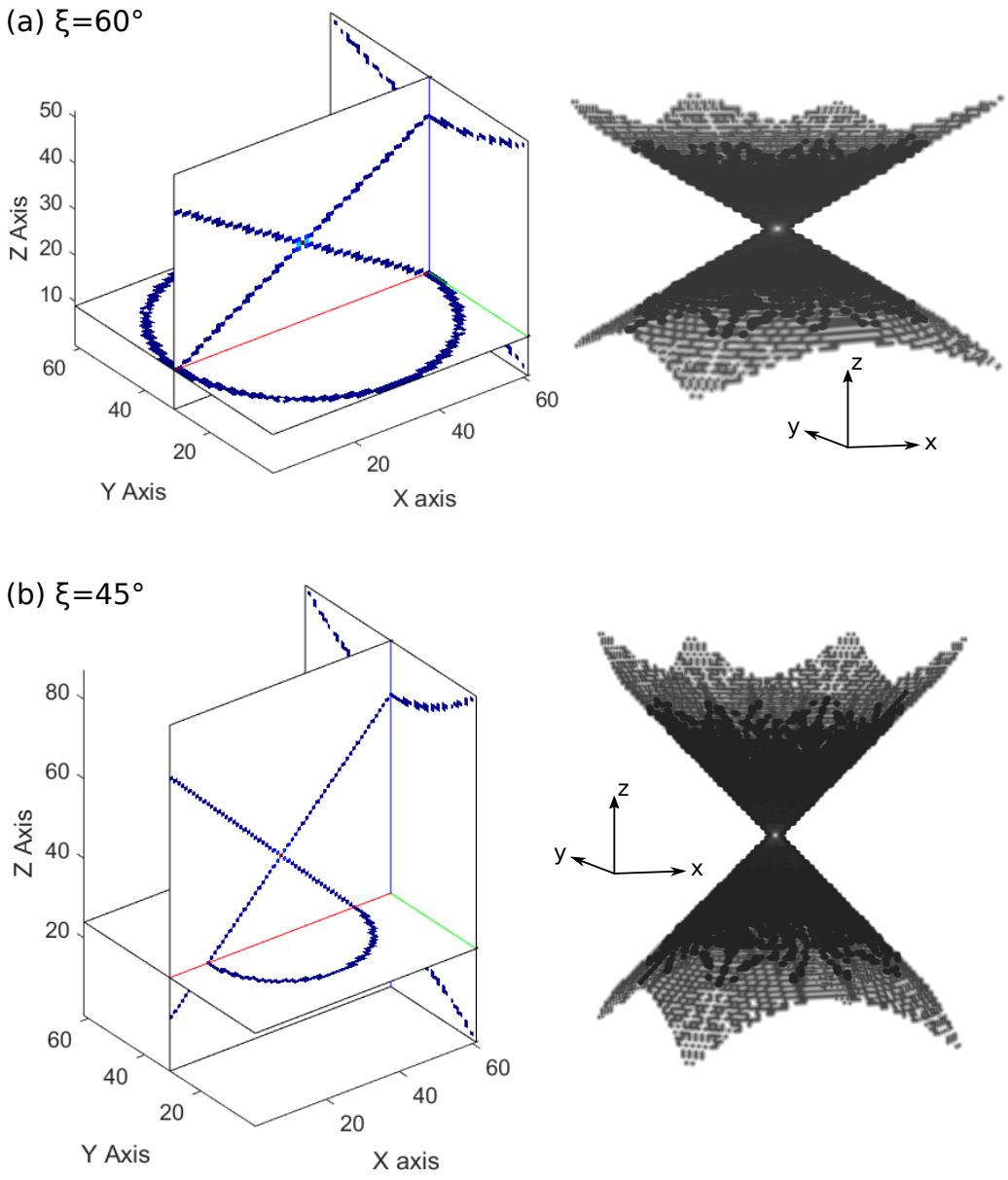

FIGURE 5.8 – Reconstruction of a single voxel for two laminographic angles (a) $\xi = 60°$ and (b) $\xi = 45°$, and a rotation step $\Delta\psi = 2°$. We observe the cross-shaped artifact on both reconstructions. *The Matlab volume viewer application used to plot the 3D objects interpolates the voxel positions, which is why they look round.*

angle ξ, as it is illustrated in Figure 5.8. This artifact always occurs because of the reconstruction algorithm consisting in back-projecting the 2D pixel information along a voxels line. Several methods should be considered to filter out this parasitic signal:

- A first idea is conducting two laminographic measurements using different angles ξ. Afterwards, the reconstruction algorithm is applied to each set of projections. The artifacts shape as a function of ξ should be the primary difference between the two reconstructed objects. As a result, comparing the two reconstructions would enable us to filter out the artifacts. However, this technique is time-consuming and data-intensive, since it requires at least two measurements and their associated post-processing.
- Another approach is to compute the 3D Point Spread Function (PSF) of the artifacts by reconstructing a single numerical voxel as shown in Figure 5.8. Then, by deconvoluting the 3D reconstructed object by the 3D PSF, we should filter out the artifacts. This method is commonly used for 2D filtering [144], and is also developed in three-dimensions for instance in confocal imaging [145] or fluorescence microscopy [146]. As with all filtering techniques, this method can distort the signal of interest. Therefore, the method should be adapted to the reconstructed object on a case-by-case basis.
- A third method consists in constraining the shape of the reconstructed object using for instance a Bayesian approach combined with the heat transfer model regarding the thermotransmittance case.

Conclusion about the numerical study

This numerical study showed us the impact of the laminographic angle and the number of projections on the shape and intensity of the reconstructed object. The laminographic angle must be high enough to discriminate the different patterns of the object, depending on their spacing. Therefore, for the experimental measurements, we work with ξ in the range between 30° and 60°. In addition, if we just want to determine the location of the different patterns of the object, only a small number of projections is required (4 projections in this study). Nevertheless, to determine sharp edges of patterns, the higher the projection number, the better the reconstruction, especially for object with complex geometries.

Finally, we expect to observe reconstruction artifacts in the 3D thermotransmittance field, depending on the laminographic angle. As a result, the challenge is to discriminate the signal of interest from these artifacts.

5.3 Infrared laminography measurements

This section presents the development of laminography applied to the infrared spectral range. We do not measure thermotransmittance yet, but only the IR transmittance of an object to develop the experimental setup. We start measurements by reconstructing calibrated objects (USAF targets) in order to evaluate the experimental setup and the reconstruction algorithm in a real case.

5.3.1 Infrared laminography experimental setup

Figure 5.9 shows the IR laminography experimental setup. As in previous studies (see sections 3.2 and 4.4.1), the sample is illuminated by a monochromatic IR flux coming from a stabilized blackbody associated with a monochromator. An InSb infrared camera (FLIR SC7000) equipped with a ×1 microscope objective measures the flux transmitted through the sample, with a spatial resolution of 15 µm/pixel. The estimation of the camera depth of field is presented in the Appendix E and is approximately 5 mm around the focal plane. The camera is still synchronized with a mechanical chopper, the subtraction of undesired radiations is processed using the two-image method described in chapter 3.

To conduct laminography measurements, the sample is placed on a 3D-printed gear prototype driven by a motorized rotary stage (Zaber) which allows the sample to be rotated by an angle ψ around its z-axis. The rotary motor, gears and sample are assembled on a support tilted by an angle ξ with respect to the optical axis (see Figure 5.9). The camera is synchronized with the rotary motor to record projections of the object for each rotation of ψ, until it has completed a 360° turn.

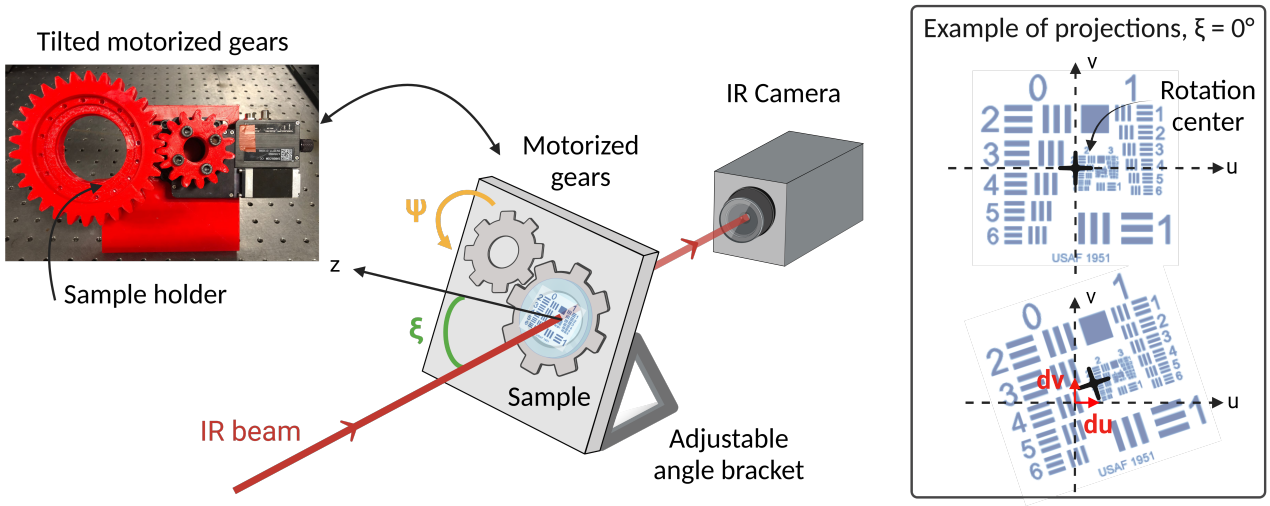

FIGURE 5.9 – Experimental setup for IR laminography with the USAF target as sample. The insert illustrates the rotation center displacement on the projections, due to mechanical slack.

Due to the prototype gear, there is mechanical slack in the rotating device, resulting in a shift of the rotation center on consecutive projections. This phenomenon is illustrated in the insert in Figure 5.9. In post-processing, we correct this displacement to improve the sharpness of the reconstructed 3D object. In future works, it will be critical to implement an improved version of the sample holder with a more stable system enabling the fine tuning of the position of the rotation center and its alignment to the optical axis.

In this study, we use two combined calibrated USAF targets as samples [91]. First, we study a single target to determine the spatial resolution of the reconstruction and develop an algorithm to correct the projections shift during the experiment. Second, we superpose two USAF targets to measure the voxel dimensions and test other measurement settings.

5.3.2 Calibration of the experimental setup - Reconstruction of USAF targets

First, we study a single USAF pattern [91], which results in the reconstruction of a single plane to measure the dimensions of the voxel along the x and y axes. Then, we examine an object composed of two superimposed USAF targets whose spacing is known to determine the dimension of the voxel along the z-axis. In addition, to asses the image quality of the reconstructed object, we examine how image contrast varies with pattern size of the USAF target.

5.3.2.1 Simple USAF target reconstruction

The USAF target is composed of reflective metallic patterns deposited on a glass medium. We measure the IR beam transmitted through the glass as a background on which reflective patterns are superimposed. In this study, we are only interested in the patterns shape to determine the quality of a single plane reconstruction, and we do not analyze the intensity of the reconstructed signal. Therefore, we inverse the image contrast to highlight patterns.

Figure 5.10 shows some raw projections of the target, measured for a laminographic angle $\xi = 45°$. The rotation step is set at $\Delta\psi = 5°$. In the following are presented the different steps to reconstruct the object, and an image quality study based on the contrast measurement.

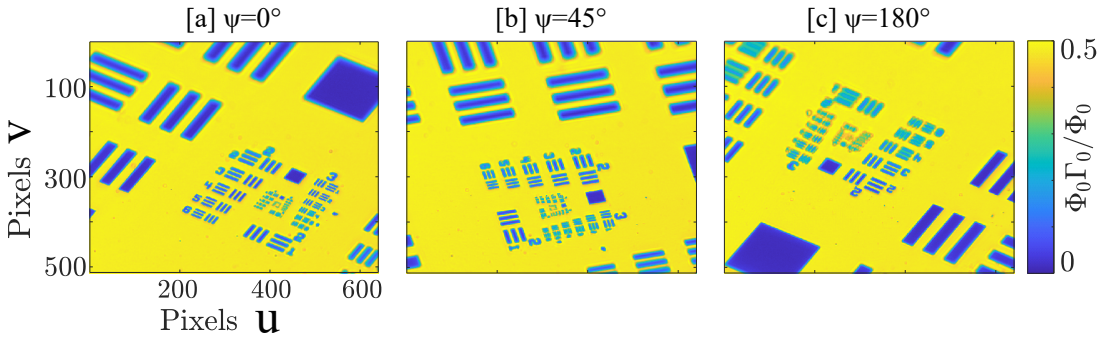

Figure 5.10 – Measured projections of the USAF target, with a laminographic angle $\xi = 45°$ and the rotation angles (a) $\psi_i = 0°$, (b) $\psi_i = 45°$, (c) $\psi_i = 180°$.

Correction of the rotation center displacement by pattern tracking and trajectory correction

In the previous section, we have mentioned that the gears mechanical slack causes a displacement (du, dv) of the rotation center between consecutive projections as illustrated in Figure 5.9. A rotation center mismatch impacts the reconstruction because the pixel (u, v) is not be back-projected onto the correct line of voxels. This results in a blurred reconstructed object, as shown in Figure 5.14 (a).

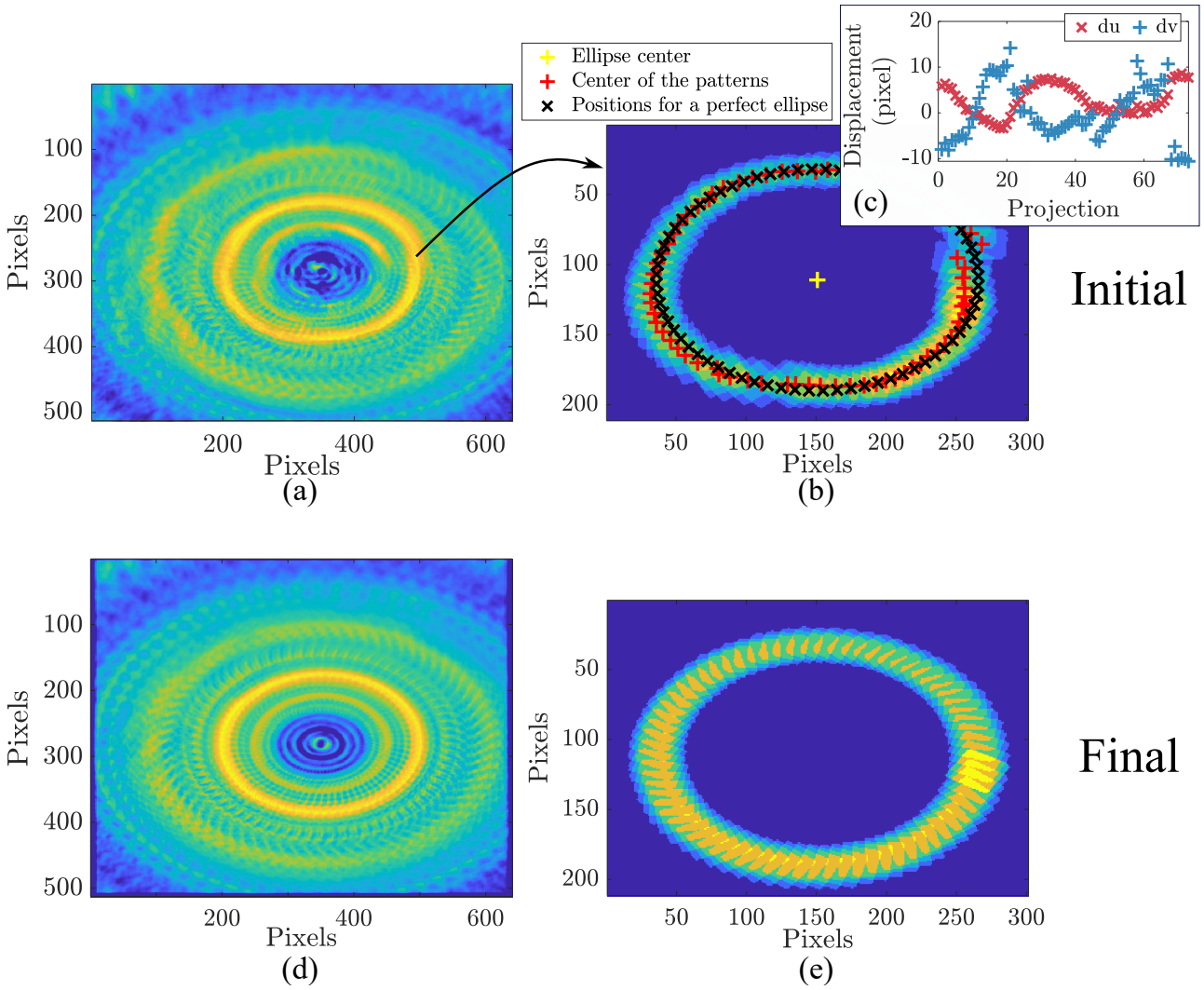

FIGURE 5.11 – Sum of all the projections $\mathcal{P}_{\xi,\psi_i}(u,v)$ of the USAF target (a), and of an isolated pattern (a square) (b). (c) Calculated displacement along u and v compared to a perfect ellipse. Sum of all the projections after displacement correction for the whole patterns (d) and the square pattern (e).

To improve the image quality of the 3D reconstruction, we correct the shift (du, dv) between consecutive projections. In a perfect case, a single pattern follows an ellipsoidal trajectory around the rotation center, depending on the angles ξ and ψ. However, mechanical slack causes disturbances in this trajectory. The correction method is based on comparing the real trajectory of a pattern with its perfect trajectory. The process is described below:

1. The trajectory of the patterns around the rotation center is calculated by summing all the measured projections. Figure 5.11 (a) shows the sum of all the projections. Elliptical trajectories can be seen around the center of the image, but they are not sharp. As it is challenging to work on all patterns at once, we select one of them and study its trajectory, as seen in Figure 5.11 (b). The chosen pattern is a square whose center is easy to identify.

2. For each position of the pattern, we first identify its real center and then calculate its

ideal position on a perfect ellipse, as labeled in Figure 5.11 (b).

3. The difference between the real and perfect positions of the pattern gives the displacements du and dv, which are plotted in Figure 5.11 (c).

4. Finally, the projections are translated by du and dv: the sums of the corrected projections are presented in Figures 5.11 (d) and (e) for the whole image and the isolated pattern. The ellipsoidal trajectory is retrieved especially near the rotation center, which was previously blurred. We assess the impact of this correction on reconstruction quality in the paragraph about image quality (see p.110).

Now the displacements of projections are corrected, we present the reconstructed object.

Reconstructed 3D object

The next step consists in reconstructing the 3D object by using the laminography algorithm described in section 5.2.2. Due to the geometry of the sample, we expect one sharp slice containing the different patterns. The other slices should contain only the reconstruction artifacts. Figure 5.12 shows different reconstructed slices of the USAF target and Figure 5.13 plots 3D views with selected planes ZY, ZX and XY. As expected, only one plane is sharp while the others contain only reconstruction artifacts. It appears that the sharp slice is in the center of cross-shape artifacts, as we already noticed in reconstruction of a single voxel (see Figure 5.8). We now focus on the measurement of voxel dimensions and on the quality of the reconstructed object, both with and without displacement correction.

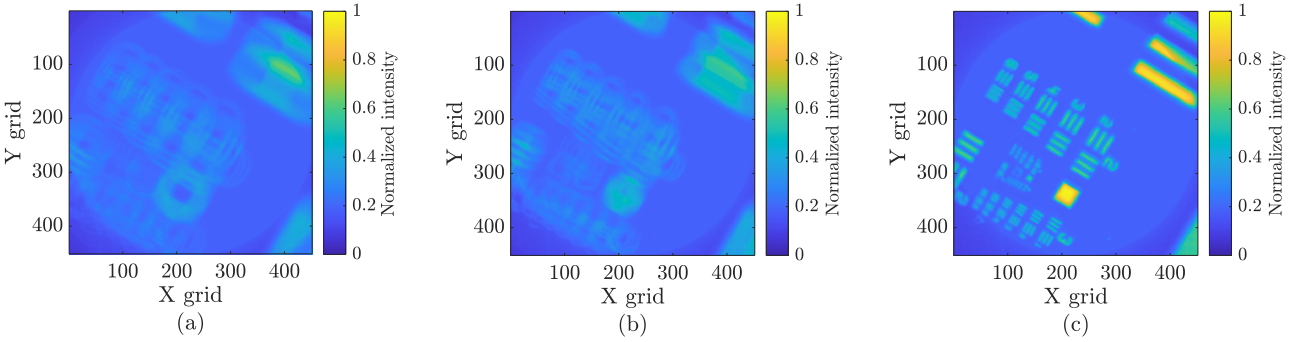

Figure 5.12 – Different slices of the reconstructed USAF target after displacement correction: (a) slice $z = 1$, (b) slice $z = 15$, and (c) slice $z = 34$.

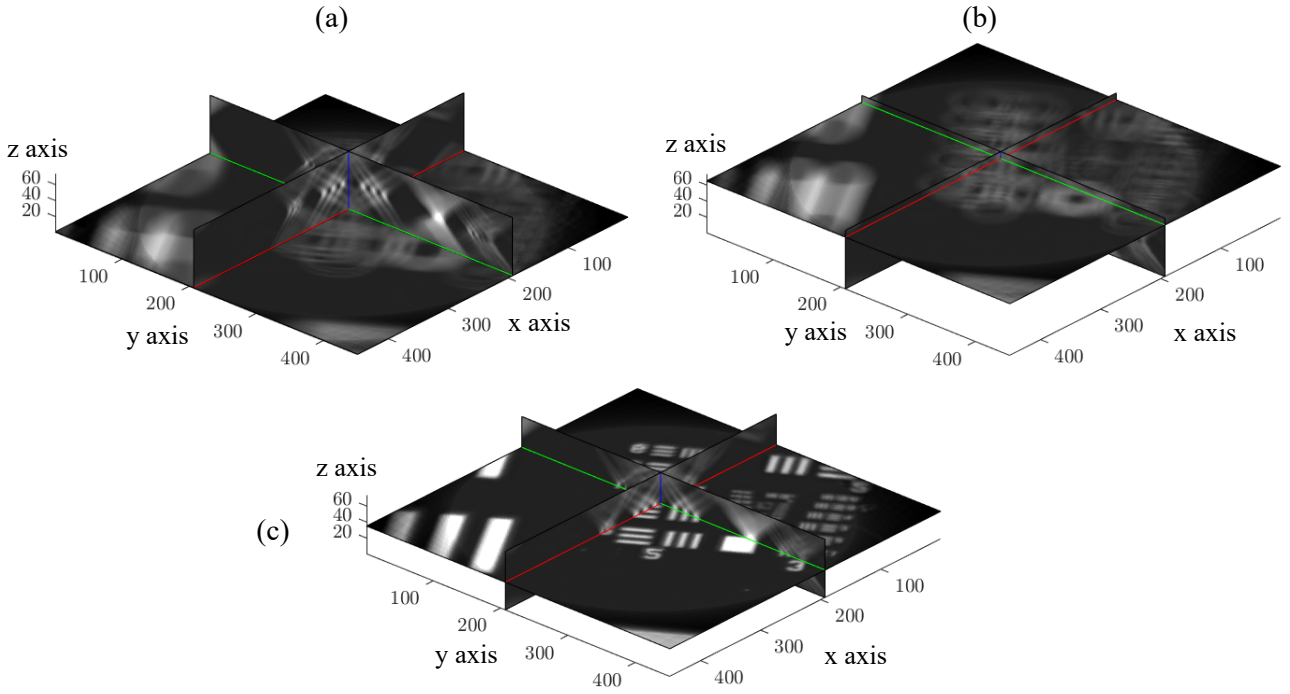

FIGURE 5.13 – 3D view of the reconstructed single USAF target after displacement correction: (a) slice $z = 1$, (b) slice $z = 70$, and (c) slice $z = 34$. The viewer application enables us to manually select planes ZY, ZX, and XY. We choose to highlight artifacts in the ZY and ZX planes.

Image quality of the reconstructed object

A metric to quantify the quality of the reconstructed object is the image contrast, $\mathcal{C}$, expressed in the equation 5.4, with I_{max} and I_{min} the maximum and minimum signals in a pattern [147]. USAF target is particularly adapted to the contrast measurement as it is composed of alternating reflective and transparent patterns of different sizes. Ideally, the contrast between two bands is $\mathcal{C} = 1$ ($I_{max} = 1$ and $I_{min} = 0$). In our case, we cannot expect to reach a contrast of 1 because the background equals 0.2 instead of 0. In addition, the reconstructed signal is normalized using the maximal intensity in the 3D object, not necessarily maximizing the value of the bands. Consequently, the absolute value of contrast must not be compared with 1. Instead, we compare the different contrasts based on pattern size and whether or not projection displacements have been corrected. As a reminder, the higher the indices of the pattern, the smaller the size of a band.

$$\mathcal{C} = \frac{I_{max} - I_{min}}{I_{max} + I_{min}} \tag{5.4}$$

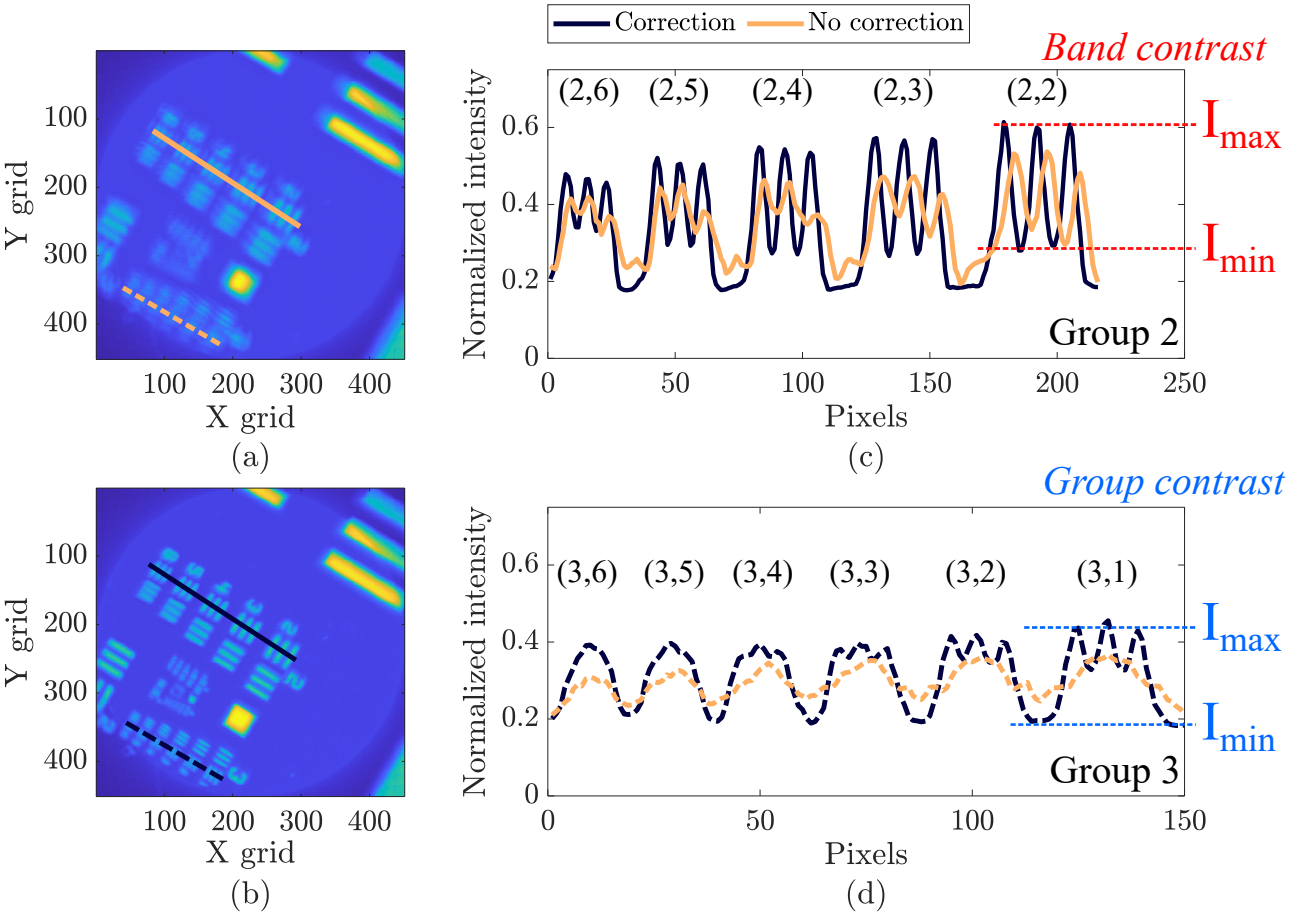

FIGURE 5.14 – Slice $z = 34$ of the reconstructed object, without (a) and with (b) displacement correction of the projections. Normalized measured intensity for two different pattern groups 2 (c) and 3 (d). *Group* and *Band* contrasts are also illustrated on the figure.

Configuration		Group 2 - Fig. 5.14 (c)					Group 3 - Fig. 5.14 (d)					
		(2,6)	(2,5)	(2,4)	(2,3)	(2,2)	(3,6)	(3,5)	(3,4)	(3,3)	(3,2)	(3,1)
Band	No corr.	0.06	0.10	0.10	0.12	0.24	-	-	-	-	-	-
	Corr.	0.17	0.27	0.33	0.36	0.36	-	-	0.04	0.07	0.09	0.16
Group	No corr.	0.27	0.29	0.37	0.42	-	0.13	0.16	0.17	0.17	0.18	-
	Corr.	0.45	0.48	0.50	0.52	-	0.30	0.35	0.34	0.36	0.38	-

TABLE 5.1 – Contrast of the reconstructed target, both with and without displacement correction, measured on the patterns highlighted in figure 5.14. *Band* means the contrast between bands of a single group, and *group* the contrast between two groups of patterns.

In Figure 5.14, we compare the reconstructed target before and after correction of the displacement of the projections. Visually, the slice is much sharper after the correction, as we can see the small patterns in the center of the target. To quantify the sharpness of the reconstruction, the contrast for different patterns is calculated and listed in Table 5.1. We measure the contrast between bands of a single group (*band*), and the contrast between two groups of patterns (*group*) as illustrated in Figure 5.14. Generally the larger the pattern, the better the contrast, as expected. In addition, based on Table 5.1, we present the following comments:

- Regarding small patterns of Group 3, we cannot distinguish the bands in the reconstructed slice from non-corrected projections. This corresponds to bands of width from 35 to 62 µm. Thus, the smallest distinguishable object without correction is 70 µm (Group 2,6), with a low contrast of 0.06. After correcting the projections, the smallest distinguishable pattern is 44 µm width, with a contrast of 0.04. The improvement in resolution is therefore around 25 µm after displacement correction.
- Regarding larger patterns of Group 2, the contrast is two to three times higher after correction.

As a result, calculating the contrast demonstrates the importance of a stable rotation device for reconstructing a 3D object with the best possible resolution. In future work, it would be interesting to reconstruct a target with patterns of the same size to measure whether the contrast is the same across an entire slice and determine the impact of camera defocus when moving away from the center of rotation.

Dimensions of a voxel along the x and y axes

In addition, the calibrated USAF target enables us to calculate the dimensions along the x and y axes of a voxel. For that, we use the (2,2) pattern whose bands are 111.36 µm in width. We measure a resolution of 14.8 ± 0.5 µm/pixel, which is in good agreement with the pixels size of the projections. To determine the voxel dimension along the z-axis, we need to reconstruct a calibrated object with at least two sharp slices whose spacing is known.

5.3.2.2 Two superposed USAF targets reconstruction

The reconstruction of a single target does not provide the voxel dimension along the z-axis. Thus, we superpose two targets whose patterns are spaced by 3.35 mm, corresponding to the total thickness of both targets. A picture of such a sample is shown in Figure 5.15 (a). To better discriminate the two targets, we change the laminographic angle from 45 to 60 degrees (with rotation steps of 2 degrees, from 5 degrees in the previous section). Since the patterns are identical to the previous section, this also allows us to investigate the impact of this angle on the voxel dimensions along x and y axes.

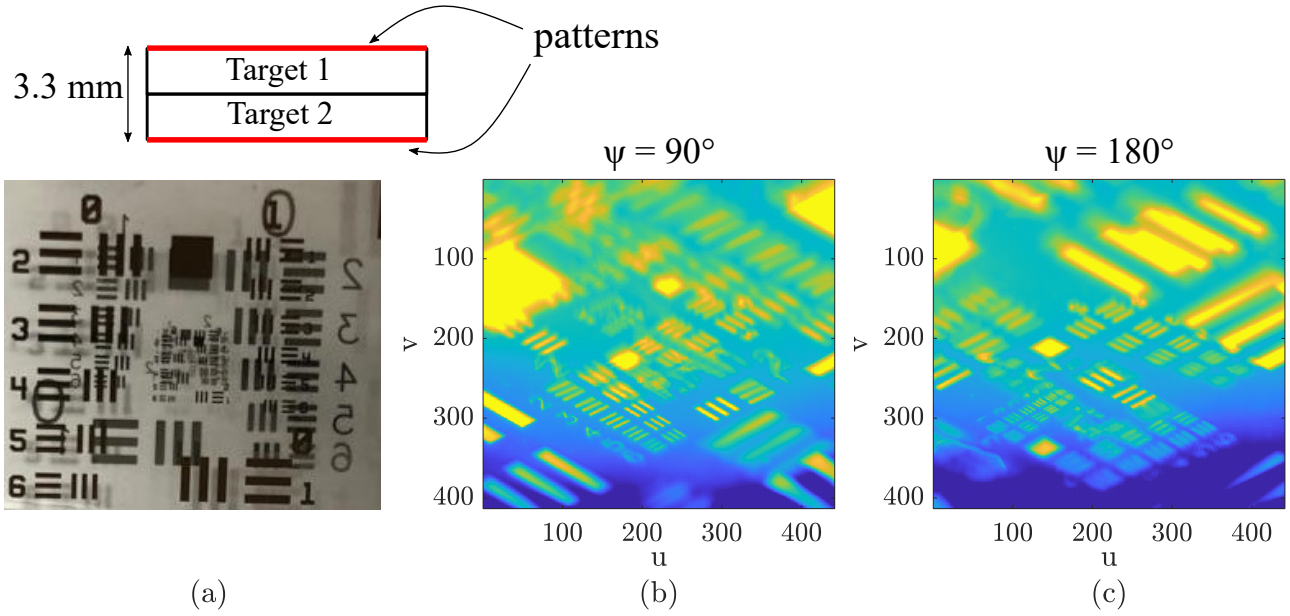

FIGURE 5.15 – (a) Image of the superposed targets in the visible light. Projections at different rotation angles (b) $\psi = 90°$, and (c) $\psi = 180°$, with a laminographic angle $\xi = 60°$.

In Figure 5.15, the projections appear blurry compared to the single target measurement because of the objective depth of field, a limiting factor in capturing sharp images of two targets spaced 3.35 mm apart. However, this configuration helps us push the limits of the current system.

Reconstructed 3D object

First, we correct the rotation center shift in the projections using the method detailed in the previous section, p.106. Figure 5.16 and 5.17 show several slices of the reconstructed object after correction. As expected, two slices are sharp, containing the USAF targets patterns, at $z = 44$ and $z = 156$. Figure 5.17 (d) allows us to visualize the sharp slices containing the targets located at the center of the cross-shape artifacts. In addition, the patterns look blurred compared to the previous study (see section 5.3.2.1) due to the camera focus being adjusted between the two targets. Therefore, we now analyze the contrast of reconstructed targets.

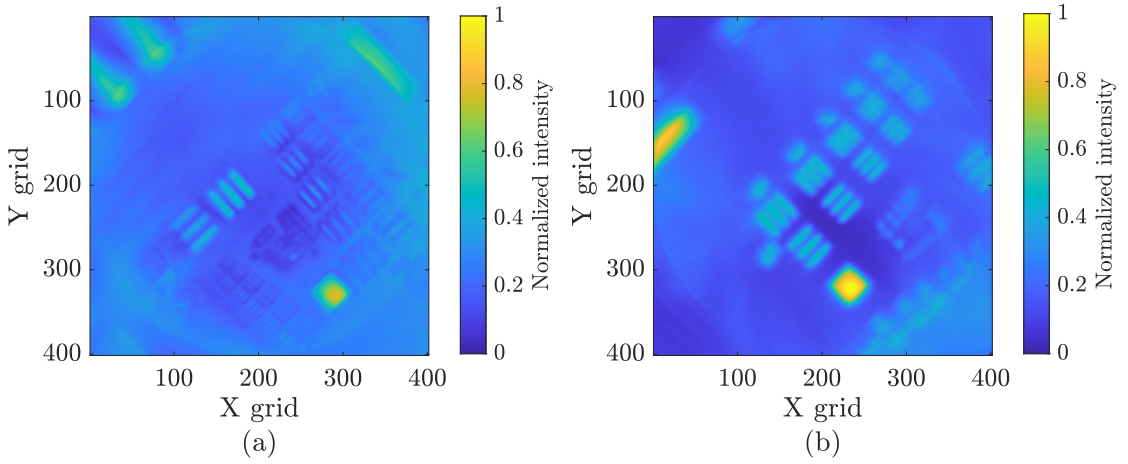

FIGURE 5.16 – Sharp slices of the reconstructed object, corresponding to both USAF targets: (a) slice $z = 44$ and (b) slice $z = 156$.

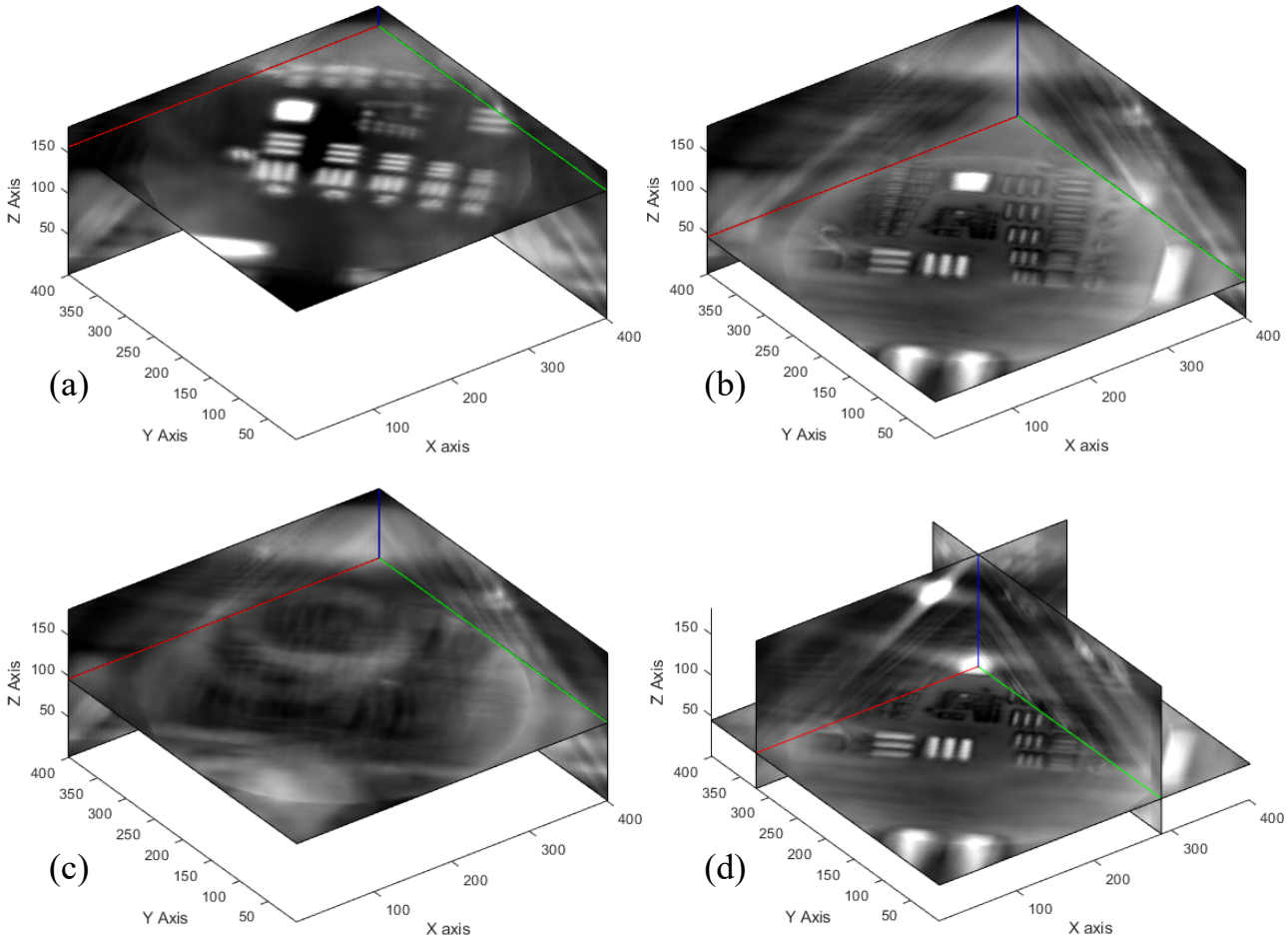

FIGURE 5.17 – Reconstructed double-target in 3D. Different slices are presented (a) $z = 156$, (b) $z = 44$, and (c) $z = 95$. Figure (d) corresponds to the plane XY $z = 44$ with others ZY and ZX slices to observe reconstruction artifacts in 3D.

Contrast of the reconstructed double-target

In Figure 5.16, the reconstructed double-target seems blurred compared to the previous study using a single target. This is because the camera focus is adjusted between the targets to capture both of them, which in turn reduces the sharpness of each test pattern individually. Table 5.2 gives the measured contrast on the group 2 in the slices containing the targets, $z = 44$ and $z = 156$.

Studied slices	(Group , pattern)				
	(2,6)	(2,5)	(2,4)	(2,3)	(2,2)
Slice $z = 44$	0.16	0.33	0.44	0.25	0.05
Slice $z = 156$	-	0.10	0.18	0.32	0.30

Table 5.2 – Contrast of the reconstructed object for slices $z = 44$ and $z = 156$.

As expected, the contrast is in average lower than the one determined on the single target (see Table 5.1 as comparison). In addition, we cannot measure it on the group 3 which is too blurry. However, the contrast depends more on the position of the pattern relative to the rotation center than on the pattern size, as shown in slice 44. Due to the high laminographic angle and distance between the targets, the patterns at the edges are less sharp than the ones at the center, due to the camera depth of field. For example, in slice $z = 44$, the patterns (2,5) and (2,4) are the closest to the center and have high contrast. On the other hand, the pattern (2,2) has larger bands but the lowest contrast because it is the pattern farthest from the center. This shows us that patterns located far from the rotation center are more difficult to reconstruct.

Dimension of the voxel

Finally, the USAF targets allow us to calculate the voxel dimensions along the axes x, y and z.

- The voxel dimensions along the x and y axes are calculated in both slices $z = 44$ and $z = 156$ to verify that it remains constant depending on z. The measured dimensions are respectively 14.2 ± 0.5 μm/pixel and 14.7 ± 0.5 μm/pixel, which is consistent with the measurement on the single USAF target (see section 5.3.2.1). The voxel dimension along x and y does not depend on the laminographic angle ξ and the number of projections, and is equal to the pixel size of the projections.
- Regarding the dimension along z, the number of slices between the two targets is 112. As the corresponding distance measured on the real object is $d = 3.35$ mm, the voxel dimension along z is 33.4 ± 0.3 μm/pixel.

Conclusion

This study allowed us to develop the first microscale laminography measurements in the infrared spectrum. We noticed the importance of having a stable rotary device to measure projections

without displacements between consecutive rotation angle. A short-term solution was to develop an algorithm to correct this error and improve the quality of the reconstruction. The USAF targets enabled us to validate the setup and the reconstruction algorithm on calibrated objects, and determine the dimensions of a voxel for different operating conditions. Finally, we have observed that the resolution of the reconstruction degrades with distance from the center of rotation, specially for thick objects, due to the limited depth of field of the camera.

5.4 3D thermotransmittance imaging

Now that the laminography experimental setup is validated, we combine the technique with microscopic thermotransmittance measurement, presented in Chapter 4, to reconstruct a 3D temperature field.

5.4.1 Laminography thermotransmittance experimental setup

To image a 3D thermotransmittance field, we use the rotary laminography setup described in the previous section (see p.105), and change the USAF targets to the SiO2 wafer with metallic resistors at its surface. As described in chapter 4, by Joule effect, the metallic resistor heats the SiO2 medium at a modulated temperature $T(t)$ at frequency f_T. We would like to measure the variations of temperature in the SiO2 close to the resistor, along x, y and z axes. The corresponding setup is illustrated in Figure 5.18.

In this experiment, the projections measured by the camera correspond to the thermotransmittance signal, $\Delta\Gamma/\Gamma_0$. For SiO2 medium (see section 3.6), this signal is proportional to the average of the temperature along the optical path L_o, which is a function of the laminographic angle ξ. Therefore, we obtain the expression 5.5 for each measurement of thermotransmittance at the angles ξ and ψ_i. Thus, measuring the projections $\Delta\Gamma/\Gamma_0(u,v)_{\xi,\psi_i}$ on a complete 360° rotation should enable us to retrieve the 3D temperature field $\Delta T(x,y,z)$ weighted by the thermotransmittance coefficient.

$$\frac{\Delta\Gamma}{\Gamma_0}(u,v)_{\xi,\psi_i} = \kappa \underbrace{\frac{1}{L_o(\xi,\psi_i)} \int_0^{L_o(\xi,\psi_i)} \Delta T(x,y,z)\,\mathrm{d}z}_{\langle \Delta T(x,y) \rangle_{L_o(\xi,\psi_i)}} \tag{5.5}$$

For each rotation angle ψ_i, the camera records a film during two modulation periods (9000 frames) which takes up more than 1 Gb. So we choose having a large rotation angle step, $\Delta\psi = 10°$, to reduce the amount of data. In addition, with high laminographic angles, we observe some parasitic reflections of the metallic resistor on the back of the sample. This phenomenon disturbs the thermotransmittance measurement, as shown in Figure 5.19 for $\xi = 60°$. In order to reduce these measurement artifacts, we choose a small laminographic angle: $\xi = 30°$. Some corresponding projections are illustrated in Figure 5.19: we observe fewer parasitic reflections.

The next step is the measurement of the thermotransmittance amplitude from the recorded films for all the angles ψ_i.

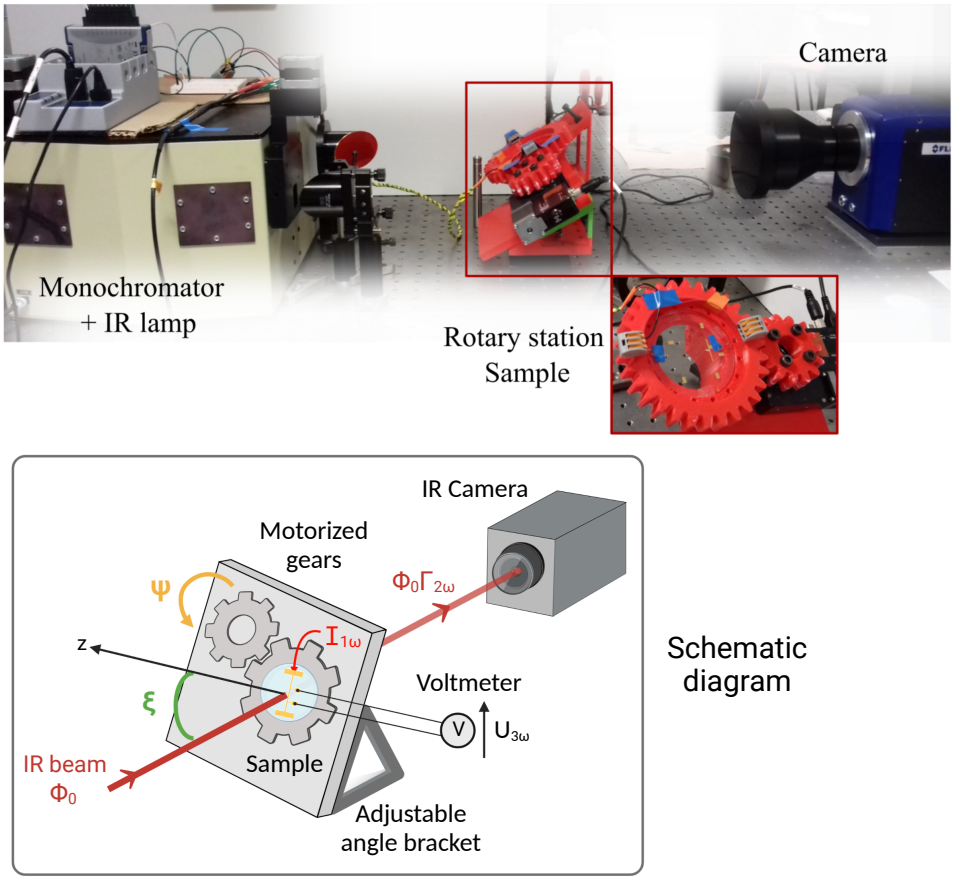

FIGURE 5.18 – Experimental setup for 3D thermotransmittance imaging using laminography.

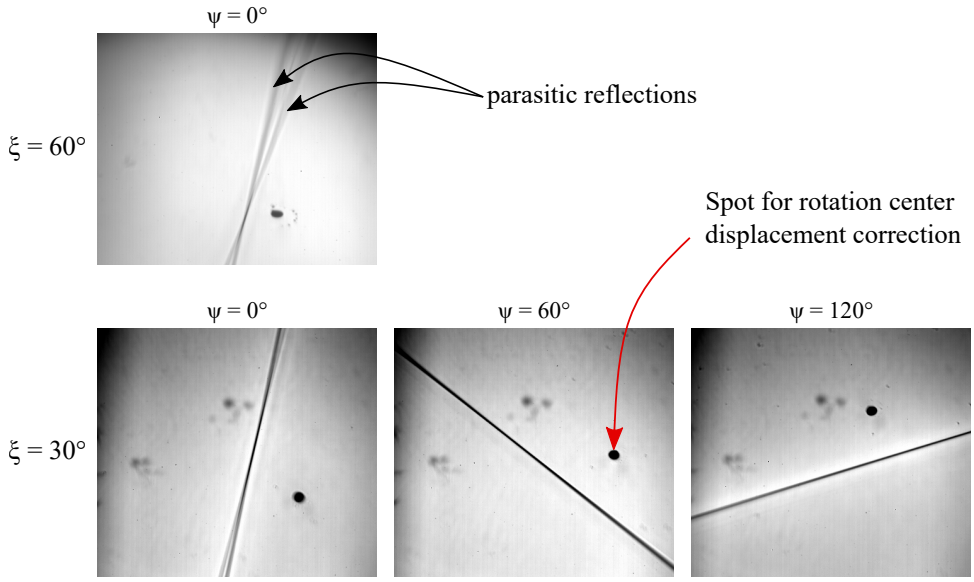

FIGURE 5.19 – Measured frames $\Phi_0\Gamma(t_0)$ at $t_0 = 0$ s, for several rotation angles ψ and laminographic angles $\xi = 30°$ and $\xi = 60°$. We observe parasitic reflections from the back of the sample for $\xi = 60°$. The black spot will help to correct the rotation center shift.

5.4.2 Reconstruction of the 3D thermotransmittance field

In this study, the spatial resolution of the measured projections is still 15 µm/pixel along u and v on the camera sensor. The temperature modulation frequency is set at 40 mHz, and the camera frame rate is 180 Hz, synchronized with the mechanical chopper to remove the proper emission of the sample.

5.4.2.1 Thermotransmittance amplitude measurement for each angle ψ_i

The transmitted signal measured by the camera is demodulated using the four-image method described in section 3.3. Figure 5.20 shows several maps of thermotransmittance amplitude, depending on the rotation angle ψ. The thermotransmittance signal is higher close to the resistor, which is consistent with the previous 2D study (see section 4.4.4). However, we observe duplication of the metallic resistor, depending on its orientation and position from the rotation center due to parasitic reflections as shown in Figure 5.19. Nevertheless, we are able to measure the averaged temperature field along the optical path L_o for each projection. Now, the challenge is to extract the temperature field $\Delta T(x, y, z)$ from these projections.

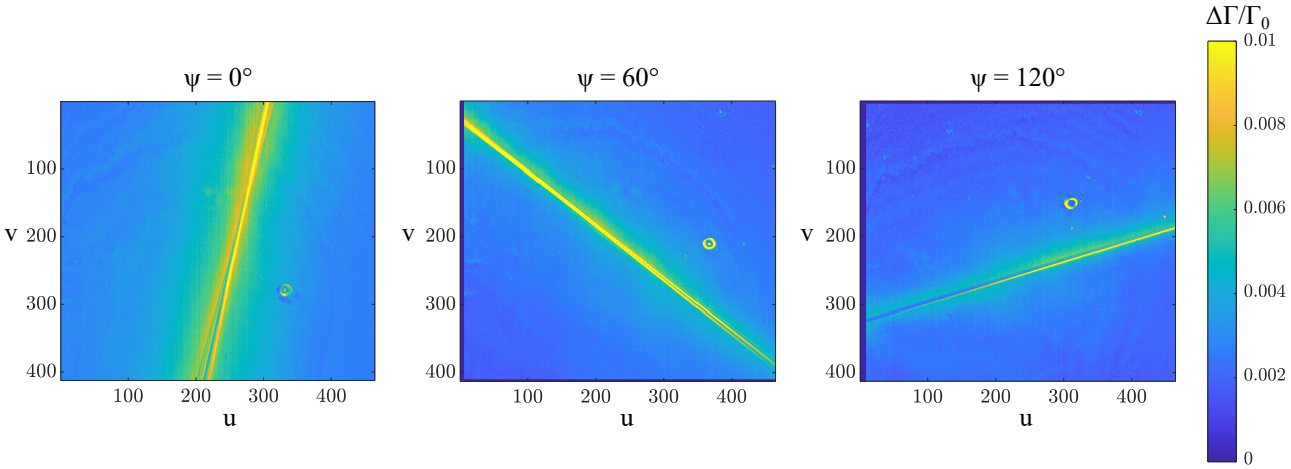

FIGURE 5.20 – Thermotransmittance amplitude maps measured for several projections with the laminographic angle $\xi = 30°$.

5.4.2.2 Correction of the rotation center displacement

Before reconstructing the 3D temperature field, we must correct the rotation center displacement, as detailed in section 5.3.2.1. As the resistor is larger than the image size, we cannot use it to calculate the rotation center shift along u and v, as one dimension is missing. Consequently, we put a spot close to the rotation center specially to perform this correction. The spot trajectory is calculated and compared to its ideal trajectory, and each projection is shifted by du and dv respectively along u and v axes. Figure 5.21 shows the sum of all the projections before and after the correction to validate the calculation.

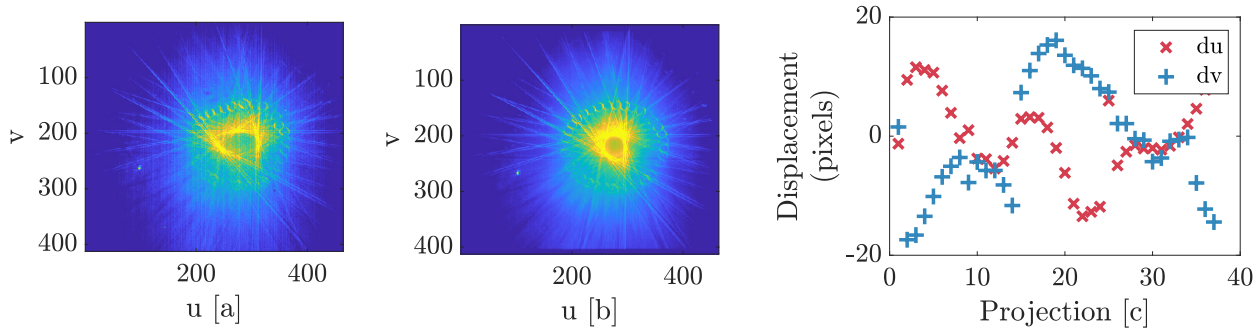

Figure 5.21 – (a) Sum of all the projections before (a) and after (b) correction. (c) Displacements du and dv for each projection.

5.4.2.3 Reconstructed 3D thermotransmittance field

Finally, the 3D thermotransmittance field is calculated using the projections presented in Figure 5.20 and the reconstruction algorithm. The result is shown in Figure 5.22 with some highlighted slices.

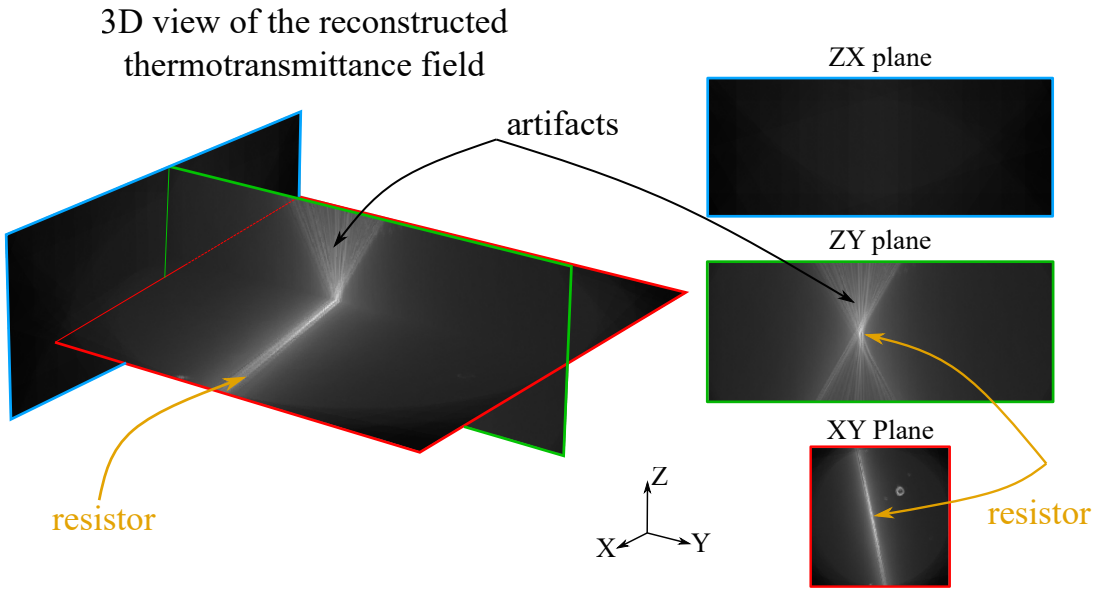

Figure 5.22 – 3D view of the reconstructed object with different highlighted slices. We observe the metallic resistor at the center, and a gradient around it. The plane ZY shows the artifacts coming from the resistor reconstruction in addition to a diffuse background from the temperature field.

We can begin with some comments about the reconstructed field:

- The reconstructed resistor is not sharp, which is due to non-perfect correction of the displacement of the rotation center (see section 5.4.2.2).
- The metallic resistor and corresponding reconstruction artifacts are predominant in the

reconstructed field. As a consequence, at this stage, we cannot differentiate from the resistor, the artifacts and the thermotransmittance field of interest.

- We observe a gradient around the resistor, corresponding to the thermotransmittance signal.

Consequently, the 3D thermotransmittance field is spoiled by the reconstructed resistor and its artifacts. An option is to filter out the resistor in the 3D reconstructed field, for instance using these techniques:

- A first option is filtering out the reconstructed field by deconvoluting the thermotransmittance field with the 3D PSF as mentioned in p.104. However, this operation requires using an arbitrary regularization coefficient and filter out the thermotransmittance field rather than eliminate resistor reconstruction artifacts.

- Another option consists in reconstructing the resistor alone and subtracting the resulting 3D field from the thermotransmittance one. Ideally, the measurement should be repeated without heating the sample to reconstruct the resistor alone. However, due to mechanical slack, we cannot reproduce exactly same measurements, and the shift correction is not perfect. As a consequence, the reconstructed resistor and its artifacts differ from one measurement to another. Therefore, we apply a threshold to the measured projections to remove the thermotransmittance signal and select only the resistor. According to the Figure 5.20, we choose $\sigma_{\text{thresh}} = 0.01$ since the thermotransmittance signal is weaker. The reconstructed resistor is presented in Figure 5.23 (b) with several XY planes, and Figure 5.23 (c) shows the difference between the total 3D field and the reconstructed resistor alone. The operation is not very successful: we observe lines in the corresponding 3D object that blur the thermotransmittance field. In addition, it is very challenging to determine if the resulting field (Fig. 5.23 (c)) is composed of residuals from the resistor subtraction, or thermotransmittance signal.

Finally, Figure 5.24 shows the signal of several voxels at different distances from the resistor, as a function of the slice in z direction (see colored crosses in (a)), after resistor removal. We observe a decrease for all the voxels, besides, their initial value at $z = 44$ is different and becomes smaller when moving away from the resistor. This behavior looks like expected temperature profile and is very encouraging, although we cannot be sure at this stage if it is the thermotransmittance signal or artifacts residuals from the resistor.

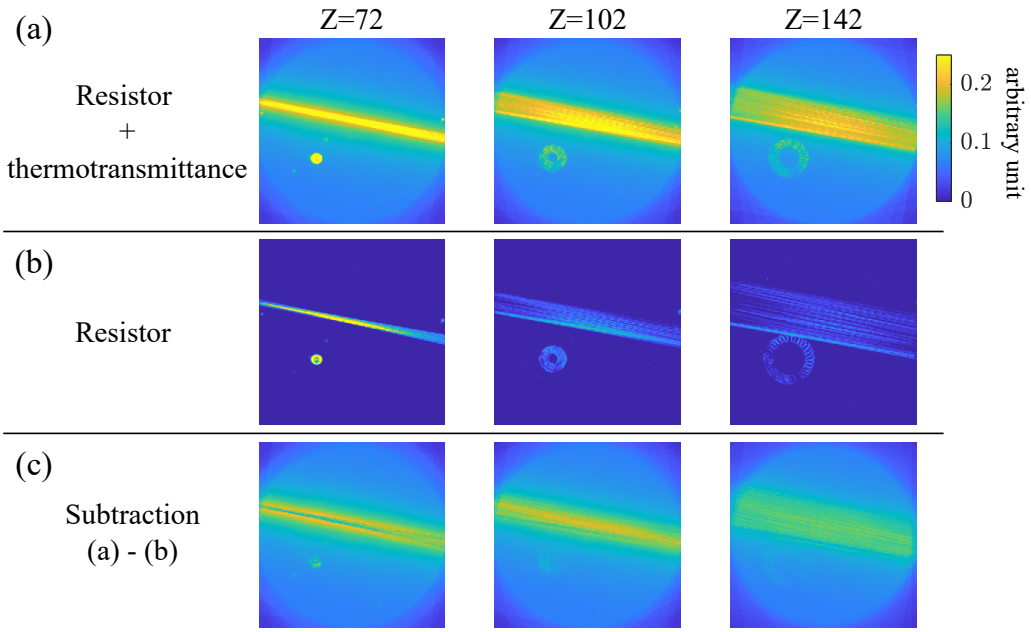

FIGURE 5.23 – XY planes of (a) the total reconstructed field containing both resistor and thermotransmittance signal, (b) the resistor alone, and (c) the subtraction between (a) and (b) to remove the resistor and its artifacts from the thermotransmittance field.

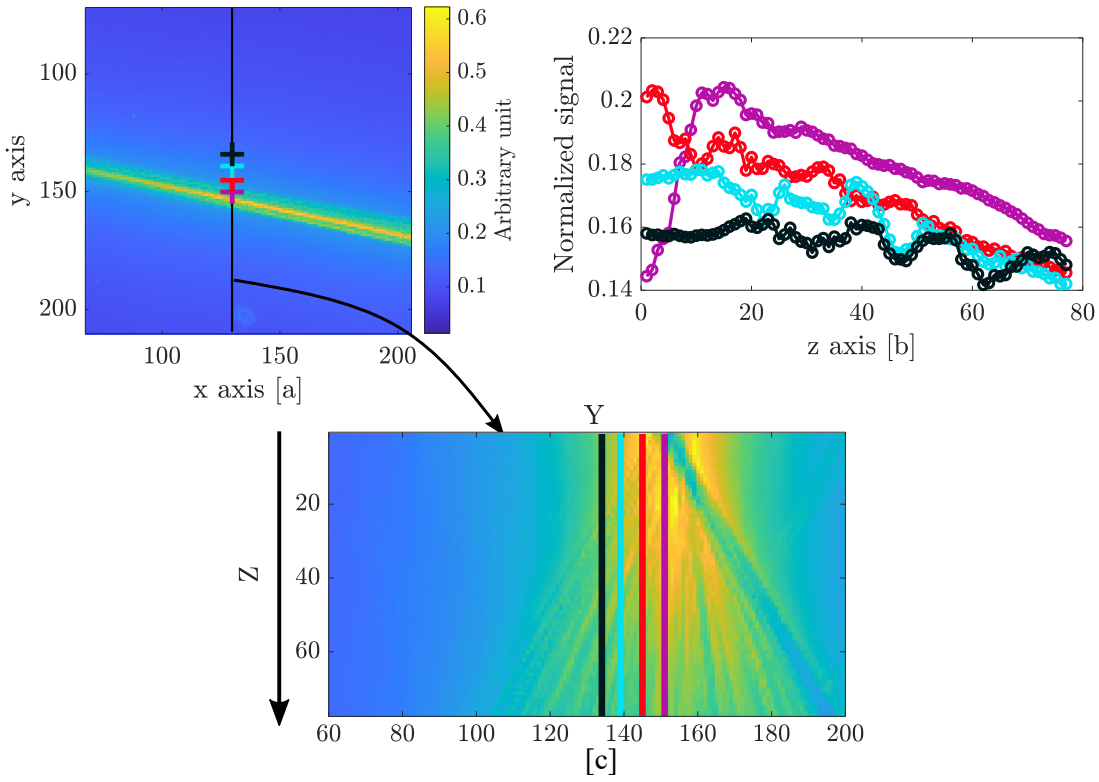

FIGURE 5.24 – (a) Sharp slice at the surface of the sample, $z = 44$. (b) Signal of some voxels represented with a colored cross as a function of z. (c) Plane ZY ($x = 131$) after resistor removal.

5.5 Conclusion about 3D temperature field measurement

In this chapter, we have developed an experimental setup to conduct laminography measurements in infrared semitransparent materials. We have validated the technique using calibrated sample, namely USAF targets. Then, we have combined laminography and thermotransmittance measurement to retrieve the 3D temperature field of the SiO2 sample presented in Chapter 4. At this stage of the work, we are able to measure quantitative 2D projections of the thermotransmittance signal, but the challenge remains in reconstructing the 3D field.

We have noticed that the reconstruction algorithm used in this exploratory work has limitations such as cross-shape artifacts or preserving the intensity ratio between the different elements. Therefore, in my opinion, the major challenge for future works is to improve the reconstruction algorithm to retrieve quantitative and artifact-free 3D temperature fields. Since we are able to model the heat transfer in simple geometries, it should be possible to constrain the reconstruction by a priori knowledge of the 3D field. In addition, it is essential to develop specific filters to weight the back-projection of the signal of a 2D pixel depending on the voxel position.

Although the reconstruction algorithm is not yet mature to perform quantitative 3D temperature measurements, these first results are encouraging to continue investigations in this direction.

General conclusion

Conclusion and future work

General conclusion

The main objective of this thesis was to develop and validate an experimental tomography setup to perform contactless measurements of 3D heat transfer in semitransparent media. This work is the first step towards the direct multi-physical characterization of complex energy systems, such as phase-change memories, microfluidic cells, micro-batteries, or biological reactions.

In the introduction, I identified the thermotransmittance phenomenon as a suitable technique for addressing this scientific challenge. However, as the method was not used in the team at the start of the thesis, the two following main objectives had to be fulfilled: first, develop and validate a quantitative thermotransmittance imaging technique on simple materials, then identify and implement a tomography setup suitable for thermotransmittance measurement.

To address these objectives, I have developed several experimental setups monitored with LabView, and implemented post-processing algorithms. Chapter 2 introduces the first setup, designed to validate the modulated thermotransmittance technique in a simple case with highly sensitive instruments, involving a mono-detector and a lock-in amplifier to improve the SNR. Enhancing the SNR is crucial using thermotransmittance as the temperature dependence of optical properties is usually weak ($\kappa \approx 10^{-4}$ K^{-1}).

Then, in Chapter 3, I adapted the single-point experimental setup to perform imaging thermotransmittance. The thermotransmittance coefficient of a Borofloat wafer was calibrated and its thermal properties was extracted. For that, I developed a thermal model and combined it with measurements using inverse methods. To go further with thermotransmittance measurement, I had to determine the signal origin: does it come from the sample surface or volume? I implemented a thermo-optical model based on Drude-Lorentz theory to answer this question. The analysis has shown that the absorbance of a material gives information on the temperature in its volume, whereas the reflectance provides the surface temperature. Consequently, I demonstrated that SiO2-based materials are good candidates for developing the 3D setup as the thermotransmittance signal mainly comes from its absorbance and, thus, its volume.

The next step was to upgrade the setup to perform 3D temperature field measurements. The first improvement was to downsize the sample and the heating system sizes to create a temperature gradient in the material thickness, as presented in Chapter 4. This change of scale meant developing a new heat transfer model and upgrading the experimental setup to perform microscale temperature measurements. In addition, I combined thermotransmittance measurement and 3ω technique to calibrate the measured signal and extract the material thermal diffusivity and thermotransmittance coefficient.

Finally, in Chapter 5, I developed a laminography experimental setup to perform 3D measurements of flat semitransparent materials in the mid-infrared. First, I implemented and

validated the 3D reconstruction algorithm and then presented the laminographic reconstruction on real calibrated objects. The final stage was combining microscale thermotransmittance imaging and laminography setup to perform 3D thermotransmittance field reconstruction.

As a result, I have validated the objectives of conducting quantitative thermotransmittance imaging measurements and developing a suitable tomography experimental setup. Nevertheless, although I have successfully measured the 2D projections of the thermotransmittance field of the sample under several rotation and tilt angles, the reconstruction algorithm used in this work generated artifacts in the 3D reconstructed field. Although these artifacts are not particularly disturbing for retrieving the shape of well-defined objects, such as USAF test patterns, they are a real issue when superimposed on a diffuse field such as thermotransmittance. This leads us to discuss improvements to be considered in future works on the experimental setup and post-processing of the data.

Future work

I start with the improvements to be made to the current experimental setup and then discuss the possibilities offered by thermotransmittance. First, we must improve the reconstruction algorithm regarding the tomography technique to remove or filter out the cross-shape artifacts. As mentioned in Chapter 5, several options have to be investigated: constraining the reconstruction using Bayesian algorithm, for instance, filtering out cross-shape artifacts with the 3D PSF of the reconstruction, or performing several measurements with different laminographic angles and comparing the results. The 3D temperature field we intend to measure is diffuse without sharp edges. Consequently, we must be careful not to cut off the spatial low-frequency components.

In addition, the detection threshold of the current setup is about $\Delta T \approx 1$ K for the Borofloat. However, this value depends on the thermotransmittance coefficient and is a function of the material and the illumination wavelength, as shown in Chapter 3. In comparison, the detection threshold of the silicon in the current imaging setup is approximately 7 K. In addition, although the current IR source is stabilized, we noticed in Chapter 3 that the measurement noise from IR beam fluctuations is twice as high as that without the IR beam. As a result, to perform thermotransmittance measurements in materials whose thermotransmittance coefficient is weak ($\kappa < 10^{-4}$ K^{-1}), we must enhance the detection threshold, using a more powerful (about 1 W/m^2 in the current setup) and well-stabilized source, and a sensitive detector.

Another key point is the thermal excitation frequencies currently in the range [5 - 50] mHz. In this work, we had to find a compromise between working frequency and minimum temperature variations to measure the thermotransmittance signal. This item is therefore linked to the detection threshold mentioned above. To work at higher frequencies, potentially with less sample heating, we need to improve the detection threshold.

In this work, we used thermotransmittance to measure temperature variations and thermal properties of semitransparent media. In addition, I believe that this technique could be used to characterize other properties of these media. To fully develop the characterization of semitransparent media using thermotransmittance, we must complete a database of the thermotransmittance coefficient as a function of the wavelength and thickness of materials. This knowledge would be valuable to discriminate semitransparent multi-layered samples and analyze the thermotransmittance signal of non-homogeneous media. In addition, the knowledge of the contributions of reflectance and absorbance in the thermotransmittance signal would allow us to have simultaneous information on interfaces and the volume of the material. Currently, we do not discriminate between these two contributions.

Being able to discriminate between the contributions of absorbance and reflectance, we would extract the thermal resistances between layers and temperature variations within the volume of the sample. Scanning the illumination wavelength will also allow us to distinguish the thermotransmittance signal of the different layers if their thermotransmittance coefficient is not constant over the spectral range under study.

In addition, in all the experiments we performed in this work, we also measured the proper emission of the sample. It would be very interesting to combine thermotransmittance measurement with proper emission to measure the emittance of the material, for instance. Furthermore, the proper emission signal is significantly less noisy than the thermotransmittance. By using thermotransmittance to calibrate the proper emission signal, we would enhance the SNR of our measurement and detect smaller temperature variations. Therefore, combining these two measurements is a key point for future work.

Another interesting phenomenon not mentioned in this study is that the transmitted signal through a semitransparent media is also a function of the concentration. Consequently, we should combine heat and mass transfer measurements using the signal transmitted through the sample [61]. This approach would perfectly suit studying microfluidic cells or diverse chemical reactions.

Finally, future works must determine the limit of application of thermotransmittance, especially regarding scattering: at the surfaces, performing BRDF measurements, for instance, and in the volume of the material. For this purpose, I suggest working with a medium doped with particles of different sizes and concentrations to determine the impact of scattering on the thermotransmittance signal.

In conclusion, the study of thermotransmittance phenomena is very promising in characterizing semitransparent media, such as determining their thermal properties (conductivity, diffusivity, contact resistance) or conducting quantitative 3D heat and mass transfer measurements.

Scientific contributions

Publications

- C. Bourgès, S. Chevalier, J. Maire, A. Sommier, C. Pradère, S. Dilhaire. *Infrared thermotransmittance-based temperature field measurements in semitransparent media*, Rev. Sci. Instrum. 1 March 2023; 94 (3): 034905
- C. Bourgès, S. Chevalier, J. Maire, A. Sommier, C. Pradère, S. Dilhaire. *Mid-infrared spectroscopic thermotransmittance measurements of dielectric materials*, (submitted, September 2023).

Conferences with peer-reviewed communications

- SFT 2023: *Microscopie infrarouge par thermotransmittance modulée : mesure de champs de température dans des milieux semi-transparents.* C. Bourgès, S. Chevalier, J. Maire, C. Pradère, S. Dilhaire. **1er accessit prix Biot et Fourier**
- QIRT 2022: *Contactless temperature field measurements in infrared semi-transparent materials using thermotransmittance imaging.* C. Bourgès, S. Chevalier, A. Sommier, J. Maire, C. Pradère, S. Dilhaire.
- SFT 2021: *Mesure transitoire et sans contact de champ de température par thermotransmittance dans des milieux semi-transparents à l'infrarouge.* C. Bourgès, S. Chevalier, A. Sommier, C. Pradère.

Other contributions

- METTI 8 2023 (tutorials): *Thermal imaging in semi-transparent media.* S. Chevalier, C. Bourgès, J. Maire, A. Sommier, C. Pradère, S. Dilhaire.
- Communication SFT 2022 (poster): *Etude de la thermotransmittance dans des milieux semi-transparents à l'infrarouge pour la mesure de température.* C. Bourgès, S. Chevalier, J. Maire, C. Pradère, S. Dilhaire.

Appendices

Appendix A

General thermotransmittance expression

At the first order, the temperature variations of the reflectance and attenuation coefficient are:

$$R(T) = R_0(1 + \kappa_R \Delta T) \tag{A.1}$$
$$\alpha(T) = \alpha_0(1 + \kappa_\alpha \Delta T) \tag{A.2}$$

As a result, in the general case with temperature gradient along the thickness of the material, the transmittance as a function of temperature is expressed in equation A.3. T_1 is the temperature of the first surface, and T_2 the temperature of the second surface.

$$\Gamma(T) = [1 - R(T_1)][1 - R(T_2)]e^{-\alpha_0 \int_0^{L_z} [1+\kappa_\alpha \Delta T(z)]dz} \tag{A.3}$$

$$\Gamma(T) - \Gamma_0 = \left[[1 - R(T_1)][1 - R(T_2)]e^{-\alpha_0 \kappa_\alpha \int_0^{L_z} \Delta T(z)dz} - [1 - R_0]^2\right] e^{-\alpha_0 L_z} \tag{A.4}$$

Ratio $\Delta\Gamma/\Gamma_0$:

$$\frac{\Delta\Gamma(T)}{\Gamma_0} = \frac{[1 - R(T_1)][1 - R(T_2)]e^{-\alpha_0 \kappa_\alpha \int_0^{L_z} \Delta T(z)dz}}{[1 - R_0]^2} - 1 \tag{A.5}$$

With: $R(T_1) = R_0[1 + \kappa_R(T_1 - T_0)]$ and $R(T_2) = R_0[1 + \kappa_R(T_2 - T_0)]$, and $\Delta T_i = T_i - T_0$.

Linearization of the exponential function:

$$\frac{\Delta\Gamma(T)}{\Gamma_0} \approx \frac{[1 - R(T_1)][1 - R(T_2)]}{[1 - R_0]^2} \left[1 - \alpha_0 \kappa_\alpha \int_0^{L_z} \Delta T(z)dz\right] - 1 \tag{A.6}$$

With:

$$\frac{[1 - R(T_1)][1 - R(T_2)]}{[1 - R_0]^2} = \frac{[1 - R_0]^2 - R_0\kappa_R[(1 - R_0)\Delta T_1 + (1 - R_0)\Delta T_2 + R_0\kappa_R \Delta T_1 \Delta T_2]}{[1 - R_0]^2} \tag{A.7}$$

We obtain the general expression:

$$\begin{aligned}\frac{\Delta\Gamma(T)}{\Gamma_0} \approx & -\frac{R_0\kappa_R}{1-R_0}\left[\Delta T_1+\Delta T_2+\frac{R_0\kappa_R}{1-R_0}\Delta T_1\Delta T_2\right] \\ & -\alpha_0\kappa_\alpha\left[1+\frac{R_0\kappa_R}{1-R_0}\left(\Delta T_1+\Delta T_2+\frac{R_0\kappa_R}{1-R_0}\Delta T_1\Delta T_2\right)\right]\int_0^{L_z}\Delta T(z)dz\end{aligned} \tag{A.8}$$

Finally, at the first order, the thermotransmittance expression is:

$$\frac{\Delta\Gamma(T)}{\Gamma_0} \approx -\underbrace{\frac{R_0\kappa_R}{1-R_0}\left[\Delta T_1+\Delta T_2\right]}_{\text{reflectance}}-\underbrace{\alpha_0\kappa_\alpha\int_0^{L_z}\Delta T(z)dz}_{\text{absorbance}} \tag{A.9}$$

Appendix B

Drude Lorentz model

First, let us introduce the complex refractive index of a material $\tilde{n}(\lambda) = n'(\lambda) + in''(\lambda)$, with n' and n'' respectively its real and imaginary parts. It is a dimensionless quantity that determines the capacity of a material to interact with light. The refractive index is a function of the wavelength λ [106, 148]. As a result, the optical properties of a material, reflectance, transmittance and absorbance, are functions of the refractive index.

The reflection coefficient at an interface air / material [62] is given in equation B.1. The refractive index of the air is $\tilde{n}_{\text{air}} \approx 1$ [149]. The material refractive index is simply noted $\tilde{n}(\lambda) = n'(\lambda) + in''(\lambda)$.

$$R(\lambda) = \frac{(n'(\lambda) - 1)^2 + n''(\lambda)^2}{(n'(\lambda) + 1)^2 + n''(\lambda)^2} \tag{B.1}$$

The attenuation coefficient only depends on the imaginary part of the refractive index of the material, n'' [62]. c is the speed of light, and $\omega = 2\pi f/c$.

$$\alpha(\lambda) = \frac{4\pi n''(\lambda)}{\lambda} = \frac{2\omega n''(\lambda)}{c} \tag{B.2}$$

The refractive index is calculated from the relative permittivity of the medium $\tilde{\varepsilon_r} = \varepsilon_r' + i\varepsilon_r''$ with the following equations [72, 75]:

$$\tilde{n}(\lambda)^2 = \tilde{\varepsilon_r}(\lambda) \tag{B.3}$$

$$n'(\lambda) = \sqrt{\frac{\sqrt{\varepsilon_r'(\lambda)^2 + \varepsilon_r''(\lambda)^2} + \varepsilon_r'(\lambda)}{2}} \tag{B.4}$$

$$n''(\lambda) = \sqrt{\frac{\sqrt{\varepsilon_r'(\lambda)^2 + \varepsilon_r''(\lambda)^2} - \varepsilon_r'(\lambda)}{2}} \tag{B.5}$$

In this work, we assume that the dielectric properties of materials under study are well-described by the Drude-Lorentz model. The electrons are considered as springs oscillating around their equilibrium position, at a resonant frequency ω_0. The oscillator is characterized by its plasma frequency ω_p and a damping factor γ.

$$\tilde{\varepsilon_r}(\omega) = \varepsilon_\infty + \frac{\omega_p^2}{\omega_0^2 - \omega^2 + i\omega\gamma} \tag{B.6}$$

The Drude-Lorentz model describes the total relative permittivity of the material as a sum of oscillators. The general expression is:

$$\tilde{\varepsilon_r}(\omega) = \varepsilon_\infty + \sum_n \frac{\omega_{p,n}^2}{\omega_{0,n}^2 - \omega^2 + i\omega\gamma_n} \tag{B.7}$$

In the relative permittivity expression, we identify three temperature dependent parameters: ω_0, ω_p, and γ. The resonant frequency shifts with temperature, ω_p is related to the density of electron which is temperature dependent [150], and γ depends on the diverse collisions in the material (electrons, phonons) [151, 152]. Several models were developed to describe the temperature dependencies of these parameters [153, 69, 154], depending on materials. To simplify the study, we consider first-order functions of temperature:

$$\omega_0(T) = \omega_0(T_0) \times (1 + \alpha_{\omega_0}\Delta T) \tag{B.8}$$
$$\omega_p(T) = \omega_p(T_0) \times (1 + \alpha_{\omega_p}\Delta T) \tag{B.9}$$
$$\gamma(T) = \gamma(T_0) \times (1 + \alpha_\gamma \Delta T) \tag{B.10}$$

Finally, the relative permittivity as a function of temperature is:

$$\tilde{\varepsilon_r}(\omega, T) = \varepsilon_\infty + \sum_n \frac{\omega_{p,n}(T)^2}{\omega_{0,n}(T)^2 - \omega^2 + i\omega\gamma_n(T)} \tag{B.11}$$

Appendix C

Comparison of heat transfer models in the SiO2

- Model 1D: semi-infinite along the x axis, no convective loss.
- Models 2D: the model without convective loss is presented in section 4.2. In addition, we calculate the case with convective losses at the surfaces $z = 0$ and $z = L_z$.

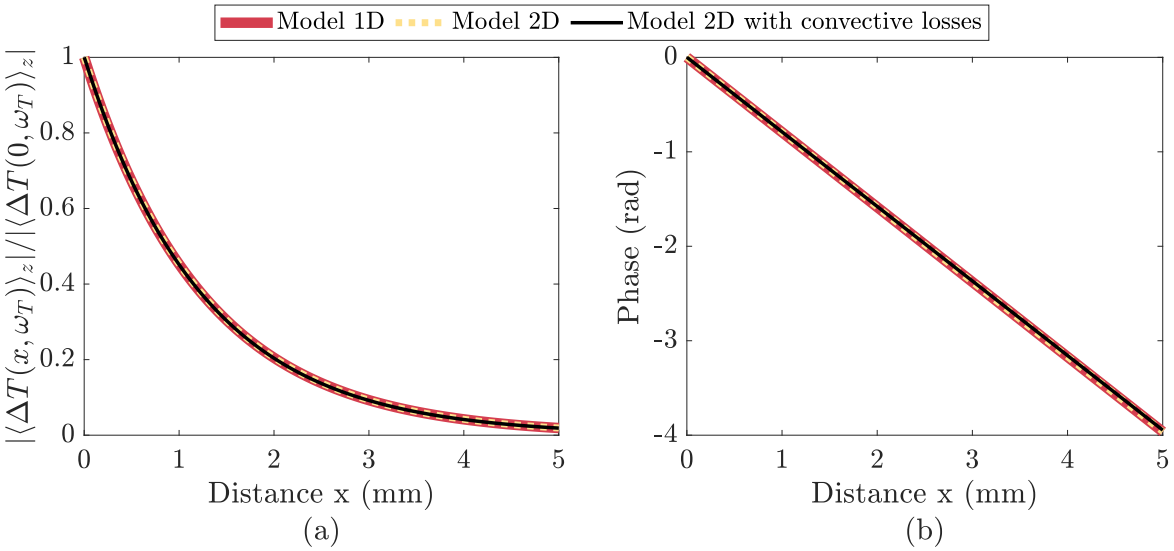

Figure C.1 – Normalized amplitude (a) and phase (b) of $\langle\Delta T\rangle_z$ as a function of the distance for the 1D model (red line), and 2D models with (black line) and without(yellow dotted line) convective losses.

Whether for the amplitude or the spatial phase shift of the field $\langle\Delta T\rangle_z(x,\omega_T)$, figure C.1 shows that the profiles from the 1D and 2D models are perfectly superimposed. We can draw several conclusions from this result:

- Convective losses are negligible regarding the temperature variations at the frequency f_T. The calculations were performed for $h \in [5-500]$ W/m^2/K without any change. This means we have one less unknown parameter to consider. However, convective losses allow the system to reach its established regime.
- We can use either the 1D model or the integrated 2D model, provided that they are normalized to be compared. As a result, we use the 1D model for extracting the thermal diffusivity as presented in section 4.4.3.
- However, the 2D model is necessary to estimate the average temperature in the thickness knowing the temperature of the resistor $|\Delta T(x=0,z=0,\omega_T)|$. The 1D model does not provide this information.

Appendix D

Properties of the resistors at the surface of the SiO2 wafer

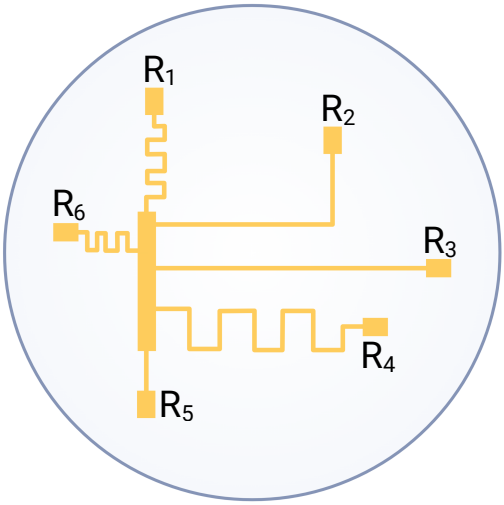

Figure D.1 – Illustration of the resistors at the surface of the SiO2 wafer.

Resistor number	Resistance, R_Ω (Ω)	Total length (mm)
R_{n1}	75	18
R_{n2}	195 / 190 (before / after repairs)	45
R_{n3}	174 / 164 (before / after repairs)	40
R_{n4}	240	55
R_{n5}	Cut	10
R_{n6}	51	13

Table D.1 – Properties of the resistors deposited on the surface of the SiO2 wafer.

Note that during the experiments, some resistors burned. They have been repaired, but their resistance has slightly changed, as it is shown in the Table D.1.

Appendix E

Depth of field of the microscope objective

Figure E.1 shows the impact of the microscope objective defocus on the contrast of the USAF target. The studied patterns are (2,2) and (2,6) with respectively bands of width 111.36 µm and 70.15 µm. Considering the dimensions of studied objects in this thesis, we will consider that the depth of field of the objective is ±5 mm around the focus position. Nevertheless, keep in mind that the further from the focus, the more blurred the pattern will be, even if we still discern it.

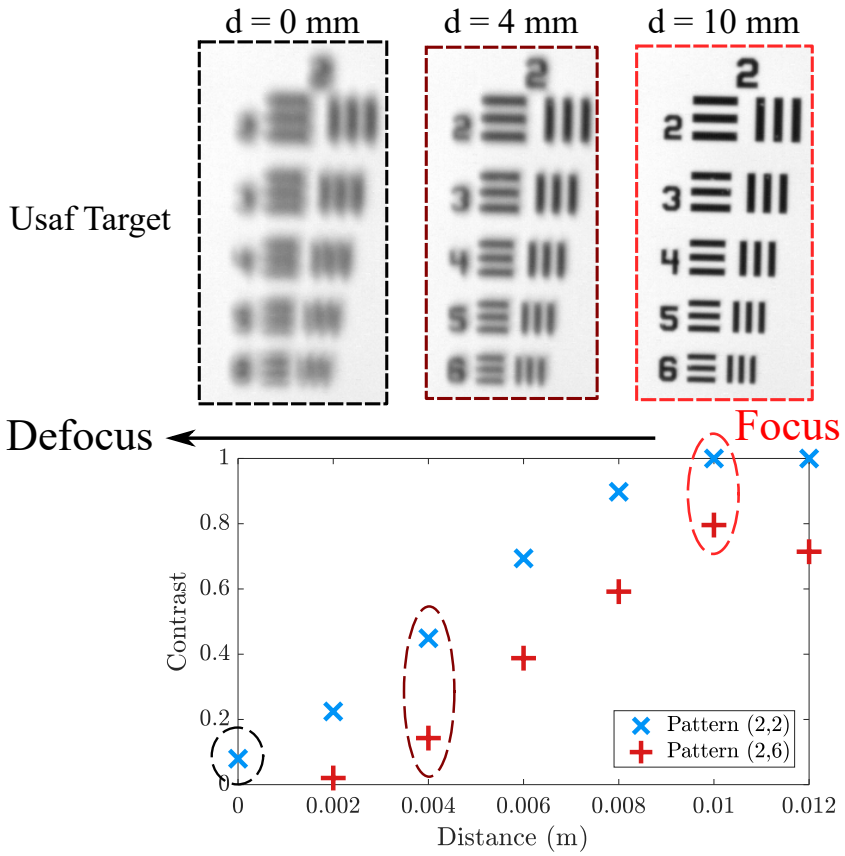

Figure E.1 – Contrast of patterns (2,2) and (2,6) of the USAF target, depending on the microscope objective defocus.

Bibliography

[1] G. M. Carlomagno and G. Cardone, *Infrared thermography for convective heat transfer measurements*, vol. 49. 2010. (Cited on page 2.)

[2] L. Ibos, M. Marchetti, A. Boudenne, S. Datcu, Y. Candau, and J. Livet, "Infrared emissivity measurement device: Principle and applications," *Measurement Science and Technology*, vol. 17, no. 11, pp. 2950–2956, 2006. (Cited on page 2.)

[3] R. Usamentiaga, P. Venegas, J. Guerediaga, L. Vega, J. Molleda, and F. G. Bulnes, "Infrared thermography for temperature measurement and non-destructive testing," *Sensors (Switzerland)*, vol. 14, no. 7, pp. 12305–12348, 2014. (Cited on page 2.)

[4] A. Kylili, P. A. Fokaides, P. Christou, and S. A. Kalogirou, "Infrared thermography (IRT) applications for building diagnostics: A review," *Applied Energy*, vol. 134, pp. 531–549, Dec. 2014. (Cited on page 2.)

[5] C. Ibarra-Castanedo, J. M. Piau, S. Guilbert, N. Avdelidis, M. Genest, A. Bendada, and X. P. Maldague, "Comparative study of active thermography techniques for the nondestructive evaluation of honeycomb structures," *Research in Nondestructive Evaluation*, vol. 20, no. 1, pp. 1–31, 2009. (Cited on page 2.)

[6] T. Li, D. P. Almond, and D. S. Rees, "Crack imaging by scanning pulsed laser spot thermography," *NDT and E International*, vol. 44, pp. 216–225, Mar. 2011. (Cited on page 2.)

[7] F. Cernuschi, A. Russo, L. Lorenzoni, and A. Figari, "In-plane thermal diffusivity evaluation by infrared thermography," *Review of Scientific Instruments*, vol. 72, no. 10, pp. 3988–3995, 2001. (Cited on page 2.)

[8] A. Bedoya, J. González, J. Rodríguez-Aseguinolaza, A. Mendioroz, A. Sommier, J. Batsale, C. Pradere, and A. Salazar, "Measurement of in-plane thermal diffusivity of solids moving at constant velocity using laser spot infrared thermography," *Measurement*, vol. 134, pp. 519–526, Feb. 2019. (Cited on page 2.)

[9] C. Zhu, M. J. Hobbs, and J. R. Willmott, "An accurate instrument for emissivity measurements by direct and indirect methods," *Measurement Science and Technology*, vol. 31, p. 044007, Jan. 2020. (Cited on page 2.)

[10] C. Chassain, A. Kusiak, K. Krause, M. Garcia, and J.-L. Battaglia, "Bayesian estimation of thermal properties using periodically pulsed photothermal radiometry: A focus on interfacial thermal resistances between layers," *physica status solidi (RRL) – Rapid Research Letters*, vol. 17, p. 2200328, Nov. 2022. (Cited on pages 2 and 54.)

[11] J.-C. Krapez, L. Spagnolo, M. Frieß, H.-P. Maier, and G. Neuer, "Measurement of in-plane diffusivity in non-homogeneous slabs by applying flash thermography," *International Journal of Thermal Sciences*, vol. 43, pp. 967–977, Oct. 2004. (Cited on page 2.)

[12] A. Sommier, J. Malvaut, V. Delos, M. Romano, T. Bazire, J. Batsale, A. Salazar, A. Mendioroz, A. Oleaga, and C. Pradere, "Coupling pulsed flying spot technique with robot automation for industrial thermal characterization of complex shape composite materials," *NDT and E International*, vol. 102, pp. 175–179, Mar. 2019. (Cited on page 2.)

[13] A. Kusiak, J. Martan, J.-L. Battaglia, and R. Daniel, "Using pulsed and modulated photothermal radiometry to measure the thermal conductivity of thin films," *Thermochimica Acta*, vol. 556, pp. 1–5, Mar. 2013. (Cited on page 2.)

[14] O. Breitenstein, M. Langenkamp, F. Altmann, D. Katzer, A. Lindner, and H. Eggers, "Microscopic lock-in thermography investigation of leakage sites in integrated circuits," *Review of Scientific Instruments*, vol. 71, no. 11, pp. 4155–4160, 2000. (Cited on page 2.)

[15] C. Chassain, A. Kusiak, C. Gaborieau, Y. Anguy, N.-P. Tran, C. Sabbione, M.-C. Cyrille, C. Wiemer, A. Lamperti, and J.-L. Battaglia, "Thermal characterization of ge-rich GST/TiN thin multilayers for phase change memories," *Journal of Applied Physics*, vol. 133, June 2023. (Cited on page 3.)

[16] C. Meola, S. Boccardi, and G. M. Carlomagno, "Measurements of very small temperature variations with LWIR QWIP infrared camera," *Infrared Physics and Technology*, vol. 72, pp. 195–203, 2015. (Cited on page 3.)

[17] T. Lafargue-Tallet, R. Vaucelle, C. Caliot, A. Aouali, E. Abisset-Chavanne, A. Sommier, R. Peiffer, and C. Pradere, "Active thermo-reflectometry for absolute temperature measurement by infrared thermography on specular materials," *Scientific Reports*, vol. 12, no. 1, pp. 1–19, 2022. (Cited on page 3.)

[18] G. Machin, R. Simpson, and M. Broussely, "Calibration and validation of thermal imagers," *Quantitative InfraRed Thermography Journal*, vol. 6, pp. 133–147, Dec. 2009. (Cited on page 3.)

[19] O. Burggraaff, N. Schmidt, J. Zamorano, K. Pauly, S. Pascual, C. Tapia, E. Spyrakos, and F. Snik, "Standardized spectral and radiometric calibration of consumer cameras," *Optics Express*, vol. 27, p. 19075, June 2019. (Cited on page 3.)

[20] N. Playà-Montmany and G. J. Tattersall, "Spot size, distance and emissivity errors in field applications of infrared thermography," *Methods in Ecology and Evolution*, vol. 12, pp. 828–840, Feb. 2021. (Cited on page 3.)

[21] R. Usamentiaga, D. F. Garcia, J. Molleda, F. G. Bulnes, and J. M. Perez, "Temperature measurement using the wedge method: Comparison and application to emissivity estimation and compensation," *IEEE Transactions on Instrumentation and Measurement*, vol. 60, pp. 1768–1778, May 2011. (Cited on page 3.)

[22] D. G. Cahill, "Analysis of heat flow in layered structures for time-domain thermoreflectance," *Review of Scientific Instruments*, vol. 75, pp. 5119–5122, Dec. 2004. (Cited on page 3.)

[23] W. J. Tropf and M. E. Thomas, "Infrared refractive index and thermo-optic coefficient measurement at apl," *Johns Hopkins Apl Technical Digest*, vol. 19, pp. 293–298, 1998. (Cited on page 3.)

[24] G. Tessier, S. Holé, and D. Fournier, "Quantitative thermal imaging by synchronous thermoreflectance with optimized illumination wavelengths," *Applied Physics Letters*, vol. 78, pp. 2267–2269, Apr. 2001. (Cited on page 3.)

[25] D. G. Cahill, P. V. Braun, G. Chen, D. R. Clarke, S. Fan, K. E. Goodson, P. Keblinski, W. P. King, G. D. Mahan, A. Majumdar, H. J. Maris, S. R. Phillpot, E. Pop, and L. Shi, "Nanoscale thermal transport. II. 2003–2012," *Applied Physics Reviews*, vol. 1, p. 011305, Mar. 2014. (Cited on page 3.)

[26] G. Pernot, M. Stoffel, I. Savic, F. Pezzoli, P. Chen, G. Savelli, A. Jacquot, J. Schumann, U. Denker, I. Mönch, C. Deneke, O. G. Schmidt, J. M. Rampnoux, S. Wang, M. Plissonnier, A. Rastelli, S. Dilhaire, and N. Mingo, "Precise control of thermal conductivity at the nanoscale through individual phonon-scattering barriers," *Nature Materials*, vol. 9, pp. 491–495, May 2010. (Cited on page 3.)

[27] J.-L. Battaglia, A. Kusiak, C. Rossignol, and N. Chigarev, "Thermal diffusivity and effusivity of thin layers using time-domain thermoreflectance," *Physical Review B*, vol. 76, Nov. 2007. (Cited on page 3.)

[28] P. Jiang, X. Qian, and R. Yang, "Tutorial: Time-domain thermoreflectance (TDTR) for thermal property characterization of bulk and thin film materials," *Journal of Applied Physics*, vol. 124, p. 161103, Oct. 2018. (Cited on page 3.)

[29] A. J. Schmidt, R. Cheaito, and M. Chiesa, "A frequency-domain thermoreflectance method for the characterization of thermal properties," *Review of Scientific Instruments*, vol. 80, p. 094901, Sept. 2009. (Cited on page 3.)

[30] K. T. Regner, D. P. Sellan, Z. Su, C. H. Amon, A. J. McGaughey, and J. A. Malen, "Broadband phonon mean free path contributions to thermal conductivity measured using frequency domain thermoreflectance," *Nature Communications*, vol. 4, Mar. 2013. (Cited on page 3.)

[31] J. Christofferson and A. Shakouri, "Thermoreflectance based thermal microscope," *Review of Scientific Instruments*, vol. 76, p. 024903, Feb. 2005. (Cited on page 3.)

[32] M. Farzaneh, K. Maize, D. Lüerßen, J. A. Summers, P. M. Mayer, P. E. Raad, K. P. Pipe, A. Shakouri, R. J. Ram, and J. A. Hudgings, "CCD-based thermoreflectance microscopy: principles and applications," *Journal of Physics D: Applied Physics*, vol. 42, p. 143001, June 2009. (Cited on page 3.)

[33] S. Sandell, E. Chávez-Ángel, A. E. Sachat, J. He, C. M. S. Torres, and J. Maire, "Thermoreflectance techniques and raman thermometry for thermal property characterization of nanostructures," *Journal of Applied Physics*, vol. 128, p. 131101, Oct. 2020. (Cited on pages 3 and 5.)

[34] S. Dilhaire, S. Grauby, and W. Claeys, "Calibration procedure for temperature measurements by thermoreflectance under high magnification conditions," *Applied Physics Letters*, vol. 84, no. 5, pp. 822–824, 2004. (Cited on page 3.)

[35] D. U. Kim, K. S. Park, C. B. Jeong, G. H. Kim, and K. S. Chang, "Quantitative temperature measurement of multi-layered semiconductor devices using spectroscopic thermoreflectance microscopy," *Optics Express*, vol. 24, no. 13, p. 13906, 2016. (Cited on page 3.)

[36] J. Gieseler, A. Adibekyan, C. Monte, and J. Hollandt, "Apparent emissivity measurement of semitransparent materials part 2: Theoretical concept," *Journal of Quantitative Spectroscopy and Radiative Transfer*, vol. 258, p. 107317, Jan. 2021. (Cited on page 5.)

[37] S. Jeon, S.-N. Park, Y. S. Yoo, J. Hwang, C.-W. Park, and G. W. Lee, "Simultaneous measurement of emittance, transmittance, and reflectance of semitransparent materials at elevated temperature," *Optics Letters*, vol. 35, p. 4015, Nov. 2010. (Cited on page 5.)

[38] J. Gieseler, A. Adibekyan, C. Monte, and J. Hollandt, "Apparent emissivity measurement of semitransparent materials part 1: Experimental realization," *Journal of Quantitative Spectroscopy and Radiative Transfer*, vol. 257, p. 107316, 2020. (Cited on page 5.)

[39] O. Rozenbaum, D. D. S. Meneses, Y. Auger, S. Chermanne, and P. Echegut, "A spectroscopic method to measure the spectral emissivity of semi-transparent materials up to high temperature," *Review of Scientific Instruments*, vol. 70, pp. 4020–4025, Oct. 1999. (Cited on page 5.)

[40] D. D. S. Meneses, P. Melin, L. del Campo, L. Cosson, and P. Echegut, "Apparatus for measuring the emittance of materials from far infrared to visible wavelengths in extreme conditions of temperature," *Infrared Physics andTechnology*, vol. 69, pp. 96–101, Mar. 2015. (Cited on page 5.)

[41] A. Adibekyan, E. Kononogova, C. Monte, and J. Hollandt, "Review of PTB measurements on emissivity, reflectivity and transmissivity of semitransparent fiber-reinforced plastic composites," *International Journal of Thermophysics*, vol. 40, Mar. 2019. (Cited on page 5.)

[42] A. Philipp, N. W. Pech-May, B. A. F. Kopera, A. M. Lechner, S. Rosenfeldt, and M. Retsch, "Direct measurement of the in-plane thermal diffusivity of semitransparent thin films by lock-in thermography: An extension of the slopes method," *Analytical Chemistry*, vol. 91, pp. 8476–8483, May 2019. (Cited on page 5.)

[43] E. Smith and G. Dent, *Modern Raman spectroscopy: a practical approach*. John Wiley & Sons, 2019. (Cited on page 5.)

[44] M. Kuball and J. W. Pomeroy, "A review of raman thermography for electronic and opto-electronic device measurement with submicron spatial and nanosecond temporal resolution," *IEEE Transactions on Device and Materials Reliability*, vol. 16, no. 4, pp. 667–684, 2016. (Cited on page 5.)

[45] D. A. Long and D. Long, *The Raman effect: a unified treatment of the theory of Raman scattering by molecules*, vol. 8. Wiley Chichester, 2002. (Cited on page 5.)

[46] W. H. Weber and R. Merlin, *Raman scattering in materials science*, vol. 42. Springer Science and Business Media, 2000. (Cited on page 5.)

[47] T. Basiev, A. Sobol, P. Zverev, L. Ivleva, V. Osiko, and R. Powell, "Raman spectroscopy of crystals for stimulated raman scattering," *Optical materials*, vol. 11, no. 4, pp. 307–314, 1999. (Cited on page 5.)

[48] J. Menéndez and M. Cardona, "Temperature dependence of the first-order raman scattering by phonons in si, ge, and alpha-sn: Anharmonic effects," *Physical Review B*, vol. 29, pp. 2051–2059, Feb. 1984. (Cited on page 5.)

[49] A. Ewinger, G. Rinke, A. Urban, and S. Kerschbaum, "In situ measurement of the temperature of water in microchannels using laser raman spectroscopy," *Chemical Engineering Journal*, vol. 223, pp. 129–134, May 2013. (Cited on page 5.)

[50] S. P. Nikitin, C. Manka, J. Grun, and J. Bowles, "A technique for contactless measurement of water temperature using Stokes and anti-Stokes comparative Raman spectroscopy," *Review of Scientific Instruments*, vol. 83, no. 3, 2012. (Cited on page 5.)

[51] D. S. Moore and S. D. McGrane, "Raman temperature measurement," *Journal of Physics: Conference Series*, vol. 500, no. PART 19, 2014. (Cited on page 5.)

[52] B. Figueroa, R. Hu, S. G. Rayner, Y. Zheng, and D. Fu, "Real-time microscale temperature imaging by stimulated raman scattering," *The Journal of Physical Chemistry Letters*, vol. 11, pp. 7083–7089, Aug. 2020. (Cited on page 5.)

[53] J. S. Reparaz, E. Chavez-Angel, M. R. Wagner, B. Graczykowski, J. Gomis-Bresco, F. Alzina, and C. M. S. Torres, "A novel contactless technique for thermal field mapping and thermal conductivity determination: Two-laser raman thermometry," *Review of Scientific Instruments*, vol. 85, p. 034901, Mar. 2014. (Cited on page 5.)

[54] T. Dieing, O. Hollricher, and J. Toporski, *Confocal raman microscopy*, vol. 158. Springer, 2011. (Cited on page 5.)

[55] H. Vaskova, "A powerful tool for material identification: Raman spectroscopy," 2011. (Cited on page 5.)

[56] E. A. A. Pogna, X. Jia, A. Principi, A. Block, L. Banszerus, J. Zhang, X. Liu, T. Sohier, S. Forti, K. Soundarapandian, B. Terrés, J. D. Mehew, C. Trovatello, C. Coletti, F. H. L. Koppens, M. Bonn, H. I. Wang, N. van Hulst, M. J. Verstraete, H. Peng, Z. Liu, C. Stampfer, G. Cerullo, and K.-J. Tielrooij, "Hot-carrier cooling in high-quality graphene is intrinsically limited by optical phonons," *ACS Nano*, vol. 15, pp. 11285–11295, June 2021. (Cited on page 6.)

[57] M. Polyanskiy, "Refractiveindex.info." (Cited on pages 6 and 86.)

[58] C. Pradere, M. Ryu, A. Sommier, M. Romano, A. Kusiak, J. L. Battaglia, J. C. Batsale, and J. Morikawa, "Non-contact temperature field measurement of solids by infrared multispectral thermotransmittance," *Journal of Applied Physics*, vol. 121, p. 085102, Feb. 2017. (Cited on pages 6 and 14.)

[59] M. Bensalem, A. Sommier, J. C. Mindeguia, J. C. Batsale, L.-D. Patino-Lope, and C. Pradere, "Contactless transient THz temperature imaging by thermo-transmittance technique on semi-transparent materials," *Journal of Infrared, Millimeter, and Terahertz Waves*, vol. 39, pp. 1112–1126, July 2018. (Cited on page 6.)

[60] N. Kakuta, Y. Fukuhara, K. Kondo, H. Arimoto, and Y. Yamada, "Temperature imaging of water in a microchannel using thermal sensitivity of near-infrared absorption," *Lab on a Chip*, vol. 11, no. 20, pp. 3479–3486, 2011. (Cited on page 6.)

[61] N. Kakuta, H. Yamashita, D. Kawashima, K. Kondo, H. Arimoto, and Y. Yamada, "Simultaneous imaging of temperature and concentration of ethanol-water mixtures in microchannel using near-infrared dual-wavelength absorption technique," *Measurement Science and Technology*, vol. 27, no. 11, 2016. (Cited on pages 6, 9, 127 and 159.)

[62] E. Hecht, *Optics*. Addison Wesley, 4 ed., 2002. (Cited on pages 7, 9 and 135.)

[63] T. Holstein, "Optical and infrared volume absorptivity of metals [8]," *Physical Review*, vol. 96, no. 2, pp. 535–536, 1954. (Cited on page 8.)

[64] J. S. McCloy, "Methods for prediction of refractive index in glasses for the infrared," *Window and Dome Technologies and Materials XII*, vol. 8016, no. May 2011, p. 80160G, 2011. (Cited on page 8.)

[65] G. Ghosh, "Temperature dispersion of refractive indices in semiconductors," *Journal of Applied Physics*, vol. 79, no. 12, pp. 9388–9389, 1996. (Cited on page 8.)

[66] M. Minissale, C. Pardanaud, R. Bisson, and L. Gallais, "The temperature dependence of optical properties of tungsten in the visible and near-infrared domains: An experimental and theoretical study," *Journal of Physics D: Applied Physics*, vol. 50, no. 45, 2017. (Cited on page 8.)

[67] R. Rosei and D. W. Lynch, "Thermomodulation spectra of Al, Au, and Cu," *Physical Review B*, vol. 5, no. 10, pp. 3883–3894, 1972. (Cited on page 9.)

[68] M. A. Ordal, R. J. Bell, R. W. Alexander, L. L. Long, and M. R. Querry, "Optical properties of fourteen metals in the infrared and far infrared: Al, Co, Cu, Au, Fe, Pb, Mo, Ni, Pd, Pt, Ag, Ti, V, and W," *Applied Optics*, vol. 24, no. 24, p. 4493, 1985. (Cited on page 9.)

[69] A. Alabastri, S. Tuccio, A. Giugni, A. Toma, C. Liberale, G. Das, F. D. Angelis, E. D. Fabrizio, and R. P. Zaccaria, "Molding of plasmonic resonances in metallic nanostructures: Dependence of the non-linear electric permittivity on system size and temperature," *Materials*, vol. 6, no. 11, pp. 4879–4910, 2013. (Cited on pages 9 and 136.)

[70] G. Tessier, G. Jerosolimski, S. Holé, D. Fournier, and C. Filloy, "Measuring and predicting the thermoreflectance sensitivity as a function of wavelength on encapsulated materials," *Review of Scientific Instruments*, vol. 74, no. 1 II, pp. 495–499, 2003. (Cited on page 9.)

[71] J. Gong, R. Dai, Z. Wang, C. Zhang, X. Yuan, and Z. Zhang, "Temperature dependent optical constants for SiO2 film on Si substrate by ellipsometry," *Materials Research Express*, vol. 4, no. 8, 2017. (Cited on page 9.)

[72] N. W. Ashcroft and N. D. Mermin, *Solid State Physics*. Holt-Saunders, 1976. (Cited on pages 9 and 135.)

[73] F. Arvani and A. A. Shishegar, "A novel model for complex permittivity of glass for propagation modeling in millimeter-wave band," *2009 Mediterrannean Microwave Symposium, MMS 2009*, no. 2, pp. 25–28, 2009. (Cited on page 9.)

[74] H. S. Sehmi, W. Langbein, and E. A. Muljarov, "Optimizing the drude-lorentz model for material permittivity: Examples for semiconductors," *Progress in Electromagnetics Research Symposium*, pp. 994–1000, 2017. (Cited on page 9.)

[75] C. Kittel, *Introduction to Solid State Physics*. Wiley, 8 ed., 2004. (Cited on pages 9 and 135.)

[76] M. Fox, *Optical properties of solids*. Oxford Master Series in Physics, London, England: Oxford University Press, 2 ed., Mar. 2010. (Cited on page 9.)

[77] Z. Instruments, "Principle of lock-in detection and the state of the art," tech. rep., Zurich Instruments, 2016. (Cited on pages 18 and 20.)

[78] M. Heideman, D. Johnson, and C. Burrus, "Gauss and the history of the fast fourier transform," *IEEE ASSP Magazine*, vol. 1, pp. 14–21, Oct. 1984. (Cited on page 18.)

[79] G. Busse, D. Wu, and W. Karpen, "Thermal wave imaging with phase sensitive modulated thermography," *Journal of Applied Physics*, vol. 71, pp. 3962–3965, apr 1992. (Cited on pages 18, 36 and 42.)

[80] S. Grauby, B. C. Forget, S. Holé, and D. Fournier, "High resolution photothermal imaging of high frequency phenomena using a visible charge coupled device camera associated with a multichannel lock-in scheme," *Review of Scientific Instruments*, vol. 70, pp. 3603–3608, sep 1999. (Cited on pages 18 and 42.)

[81] H. R. Shanks, P. D. Maycock, P. H. Sidles, and G. C. Danielson, "Thermal conductivity of silicon from 300 to 1400k," *Physical Review*, vol. 130, pp. 1743–1748, June 1963. (Cited on pages 24 and 26.)

[82] S. W. Churchill and H. H. Chu, "Correlating equations for laminar and turbulent free convection from a vertical plate," *International Journal of Heat and Mass Transfer*, vol. 18, no. 11, pp. 1323–1329, 1975. (Cited on pages 24, 26 and 55.)

[83] D. W. Hahn and M. N. Ozisik, *Heat Conduction*. Wiley and Sons, 2012. (Cited on pages 25, 78, 90 and 153.)

[84] P. R. Griffiths, J. A. De Haseth, and J. D. Winefordner, *Fourier Transform Infrared Spectrometry*. Chichester, England: Wiley-Blackwell, 2 ed., 2007. (Cited on pages 29, 56 and 149.)

[85] H. H. Li, "Refractive index of silicon and germanium and its wavelength and temperature derivatives," *Journal of Physical and Chemical Reference Data*, vol. 9, no. 3, pp. 561–658, 1980. (Cited on pages 32, 33, 34, 149 and 153.)

[86] D. Chandler-Horowitz and P. M. Amirtharaj, "High-accuracy, midinfrared (450cm-1$\leqslant\omega\leqslant$4000cm-1) refractive index values of silicon," *Journal of Applied Physics*, vol. 97, p. 123526, June 2005. (Cited on page 32.)

[87] C. Schinke, P. C. Peest, J. Schmidt, R. Brendel, K. Bothe, M. R. Vogt, I. Kröger, S. Winter, A. Schirmacher, S. Lim, H. T. Nguyen, and D. MacDonald, "Uncertainty analysis for the coefficient of band-to-band absorption of crystalline silicon," *AIP Advances*, vol. 5, p. 067168, June 2015. (Cited on page 32.)

[88] M. A. Green, "Self-consistent optical parameters of intrinsic silicon at 300k including temperature coefficients," *Solar Energy Materials and Solar Cells*, vol. 92, pp. 1305–1310, Nov. 2008. (Cited on page 32.)

[89] E. Shkondin, O. Takayama, M. E. A. Panah, P. Liu, P. V. Larsen, M. D. Mar, F. Jensen, and A. V. Lavrinenko, "Large-scale high aspect ratio al-doped ZnO nanopillars arrays as anisotropic metamaterials," *Optical Materials Express*, vol. 7, p. 1606, Apr. 2017. (Cited on page 32.)

[90] M. Romano, M. Ryu, J. Morikawa, J. Batsale, and C. Pradere, "Simultaneous microscopic measurements of thermal and spectroscopic fields of a phase change material," *Infrared Physics and Technology*, vol. 76, pp. 65–71, May 2016. (Cited on pages 36 and 39.)

[91] US Defense Air Force, "Standard MIL-STD-150A," 1951. (Cited on pages 37, 84, 105 and 106.)

[92] P. Linstrom, "Nist chemistry webbook, nist standard reference database 69," 1997. (Cited on page 38.)

[93] Y. Souhar, *Caractérisation thermique de matériaux anisotropes à hautes températures*. Theses, Institut National Polytechnique de Lorraine, May 2011. (Cited on page 38.)

[94] J. H. Lienhard, IV and J. H. Lienhard, V, *A Heat Transfer Textbook*. Mineola, NY: Dover Publications, 5th ed., Dec. 2019. (Cited on pages 45 and 46.)

[95] C. Bourgès, S. Chevalier, J. Maire, A. Sommier, C. Pradère, and S. Dilhaire, "Infrared thermotransmittance-based temperature field measurements in semitransparent media," *Review of Scientific Instruments*, vol. 94, p. 034905, Mar. 2023. (Cited on page 54.)

[96] J. A. Nelder and R. Mead, "A simplex method for function minimization," *Comput. J.*, vol. 7, pp. 308–313, 1965. (Cited on page 54.)

[97] "fminsearch documentation Matlab." `https://fr.mathworks.com/help/matlab/ref/fminsearch.html`. (Cited on pages 54 and 67.)

[98] J. O. Berger, *Statistical Decision Theory and Bayesian Analysis*. Springer Science and Business Media, 3 2013. (Cited on page 54.)

[99] M. Groz, A. Sommier, E. Abisset, S. Chevalier, J. Battaglia, J. Batsale, and C. Pradere, "Thermal resistance field estimations from IR thermography using multiscale bayesian inference," *Quantitative InfraRed Thermography Journal*, vol. 18, pp. 332–343, July 2020. (Cited on page 54.)

[100] H. B. Curry, "The method of steepest descent for non-linear minimization problems," *Quarterly of Applied Mathematics*, vol. 2, pp. 258–261, 10 1944. (Cited on page 54.)

[101] SCHOTT Technical Glass Solutions GmbH, "Schott Borofloat 33," 2009. (Cited on page 55.)

[102] A. Edwards, "A compilation of thermal property data for computer heat-conduction calculations," 01 1969. (Cited on page 55.)

[103] "EMVA Standard 1288, Standard for Characterization of Image Sensors and Cameras Release 3.0," standard, European Machine Vision Association, emva.org, May 2010. (Cited on page 60.)

[104] I. H. Malitson, "Interspecimen comparison of the refractive index of fused silica∗,†," *J. Opt. Soc. Am.*, vol. 55, pp. 1205–1209, Oct 1965. (Cited on page 62.)

[105] C. Tan, "Determination of refractive index of silica glass for infrared wavelengths by ir spectroscopy," *Journal of Non-Crystalline Solids*, vol. 223, no. 1, pp. 158–163, 1998. (Cited on page 62.)

[106] H. G. Tompkins and E. A. Irene, *Handbook of Ellipsometry*. 2005. (Cited on pages 63 and 135.)

[107] D. Maillet and J. C. Batsale, *Thermal Quadrupoles: Solving the Heat Equation through Integral Transforms*. 2000. (Cited on page 76.)

[108] D. G. Cahill, "Thermal conductivity measurement from 30 to 750 K: The 3ω method," *Review of Scientific Instruments*, vol. 61, no. 2, pp. 802–808, 1990. (Cited on page 80.)

[109] R. A. Serway, *Principles of Physics*. Brooks/Cole, 2 ed., 1997. (Cited on page 82.)

[110] T. M. Buzug, *Computed tomography*. Springer, 2011. (Cited on page 93.)

[111] P. J. Withers, C. Bouman, S. Carmignato, V. Cnudde, D. Grimaldi, C. K. Hagen, E. Maire, M. Manley, A. Du Plessis, and S. R. Stock, "X-ray computed tomography," *Nature Reviews Methods Primers*, vol. 1, no. 1, p. 18, 2021. (Cited on page 93.)

[112] M. MINSKY, "Microscopy apparatus," Dec 1961. (Cited on page 93.)

[113] J. B. Pawley, ed., *Handbook of Biological Confocal Microscopy*. Springer US, 1990. (Cited on page 93.)

[114] D. Huang, E. A. Swanson, C. P. Lin, J. S. Schuman, W. G. Stinson, W. Chang, M. R. Hee, T. Flotte, K. Gregory, C. A. Puliafito, and J. G. Fujimoto, "Optical coherence tomography," *Science*, vol. 254, pp. 1178–1181, Nov. 1991. (Cited on page 93.)

[115] J. G. Fujimoto, C. Pitris, S. A. Boppart, and M. E. Brezinski, "Optical coherence tomography: An emerging technology for biomedical imaging and optical biopsy," *Neoplasia*, vol. 2, pp. 9–25, Jan. 2000. (Cited on page 93.)

[116] R. W. Brown, Y.-C. N. Cheng, E. M. Haacke, M. R. Thompson, and R. Venkatesan, eds., *Magnetic Resonance Imaging*. John Wiley and Sons Ltd, Apr. 2014. (Cited on page 93.)

[117] B. Quesson, J. A. de Zwart, and C. T. Moonen, "Magnetic resonance temperature imaging for guidance of thermotherapy," *Journal of Magnetic Resonance Imaging*, vol. 12, no. 4, pp. 525–533, 2000. (Cited on page 93.)

[118] A. Aouali, S. Chevalier, A. Sommier, E. Abisset-Chavanne, J.-C. Batsale, and C. Pradere, "3d infrared thermospectroscopic imaging," *Scientific Reports*, vol. 10, Dec. 2020. (Cited on page 94.)

[119] J. Radon, "Uber die bestimmung von funktionen durch hre integralwerte langs gewisser mannigfaltigkeiten," *Berichte Sashsische Akadamie der Wissenschaffen, Leipez, Math-Phys. K1.*, vol. 69, pp. 262–267, 1987. (Cited on page 94.)

[120] J. B. Garrison, D. G. Grant, W. H. Guier, and R. J. Johns, "Three dimensional roentgenography," *American Journal of Roentgenology*, vol. 105, pp. 903–908, Apr. 1969. (Cited on page 94.)

[121] D. G. Grant, "Tomosynthesis: A three-dimensional radiographic imaging technique," *IEEE Transactions on Biomedical Engineering*, vol. BME-19, pp. 20–28, Jan. 1972. (Cited on page 94.)

[122] J. T. Dobbins and D. J. Godfrey, "Digital x-ray tomosynthesis: current state of the art and clinical potential," *Physics in Medicine and Biology*, vol. 48, pp. R65–R106, oct 2003. (Cited on pages 94 and 96.)

[123] M. D. Sutton, "Tomographic techniques for the study of exceptionally preserved fossils," *Proceedings of the Royal Society B: Biological Sciences*, vol. 275, pp. 1587–1593, July 2008. (Cited on page 94.)

[124] S. R. Stock and J. D. Almer, "Diffraction microcomputed tomography of an al-matrix SiC-monofilament composite," *Journal of Applied Crystallography*, vol. 45, pp. 1077–1083, Oct. 2012. (Cited on page 94.)

[125] J. Beaulieu and P. Dutilleul, "Applications of computed tomography (CT) scanning technology in forest research: a timely update and review," *Canadian Journal of Forest Research*, vol. 49, pp. 1173–1188, Oct. 2019. (Cited on page 94.)

[126] C. Thiery, "Tomographie à rayons x," *Editions Techniques de l'Ingenieur, Techniques d'analyse*, Dec. 2013. (Cited on page 94.)

[127] J. Sharpe, U. Ahlgren, P. Perry, B. Hill, A. Ross, J. Hecksher-Sørensen, R. Baldock, and D. Davidson, "Optical projection tomography as a tool for 3d microscopy and gene expression studies," *Science*, vol. 296, pp. 541–545, Apr. 2002. (Cited on page 94.)

[128] M. C. Martin, C. Dabat-Blondeau, M. Unger, J. Sedlmair, D. Y. Parkinson, H. A. Bechtel, B. Illman, J. M. Castro, M. Keiluweit, D. Buschke, B. Ogle, M. J. Nasse, and C. J. Hirschmugl, "3D spectral imaging with synchrotron Fourier transform infrared spectro-microtomography," 2013. (Cited on page 94.)

[129] L. Koutsantonis, A.-N. Rapsomanikis, E. Stiliaris, and C. N. Papanicolas, "Examining an Image Reconstruction Method in Infrared Emission Tomography," *Infrared Physics & Technology*, vol. 98, pp. 266–277, May 2019. arXiv:1903.06609 [physics]. (Cited on page 94.)

[130] E. Maire and P. J. Withers, "Quantitative x-ray tomography," *International Materials Reviews*, vol. 59, pp. 1–43, Dec. 2013. (Cited on page 94.)

[131] N. S. O'Brien, R. P. Boardman, I. Sinclair, and T. Blumensath, "Recent advances in X-ray cone-beam computed laminography," *Journal of X-Ray Science and Technology*, vol. 24, no. 5, pp. 691–707, 2016. (Cited on pages 94 and 151.)

[132] H. Gao, L. Zhang, Z. Chen, Y. Xing, J. Cheng, and Z. Qi, "Direct filtered-backprojection-type reconstruction from a straight-line trajectory," *Optical Engineering*, vol. 46, p. 057003, 2007. (Cited on page 94.)

[133] M. Maisl, F. Porsch, and C. Schorr, "Computed laminography for x-ray inspection of lightweight constructions," 2010. (Cited on page 94.)

[134] L. Helfen, A. Myagotin, P. Mikulík, P. Pernot, A. Voropaev, M. Elyyan, M. Di Michiel, J. Baruchel, and T. Baumbach, "On the implementation of computed laminography using synchrotron radiation," *Review of Scientific Instruments*, vol. 82, p. 063702, jun 2011. (Cited on pages 94, 96 and 97.)

[135] A. Myagotin, A. Voropaev, L. Helfen, D. Hanschke, and T. Baumbach, "Efficient Volume Reconstruction for Parallel-Beam Computed Laminography by Filtered Backprojection on Multi-Core Clusters," *IEEE Transactions on Image Processing*, vol. 22, pp. 5348–5361, dec 2013. (Cited on pages 94, 97 and 99.)

[136] J. Zhou, X. Rao, X. Liu, T. Li, L. Zhou, Y. Zheng, and Z. Zhu, "Temperature dependent optical and dielectric properties of liquid water studied by terahertz time-domain spectroscopy," *AIP Advances*, vol. 9, no. 3, 2019. (Cited on page 94.)

[137] T. Blumensath, "Backprojection inverse filtration for laminographic reconstruction," *IET Image Processing*, vol. 12, pp. 1541–1549, sep 2018. (Cited on page 96.)

[138] A. Voropaev, A. Myagotin, L. Helfen, and T. Baumbach, "Direct Fourier Inversion Reconstruction Algorithm for Computed Laminography," *IEEE Transactions on Image Processing*, vol. 25, pp. 2368–2378, may 2016. (Cited on pages 96 and 99.)

[139] S. Harasse, W. Yashiro, and A. Momose, "Iterative reconstruction in x-ray computed laminography from differential phase measurements," *Optics Express*, vol. 19, p. 16560, aug 2011. (Cited on page 96.)

[140] S. V. Venkatakrishnan, E. Cakmak, H. Billheux, P. Bingham, and R. K. Archibald, "Model-based iterative reconstruction for neutron laminography," in *2017 51st Asilomar Conference on Signals, Systems, and Computers*, IEEE, Oct. 2017. (Cited on page 96.)

[141] K. M. Hanson, "Bayesian and related methods in image reconstruction from incomplete data," *Image Recovery: Theory and Application*, pp. 79–125, 1987. (Cited on page 96.)

[142] A. C. Kak and M. Slaney, *Principles of Computerized Tomographic Imaging*. Society for Industrial and Applied Mathematics, jan 2001. (Cited on page 96.)

[143] J.-M. Que, D.-Q. Cao, W. Zhao, X. Tang, C.-L. Sun, Y.-F. Wang, C.-F. Wei, R.-J. Shi, L. Wei, Z.-Q. Yu, and Y.-L. Yan, "Computed laminography and reconstruction algorithm," *Chinese Physics C*, vol. 36, pp. 777–783, aug 2012. (Cited on page 97.)

[144] G. Dougherty and Z. Kawaf, "The point spread function revisited: image restoration using 2-d deconvolution," *Radiography*, vol. 7, pp. 255–262, Nov. 2001. (Cited on page 104.)

[145] M. J. Nasse, J. C. Woehl, and S. Huant, "High-resolution mapping of the three-dimensional point spread function in the near-focus region of a confocal microscope," *Applied Physics Letters*, vol. 90, p. 031106, Jan. 2007. (Cited on page 104.)

[146] J. Li, F. Xue, and T. Blu, "Fast and accurate three-dimensional point spread function computation for fluorescence microscopy," *Journal of the Optical Society of America A*, vol. 34, p. 1029, May 2017. (Cited on page 104.)

[147] E. Peli, "Contrast in complex images," *Journal of the Optical Society of America A*, vol. 7, p. 2032, Oct. 1990. (Cited on page 110.)

[148] P. Uprety, M. M. Junda, and N. J. Podraza, "Optical properties of borosilicate glass from 3.1 mm to 210 nm (0.4 meV to 5.89 eV) by spectroscopic ellipsometry," *Surface Science Spectra*, vol. 24, no. 2, p. 026003, 2017. (Cited on page 135.)

[149] R. J. Mathar, "Refractive index of humid air in the infrared: Model fits," *Journal of Optics A: Pure and Applied Optics*, vol. 9, no. 5, 2007. (Cited on page 135.)

[150] A. Block, M. Liebel, R. Yu, M. Spector, Y. Sivan, F. J. García De Abajo, and N. F. Van Hulst, "Tracking ultrafast hot-electron diffusion in space and time by ultrafast thermomodulation microscopy," *Science Advances*, vol. 5, no. 5, pp. 1–8, 2019. (Cited on page 136.)

[151] W. E. Lawrence and J. W. Wilkins, "Electron-electron scattering in the transport coefficients of simple metals," *Physical Review B*, vol. 7, pp. 2317–2332, Mar. 1973. (Cited on page 136.)

[152] M. Xu, J.-Y. Yang, and L. Liu, "Temperature-dependent dielectric functions of bcc transition metals cr, mo, and w from ultraviolet to infrared regions: A theoretical and experimental study," *Journal of Applied Physics*, vol. 123, p. 155102, Apr. 2018. (Cited on page 136.)

[153] A. N. Smith and P. M. Norris, "Influence of intraband transitions on the electron thermoreflectance response of metals," *Applied Physics Letters*, vol. 78, no. 9, pp. 1240–1242, 2001. (Cited on page 136.)

[154] L. Yu, S. Vudayagiri, L. A. Jensen, and A. L. Skov, "Temperature dependence of dielectric breakdown of silicone-based dielectric elastomers," *International Journal of Smart and Nano Materials*, vol. 11, no. 2, pp. 129–146, 2020. (Cited on page 136.)

List of Figures

List of Tables

Traduction française de l'introduction

Cette thèse a été réalisée au laboratoire I2M au sein de l'équipe ICT (Imagerie et Caractérisation Thermique). L'activité principale est la caractérisation thermique quantitative non-destructive de systèmes énergétiques et de matériaux multi-échelles. Les méthodes utilisées par l'équipe de recherche combinent la thermographie infrarouge et les méthodes inverses pour caractériser les transferts de chaleur et de masse dans les milieux étudiés. Cependant, en ce qui concerne les systèmes comportant des géométries complexes ou des milieux inhomogènes avec des sources de température volumiques par exemple, nous avons besoin de connaissances a priori pour pouvoir utiliser les méthodes inverses pour déterminer les propriétés thermiques ou la structure du matériau. D'où le besoin de mesures tomographiques multi-physiques, et notamment à l'échelle micrométrique pour l'étude des systèmes énergétiques miniaturisés.

Deux options sont possibles pour réaliser une caractérisation 3D du transfert de chaleur dans un échantillon en utilisant la thermographie infrarouge. Si le matériau est opaque aux infrarouges, on peut effectuer une mesure de la température de surface et utiliser des méthodes inverses pour reconstruire le volume. Cette méthode est efficace pour les milieux dont la géométrie et les propriétés thermiques sont connues : l'inversion est possible bien que limitée par le bruit de mesure. Cette méthode est déjà appliquée et continue d'être développée par l'équipe. D'autre part, si l'échantillon est semi-transparent, on peut effectuer des mesures directes de son volume ce qui permet d'aborder des géométries plus complexes sans connaissance préalable du système. Cette technique permet de déterminer les propriétés thermiques de systèmes complexes à l'aide d'une seule tomographie et d'un modèle approprié.

Dans la communauté thermique, l'étude de milieux semi-transparents à l'infrarouge est encore assez peu développée en raison de la difficulté d'analyser la provenance du signal IR émis par ces matériaux. Par conséquent, ce travail de thèse vise à proposer un dispositif expérimental et des méthodes de post-traitement associées pour la mesure directe des propriétés thermiques des milieux semi-transparents, dans un premier temps en 2D, puis en 3D pour réaliser un tomographe thermique. Afin de ne pas endommager l'échantillon, j'ai choisi une méthode de mesure sans contact, ce qui est maintenant une condition essentielle pour de nombreuses applications industrielles et pour ne pas perturber le transfert de chaleur étudié.

Ainsi, la première étape consiste à identifier une méthode sans contact adaptée à la mesure des champs de température volumiques dans des milieux semi-transparents à l'infrarouge. Le chapitre introductif comprend une section bibliographique sur différentes méthodes de mesure de température sans contact. Dans un premier temps sont présentées les méthodes utilisées en présence de milieux opaques, l'accent est mis sur la thermographie infrarouge. Dans un second temps sont présentées les méthodes utilisées pour la caractérisation de milieux semi-transparents, avec notamment l'introduction du phénomène de thermotransmittance étudié dans ces travaux de thèse. Ainsi, la section suivante développe davantage la méthode de thermotransmittance et introduit la relation entre le signal de thermotransmittance et le champ de température qui est utilisée dans la suite du manuscrit.

L'objectif final de ce travail de thèse est de mesurer le transfert de chaleur en 3D dans des matériaux semi-transparents à l'infrarouge. Nous avons identifié que la thermotransmittance est

un excellent candidat pour effectuer de telles mesures. Afin d'atteindre notre objectif, nous devons d'abord résoudre les défis suivants :

→ Développer et valider la technique d'imagerie utilisant la thermotransmittance, puisque cette mesure n'était pas disponible dans le laboratoire au début de la thèse. Le principal défi consiste à détecter le signal de thermotransmittance, car les variations des propriétés optiques en fonction de la température sont faibles (variations inférieures à 1 pour 1000 pour un DT de 1K en fonction des matériaux et des longueurs d'onde d'illumination).

→ Etalonner le coefficient de thermotransmittance pour convertir le signal mesuré en température, ce qui nécessite de connaître la température de l'échantillon à l'aide d'un modèle thermique, d'une mesure directe ou d'une combinaison des deux.

→ Sélectionner un échantillon approprié pour développer le banc expérimental de mesure de thermotransmittance en 3D. Comme mentionné dans la section présentant la thermotransmittance, le signal d'intérêt doit provenir du volume de l'échantillon par le biais de son absorbance.

→ Développer et valider un banc expérimental tomographique puis intégrer la mesure la thermotransmittance pour obtenir un tomographe thermique.

Pour développer le thermographe 3D, le travail a été progressivement étendu de mesures 1D sur un échantillon macroscopique à des mesures 3D sur un échantillon microscopique. Ce manuscrit est divisé en deux parties, chacune composée de deux chapitres. L'objectif principal de la partie 1 est de développer et de valider le dispositif expérimental de thermotransmittance par imagerie avec des milieux homogènes macroscopiques.

- Dans le chapitre 2, nous utilisons des instruments de mesure très sensibles mais à mono-point pour améliorer le rapport signal/bruit et valider la mesure d'un signal de thermotransmittance. De plus, unun modèle thermique est développé pour déterminer les conditions de mesure optimales. Dans cette section, nous choisissons un échantillon simple homogène avec des propriétés optiques non dispersives dans la game spectrale étudiée.

- Dans le chapitre 3, nous améliorons le banc de mesure 1D pour faire de l'imagerie par thermotransmittance. De plus, l'échantillon est remplacé par un un autre matériau plus sophistiqué dont les propriétés thermo-optiques varient avec la longueur d'onde d'illumination, ce qui permet d'étudier l'origine du signal de thermotransmittance. Pour mieux comprendre la dépendance thermique des propriétés optiques et déterminer si l'échantillon convient au développement tomographique, nous utilisons un modèle optique basé sur la théorie de Drude-Lorentz.

La seconde partie du manuscrit se concentre sur la mise en œuvre du banc tomographique à micro-échelle.

- Le chapitre 4 présente l'échantillon et le dispositif de chauffage microscopiques conçus pour le développement de la tomographie, afin d'obtenir des gradients de température dans l'épaisseur du matériau. Nous améliorons le banc décrit au chapitre 3 pour réaliser des mesures de thermotransmittance à l'échelle micrométrique. Ensuite, nous mesurons le champ de thermotransmittance 2D de l'échantillon qui est proportionnel à la moyenne de la température dans l'épaisseur du matériau.

- Enfin, dans le chapitre 5, nous présentons les différentes options pour les mesures tomographiques et expliquons le choix de la laminographie. Le dispositif expérimental de laminographie est développé, ainsi que l'algorithme de reconstruction tomographique. Enfin, sont commentées les premières mesures de thermotransmittance 3D à micro-échelle.

Traduction française de la conclusion

L'objectif principal de cette thèse consistait à développer et valider un banc expérimental de tomographie pour mesurer des transferts de chaleur volumiques dans des milieux semi-transparents à l'infrarouge. Ce travail est le premier pas vers la caractérisation multi-physique de systèmes énergétiques complexes, comme les mémoires à changement de phase, les piles microfluidiques, ou encore les micro-batteries.

Dans l'introduction, le phénomène de thermotransmittance a été identifié pour répondre à ce challenge scientifique. Toutefois, la méthode n'étant pas disponible dans l'équipe de recherche d'accueil au début de la thèse, deux sous-objectifs sont apparus: dans un premier temps, développer et valider la mesure de thermotransmittance 2D quantitative pour des matériaux homogènes, puis dans un second temps, identifier et implémenter un dispositif tomographique adapté à la mesure de thermotransmittance.

Pour atteindre ces objectifs, j'ai développé plusieurs dispositifs expérimentaux pilotés avec LabView et implémenté des algorithmes de post-traitement des mesures de thermotransmittance. Le Chapitre 2 introduit le premier banc expérimental qui a permis de valider la technique de thermotransmittance modulée en utilisant un matériau homogène et des instruments de mesure sensibles mais mono-point pour améliorer le rapport signal-à-bruit (RSB). En effet, améliorer le RSB est crucial lorsque l'on travaille avec la thermotransmittance puisque la dépendance en température des propriétés optiques des matériaux est généralement faible ($\kappa \approx 10^{-4} K^{-1}$).

Le Chapitre 3 présente l'adaptation du premier dispositif expérimental pour faire de l'imagerie par thermotransmittance, notamment en utilisant comme détecteur une caméra infrarouge. Un modèle thermique a été développé puis combiné aux mesures en utilisant des méthodes inverses, ce qui a permis d'extraire les propriétés thermiques d'une lame de Borofloat ainsi que son coefficient de thermotransmittance. Pour aller plus loin dans la compréhension du phénomène de thermotransmittance, un modèle thermo-optique basé sur la théorie des oscillateurs de Lorentz a été développé pour comprendre l'origine du signal. L'analyse a montré que l'absorbance d'un matériau donne une information sur la température volumique tandis que la réflexion est sensible à la température de surface. Par conséquent, les matériaux composés de SiO , comme le Borofloat, sont de bons candidats pour développer le tomographe thermique puisqu'ils sont absorbant et peu réfléchissant dans l'infrarouge.

Après avoir validé la mesure de thermotransmittance par imagerie infrarouge, la prochaine étape consistait donc à développer le tomographe thermique. Avant cela, afin de créer un champ de température volumique non uniforme dans le matériau, les dimensions du dispositif de chauffage et de l'échantillon ont été réduites (mesure à l'échelle micrométrique). Le Chapitre 4 présente donc le nouveau modèle thermique et les modifications sur le précédent banc expérimental pour réaliser des mesures de thermotransmittance à l'échelle micrométrique. De plus, la mesure de thermotransmittance a été combinée à la technique 3ω pour calibrer le signal mesuré et extraire la diffusivité thermique et le coefficient de thermotransmittance du matériau étudié.

Enfin, le Chapitre 5 présente le banc expérimental de laminographie infrarouge pour mesurer le signal de thermotransmittance 3D d'un échantillon semi-transparent. Tout d'abord, j'ai implémenté et validé l'algorithme de reconstruction 3D à l'aide de premières reconstructions sur des objets

numériques, puis sur des objets réels calibrés. La dernière étape a été de combiner la mesure de thermotransmittance et le tomographe pour reconstruire un champ de thermotransmittance 3D. Ainsi, j'ai validé expérimentalement la mesure de thermotransmittance par imagerie infrarouge pour réaliser des mesures quantitatives de température dans des milieux semi-transparents à l'infrarouge, et développé un dispositif tomographique thermique.

Travaux futurs

Concernant les travaux futurs à mener en thermotransmittance, je commencerai par évoquer les pistes d'améliorations à apporter au dispositif expérimental actuel, puis je discuterai des possibilités offertes par la thermotransmittance.

Tout d'abord, les prochains travaux sur le tomographe thermique doivent se concentrer sur l'amélioration de l'algorithme de reconstruction 3D afin de filtrer les artefacts de reconstruction et de permettre des mesures quantitatives. Comme mentionné au chapitre 5, plusieurs options peuvent être étudiées : contraindre la reconstruction à l'aide de méthodes bayésiennes par exemple, filtrer les artefacts à l'aide de la PSF 3D de la reconstruction, ou encore effectuer des mesures avec différents angles de laminographie et comparer les résultats. Cependant, comme le champ de température 3D que nous avons l'intention de mesurer est diffus et sans bords nets, nous devons veiller à ne pas couper les composantes spatiales à basse fréquence en cherchant à filtrer les artefacts.

Par ailleurs, le seuil de détection du dispositif actuel est d'environ $\Delta T = 1$K pour le Borofloat. Cependant, cette valeur dépend du coefficient de thermotransmittance et est donc fonction du matériau et de la longueur d'onde d'illumination, comme le montre le chapitre 3. En comparaison, le seuil de détection du silicium avec le banc expérimental actuel est d'environ 7 K. En outre, bien que la source IR actuelle soit stabilisée, nous avons remarqué au chapitre 3 que le bruit de mesure dû aux fluctuations du faisceau IR est deux fois plus élevé que le bruit de mesure de la caméra IR. Par conséquent, pour effectuer des mesures de thermotransmittance dans des matériaux dont le coefficient de thermotransmittance est faible ($< 10^{-4}K^{-1}$), il faut augmenter le seuil de détection, en utilisant un faisceau IR plus puissant (environ 1 W/m^2 actuellement), une source bien stabilisée, et un détecteur sensible.

Un autre point clé est la fréquence d'excitation thermique qui se situe actuellement dans la gamme [5 - 50] mHz. Dans ces travaux de thèse, j'ai dû trouver un compromis entre la fréquence de travail et les variations minimales de température pour mesurer un signal de thermotransmittance. Pour travailler à des fréquences plus élevées, potentiellement avec un échauffement moindre de l'échantillon, nous devons améliorer le seuil de détection.

Dans ce travail, nous avons utilisé la thermotransmittance pour mesurer les variations de température et les propriétés thermiques de milieux semi-transparents à l'infrarouge. En outre, je pense que cette technique pourrait être utilisée pour caractériser d'autres propriétés de ces milieux. Pour développer pleinement la caractérisation des milieux semi-transparents à l'aide de la thermotransmittance, nous devons compléter une base de données du coefficient de thermotransmittance en fonction de la longueur d'onde et de l'épaisseur des matériaux. Cette connaissance serait précieuse pour l'analyse d'échantillons multicouches semi-transparents et la compréhension du signal de thermotransmittance de milieux non homogènes. De plus, la connaissance des contributions de la réflectance et de l'absorbance dans le signal de thermotransmittance nous permettrait d'obtenir des informations

simultanées sur les interfaces et le volume du matériau. Nous pourrions par exemple extraire les résistances thermiques entre différentes couches et les variations de température dans le volume de l'échantillon. Le balayage de la longueur d'onde d'illumination nous permettra également de distinguer le signal de thermotransmittance des différentes composantes du matériau si leur coefficient de thermotransmittance n'est pas constant sur la gamme spectrale étudiée.

Dans toutes les expériences que nous avons présentées dans ce manuscrit, nous avons également mesuré l'émission propre de l'échantillon. Il serait très intéressant de combiner la mesure de la thermotransmittance avec celle de l'émission propre pour déterminer l'émittance du matériau par exemple. En outre, le signal de l'émission propre est nettement moins bruité que celui de la thermotransmittance. En utilisant la thermotransmittance pour étalonner le signal d'émission propre, nous pourrions améliorer le RSB de notre mesure et détecter des variations de température plus faibles. Par conséquent, la combinaison de ces deux mesures est un point clé pour les travaux futurs.

Un autre phénomène intéressant non mentionné dans cette étude est que le signal transmis à travers un milieu semi-transparent est également une fonction de la concentration du milieu. Par conséquent, nous pourrions combiner les mesures de transfert de chaleur et de masse en utilisant le signal transmis à travers l'échantillon [61] et un balayage multispectral. Cette approche conviendrait parfaitement à l'étude de piles microfluidiques ou de diverses réactions chimiques.

Enfin, les prochains travaux devront déterminer la limite d'application de la mesure de thermotransmittance, notamment en ce qui concerne la diffusion : au niveau des surfaces, avec des mesures de BRDF par exemple, et dans le volume du matériau. Pour ce faire, je suggère de travailler avec un milieu dopé de particules de différentes tailles et concentrations afin de déterminer l'impact de la diffusion sur le signal de thermotransmittance.

En conclusion, l'étude des phénomènes de thermotransmittance est très prometteuse pour caractériser des milieux semi-transparents, comme la détermination de leurs propriétés thermiques (conductivité, diffusivité, résistance de contact) ou pour réaliser des mesures quantitatives de transferts de chaleur et de masse volumiques.

Thermographie dans des milieux semi-transparents à l'infrarouge par thermotransmittance

Résumé

Ces travaux de thèse s'inscrivent dans le cadre d'un besoin grandissant de caractérisation multi-physique de nouveaux matériaux ou de systèmes énergétiques. A l'échelle du laboratoire, le développement des études sur les systèmes microfluidiques et les matériaux multicouches nécessitent d'investiguer les transferts thermiques volumiques. Ces systèmes étant pour la plupart des milieux semi-transparents à l'infrarouge (IR), la caractérisation quantitative sans contact des champs de température est un véritable enjeu scientifique et industriel.

L'objectif de ces travaux de thèse est donc de développer et de valider une méthode de mesure quantitative de tomographie microscopique IR pour caractériser des milieux semi-transparents. Nous avons choisi une méthode basée sur la dépendance en température des propriétés optiques des matériaux, et particulièrement leur transmittance. Ce phénomène est appelé thermotransmittance et donne une information sur la température moyenne dans l'épaisseur du matériau. Ainsi, la mesure de thermotransmittance combinée à un dispositif tomographique doit permettre la mesure de température des milieux semi-transparents.

Le principal verrou scientifique identifié pour l'utilisation de cette méthode est le très faible niveau de signal de thermotransmittance mesuré en comparaison du bruit de mesure et du rayonnement IR parasite. Dans un premier temps, les travaux se sont donc focalisés sur le développement d'une méthode de détection mono-point du signal de thermotransmittance avec la mise en place d'un dispositif expérimental robuste aux bruits de mesure. Un modèle thermo-optique a également accompagné ce développement de la mesure pour apporter une compréhension quantitative du phénomène de thermotransmittance. Puis, une fois validée, l'instrumentation a évoluée vers une mesure de champs de température en 2D par caméra IR. Enfin, couplées à des modèles thermiques, ces mesures de champs ont permis d'estimer les propriétés thermophysiques des matériaux étudiés.

Une fois la mesure quantitative de thermotransmittance par imagerie IR validée, la suite des travaux porte sur l'implémentation d'un dispositif de mesure tomographique par laminographie. L'imagerie par thermotransmittance couplée à l'instrumentation par laminographie et à des méthodes de reconstruction permet de reconstruire des champs volumiques de température. Une preuve de concept de cette méthode est présentée à la fin du manuscrit.

Mots-clés : Thermotransmittance infrarouge, Milieux semi-transparents, Transferts de chaleur, Laminographie, Microscopie

Thermography in semitransparent media based on mid-infrared thermotransmittance

Abstract

This thesis work is part of a growing need for multi-physics characterization of new materials or energy systems. At laboratory level, the development of studies on micro-fluidic systems and multi-layer materials requires the investigation of 3D heat transfer. Since most of these systems are semi-transparent in the infrared (IR), conventional thermography methods are not well suited to their characterization. The development of a new technique for contactless quantitative characterization of temperature fields in these semitransparent media is a scientific and industrial challenge.

The aim of this thesis work is developing and validating a quantitative measurement technique using IR microscopic tomography to characterize semi-transparent media. We have chosen a method based on the temperature dependence of materials optical properties, particularly their transmittance. This phenomenon is known as thermotransmittance, and provides information on the average temperature across the thickness of the material. Thermotransmittance measurement combined with a tomographic device will enable us to measure the 3D temperature field of semitransparent media.

The main scientific drawback identified for the use of this method is the weak thermotransmittance signal measured, compared with measurement noise and parasitic IR radiation. Initially, work focused on developing a single-point detection method for the thermotransmittance signal, with the implementation of an experimental setup robust to measurement noise. A thermo-optical model was also developed to provide a quantitative understanding of the thermotransmittance phenomenon. Once validated, the instrumentation was upgraded to 2D temperature field measurement using an IR camera. Finally, coupled with thermal models, these field measurements were used to estimate the thermophysical properties of the studied materials.

Once quantitative measurement of thermotransmittance using IR imaging had been validated, the next step was to implement a tomographic measurement system using laminography. Thermotransmittance imaging, coupled with laminographic instrumentation and reconstruction methods, enables 3D temperature fields to be reconstructed. A proof-of-concept of this method is presented at the end of the manuscript.

Keywords: Infrared thermotransmittance, semitransparent media, heat transfer, laminography, microscopy

Unité de recherche
UMR 5295, Université de Bordeaux, Talence 33400, France